

South Taranaki Bight Iron Sand Mining Nearshore Wave Modelling

Phase 4 Studies

Prepared for Trans-Tasman Resources

Updated November 2015

Authors/Contributors:

Richard Gorman

For any information regarding this report please contact:

Richard Gorman
Coastal and Estuarine Research
+64-7-856 7026
r.gorman@niwa.co.nz

National Institute of Water & Atmospheric Research Ltd
Gate 10, Silverdale Road
Hillcrest, Hamilton 3216
PO Box 11115, Hillcrest
Hamilton 3251
New Zealand

Phone +64-7-856 7026
Fax +64-7-856 0151

NIWA Client Report No: HAM2013-091
Report Date: October 2013
NIWA Project: TTR12204

© All rights reserved. This publication may not be reproduced or copied in any form without the permission of the copyright owner(s). Such permission is only to be given in accordance with the terms of the client's contract with NIWA. This copyright extends to all forms of copying and any storage of material in any kind of information retrieval system.

Whilst NIWA has used all reasonable endeavours to ensure that the information contained in this document is accurate, NIWA does not give any express or implied warranty as to the completeness of the information contained herein, or that it will be suitable for any purpose(s) other than those specifically contemplated during the Project or agreed by NIWA and the Client.

Contents

- Executive summary9**
- 1 Introduction13**
- 2 Modelling methods.....15**
 - 2.1 The SWAN model15
 - 2.2 Model domains for SWAN simulations15
 - 2.3 External forcing18
 - 2.4 Sensitivity testing – Phase 4.....19
 - 2.5 Bathymetry modifications – Phase 419
 - 2.6 Environmental scenarios – Phase 423
 - 2.7 Long-term simulations23
 - 2.8 Nearshore processes26
 - 2.9 Moored vessel simulations27
- 3 Model verification.....28**
 - 3.1 Field measurements.....28
 - 3.2 Model Verification – Phase 4.....29
- 4 Wave sensitivity test results31**
 - 4.1 Sensitivity to bathymetry modifications – Phase 431
 - 4.2 Sensitivity to moored vessels – Phase 463
- 5 References.....73**
- Appendix A Spectral wave statistics75**
- Appendix B Nearshore wave and sediment transport statistics.....77**
- Appendix C Wave model verification - Phase 4 full results80**
- Appendix D Sensitivity to bathymetry modifications - Phase 4 full results124**

Tables

- Table 2-1: Parameters specifying grids established for SWAN simulations. 16
- Table 2-2: Environmental scenarios used in Phase 4 sensitivity studies. 23
- Table 2-3: Mooring positions for the FPSO used in simulations of wave blocking. 27
- Table 3-1: Locations of instruments collecting wave data. 29
- Table 4-1: Maximum changes in significant wave height predicted for the eight bathymetry modification cases. 38

Figures

Figure 2-1: Map showing bathymetry in the Greater Cook Strait region, with the extent of grid domains marked.	17
Figure 2-2: Bathymetry for the Xantia_100mB model domain – Phase 4.	18
Figure 2-3: Location of proposed mining areas in the South Taranaki Bight.	21
Figure 2-4: Outlines of the hypothetical bathymetry changes tested in Phase 4 modelling.	22
Figure 2-5: Probability distribution functions for significant wave height at (40°S, 174°E), in the years 2008 through 2012, from NZWAVE-12 forecasts.	24
Figure 2-6: Probability distribution functions for second moment mean wave period at (40°S, 174°E), in the years 2008 through 2012, from NZWAVE-12 forecasts.	25
Figure 2-7: Probability distribution functions for mean wave direction at (40°S, 174°E), in the years 2008 through 2012, from NZWAVE-12 forecasts.	25
Figure 4-1: Wave conditions in environmental scenario 6 of the Phase 4 simulations, with existing bathymetry.	32
Figure 4-2: Difference between significant wave height (in metres) for case 1 and existing bathymetry, over the model domain, for environmental scenario 6.	33
Figure 4-3: Wave conditions in all six environmental scenarios of the Phase 3 simulations, with existing bathymetry.	34
Figure 4-4: Directional wave spectrum at (39.955°S, 174.069°E), or (X, Y) = (-19713.3, 93803.1), from all six environmental scenarios using baseline bathymetry.	35
Figure 4-5: Difference between significant wave height for case 1 and existing bathymetry, over the model domain, for each of the six environmental scenarios.	36
Figure 4-6: Wave parameters at the 10 m isobath with existing bathymetry, in all 6 environmental scenarios.	39
Figure 4-7: Difference between wave parameters at the 10 m isobath for case 1 and existing bathymetry, in all 6 environmental scenarios.	40
Figure 4-8: Maximum (over six environmental scenarios) of the absolute change in wave parameters at the 10m isobath.	41
Figure 4-9: Mean (over six environmental scenarios) of the absolute change in wave parameters (in metres) at the 10m isobath.	42
Figure 4-10: Maximum (over six environmental scenarios) of the relative change in wave parameters (as a fraction of the baseline values) at the 10m isobath.	43
Figure 4-11: Mean (over six environmental scenarios) of the relative change in wave parameters (as a fraction of the baseline values) at the 10m isobath.	44
Figure 4-12: Mean values and standard deviation of wave statistics at the 10 m isobath, from the baseline long-term simulation.	47
Figure 4-13: Mean (bias) and standard deviation of the difference between the case 1 and baseline long-term simulations of wave statistics at the 10 m isobath.	48
Figure 4-14: Root-mean-square difference in wave statistics at the 10 m isobath, between the case 1 and baseline long-term simulations.	49
Figure 4-15: Mean fractional difference in values of wave statistics at the 10 m isobath, between the case 1 and baseline long-term simulations.	50
Figure 4-16: Normalised root-mean-square difference in wave statistics at the 10 m isobath, between the case 1 and baseline long-term simulations.	51

Figure 4-17:	Breaking wave height H_b at the coast.	54
Figure 4-18:	Net onshore flux factor P_{os} at the coast.	55
Figure 4-19:	Net longshore flux factor P_{ls} (black scales) and sediment flux Q (gold scales) at the coast.	56
Figure 4-20:	Magnitude of the longshore flux factor P_{ls} (black scales) and sediment flux Q (gold scales).	57
Figure 4-21:	Magnitude of the longshore flux factor P_{ls} (black scales) and sediment flux Q (gold scales), averaged over times when they have positive values. 58	
Figure 4-22:	Magnitude of the longshore flux factor P_{ls} (black scales) and sediment flux Q (gold scales), averaged over times when they have negative values.	59
Figure 4-23:	Divergence of the longshore flux factor P_{ls} (black scales) and sediment flux Q (gold scales).	60
Figure 4-24:	Component of longshore mean current associated with oblique wave incidence $V_{ls,obl}$.	61
Figure 4-25:	Component of longshore mean current associated with wave height gradient $V_{ls,hgrad}$.	62
Figure 4-26:	Difference between significant wave height over the model domain in simulations with and without a FPSO moored at Position 1 in orientation 1 (E-W), for each of the six environmental scenarios, assuming full reflection.	64
Figure 4-27:	Difference between wave parameters at the 10 m isobath in simulations with and without a FPSO moored at position 1 in orientation 1 (E-W), for each of the six environmental scenarios, assuming full reflection.	65
Figure 4-28:	Difference between significant wave height over the model domain in simulations with and without a FPSO moored at position 2 in orientation 3 (N-S), for each of the six environmental scenarios, assuming full reflection.	66
Figure 4-29:	Difference between wave parameters at the 10 m isobath in simulations with and without a FPSO moored at Position 2 in orientation 3 (N-S), for each of the six environmental scenarios, assuming full reflection.	67
Figure 4-30:	Mean values, over the 6 environmental scenarios, of the magnitude of the difference between wave parameters at the 10 m isobath in simulations with and without a moored FPSO assuming full reflection.	68
Figure 4-31:	Mean values, over the 6 environmental scenarios, of the magnitude of the relative difference between wave parameters at the 10 m isobath in simulations with and without a moored FPSO assuming full reflection.	69
Figure 4-32:	Difference between significant wave height over the model domain in simulations with and without a FPSO moored at Position 1 in orientation 1 (E-W), for each of the six environmental scenarios, assuming no reflection.	70
Figure 4-33:	Mean values, over the 6 environmental scenarios, of the magnitude of the difference between wave parameters at the 10 m isobath in simulations with and without a moored FPSO assuming no reflection.	71
Figure 4-34:	Mean values, over the 6 environmental scenarios, of the magnitude of the relative difference between wave parameters at the 10 m isobath in simulations with and without a moored FPSO assuming no reflection.	72

Figure C-1: Comparison of wave statistics measured at the Baring Head Waverider buoy, with outputs from the Greater Cook Strait wave model.	83
Figure C-2 (a): Comparison of wave statistics measured at the Site 8 Waverider buoy, with outputs from the Xantia 100m wave model.	84
Figure C-3 (a): Comparison of wave statistics measured at the Site 7 ADCP with outputs from the Xantia 100m wave model.	87
Figure C-4 (a): Comparison of wave statistics measured at the Site 6 ADCP, with outputs from the Xantia 100m wave model.	90
Figure C-5 (a): Comparison of wave statistics measured at the Site 5 ADCP, with outputs from the Xantia 100m wave model.	93
Figure C-6 (a): Comparison of wave statistics measured at the Site 4 Dobie, with outputs from the Xantia 100m wave model.	96
Figure C-7 (a): Comparison of wave statistics measured at the Site 3 Dobie, with outputs from the Xantia 100m wave model.	98
Figure C-8 (a): Comparison of wave statistics measured at the Site 2 Dobie, with outputs from the Xantia 100m wave model.	100
Figure C-9 (a): Comparison of wave statistics measured at the Site 1 Dobie, with outputs from the Xantia 100m wave model.	102
Figure C-10: Time sequence of frequency spectra at Site 8.	104
Figure C-11: Time sequence of frequency spectra at Site 7.	105
Figure C-12: Time sequence of frequency spectra at Site 6.	106
Figure C-13: Time sequence of frequency spectra at Site 5.	107
Figure C-14: Time sequence of frequency spectra at Site 4.	108
Figure C-15: Time sequence of frequency spectra at Site 3.	109
Figure C-16: Time sequence of frequency spectra at Site 2.	110
Figure C-17: Time sequence of frequency spectra at Site 1.	111
Figure C-18: Comparison of surface sea level variance within selected frequency bands at Site 8.	112
Figure C-19: Comparison of surface sea level variance within selected frequency bands at Site 7.	113
Figure C-20: Comparison of surface sea level variance within selected frequency bands at Site 6.	114
Figure C-21: Comparison of surface sea level variance within selected frequency bands at Site 5.	115
Figure C-22: Comparison of surface sea level variance within selected frequency bands at Site 4.	116
Figure C-23: Comparison of surface sea level variance within selected frequency bands at Site 3.	117
Figure C-24: Comparison of surface sea level variance within selected frequency bands at Site 2.	118
Figure C-25: Comparison of surface sea level variance within selected frequency bands at Site 1.	119
Figure C-26: Comparison of surface sea level variance within selected frequency bands at Site 4 normalised by the corresponding values at Site 8.	120
Figure C-27: Comparison of surface sea level variance within selected frequency bands at Site 3 normalised by the corresponding values at Site 8.	121
Figure C-28: Comparison of surface sea level variance within selected frequency bands at Site 2 normalised by the corresponding values at Site 8.	122

Figure C-29: Comparison of surface sea level variance within selected frequency bands at Site 1 normalised by the corresponding values at Site 8.	123
Figure D-1: Wave conditions in environmental scenario 1 of the Phase 4 simulations, with existing bathymetry.	124
Figure D-2: Wave conditions in environmental scenario 2 of the Phase 4 simulations, with existing bathymetry.	125
Figure D-3: Wave conditions in environmental scenario 3 of the Phase 4 simulations, with existing bathymetry.	126
Figure D-4: Wave conditions in environmental scenario 4 of the Phase 4 simulations, with existing bathymetry.	127
Figure D-5: Wave conditions in environmental scenario 5 of the Phase 4 simulations, with existing bathymetry.	128
Figure D-6: Wave conditions in environmental scenario 6 of the Phase 4 simulations, with existing bathymetry.	129
Figure D-7: Wave parameters at the 10 m isobath with existing bathymetry, in all 6 environmental scenarios.	130
Figure D-8: Difference between significant wave height for case 1 and existing bathymetry, over the model domain, for each of the six environmental scenarios.	131
Figure D-9: Difference between wave parameters at the 10 m isobath for case 1 and existing bathymetry, in all 6 environmental scenarios.	132
Figure D-10: Difference between significant wave height for case 2 and existing bathymetry, over the model domain, for each of the six environmental scenarios.	133
Figure D-11: Difference between wave parameters at the 10 m isobath for case 2 and existing bathymetry, in all 6 environmental scenarios.	134
Figure D-12: Difference between significant wave height for case 3 and existing bathymetry, over the model domain, for each of the six environmental scenarios.	135
Figure D-13: Difference between wave parameters at the 10 m isobath for case 3 and existing bathymetry, in all 6 environmental scenarios.	136
Figure D-14: Difference between significant wave height for case 4 and existing bathymetry, over the model domain, for each of the six environmental scenarios.	137
Figure D-15: Difference between wave parameters at the 10 m isobath for case 4 and existing bathymetry, in all 6 environmental scenarios.	138
Figure D-16: Difference between significant wave height for case 5 and existing bathymetry, over the model domain, for each of the six environmental scenarios.	139
Figure D-17: Difference between wave parameters at the 10 m isobath for case 5 and existing bathymetry, in all 6 environmental scenarios.	140
Figure D-18: Difference between significant wave height for case 6 and existing bathymetry, over the model domain, for each of the six environmental scenarios.	141
Figure D-19: Difference between wave parameters at the 10 m isobath for case 6 and existing bathymetry, in all 6 environmental scenarios.	142
Figure D-20: Difference between significant wave height for case 7 and existing bathymetry, over the model domain, for each of the six environmental scenarios.	143

Figure D-21: Difference between wave parameters at the 10 m isobath for case 7 and existing bathymetry, in all 6 environmental scenarios. 144

Figure D-22: Difference between significant wave height for case 8 and existing bathymetry, over the model domain, for each of the six environmental scenarios. 145

Figure D-23: Difference between wave parameters at the 10 m isobath for case 8 and existing bathymetry, in all 6 environmental scenarios. 146

Reviewed by



Mark Pritchard

Approved for release by



David Roper

Formatting checked by



Executive summary

Trans-Tasman Resources Ltd (TTR) has secured permits and is prospecting for offshore iron sands in the South Taranaki Bight along the West Coast, North Island. Mining will involve dredging large pits in the seabed, concentrating iron ore on board vessels and then returning the de-ored sand to the seabed, where it will partially fill the pits and also form mounds. Tentative mining sites and areas where de-ored sand might be dumped are about 15 to 35 km offshore from Patea. Pits and mounds on the seabed have the potential to alter the direction of wave approach and wave height at the shoreline and therefore longshore transport and patterns of erosion and accretion at the shoreline, depending on the scale of the operations.

A numerical modelling study has been carried out to investigate the impacts on wave conditions in the South Taranaki Bight that may result from modifications to the seabed as a result of mining operations. The wave modelling studies form part of a wider, staged investigation of potential mining effects. The present report describes Phase 4 of the wave modelling study, following on from three earlier stages that have been reported separately. Phase 1 described the wave climate of the South Taranaki Bight using previously available data. In Phase 2, the SWAN nearshore wave model was applied to carry out initial tests of sensitivity of nearshore wave climate in the South Taranaki Bight to bathymetry modifications expected under an early version of the mining plan. Following an extensive field programme, Phase 3 validated the model against those data, and applied it to test sensitivity of nearshore wave climate to a revised mining plan, including effects of both bathymetry modification and shadowing by moored vessels.

Further revisions were made to the proposed mining plan in June 2013. This envisages that mining activity taking place in three extraction blocks, each of which is divided into a set of corridors or lanes in which extraction will take place. The proposed direction of each extraction corridor (or lane) is parallel to the prevailing SW wind/wave direction. The lanes are about 500 m wide and vary in length from about 1 km to 14 km. A Floating Production, Storage and Offloading (FPSO) vessel will move about the mining areas, with its position controlled by a four-point cable mooring system. Seabed material will be excavated using a Subsea Sediment Extraction Device (SSED) operating from the stern of the FPSO. Mined sediment will be transferred to the FPSO, where extracted sediment will be processed into iron ore concentrate, with de-ored sand discharged to the seabed near the bow of the 330 m long FPSO, into previously worked-over areas. The FPSO will generally remain oriented with its bow facing into the prevailing dominant wave direction as it is progressively repositioned as the lane is mined. At the commencement of mining a new area, with no pre-existing cut to fill, sediment will need to be deposited in a mound outside the SW end of the lane. Similarly, a pit will be left unfilled on completion of mining operations at the end of a lane. As a result, at various stages of the mining operation, certain pits will have been partly refilled (to approximately 1 m below their initial level), some deeper pits (of approximately 9-10 m depth) will remain unfilled, and some mounds of de-ored sediment of height 8-9 m will remain above the original seabed level.

Revisions to the mining plan required a new set of sensitivity tests to be carried out. Hence in Phase 4 of the project, reported here, the near shore model was updated with new bathymetry data, and verification simulations run for a September-October 2011 test period,

using wave data available from the field campaign. It was found that the model provides a satisfactory simulation of the nearshore transformation of wave conditions reaching the South Taranaki coast.

Further investigations were then carried out using the calibrated nearshore wave model to simulate the effects on nearshore wave conditions of revised mining operations. Eight hypothetical new configurations of the seabed were intended to represent some possible states of the seabed during the proposed mining operations. These included some representing “worst case” conditions consistent with this mining strategy, notably “case 1”, which consisted of a remnant 8-9 m mound at the SW end, and a remnant 9-10 m pit at the NE end of every lane in all three mining blocks, both of 300 m width, with all remaining mined lanes returned to 1 m below their initial level. Other case represented lesser levels of disturbance, at intermediate stages in the mining operations.

The complete set of hypothetical bathymetry modifications was tested using a set of scenario-based simulations. It was found that the simulated changes in significant wave height at the 10 m isobath were all less than 12 cm for case 1, and less than 5 cm for all other cases. These are closely correlated with changes in mean period, which were all less than 0.5 seconds for case 1, and less than 0.25 seconds for all other cases. In relative terms, i.e., the magnitude of change as a percentage of the baseline value, changes in significant wave height and mean period are less than 8.6% for case 1, and less than 4.5% for all other cases.

The maximum effects on wave characteristics considered over the whole of the study area will occur in the immediate vicinity of the dredged pits and mounds. Most of the cases tested produced local changes in wave height of up to 0.436 m, or 12.6% of baseline values. Because waves refracted near the mining pits and mounds have a wide directional spread, the magnitude of any changes in wave height diminish with distance from the affected area, but the large spatial extent of some of the hypothetical bathymetry modifications, particularly case 1, means that these “local” changes in wave height can be similarly extensive.

Additionally, the effects of bathymetry changes on the nearshore wave climate were investigated using a 12 month direct simulation, applied to one of the bathymetry cases (case 1) that had been found, as expected, to produce some of the largest effects on wave conditions. The results of the two simulation methods were found to be closely consistent. Taking a time average of differences induced by the bathymetry change, it was found that wave heights at 10 m water depth generally tend to be decreased (by less than 5 cm) along the coast east of Patea and increased (by less than 2.5 cm) further west. In terms of the temporal variability in these differences, the mean changes are typically around one standard deviation from zero.

Mean wave period in 10 m water depth shows a similar spatial pattern of change, decreasing (by less than 0.1 seconds) in the vicinity of Patea, and increasing (by less than 0.05 seconds) to the west. These changes generally differ from zero by much less than one standard deviation.

Mean wave direction is slightly decreased (i.e., changes in an anticlockwise sense) on average along the majority of the coast, by less than 1°. The mean differences are typically around one standard deviation from zero.

From the 12 month simulation it was found that the root-mean-square difference (RMSD) between test and baseline significant heights was less than 2.0 cm for much of the coast, up to a maximum of 5.5 cm near Patea. In relative terms, comparing with natural ranges of variability derived from the baseline simulation, it was found that changes associated with the case 1 bathymetry modifications typically correspond to less than 8% of one standard deviation for significant wave height and for mean direction, less than 15% of one standard deviation for mean period, and less than 10% of one standard deviation for bed-orbital velocity.

The results of the 12 month simulation were then used to estimate wave and sediment transport parameters at the beach. It was found that the case 1 bathymetry modifications act to reduce mean values of breaking wave height (H_b) in the vicinity of Patea by less than 5.5 cm, and to increase values by up to 2 cm in parts of the coast further west. The root mean square difference in H_b , and also of the onshore wave flux factor P_{os} , associated with the bathymetry change, are generally less than 20% of one standard deviation associated with interannual variability of the respective monthly means.

Changes in the wave-driven longshore sediment flux Q were estimated. The bathymetry modifications tested would act to decrease the longshore sediment flux near Patea (i.e., slightly reduce the positive eastward sediment flux) by up to 12% of the mean. There would be a smaller net increase in longshore sediment flux on a small part of the coast west of Manawapou.

Waves at the coast can drive mean longshore surf zone currents either due to an oblique angle of incidence, or through longshore variability in wave height setting up sea level gradients. Due to the coast's alignment, in existing conditions oblique wave incidence will drive eastward currents throughout the region, with magnitudes of up to 1-2 ms^{-1} . Introducing the bathymetry changes could affect this quantity in a similar manner to the wave-driven sediment flux, with decreases in the order of 5% of a standard deviation in sections of the coast around Patea, and smaller increases in western parts of the coast.

Finally, scenario-based tests were also done of the effect on nearshore wave conditions (particularly on the 10 m isobath) arising from mooring a large Floating Processing, Storage and Offloading (FPSO) vessel off the coast. It was found that in the worst case some vessel orientations produce wave height changes of up to 2 cm on the part of the coast near Patea, and (other) orientations that produce wave height changes of up to 1.0 cm on the western part of the coast. Relative to the baseline mean values, these correspond to changes of less than 1.0% and 0.5%, respectively. The wave height increases on the western coast are associated with wave reflections off the vessels, which were conservatively assumed to provide 100% specular reflection, which is likely to be an overestimate.

To summarise, changes in nearshore wave parameters associated with seabed pits and mounds formed during mining operations as presently proposed are expected to be minor in comparison with the natural level of variability in those values. Corresponding effects from the presence of a large moored vessel during mining operations are expected to be comparable to, or smaller than, the effects of the pits and mounds as presently envisioned.

Information relating to TTR's additional scientific work undertaken since 2014 has been provided and the conclusions in this report remain valid.

1 Introduction

NIWA was commissioned by Trans-Tasman Resources LTD (TTR) to investigate potential environmental impacts of proposed seabed mining operations in the South Taranaki Bight. These proposed operations will result in pits and mounds in the seabed that can affect waves by refracting (bending the wave direction) and shoaling (changing the wave height) them as they pass over the modified seabed. Such changes in the wave field introduced at the mining site may be propagated shoreward, leading to potential changes in wave conditions nearshore with consequent changes in shoreline processes (erosion and accretion) along the South Taranaki coast. The magnitude of any such changes will depend on a number of factors, including the natural wave climate of the region, the water depth at the mining site, the configuration of the modified seabed and the distance offshore.

The present study, forming one part of a wider assessment of environment effects, addresses the task of quantifying the magnitude of such potential impacts of proposed mining operations on coastal wave conditions. This is done through numerical modelling (using the SWAN near shore wave model) to predict the wave conditions that will be produced as a result of specified wind conditions acting over a region with specified bathymetry (spatially-varying water depth), also taking into account swell entering from outside the study region. In particular, the model is first used to simulate regional wave conditions with the existing bathymetry under several environmental conditions, then rerunning the model for the same conditions with modified bathymetry, and quantifying any resulting differences in wave properties (e.g., height, period, direction), with particular attention to any changes near the coast.

The study has been carried out in phases. Phase 1 was a preliminary desktop study, separately reported (MacDiarmid et al. 2010), which included an analysis of wave climate information from existing sources. In Phase 2, near shore wave models were established and, with limited validation from existing data, used to carry out preliminary tests of sensitivity to mining operations. In Phase 2, the method of mining was in an early stage of planning, and hence the exact configuration of pits and mounds in the seabed at each stage of mining operations could not be fully specified. For the purposes of the Phase 2 study, we assumed that operations would be carried out in the Xantia area, and tested a range of likely seabed configurations of square 10 m high mounds and 10 m deep pits, both of 500 m × 500 m extent and in relatively close proximity, in order to provide some initial estimates of the likely magnitude of effects.

Phase 3 of the study was commenced after wave data and additional bathymetry data became available from a measurement campaign in the study region, allowing for more detailed calibration of the near shore models. The calibrated model was used to further refine estimates of the effects of mining-related bathymetry changes on wave conditions at the South Taranaki coast, incorporating revised plans for mining operations that had evolved since the Phase 2 study, and were documented in a prefeasibility study (Technip Mines 2012a, Technip Mines 2012b). This envisaged that sediment would be dredged from relatively extensive pits of a range of depths (9 – 15 m) in the various mining areas, transferred to a large Floating Processing, Storage and Offloading (FPSO) vessel on a long-term mooring outside the mining areas. After processing, de-ored sands would be returned to the seabed in a separate deposition area to form an extensive mound up to 2 m in height. The model study was also extended to investigate the effects on nearshore wave conditions

of the long-term presence of large moored ships associated with the mining operations. The results of the model studies carried out in Phases 2 and 3 have been documented in a previous report (Gorman 2012).

In June 2013 a new mining plan was selected by Trans-Tasman Resources Limited, the details of which are presented in Section 2.5 below. Further sensitivity studies were therefore needed, in what we describe as Phase 4 of the wave modelling investigations. At the same time, some changes to the wave modelling methods have been implemented, and the model verification revisited. The present report describes the results of this work, looking at the effects of possible changes to the seabed, as well as the presence of a large moored vessel, associated with mining activities on nearshore wave conditions.

2 Modelling methods

2.1 The SWAN model

The SWAN model (Booij et al. 1999, Ris et al. 1999) is a spectral wave model intended for shallow water applications in coastal and estuarine environments. It computes the evolution of the wave energy spectrum in position (x, y) and time (t), explicitly taking into account the various physical processes acting on waves in shallow water. These include the effects of refraction by currents and bottom variation, and the processes of wind generation, white-capping, bottom friction, quadruplet wave-wave interactions, triad wave-wave interactions and depth-induced breaking. The model can incorporate boundary conditions representing waves arriving from outside the model domain.

2.2 Model domains for SWAN simulations

All simulations were carried out in a Cartesian coordinate system, using a Mercator projection with origin $(X, Y) = (0,0)$ corresponding to (latitude, longitude) = $(40.8^\circ\text{S}, 174.3^\circ\text{E})$, based on the NZDG2000 (WGS84) Spheroid. A set of nested rectangular model grids was used.

An outer Greater Cook Strait grid (“GCS_1km”) was established at 1 km resolution in both X and Y, at 0° orientation so that its open western and eastern boundaries correspond approximately to longitudes 172.125°E and 176.625°E , while its open southern and northern boundaries are at approximately 42.750°S and 38.250°S . Its parameters are listed in Table 2-1. The bathymetry for this grid (Figure 2-1) was derived from existing NIWA bathymetry data sets using the Gerris Terrain modelling system.

A nested 500 km resolution grid (“SthTar_500m”) was set up, tested and run for a simulation from July 2011 through August 2012 to provide outputs to associated hydrodynamic/sediment transport model studies (Hadfield 2012, Hadfield 2013). This was not used in the present work, but its extent is shown in Figure 2-1 and its parameters are included in Table 1 for reference.

For sensitivity studies, bathymetry data was established on a 100 m resolution grid (“Xantia_100mB”), delineated in orange in Figure 2-1, was established at 0° orientation covering the coast from Hawera to Wanganui, and including the Xantia formation and Patea Banks.

The bathymetry used in this domain has evolved as new data has become available. In Phase 2, pre-existing data sources were used. For Phase 3, the bathymetry in the 100 m grid was updated using results of additional surveys, with the gridded bathymetry shown in Figure 2-2. Details of techniques used to process the new bathymetry are given in a separate report (Pallentin & Gorman 2012). The need to incorporate more accurate bathymetry in the model is illustrated in Appendix A of Gorman (2012), which discusses the errors associated with the uncertainty in accuracy in the bathymetry available for the Phase 2 study. Further surveys carried out prior to commencement of Phase 4 modelling have also been incorporated using similar methods.

In all Phase 4 simulations the spectral grid consisted of 33 frequencies between 0.0418 Hz and 0.8018 Hz geometrically spaced, so that successive frequencies were in the ratio

$f_{n+1} / f_n = 1.125$, while 72 direction bins of 5° width were used. Note that this is a finer directional resolution introduced during Phase 3 to alleviate the “Garden Sprinkler Effect” (Tolman 2002), in which disturbances in the wave field tend to preferentially propagate along the discrete “binned” directions. This is particularly a problem using SWAN in stationary mode for problems such as shadowing by vessels with highly localised obstructions. Wind input, whitecapping dissipation and nonlinear interactions (three-wave and four-wave) were activated in the 1 km and 500 m resolution simulations, but deactivated in the innermost (100 m resolution) nested simulations. The shallow water effects of depth-limited breaking and bed friction were activated in all simulations, with default parameterisations for SWAN Version 40.85 (SWAN 2011) used unless noted otherwise.

Table 2-1: Parameters specifying grids established for SWAN simulations.

	Grid		
	GCS_1km	SthTar_500m_ext	Xantia_100mB
origin X_0	-184000	-100422	-32000
origin Y_0	-217000	+129627	+67000
origin lon 0	172.0533°E	173.1304°E	173.9242°E
origin lat 0	42.7317°S	39.6267°S	40.1960°S
grid spacing (m)	1000	500	100
orientation	0°	-40°	0°
number of cells N_x	381	427	981
number of cells N_y	581	157	781

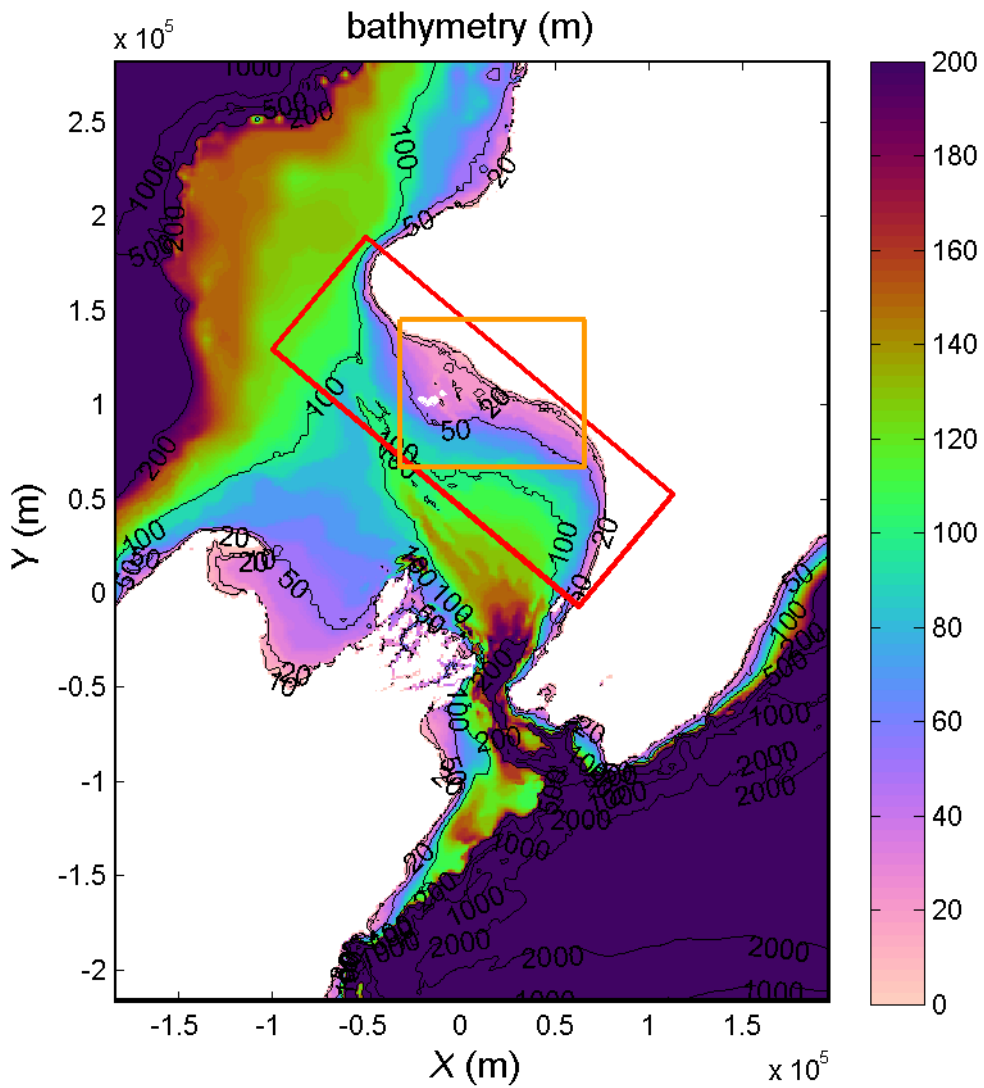


Figure 2-1: Map showing bathymetry in the Greater Cook Strait region, with the extent of grid domains marked. Grids are GCS_1km (black, full image), SthTar_500m_ext (red), Xantia_100mB (orange), while the mining areas are outlined in white. The X and Y axes are in model Cartesian coordinates.

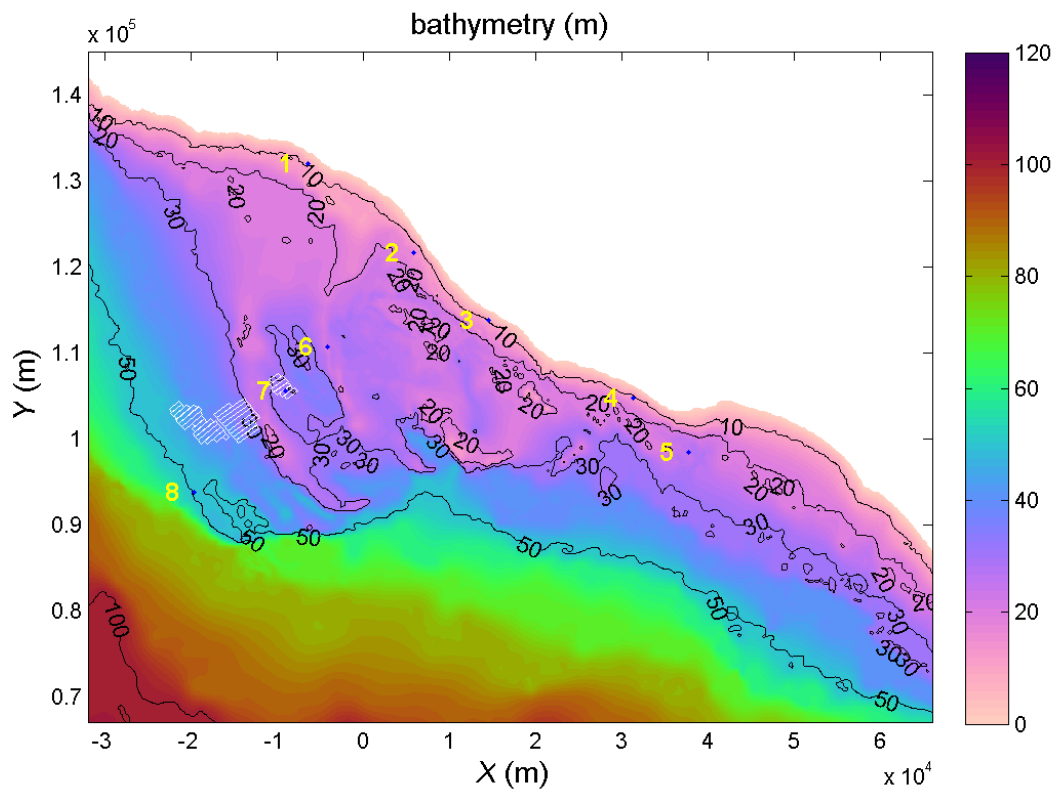


Figure 2-2: Bathymetry for the Xantia_100mB model domain – Phase 4. The mining areas are outlined in white, and the positions of wave-recording instruments are shown by yellow-numbered blue dots. The X and Y axes are in model Cartesian coordinates.

2.3 External forcing

In order to simulate wave development in a given region, it is necessary to specify the winds blowing over the region. Waves entering the region through any open boundaries also need to be included, while the effects of changing water levels and currents can also be accounted for if these can be provided. In general all of these inputs vary both in space and time.

As part of NIWA's EcoConnect forecasting system for weather-related hazards, weather, tide and wave models (NZLAM-12, NZTIDE-12 and NZWAVE-12, respectively) are all operated to provide twice-daily 48-hour forecasts on domains covering the New Zealand region at approximately 12 km resolution.

Wind fields from the NZLAM-12 forecast model were applied as hourly inputs at their original (~12 km) resolution.

The NIWA tidal model is based on an unstructured mesh that provides much finer resolution in coastal waters than the 12 km regular grid used to display operational outputs in the EcoConnect forecast system. Hence for the present study, tidal currents and sea levels were input on a 1 km resolution regular grid (GCSTIDE-1) covering the Greater Cook Strait region, at 15 minute intervals.

The SWAN model performs interpolation of input wind, sea level and current fields to the required spatial and temporal resolution of the nearshore model.

Wave boundary conditions from NZWAVE-12 forecasts were specified on the open boundaries of the Greater Cook Strait SWAN grid, using directional wave spectra output at hourly intervals taken from the nearest NZWAVE-12 grid cells.

2.4 Sensitivity testing – Phase 4

After completion of Phase 3, revised mining plans gave rise to an updated set of configurations of modified bathymetry, described below in Section 2.5, to be tested for potential effects on nearshore wave conditions. Two modelling approaches were used. In the first, similar to Phases 2 and 3, a set of six environmental scenarios, based on defined inputs (wind and incident waves) was selected, as described in Section 2.6. For each of these, SWAN was run in stationary mode to establish equilibrium wave conditions. This was done first on the GCS_1 km domain, using unmodified bathymetry, to generate boundary conditions for the nested Xantia_100m domain. SWAN was then run on the Xantia_100m domain for each of the bathymetry configurations. Tidal sea level and current inputs were not used in these scenario-based simulations.

The second approach, outlined in Section 2.7, was to run direct simulations of sufficiently long duration to characterise the nearshore wave climate, with both existing and modified bathymetry. This allows for the effects of the bathymetry modifications to be tested over a wide sampling of the local wave climate. But because of the high computing resource required for this simulation (running on the NIWA supercomputer), it was only practical to test one representative bathymetry case in this way. On the other hand, the scenario-based approach requires much shorter computing times, making it suitable for the efficient inter-comparison of a relatively large number of bathymetry modifications.

In addition to tests of bathymetry modifications, the scenario-based approach was also used to examine the effects on wave conditions of mooring large vessels in the vicinity of the mining areas.

2.5 Bathymetry modifications – Phase 4

In the Phase 4 study, a set of hypothetical bathymetry modifications were developed consistent with a new mining plan defined in June 2013.

Figure 2-3 sets out the proposed TTR mine plan layout, illustrating the three extraction blocks, and the corridors or lanes in which extraction will take place. The proposed direction of each extraction corridor (or lane) is parallel to the prevailing SW wind/wave direction as this is the preferred alignment for directional control of both the FPSO and the SSED. The lanes are about 500 m wide and vary in length from about 1 km to 14 km. The SSED will extract sand from under the stern of the 330 m long FPSO and the de-ored sediment will be discharged to the seabed (to backfill the cut) from the bow of the FPSO as the vessel is winched backwards and toward the NE. At the commencement of mining a new area, with no pre-existing cut to fill, sediment will need to be deposited in a mound outside the SW end of the lane. Similarly, a pit will be left unfilled on completion of mining operations.

In the central block of the three, a mining depth of 10 m is assumed, while in the other two blocks the mining depth is taken as 9 m.

The resulting pattern of cut and fill in general terms is for a pit to about 300 x 500 m dimension and 9 or 10 m depth at the SW end of the lane, a depression 1 m deep in the

backfilled lane (90% of the extracted volume will be returned), and a mound about 300 x 500 m dimension and 8 or 9 m tall at the NE end of the lane. The exact pattern of cut and fill, and therefore whether there are 9-10 m deep pits and 8-9 m tall mounds at the start and end of each lane, depends on the path that the operation takes.

The seabed will evolve continuously during mining operations. For the purposes of this exercise, we have made a selection of possible states of the seabed during mining operations. The outlines of the eight resulting patterns of hypothetical remnant pits and mounds are shown in Figure 2-4.

Case 01 gives the final pattern on completion of all mining operations in all mining blocks, assuming that every lane is mined from SW to NE, leaving a mound outside the SW end, and a pit inside the NE end of every lane.

Case 02 works on the assumption that at the completion of a lane (e.g., from SW to NE), the next adjacent lane can be mined in the reverse direction (i.e., NE to SW), with sediment initially mined from the end of the new lane returned to fill the deep pit left at the end of the previous lane. In this way, mining successive lanes in alternating directions¹ as a field might be ploughed, only one remnant pit and one remnant mound are left for each block.

The remaining cases (03 to 08) are versions of cases 01 and 02 in which only one mining block has been completed.

These hypothetical cases are somewhat simplified, with vertical pit and mound walls, ignoring the sloping sides of the pits and mound, as well as the natural winnowing of mounds and infilling of pits that would be expected during mining operations. These effects would tend to smooth out the topographic changes produced by mining, and hence somewhat reduce the impacts on wave climate, so these simplifying assumptions are intended to be conservative.

¹ this pattern when seen in ancient texts and inscriptions is referred to as “boustrophedon”, from the Greek word meaning “as the ox ploughs”.

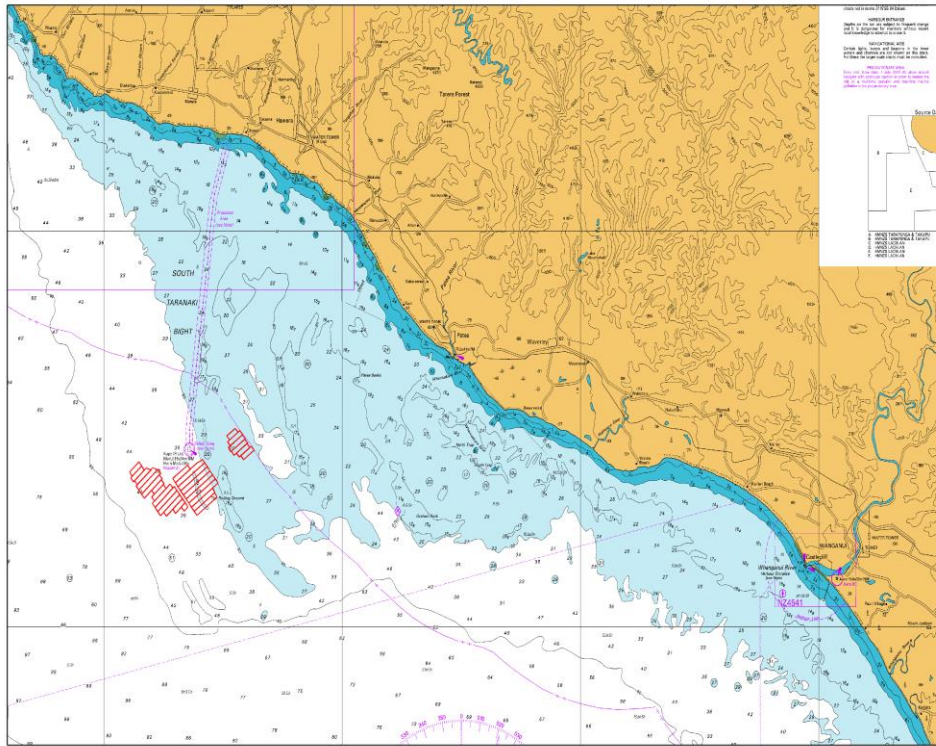


Figure 2-3: Location of proposed mining areas in the South Taranaki Bight.

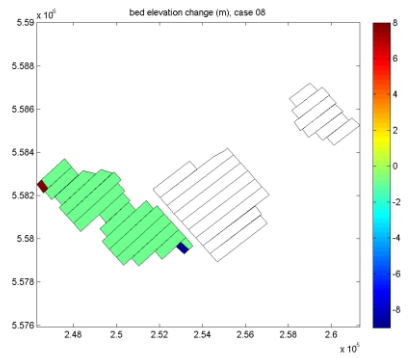
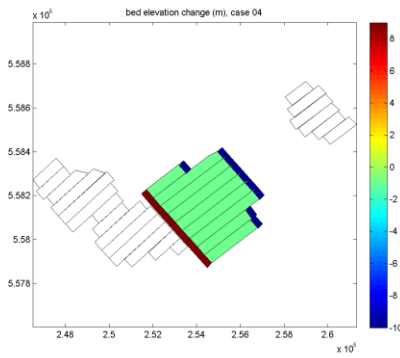
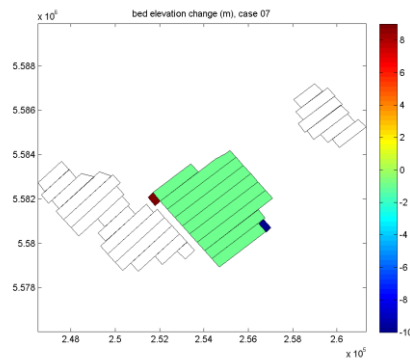
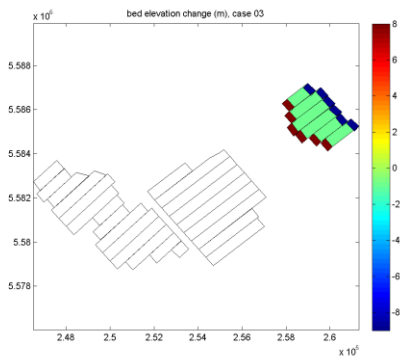
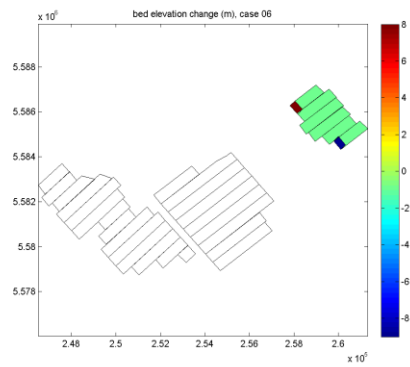
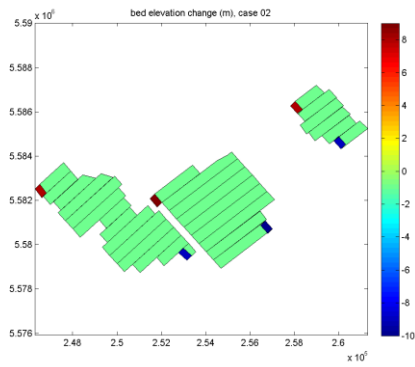
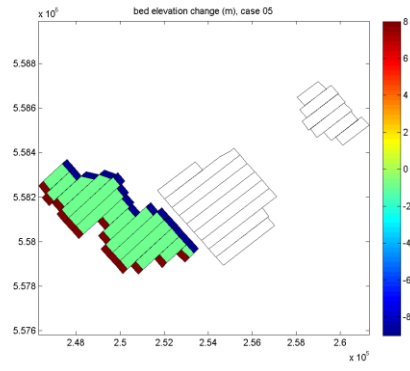
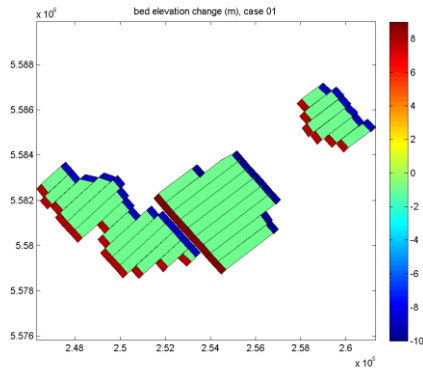


Figure 2-4: Outlines of the hypothetical bathymetry changes tested in Phase 4 modelling. Remnant mounds (maroon) have heights of 8m or 9m, remnant pits have depths of 9m or 10m, while refilled areas (light green) are assumed to have a depth of 1m.

2.6 Environmental scenarios – Phase 4

For the Phase 4 sensitivity studies, a limited set of environmental conditions was selected from the November 2011 period for which model inputs (described above) were available.

In this case, we selected scenarios based on input wave conditions at 40.00°S, 174.0°E near the southwest corner of the Xantia_100m grid with the intention of covering a range of input directions, and representing storm conditions as well as moderate conditions.

Events were selected by first choosing three subsets of the record:

- records with north-westerly waves (peak direction greater than 290°)
- records with south-westerly waves (peak direction between 225° and 255°)
- records with southerly waves (peak direction less than 225°).

Then, from each of the three subsets, the record with the highest significant height was chosen, as well as the record with significant height closest to a target value of 2 m. These corresponded to the events listed in Table 2-2.

Each of the six environmental scenarios described above were applied in testing each variation of bathymetry tested, as described in Section 2.5.

Table 2-2: Environmental scenarios used in Phase 4 sensitivity studies.

Event No.	Date & time	Height H_{m0} (m)	Direction θ_{peak} (°)
1	03Z 11/09/2011	2.12	321
2	01Z 12/09/2011	4.76	295
3	15Z 17/09/2011	2.00	254
4	10Z 19/09/2011	1.87	173
5	14Z 19/09/2011	2.42	162
6	08Z 25/09/2011	2.43	254

2.7 Long-term simulations

In order to provide a test of potential effects of bathymetry modification on the nearshore wave climate, a simulation was run from 12:00 NZST (00UT) on 21 December 2010 to 12:00 NZST (00UT) on 1 January 2012. One full year of outputs were used, i.e., calendar year 2011, discarding the 11 days of spinup in December 2010. Nested runs were carried out, first on the Greater Cook Strait 1 km resolution grid using wave boundary conditions sourced from archived outputs of directional wave spectra from NIWA's NZWAVE-12 operational wave forecast, from which the SWAN model derived directional spectra to apply at the boundaries (note that in the Phase 2 and Phase 3 studies, parametric wave statistics were used). Output directional spectra from the Greater Cook Strait model provided boundary conditions for the Xantia 100 m resolution near shore model.

Both models took input wind fields from archived outputs of NIWA's NZLAM-12 operational weather forecast (the same winds used by the NZWAVE-12 forecast), and tidal currents and water levels from NIWA's tidal model of New Zealand's EEZ.

In order to check whether 2011 was a suitably representative year, the statistical occurrence of wave statistics at 40.00°S, 174.0°E for five years for which NZWAVE-12 outputs are available are compared in Figure 2-5 (significant wave height), Figure 2-6 (mean wave period) and Figure 2-7 (mean wave direction). The deviations of the 2011 occurrence distributions from the five-year average are of similar magnitude to those of other years in the record. Perhaps the most notable feature is that mean direction is somewhat more concentrated into the two main peaks than for other four years.

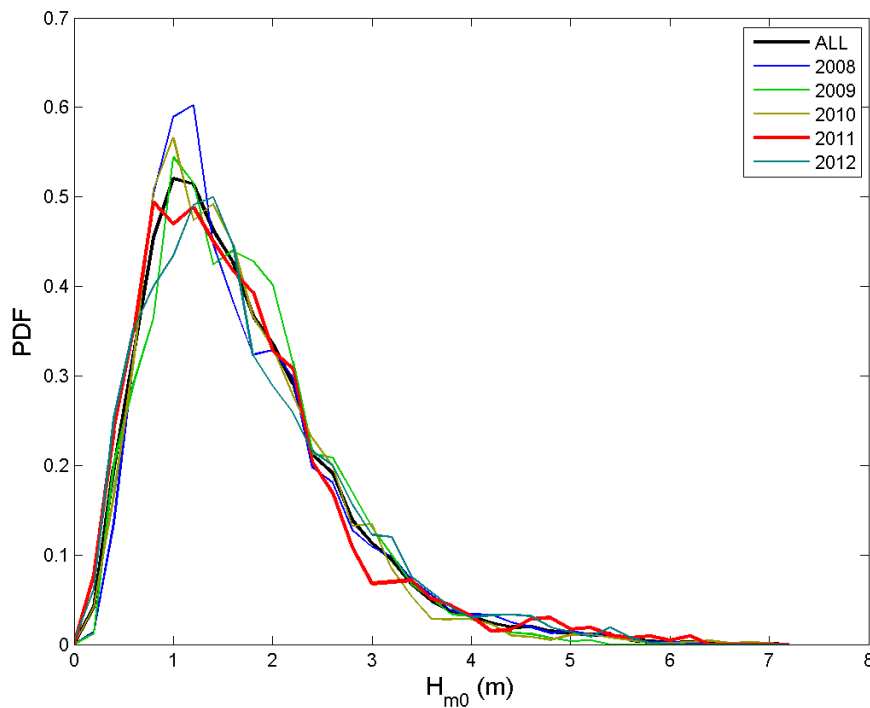


Figure 2-5: Probability distribution functions for significant wave height at (40°S, 174°E), in the years 2008 through 2012, from NZWAVE-12 forecasts. Values for the 2011, and for all five years, are highlighted by thicker red and black lines, respectively.

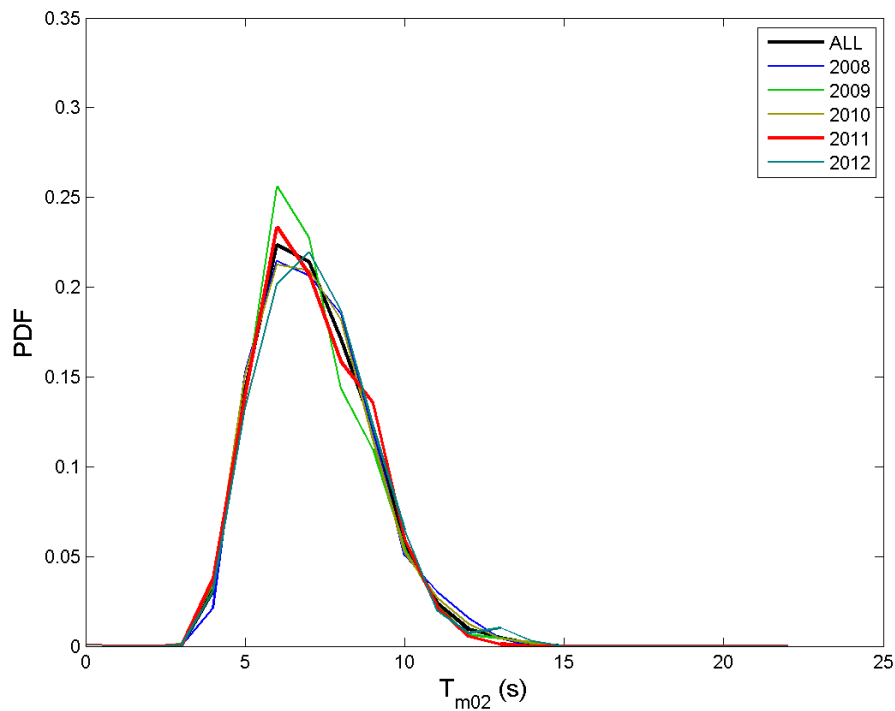


Figure 2-6: Probability distribution functions for second moment mean wave period at (40°S, 174°E), in the years 2008 through 2012, from NZWAVE-12 forecasts. Values for the 2011, and for all five years, are highlighted by thicker red and black lines, respectively.

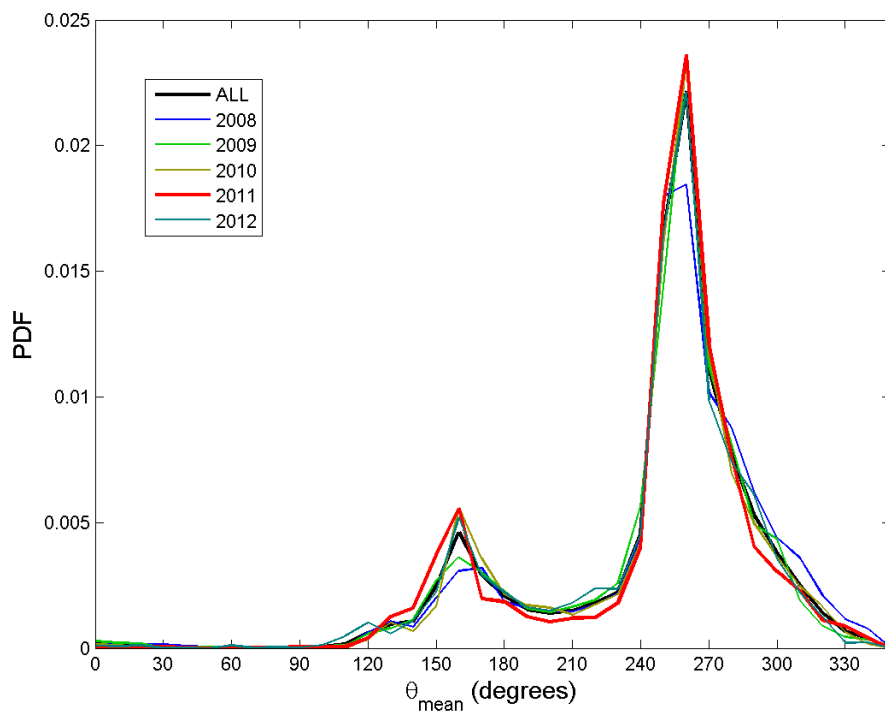


Figure 2-7: Probability distribution functions for mean wave direction at (40°S, 174°E), in the years 2008 through 2012, from NZWAVE-12 forecasts. Values for the 2011, and for all five years, are highlighted by thicker red and black lines, respectively.

2.8 Nearshore processes

The SWAN model of the South Taranaki Bight at 100 m resolution provides a satisfactory representation of wave conditions into 10 m water depth, as demonstrated by the verification against Dobie data at similar depths. The 10 m isobath, however, marks the approximate shoreward limit of new bathymetry survey data incorporated in the model, and the model bathymetry is too poorly defined further shoreward to reliably use the SWAN model to take wave conditions into the coast from there.

From the nearshore wave modelling results at the 10 m isobath, wave conditions at the beach were derived by refraction and shoaling relationships using piece-wise straight coast approximations, and sediment transport parameters were then derived using a set of relationships from the Shore Protection Manual (CERC 1984) as described in Appendix B.

For the present study we have not attempted to incorporate information on varying beach sediment properties (e.g., grain size, density) across the South Taranaki region, rather the assessment aims to identify potential variability and relative change in the nearshore wave climate and associated potential sediment transport patterns at a regional scale. Parameters assessed include the following (for which detailed definitions and further discussion are provided in Appendix B):

- Root mean square breaking wave height along the coastline.
- Mean onshore wave energy flux² P_{os} .
- Mean net longshore wave energy flux P_{ls} and sediment flux Q .
- Mean positive (clockwise) longshore wave energy flux P_{ls} and sediment flux Q .
- Mean negative (anticlockwise) longshore wave energy flux P_{ls} and sediment flux Q .
- Divergence³ of mean longshore wave energy flux P_{ls} and sediment flux Q .
- Mean longshore current at the wave breakpoint produced by oblique wave incidence.
- Mean longshore current at the wave breakpoint produced by longshore wave height gradient.

We have assumed that the longshore sediment flux Q is related to the longshore wave energy flux factor P_{ls} by a simple linear scaling

$$Q = fKP_{ls}$$

where $f = 3308 \text{ m}^2 \cdot \text{s}^3 \cdot \text{kg}^{-1} \cdot \text{year}^{-1} = 1.05 \times 10^{-4} \text{ m}^2 \cdot \text{s}^2 \cdot \text{kg}^{-1}$ is a unit-conversion constant, while K is a dimensionless efficiency factor dependent on sediment properties. In general, therefore, K may vary along the coast due to changes in sediment characteristics, but we have applied a uniform value of $K = 0.8$, which has been found to be appropriate for sandy beaches on the New Zealand east coast (Hicks 1993), although much lower values may be required where

² Wave energy flux is the rate at which waves carry energy across each length of wave crest: for example if the flux is 20 kW/m, an ideal wave energy device could extract 20 kW of electricity from each metre of wave crest it intercepts.

³ Divergence is a measure of spatial variability, i.e., how much a quantity changes per length of coastline.

coarser material is present. As a result, for convenience we have plotted P_{ls} and Q together on the same figures with dual axis scales. It should be borne in mind that P_{ls} is a direct prediction of the wave model, independent of sediment properties, while estimates of sediment flux Q also rely on further assumptions about sediment characteristics.

For the present study in the South Taranaki Bight, transport along the coast from the north-west towards the south-east was deemed to be positive.

2.9 Moored vessel simulations

A set of simulations was also carried out to investigate the effects of the presence of a moored Floating Production, Storage and Offloading (FPSO) vessel, operating in the mining areas.

This vessel was represented in the wave model as an obstruction element, consisting of a rectangular polygon of 336 m x 60 m corresponding to the dimensions used in the mooring analysis carried out for the prefeasibility study (Technip Mines 2012a, Technip Mines 2012b) The FPSO was assumed to be moored at one of two positions in the mining areas, listed in Table 2-3, and aligned in one of 4 different orientations (E-W, NE-SW, N-S, NW-SE), noting that the vessel is treated as symmetric between bow and stern.

The SWAN model can in general allow for wave energy to be partly transmitted, and partly reflected by obstruction elements. In this case the vessel was assumed to have a transmission coefficient of zero. Reflection may be a somewhat more complex issue. In the ideal case of a shear vertical wall extending to the seabed, we might expect specular reflection with a reflection coefficient of 1. While the types of vessel being considered would have near-vertical sides, the finite draft, non-uniform geometry and partial breaking mean this may not be exactly the case in reality. For simplicity, in the main series of tests we made the conservative assumption of complete specular reflection, but also tested the case of zero reflection.

The same methodology was used as in the scenario-based bathymetry sensitivity test, comparing simulations with the vessel in place for each of the same six environmental scenarios listed in Table 2-2, and comparing results with the corresponding simulation with no vessel present.

Table 2-3: Mooring positions for the FPSO used in simulations of wave blocking.

	Position 1	Position 2
latitude	-39.8421	-39.8842
longitude	174.1950	174.0764
model coordinates		
X	-8985	-19128
Y	106358	101664

3 Model verification

3.1 Field measurements

A programme of oceanographic field measurements was carried out in the South Taranaki Bight starting from September 2011. The positions of the instrument deployments are shown in Table 3-1. Full details of these deployments are given in a separate report (MacDonald et al. 2013), but we briefly describe here the measurements from these deployments that were used in the wave modelling work, and some additional processing of the data carried out for this purpose.

For the purposes of this study, and particularly for comparisons of measurements and model results, a spectral description of wave conditions is used, as outlined in Appendix A.

Three types of instrument were used to collect wave data, deployed at positions listed in Table 3-1 and plotted in Figure 2-2. Closest to shore were Dobie pressure recorders, deployed on the seabed in approximately 10 m water depth, at sites 1-4 spaced along the South Taranaki coast.

Acoustic Doppler Current Profilers (ADCPs) were deployed at sites 5-7. These instruments use acoustic beams to make Doppler measurements of water velocities through the water column up to the surface. Processing of these data using the manufacturer's software can provide estimates of the directional wave spectrum at the water surface.

A Directional Waverider™ buoy was deployed at the most offshore site (Site 8) in approximately 50 m water depth. Internal accelerometers measure the displacement of the buoy in three dimensions. These were sampled at 1.28 Hz in bursts of 2304 records at 30 minute intervals.

Data from the Site 8 Waverider, in the form of 3-dimensional displacement records, were processed with the DIWASP Matlab toolbox (Johnson 2001), using an Extended Maximum Likelihood Method (Isobe et al. 1984) to estimated directional spectra from the burst data.

The estimation of directional wave spectra from ADCP data (using RDI software), and of frequency spectra from Dobie pressure records, is described in a separate report (in preparation) on the field measurements.

For comparisons with instrument data, we adjusted model output and spectra recorded by the instrument to a consistent form. In particular, this meant applying a vertical attenuation function (using the measured mean water depth) to spectra recorded by the Dobies, which were mounted 20 cm above the seabed records to the surface, with a 0.25Hz cutoff, which was also applied to model spectra before obtaining spectral moments. A 0.6 Hz cutoff was applied to spectra at other locations before deriving summary statistics: the second moment mean period is particularly sensitive to the high frequency range. This cutoff was chosen to match the frequency range over which a Waverider buoy can accurately respond to surface motion. All directions were converted from Magnetic to True bearings, using a magnetic variation of 21.4°E.

Data were also available during the simulation period from the Baring Head Waverider in the form of non-directional statistics (spectra were not available). The position of this buoy lies

outside the Xantia grid, so we compare these measurements with outputs from simulations on the 1 km resolution Greater Cook Strait grid.

Unless otherwise stated, measurements from the instruments deployed at Sites 1-8 in the South Taranaki Bight are compared with outputs from the nested Xantia 100 m resolution grid.

Table 3-1: Locations of instruments collecting wave data.

Longitude	Latitude	Identification	Instrument
174.2243	-39.6109	Site 1	Dobie
174.3681	-39.7048	Site 2	Dobie
174.4686	-39.7745	Site 3	Dobie
174.6658	-39.8556	Site 4	Dobie
174.7416	-39.9126	Site 5	ADCP
174.2506	-39.8030	Site 6	ADCP
174.1938	-39.8496	Site 7	ADCP
174.0690	-39.9550	Site 8	Waverider
174.8500	-41.4000	Baring Head	Waverider

3.2 Model Verification – Phase 4

In order to provide more detailed verification of the near shore wave models, a simulation was run from 12:00 NZST (00UT) on 1 September 2011 to the same time on 31 October 2011, during the first instrument deployment. Nested runs were carried out, first on the Greater Cook Strait 1 km resolution grid using wave boundary conditions sourced from directional spectra output from NIWA’s NZWAVE-12 operational wave forecast. This is a change from the corresponding Phase 3 simulations, in which the boundary conditions took the form of significant wave height, peak wave period and directional spreading time series from which the SWAN model derived parametric directional spectra to apply at the boundaries. Output directional spectra from the Greater Cook Strait model then provided boundary conditions for the Xantia 100 m resolution near shore model.

Both models took input wind fields from archived outputs of NIWA’s NZLAM-12 operational weather forecast (the same winds used by the NZWAVE-12 forecast), and tidal currents and water levels from NIWA’s tidal model of New Zealand’s EEZ.

A detailed description of the results is provided in Appendix C.

Those results indicate that the model is able to provide a satisfactory representation of the transformation of waves into the South Taranaki coast. It should be noted, however, that the model tends to overestimate wave heights at the offshore measurement sites, particularly for shorter period components during westerly-dominated conditions, suggesting that these may be over-represented in the boundary conditions. This would need to be taken into account in

applications where the absolute value of predicted historical wave statistics is of primary importance.

For the present purpose of characterising potential changes in wave conditions associated with mining activities, it is more important that the model provide accurate representation of nearshore conditions *relative to* the imposed offshore conditions. Comparisons of nearshore to offshore energy ratios indicate that this is generally the case, apart from some localised bathymetric influences on swell which may not be fully represented.

4 Wave sensitivity test results

4.1 Sensitivity to bathymetry modifications – Phase 4

In this chapter we move to the results of Phase 4 sensitivity studies investigating the effects of possible seabed modifications under a mining plan as outlined in Section 2.5.

We present results from two approaches: firstly the scenario-based simulations which tested all hypothetical bathymetry modifications using a limited set of environmental conditions, allowing an efficient evaluation and intercomparison of the relative effects of different mining options. The second approach was to carry out a long term climate simulation to ensure that a more complete range of environmental conditions have been sampled, and to enable robust nearshore wave-climate statistics to be established, and effects of bathymetry modifications on those statistics to be quantified. The trade-off is that computing resources limit this approach to a small number of test cases.

4.1.1 Scenario-based simulations

The first step in the modelling exercise was to run baseline simulations with unmodified bathymetry. For example, in scenario 6, an event was simulated with incident waves of around 2 m significant height from the WSW. Wave heights in this scenario (Figure 4-1), reduce shoreward, while close to shore refraction turns the wave directions closer to shore-normal.

The next step is to rerun the simulation with the same environmental conditions (incident waves, winds), but with bathymetry modified for each of the hypothetical test cases, and look at the change in wave parameters between the two simulations. For example, Figure 4-2 shows the difference (test case minus baseline) in significant wave height under environmental scenario 6 for bathymetry case 1, which corresponds to remnant mounds being left at the SW end, and remnant pits at the NE end, of all lanes in all three mining blocks. Red colours indicate where higher wave heights result, while blue colours indicate decreased wave heights.

In this case, the majority of the mining blocks now consist of a 1 m deep pit, with a deeper pit at the NE end and a mound at the SW end, but on average the mined areas have increased depth. The net result is a pattern of reduced heights (by some 10 cm) for waves in the down-wave shadow of the mining areas, while heights are increased (by around 10 cm) on the northwest and southeast sides of this shadow area. We see more amplified version of this refraction effects in the vicinity of the deeper pits at the NE end of the lanes, and some focussing effects over the mounds at the SW ends. Those wave components refracted away from the initial direction continue to propagate in a wide range of north-eastward and south-eastward directions. The large spatial extent of the affected mining area in this particular bathymetry case means that the effects on wave conditions are also quite widely spread. In other cases with more localised seabed modifications, the wide directional spread of the refracted waves acts to reduce the energy of this refracted component as it travels shoreward, so it makes a relatively minor contribution to the sea state further shoreward, on top of the incident waves travelling generally north-eastward that bypass the mining area.

The six environmental scenarios provide a spread of baseline conditions (Figure 4-3), including a range of southerly through westerly incident directions (Figure 4-4). The pattern of disturbance by the modified bathymetry, shown for case 1 in Figure 4-5, is reasonably consistent between scenarios, though varying in magnitude.

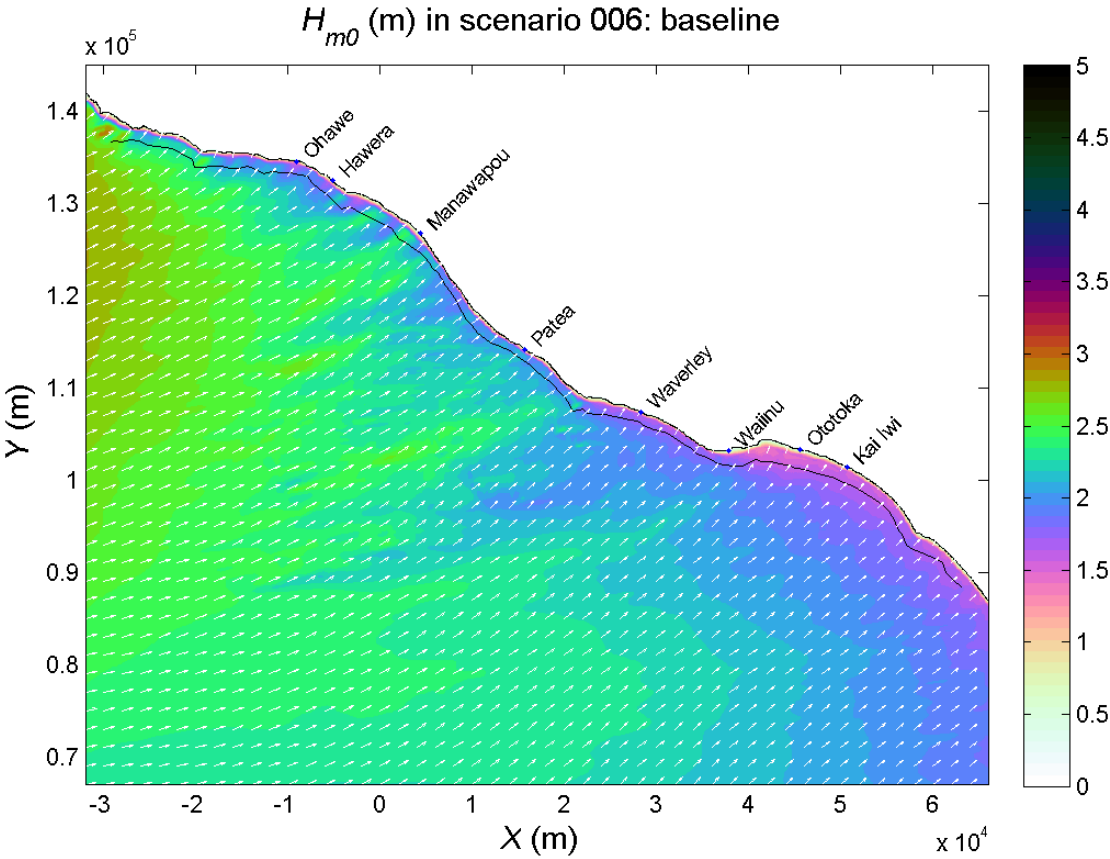


Figure 4-1: Wave conditions in environmental scenario 6 of the Phase 4 simulations, with existing bathymetry. Significant wave height (in metres) is shown by the colour scale, and mean wave direction by arrows. Beaches surveyed in related studies are named, and the 10m isobath (depth contour) is marked by a black line.

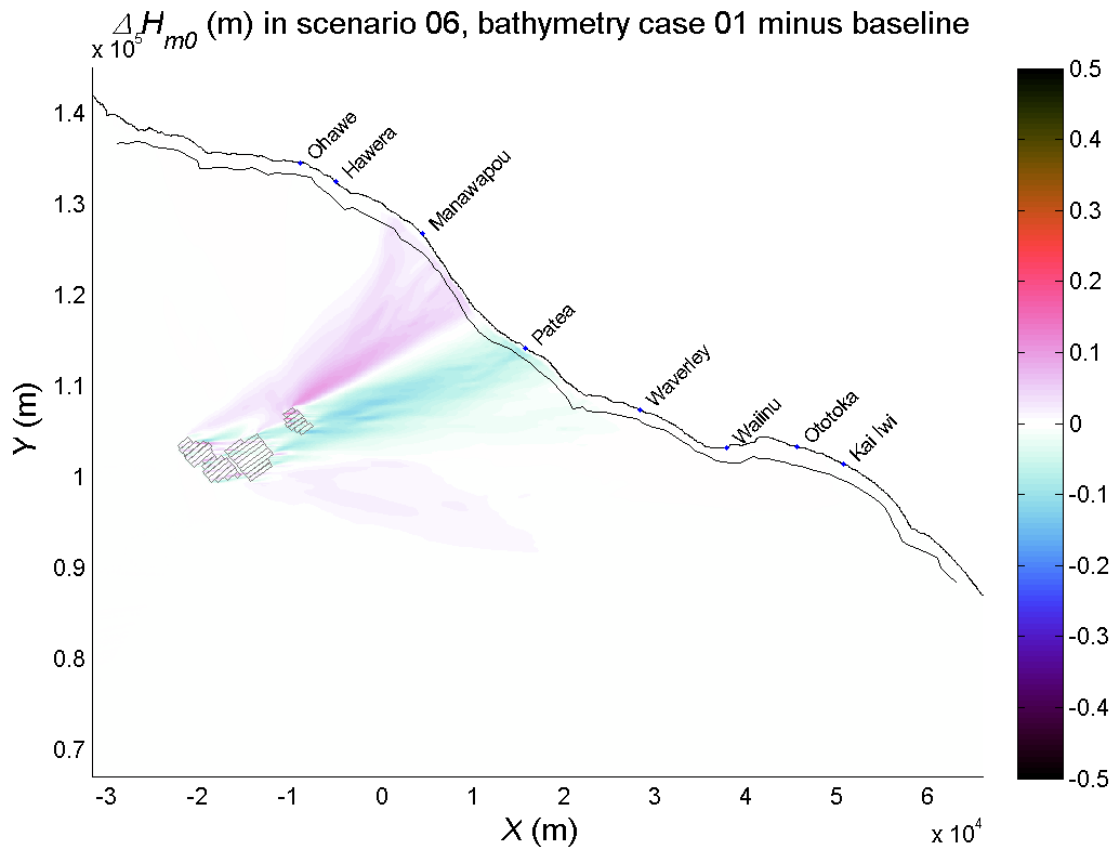


Figure 4-2: Difference between significant wave height (in metres) for case 1 and existing bathymetry, over the model domain, for environmental scenario 6. The locations of the mining areas are marked in grey.

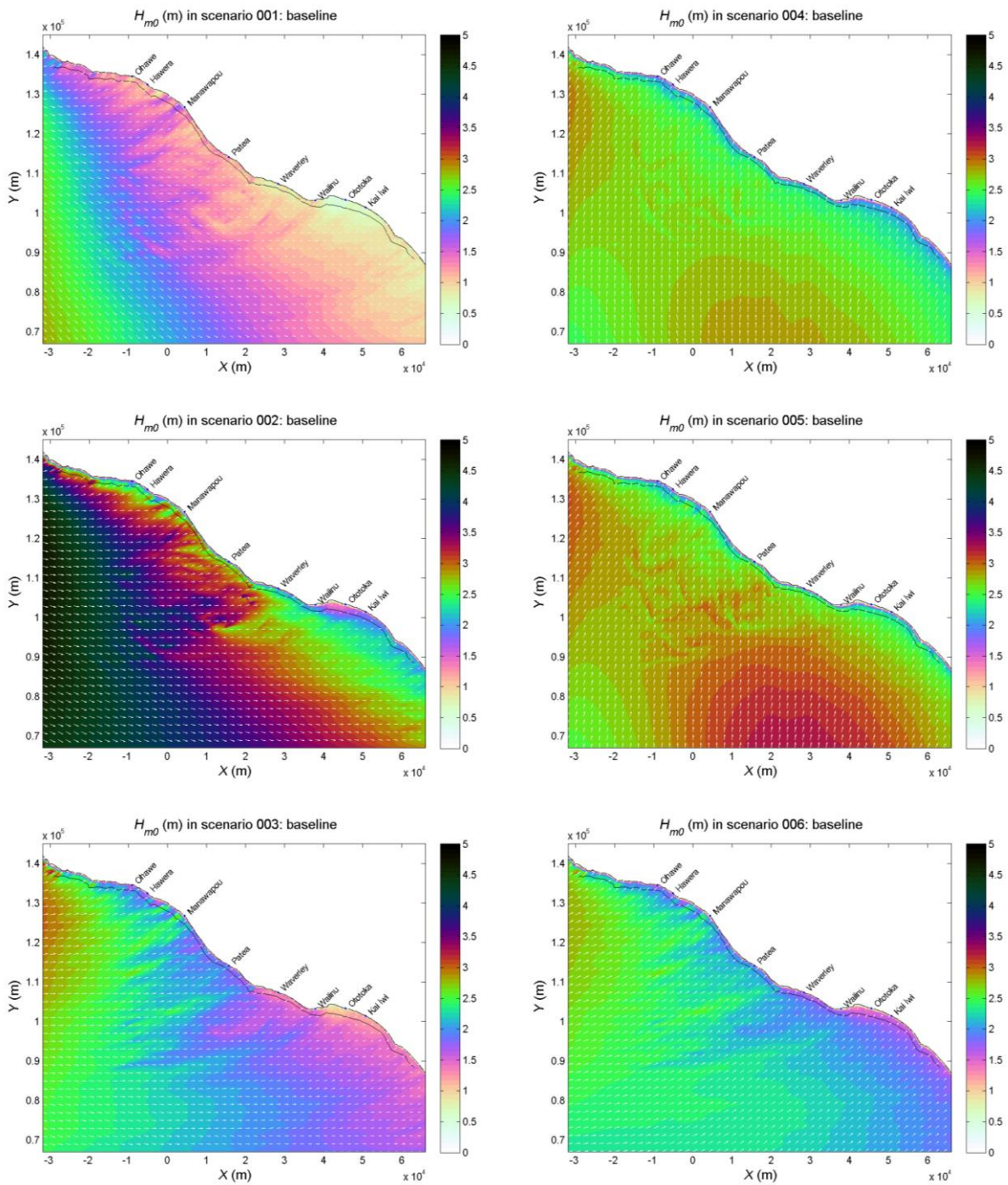


Figure 4-3: Wave conditions in all six environmental scenarios of the Phase 3 simulations, with existing bathymetry. Significant wave height is shown by the colour scale, and mean wave direction by arrows.

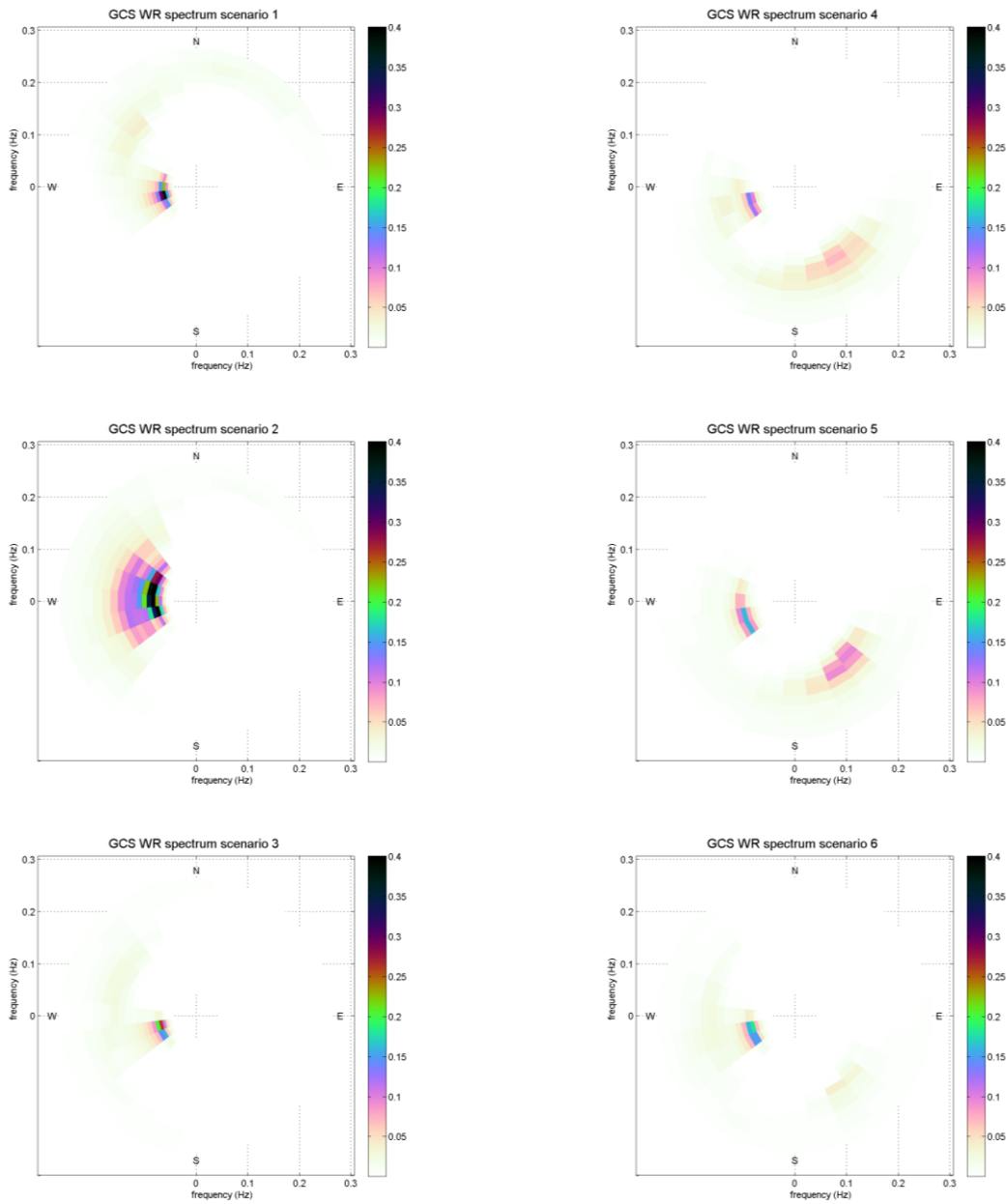


Figure 4-4: Directional wave spectrum at (39.955°S, 174.069°E), or (X, Y) = (-19713.3, 93803.1), from all six environmental scenarios using baseline bathymetry. Wave frequency increases radially outward from the centre (with scales marked on the x and y axes).

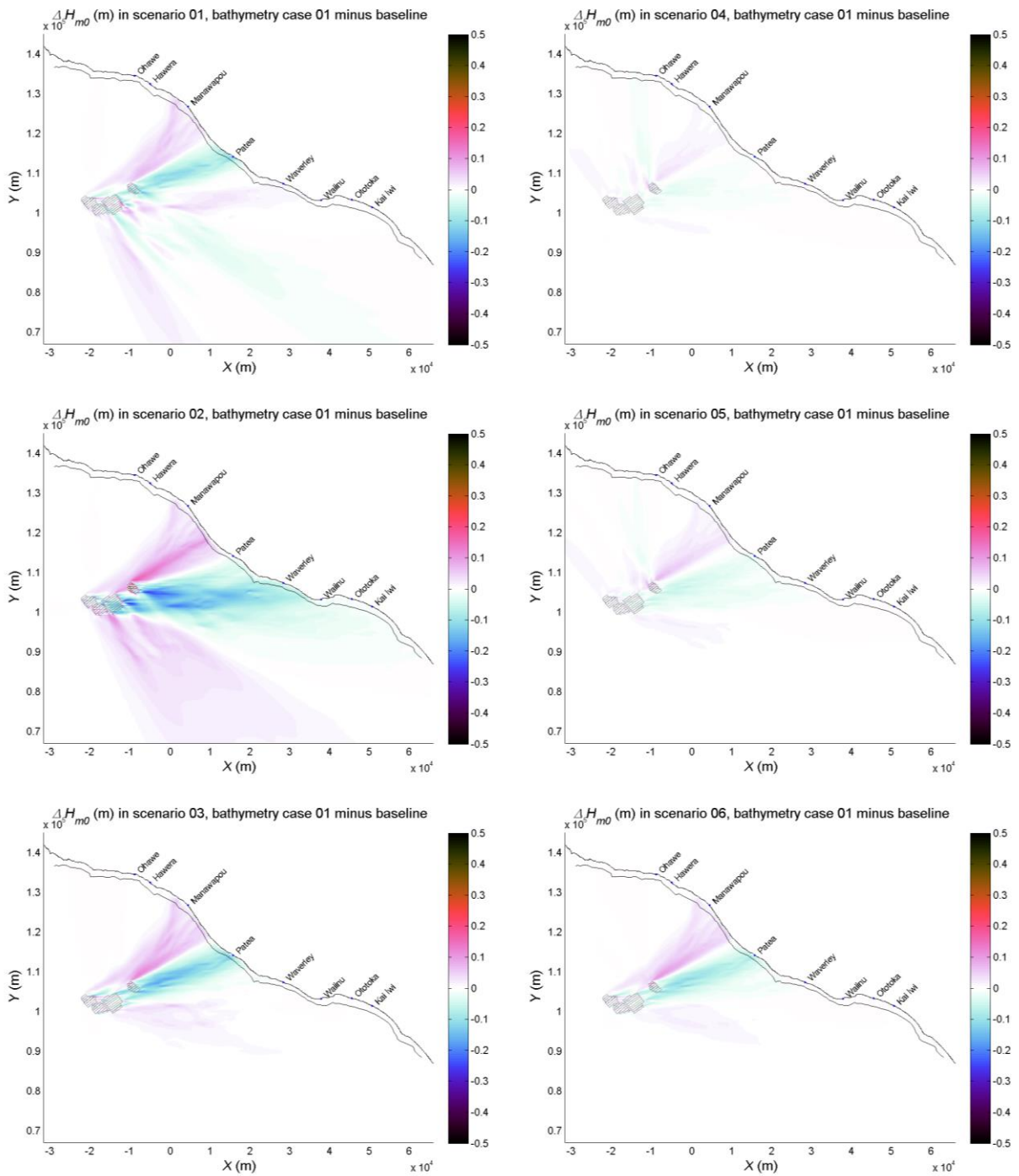


Figure 4-5: Difference between significant wave height for case 1 and existing bathymetry, over the model domain, for each of the six environmental scenarios.

As we are particularly interested in nearshore wave conditions, we now look at values of wave statistics extracted along the 10 m isobath. These are shown for the baseline simulations (for all environmental scenarios) in Figure 4-6. Here the horizontal scale is distance along the section of the 10 m isobath marked in the map plots (e.g. Figure 4-1) moving from northwest (near Hawera) to southeast (near Wanganui). We note that all environmental scenarios show generally similar spatial variation, although the mean values vary between scenarios. This is a result of refraction and shoaling over bathymetric features imposing a consistent finer scale structure on wave fields that are more homogeneous further offshore.

Again using the case 1 bathymetry modifications as an example (Figure 4-7), we observe a consistent pattern of decreases in wave height, by up to 10 cm, on the coast southeast of Patea (longshore distances greater than 50 km), with more modest height increases (mostly less than 5 cm) to the northwest. The changes in mean period show a similar pattern, because changes associated with refraction by bathymetric features will have a greater influence on long period wave components, so in places where some energy has been removed, this will tend to reduce the mean period as well as the significant wave height (and vice versa). Changes in mean wave direction are generally less than 1° , either positive (i.e. clockwise) or negative, but with larger changes, around -2° (i.e., an anticlockwise shift) in a localised area west of Manawapou.

Similar results for all the other bathymetry cases are contained in Appendix D. In this section of the report, though, we summarise these results by looking at the maximum and mean (across all environmental scenarios) value in magnitude changes of wave parameters at the 10 m isobath, shown in Figure 4-8 and Figure 4-9, respectively, for all bathymetry cases. Changes in significant wave height are all less than 12 cm for case 1, and less than 5 cm for other cases. These are closely correlated with changes in mean period, all less than 0.5 seconds for case 1, and half that for other cases. The largest impacts (from case 1) occur as a decrease in heights and periods near Patea.

We can also look at this in relative terms, i.e., the magnitude of change as a percentage of the baseline value, plotted as maximum and mean values in Figure 4-10 and Figure 4-11, respectively. These show changes in significant wave height and mean period remain less than 8.6% for the maxima in case 1, 4.5% for other cases, while average changes are less than 3.5% for case 1, or 1.5% for other cases. Changes in bed-orbital velocity, which tend to compound coincident changes in height and period, are slightly higher in percentage terms.

The maximum changes in significant wave height ($|H_{m0} - H_{m0}(\text{baseline})|$) are summarised in Table 4-1. Some local effects, nearer than the mining areas, are larger than seen at the 10 m isobath. Cases 1-8 show maximum changes in wave height (over all environmental scenarios, and over the whole modelling domain) of up to 0.436 m, or 12.6% of baseline values.

Table 4-1: Maximum changes in significant wave height predicted for the eight bathymetry modification cases. Changes are expressed in absolute terms (metres) and relative terms (%), either over the full model domain or along the 10 m isobath.

case	full domain		10 m isobath	
	max (m)	max (%)	max (m)	max (%)
1	0.436	12.6	0.116	9.2
2	0.232	9.0	0.045	3.8
3	0.348	10.9	0.050	3.5
4	0.245	10.0	0.050	4.3
5	0.228	9.1	0.052	4.8
6	0.239	7.9	0.018	1.4
7	0.177	6.6	0.022	1.9
8	0.096	4.6	0.010	0.9

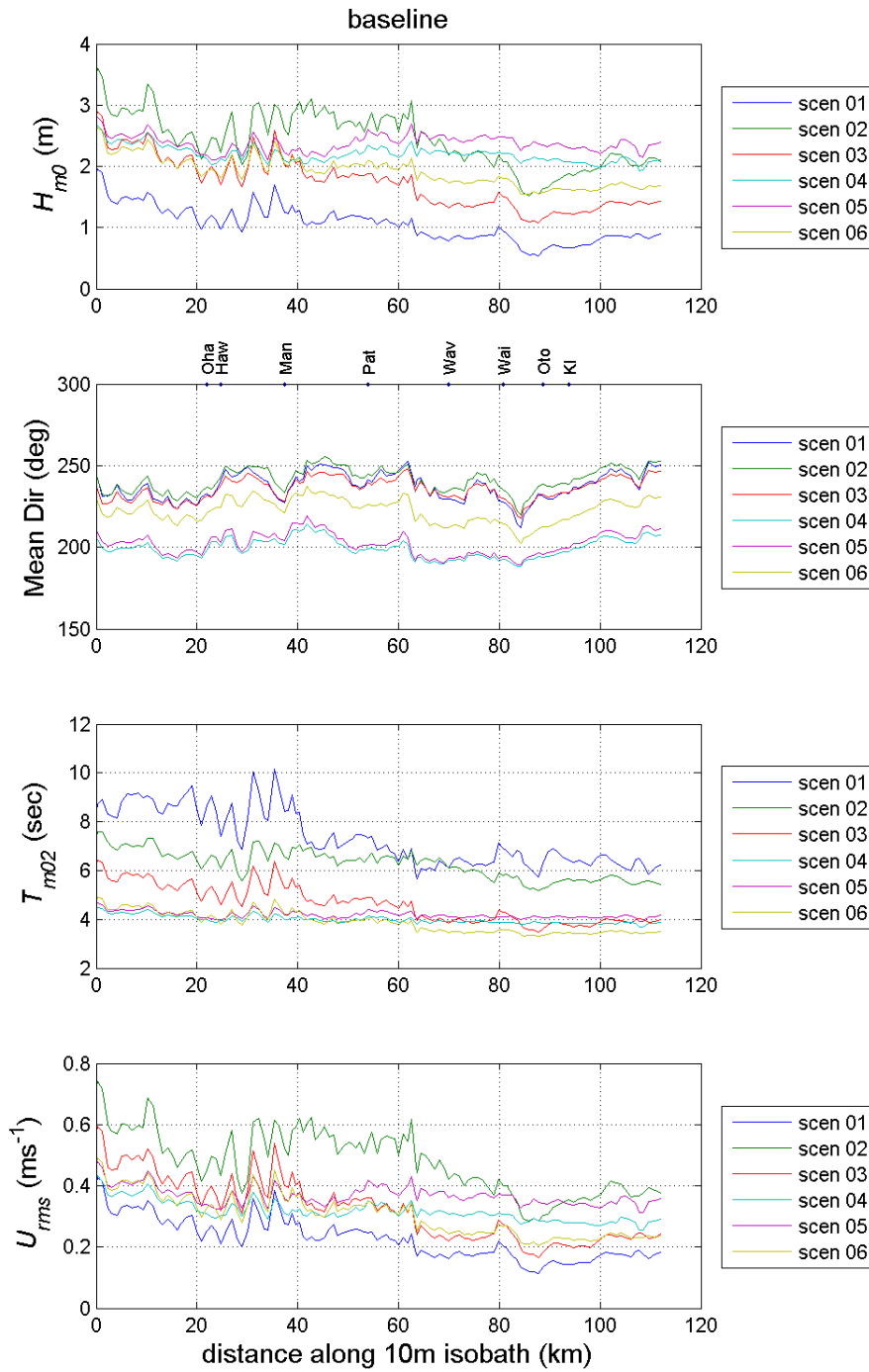


Figure 4-6: Wave parameters at the 10 m isobath with existing bathymetry, in all 6 environmental scenarios. From top to bottom: significant wave height, mean wave direction, mean wave period, and root-mean-square bed orbital velocity. Positions of beaches referred to on output maps (e.g., Figure 4-1) are marked in abbreviated form along the top of the direction plot for reference.

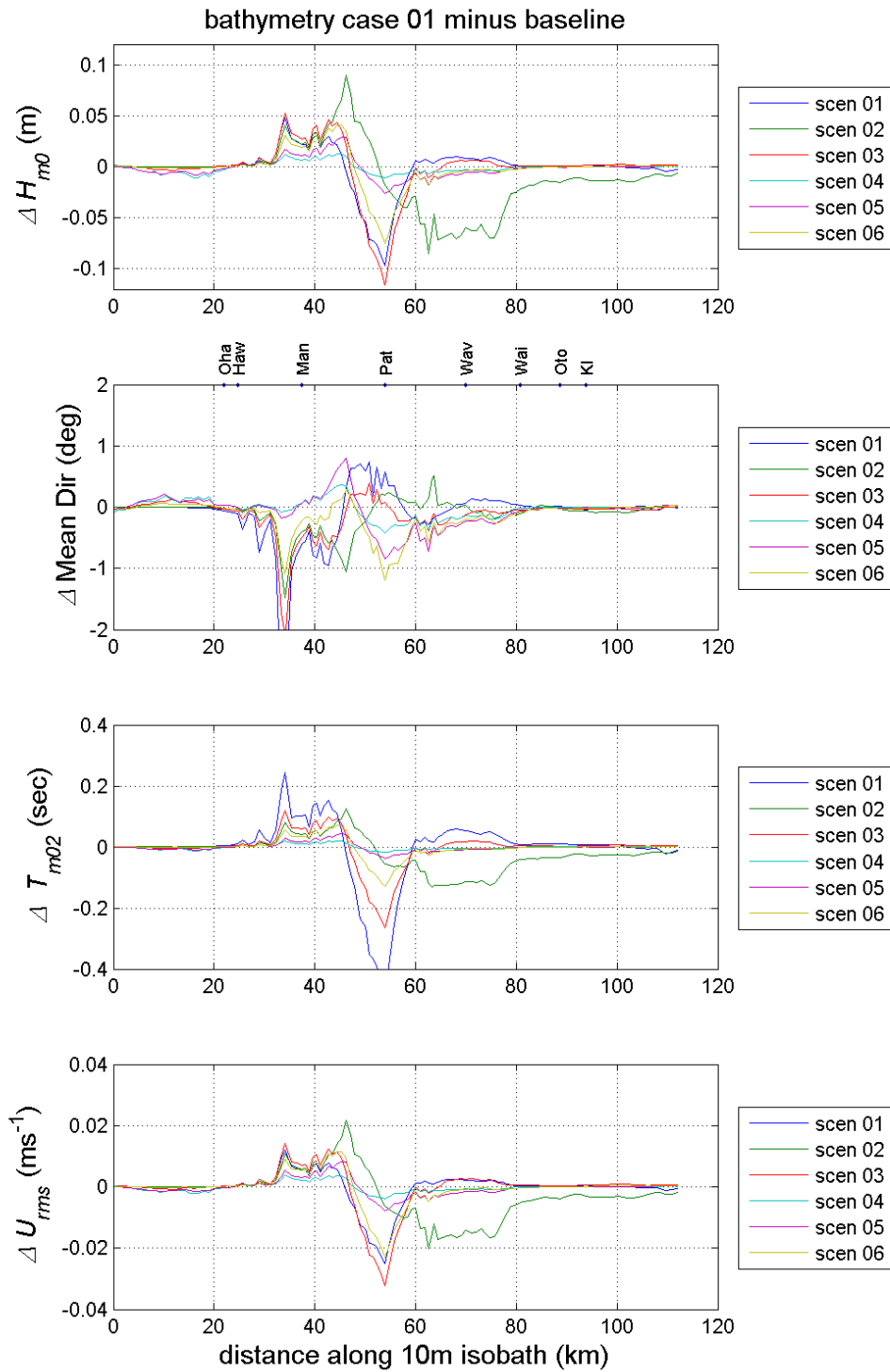


Figure 4-7: Difference between wave parameters at the 10 m isobath for case 1 and existing bathymetry, in all 6 environmental scenarios. From top to bottom: significant wave height, mean wave direction, mean wave period, and root-mean-square bed orbital velocity are plotted as a function of distance along the 10 m isobath.

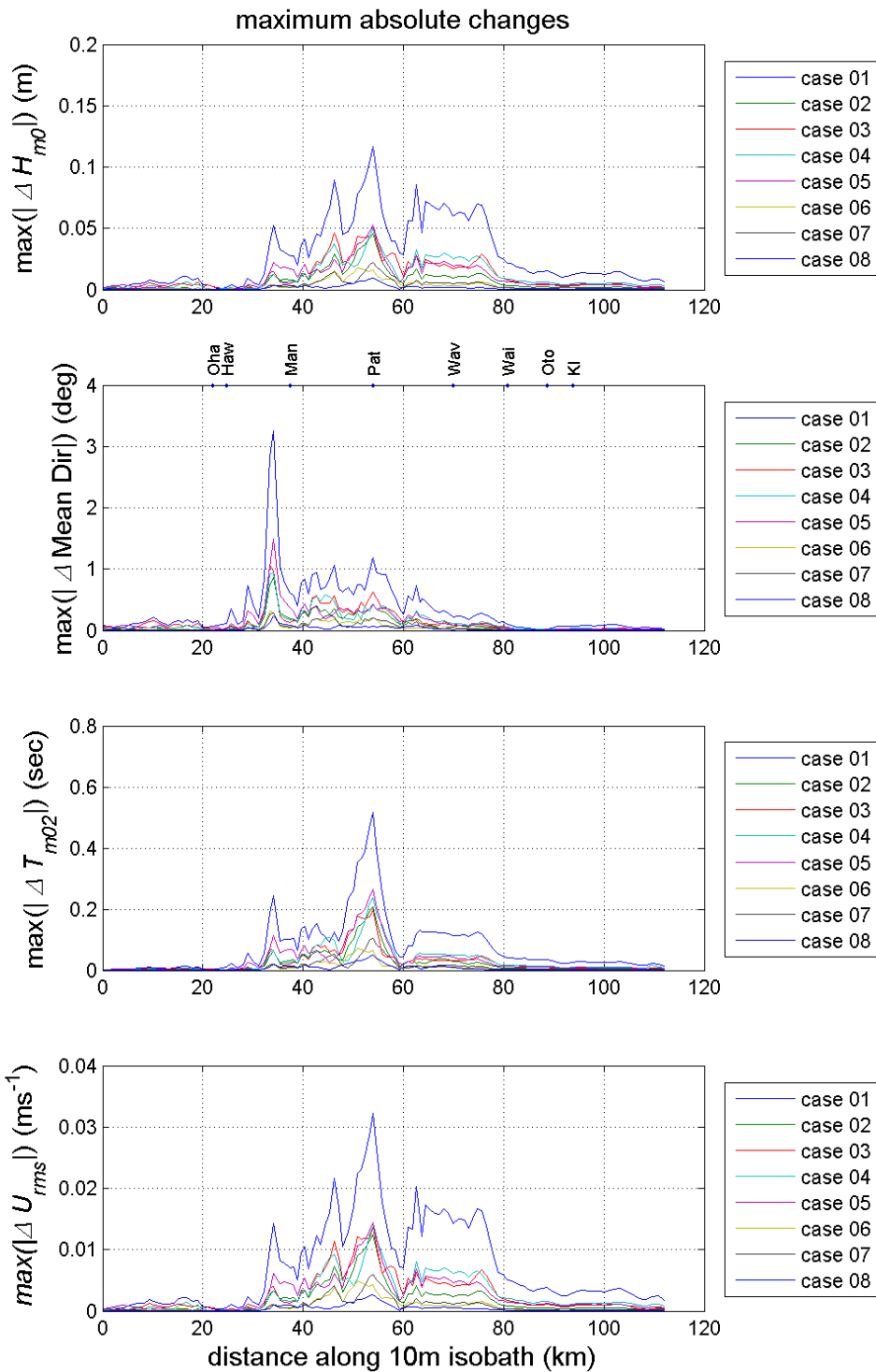


Figure 4-8: Maximum (over six environmental scenarios) of the absolute change in wave parameters at the 10m isobath. Values are plotted for all bathymetry cases, as a function of distance along the 10 m isobath.

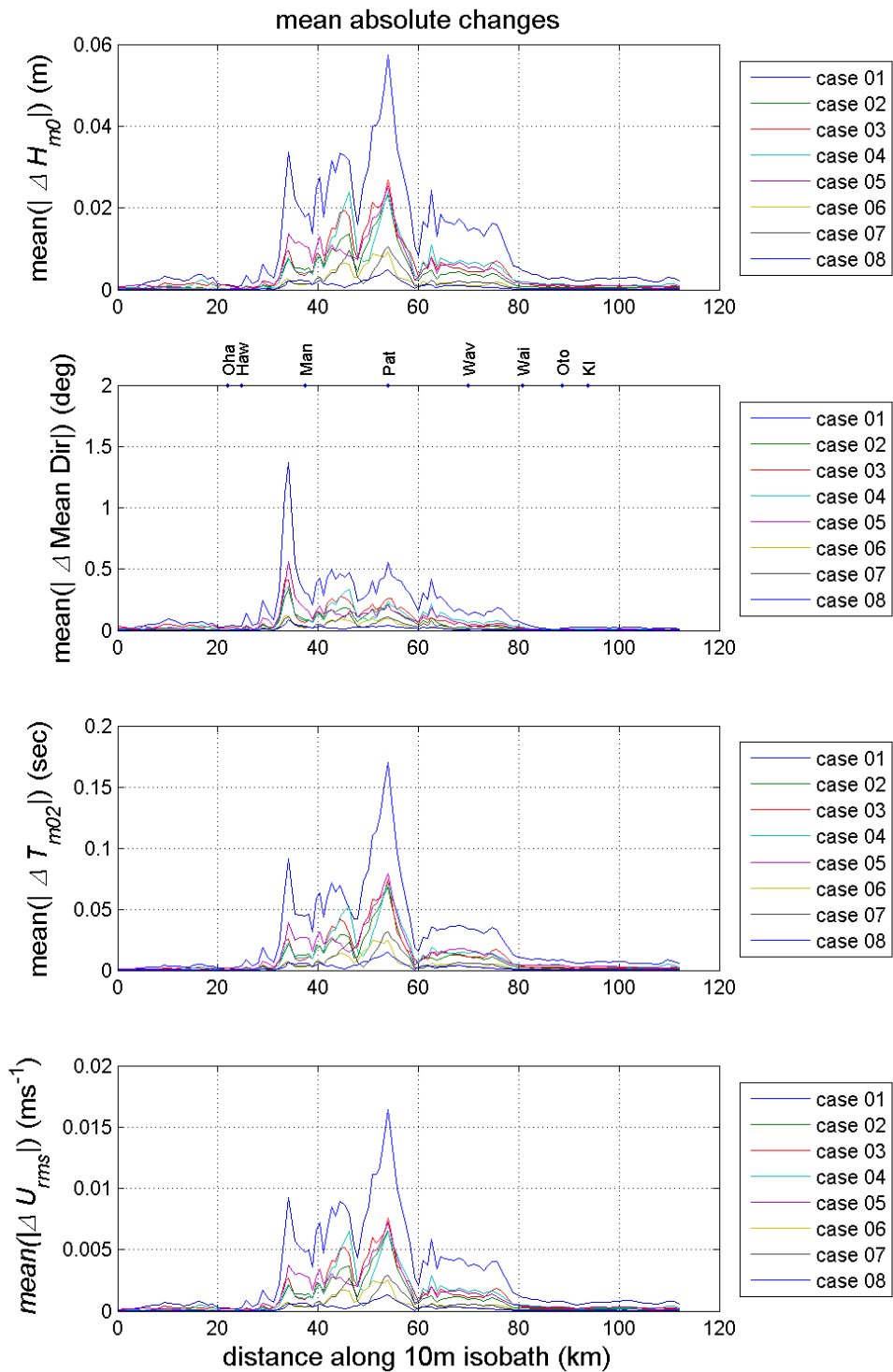


Figure 4-9: Mean (over six environmental scenarios) of the absolute change in wave parameters (in metres) at the 10m isobath. Values are plotted for all bathymetry cases, as a function of distance along the 10 m isobath.

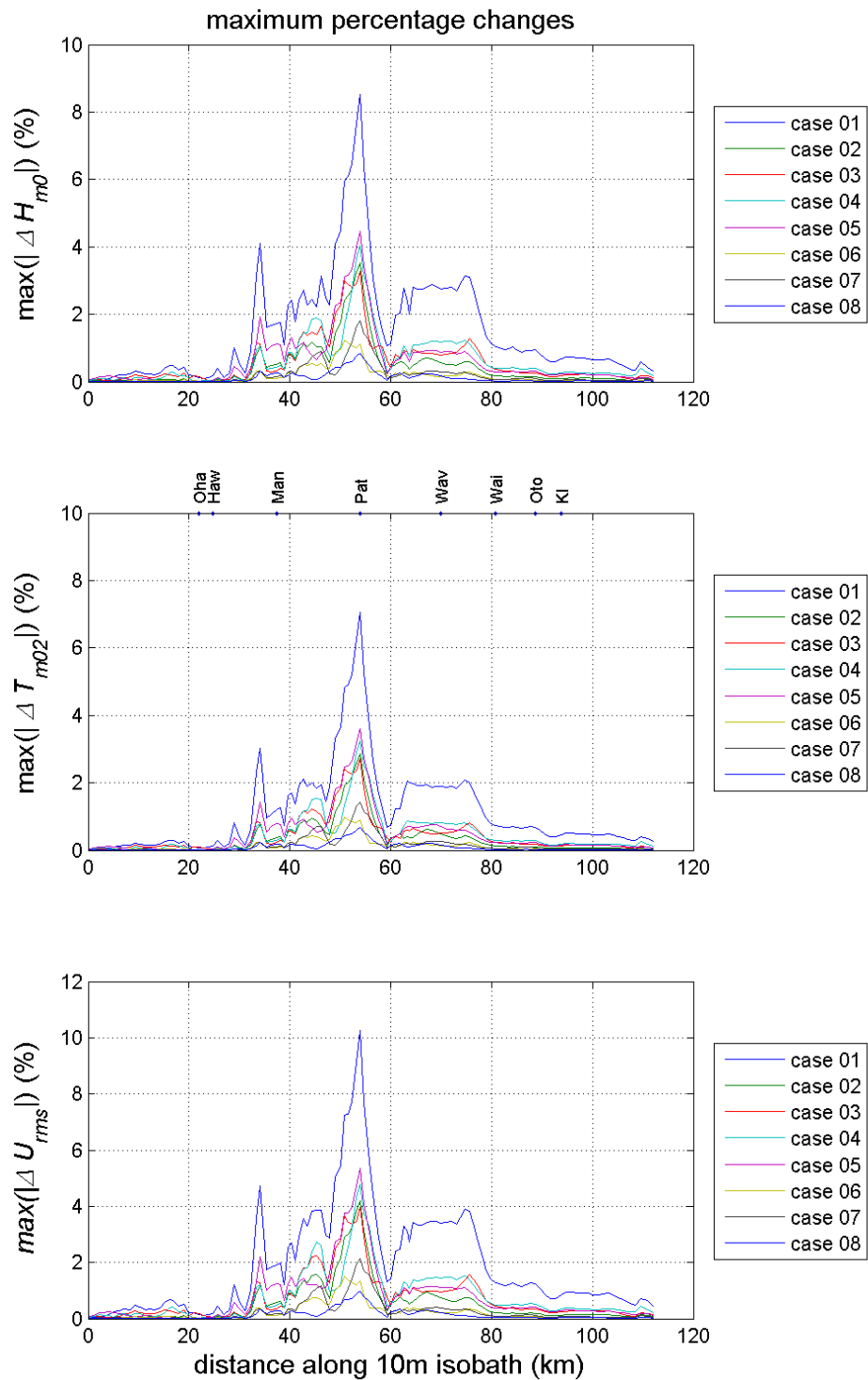


Figure 4-10: Maximum (over six environmental scenarios) of the relative change in wave parameters (as a fraction of the baseline values) at the 10m isobath. Values are plotted for all bathymetry cases, as a function of distance along the 10 m isobath.

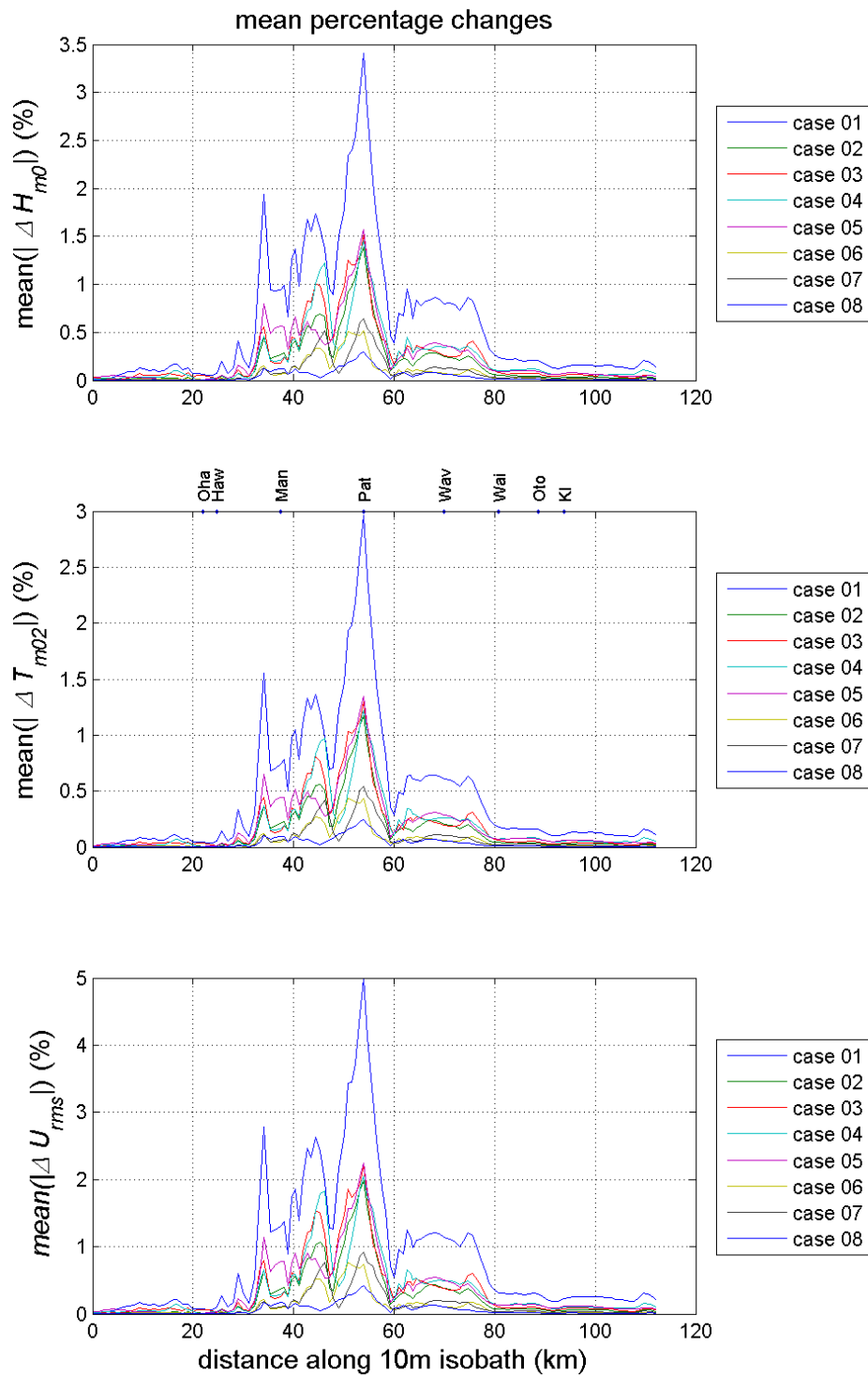


Figure 4-11: Mean (over six environmental scenarios) of the relative change in wave parameters (as a fraction of the baseline values) at the 10m isobath. Values are plotted for all bathymetry cases, as a function of distance along the 10 m isobath.

4.1.2 Long-term simulation

The long-term simulations used the SWAN wave model established on the Xantia_100m grid to simulate wave conditions over a twelve month period (January 2011 through December 2011) after a “spinup” period to from December 21, 2010 to initialise the model. These simulations provided full time series outputs of wave statistics on the 10 m isobath.

This was done first for the existing bathymetry, to provide a baseline. Figure 4-12 shows the time averages, and standard deviations (SDh), of hourly output wave parameters on the 10 m isobath for the baseline simulation. Comparison with Figure 4-6 shows that the nearshore outputs of individual scenario runs are consistent with the longer term statistics, with the spatial variation of significant wave height, mean period and bed orbital velocity lying around or above one standard deviation (SDh) over the yearly mean. This is as we would expect for conditions selected from the more energetic parts of a one-month record. Also, the envelope of nearshore wave directions overlaps closely with a one standard deviation range above the mean.

Bathymetry case 1 was selected for the single test simulation. Figure 4-13 shows the mean difference, or bias, between wave statistics from the test and baseline simulations. If a variable has a value $V(t_n, x)$ at time t_n and position x in the test simulation, and a value $V_0(t_n, x)$ in the baseline simulation, the bias is defined as

$$bias = \langle \Delta v(x) \rangle = \frac{1}{N} \sum_{n=1}^N v(t_n, x) - v_0(t_n, x)$$

We see that the bathymetry modifications introduce a mean decrease (by less than 5 cm) in significant wave height on the coast near Patea, with smaller increases (of less than 2.5 cm) further west. Comparisons with Figure 4-7 show that the behaviour of the individual scenarios are consistent with the yearly averages, which generally correspond to the lower end of the range of variability covered by the scenarios. The standard deviation in the differences

$$st.dev. = \sqrt{\frac{1}{N} \sum_{n=1}^N (v(t_n, x) - v_0(t_n, x) - \langle \Delta v(x) \rangle)^2}$$

is also included in Figure 4-13, which illustrates that the mean differences in significant wave height associated with the bathymetry change generally differ from zero by around one standard deviation, which corresponds to a 68% confidence level. Similar results apply to mean wave direction and bed orbital velocity, while the bias in mean period differs from zero by somewhat less than one standard deviation. For all four variables, this range of variability in the differences associated with the bathymetry changes is considerably less than the corresponding natural range of variability in baseline values illustrated in Figure 4-12. Mean wave period decreases (by less than 0.1 seconds) in the vicinity of Patea, and increases (by less than 0.05 seconds) to the west. Mean wave direction is slightly decreased (i.e., changes in an anticlockwise sense) on average along the majority of the coast, by less than 1°.

Various other statistical measures of the effects of bathymetry modification can be calculated. Figure 4-14 shows the root-mean-square difference (RMSD), defined as

$$RMSD = \sqrt{\frac{1}{N} \sum_{n=1}^N (v(t_n, x) - v_0(t_n, x))^2}$$

between test and baseline statistics, which shows the typical wave height differences less than 2.0 cm for much of the coast, up to a maximum of 5.5 cm near Patea.

The mean relative magnitude difference (Figure 4-15) is defined as

$$\frac{1}{N} \sum_{n=1}^N \frac{|v(t_n, x) - v_0(t_n, x)|}{|v_0(t_n, x)|}$$

and can be compared directly with Figure 4-11, which again shows consistency. By this measure the effects of the bathymetry changes are less than 3% for significant height and mean period, and less than 5% for bed-orbital velocity.

The root-mean-square difference can also be divided by either the standard deviation or the mean of the baseline value to give a normalised measure (Figure 4-16). Note that for mean wave direction it only makes sense to normalise by the standard deviation. Using the first of these measures we see that the effects of this particular bathymetry modification remain less than 8% of one standard deviation for significant wave height, less than 15% of one standard deviation for mean period, and less than 10% of one standard deviation for bed-orbital velocity.

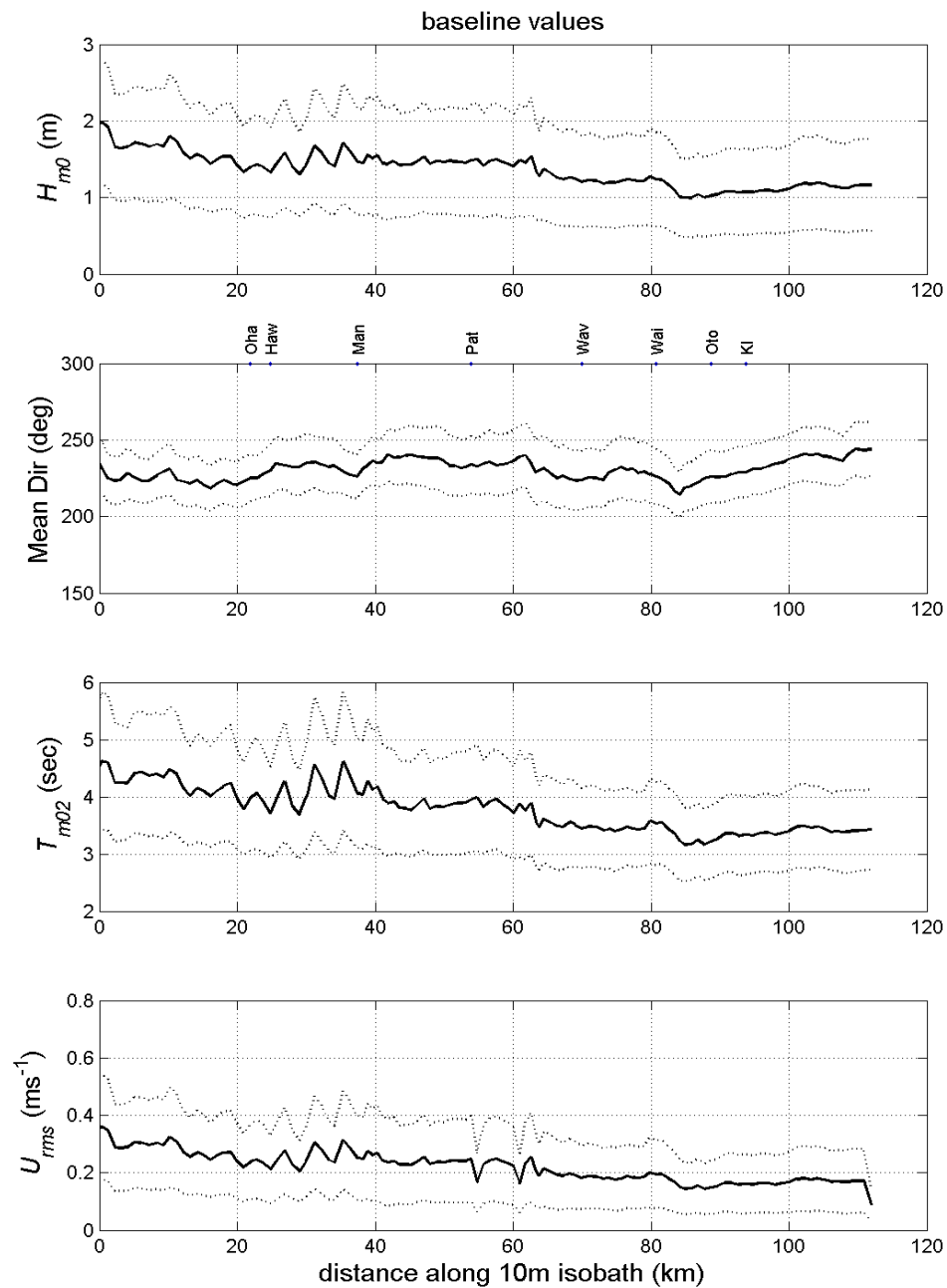


Figure 4-12: Mean values and standard deviation of wave statistics at the 10 m isobath, from the baseline long-term simulation. Mean values (over a 12 month period) from the baseline simulation are shown by solid black lines, plus and minus one standard deviation (SDh) (dashed lines). Statistics shown are, from the top, significant wave height, mean wave direction, second-moment mean wave period and root-mean square bed orbital velocity.

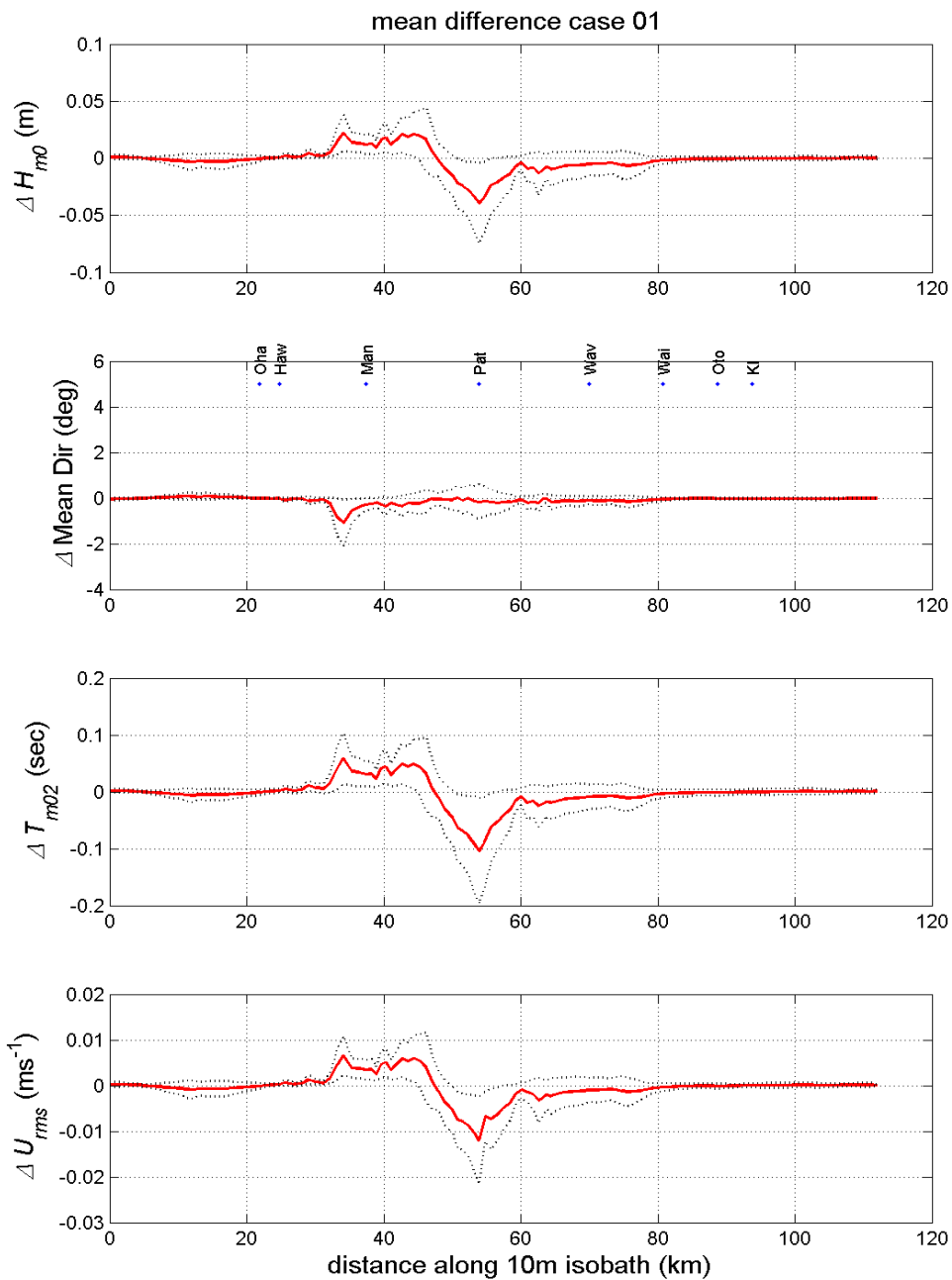


Figure 4-13: Mean (bias) and standard deviation of the difference between the case 1 and baseline long-term simulations of wave statistics at the 10 m isobath. Statistics shown are, from the top, significant wave height, mean wave direction, second-moment mean wave period and root-mean square bed orbital velocity. The dashed lines show one standard deviation (SDh) either side of the mean (solid red lines).

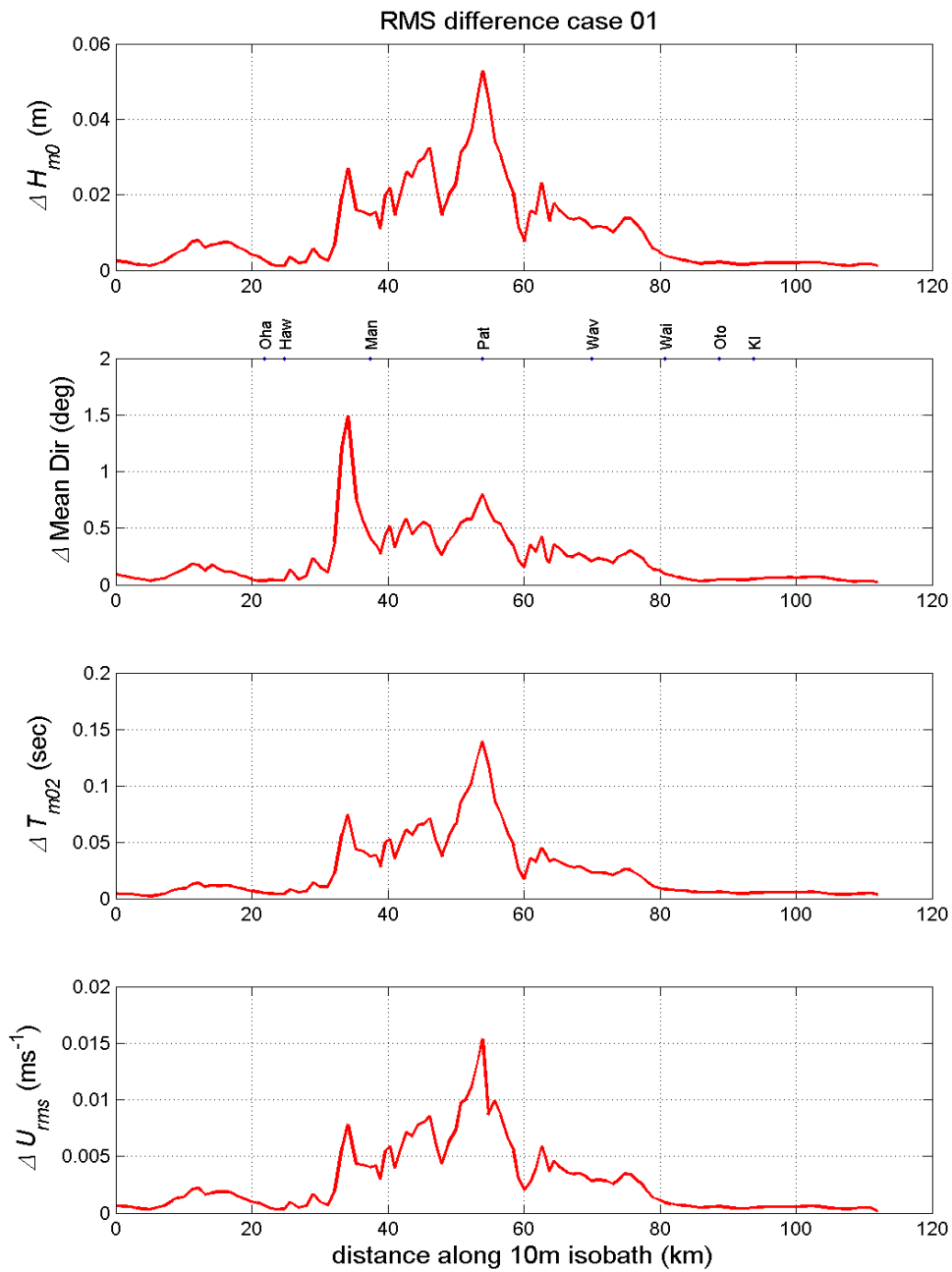


Figure 4-14: Root-mean-square difference in wave statistics at the 10 m isobath, between the case 1 and baseline long-term simulations. Statistics shown are, from the top, significant wave height, mean wave direction, second-moment mean wave period and root-mean square bed orbital velocity.

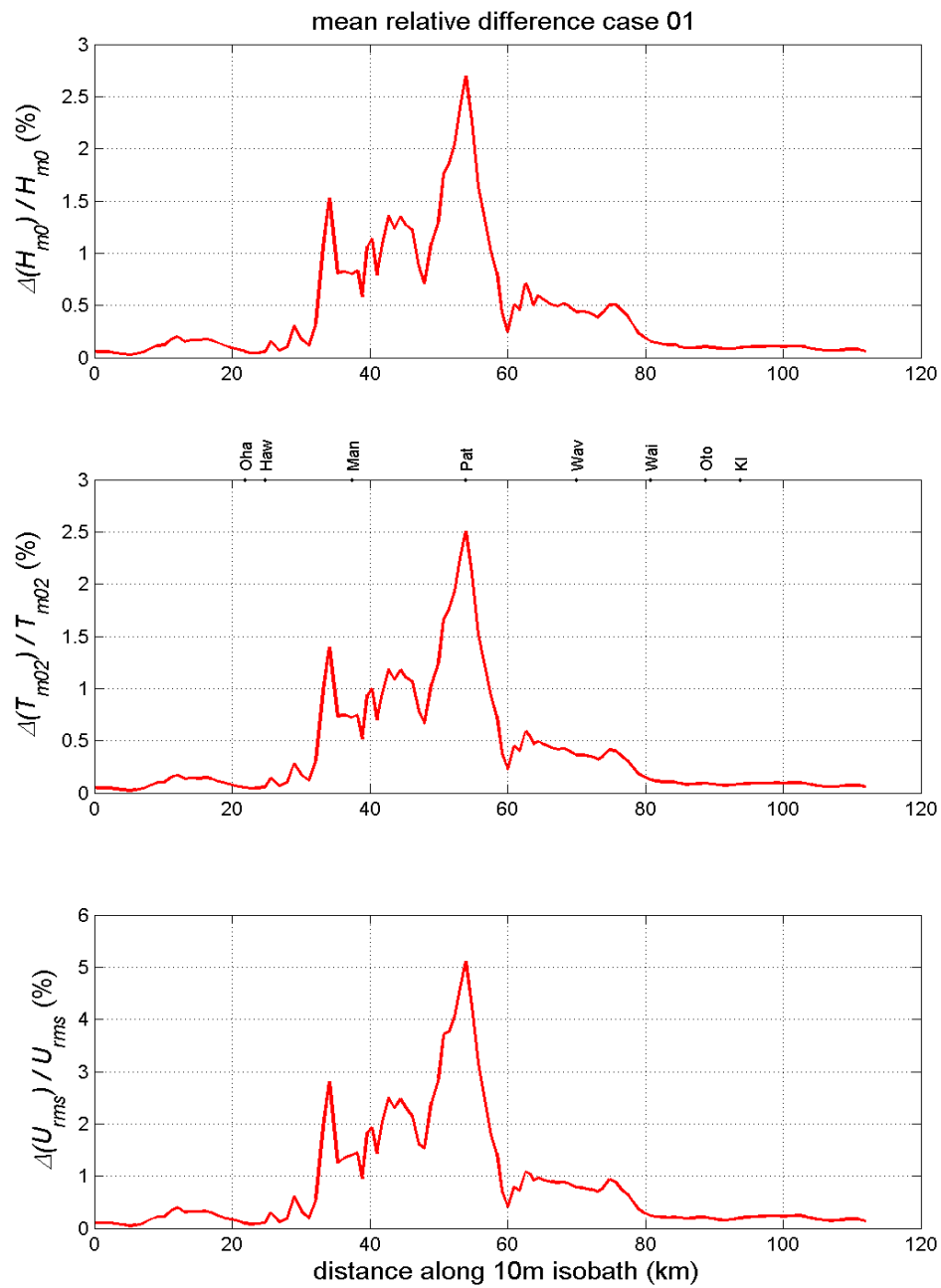


Figure 4-15: Mean fractional difference in values of wave statistics at the 10 m isobath, between the case 1 and baseline long-term simulations. Statistics shown are, from the top, significant wave height, second-moment mean wave period and root-mean square bed orbital velocity.

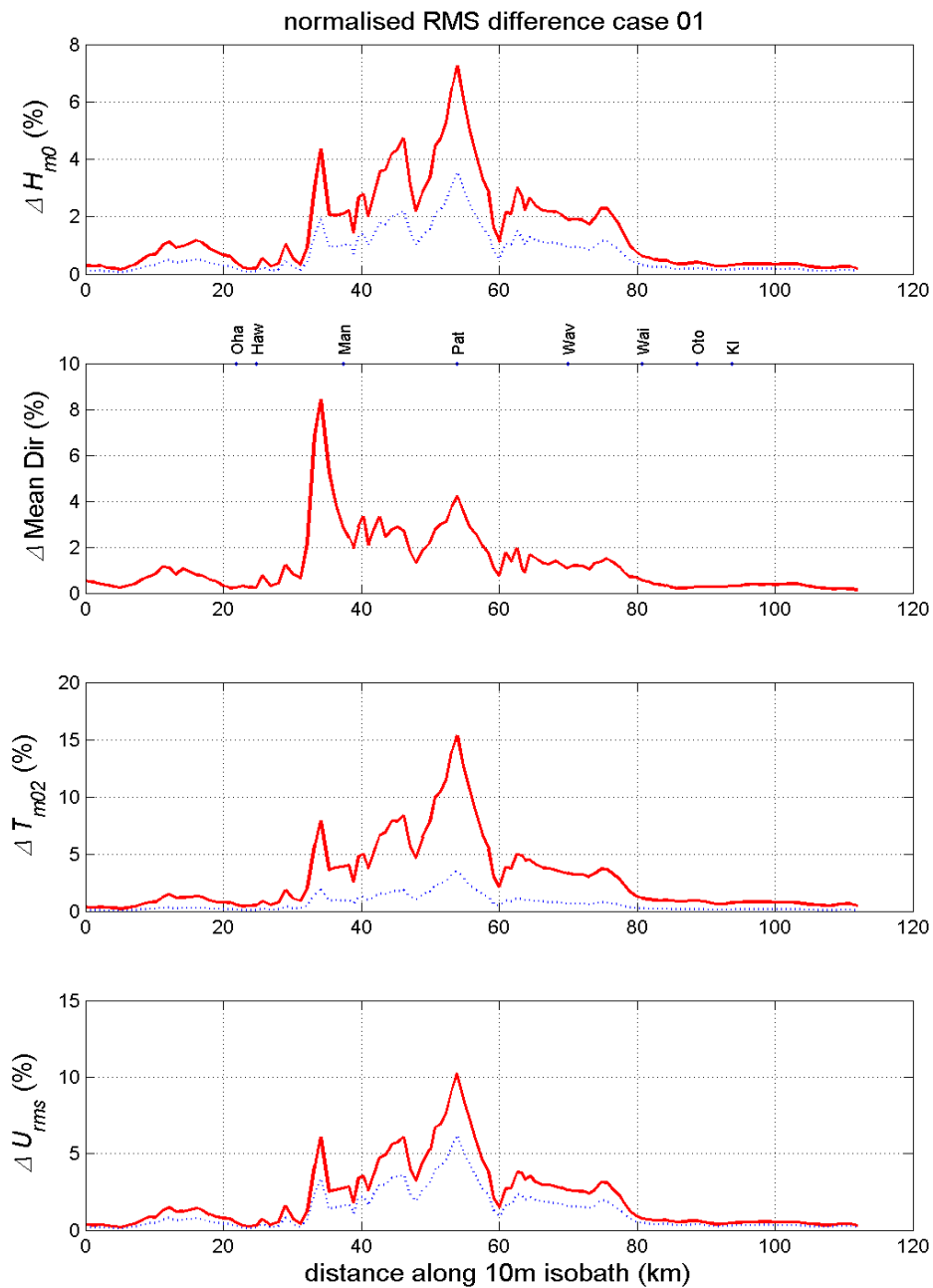


Figure 4-16: Normalised root-mean-square difference in wave statistics at the 10 m isobath, between the case 1 and baseline long-term simulations. The solid red lines and the dashed blue lines show the RMS difference normalised by the standard deviation (SD) and the mean, respectively, of the baseline value. Statistics shown are, from the top, significant wave height, mean wave direction, second-moment mean wave period and root-mean square bed orbital velocity.

4.1.3 Nearshore wave and sediment transport statistics

Having used the SWAN model to obtain detailed synthetic records of wave statistics at 10 m water depth, we then rely on empirical methods to estimate behaviour through the nearshore and surf zone, where the numerical model cannot be relied upon, largely due to limited availability of accurate and highly-resolved bathymetric data. The empirical methods used for this are outlined in Appendix B. This produces time series of various quantities at the shoreline, including breaking wave height H_b , longshore wave flux factor P_{ls} , onshore wave flux factor P_{os} , and contributions to the longshore mean current from the processes of oblique wave incidence ($V_{ls,obl}$) and wave height gradient ($V_{ls,hgrad}$). As described in Appendix B, the wave-driven longshore sediment flux Q is taken as directly proportional to P_{ls} .

In the following plots we show the spatial variation of various statistics derived from these quantities, both as coloured ribbon plots for means of baseline values, and as line plots against distance along the shore. We also show line plots of statistics quantifying the effect of the bathymetry modifications, in the form of bias and root mean square difference, both as absolute quantities and normalise by either the standard deviation or mean of the corresponding baseline values.

In this case to characterise the differences we use a more appropriate statistic for the standard deviation (SDm) calculated by first computing monthly means for the one year record and then taking the standard deviation of the 12 values.

For baseline bathymetry, mean values of breaking wave height (H_b) vary between 1.2 m and 2.2 m along the South Taranaki coast (Figure 4-17), generally decreasing from northwest to southeast. The case 1 bathymetry modifications acts to reduce mean values in the vicinity of Patea by less than 5 cm, and to increase values by up to 2.5 cm in parts of the coast further west. The root mean square difference in H_b is generally less than 20% of one standard deviation (SDm).

The onshore wave energy flux factor P_{os} (Figure 4-18) shows generally similar behaviour to the breaking wave height, apart from having values somewhat elevated east of Manawapou where the coast is aligned more normal to the prevailing wave direction. The case 1 bathymetry modification introduces RMS differences generally less than 20% of one standard deviation (SDm).

The longshore wave energy flux factor P_{ls} (Figure 4-19) is important as the driver of longshore sediment transport. Indeed, we have assumed that the longshore sediment transport Q is directly proportional to P_{ls} so have simply used double axis scales to show both quantities on the same plot. The longshore flux can, in general, act in either direction along the coast. Here, positive values are defined as acting along the coast towards the southeast, and we note that the time-average values of P_{ls} and Q are positive everywhere along the South Taranaki coast, as a result of its alignment to the generally westerly wave climate. It has its largest values at the western end, and generally decreases eastwards with decreasing incident wave height, but with some variation due to local coastal alignment. This quantity also has a relatively large temporal variability, with the mean value generally less than one standard deviation (SDh) from zero.

The case 1 bathymetry modifications would act to decrease the longshore wave energy flux factor near Patea (i.e., slightly reduce the positive SE sediment flux) by up to 8% of a

standard deviation (SDh), or 12% of the mean. There would be a smaller net increase in longshore flux on a small part of the coast west of Manawapou. Overall the change in longshore wave energy flux lies well within half the baseline standard deviation (SDm) (3rd panel from the top of Figure 4-19).

As P_{ls} and Q can take either positive or negative values, it can in general be instructive to also examine time averages of their magnitudes $|P_{ls}|$ and $|Q|$ (Figure 4-20) and their values restricted to times when it is either positive (Figure 4-21) or negative (Figure 4-22). In this case, however, where P_{ls} is strongly weighted to positive values, the first two quantities have rather similar behaviour to the net statistic. Figure 4-22 does show that the bathymetry modifications would lead to a very small, localised, increase in the magnitude of the relatively rare negative (westward) sediment transport events near Manawapou.

The divergence in P_{ls} and hence Q (Figure 4-23) is a quantity that can contribute to either erosion or accretion of a beach where the divergence is positive or negative, respectively. The former would be the case, for example, on a section of beach with eastward transport that increases in magnitude with distance eastward along the beach, meaning more sediment is leaving the beach segment through its eastern end than is entering at its westward end. Positive divergence tends to occur around headlands, or other convex segments of coast. On the South Taranaki coast there is considerable spatial and temporal variability in this quantity in the baseline case. The bathymetry modification introduces some biases, at a level generally less than the standard deviation (SDh), which also has high spatial variability.

Waves at the coast can drive mean longshore currents either due to an oblique angle of incidence, or through longshore variability in wave height setting up sea level gradients. The corresponding components $V_{ls,obl}$ and $V_{ls,hgrad}$ of longshore current are plotted in Figure 4-24 and Figure 4-25, respectively. Due to the coast's alignment, we can expect oblique wave incidence to drive eastward currents throughout the region, with magnitudes of up to 1-2 m/s. Introducing the bathymetry changes could affect this quantity in a similar manner to P_{ls} , with decreases of order 5% of a standard deviation (SDh) in sections of the coast around Patea. The component due to height gradient has a high level of spatial and temporal variability, and could expect to show a highly variable (but relatively small in magnitude) pattern of bathymetry-related changes.

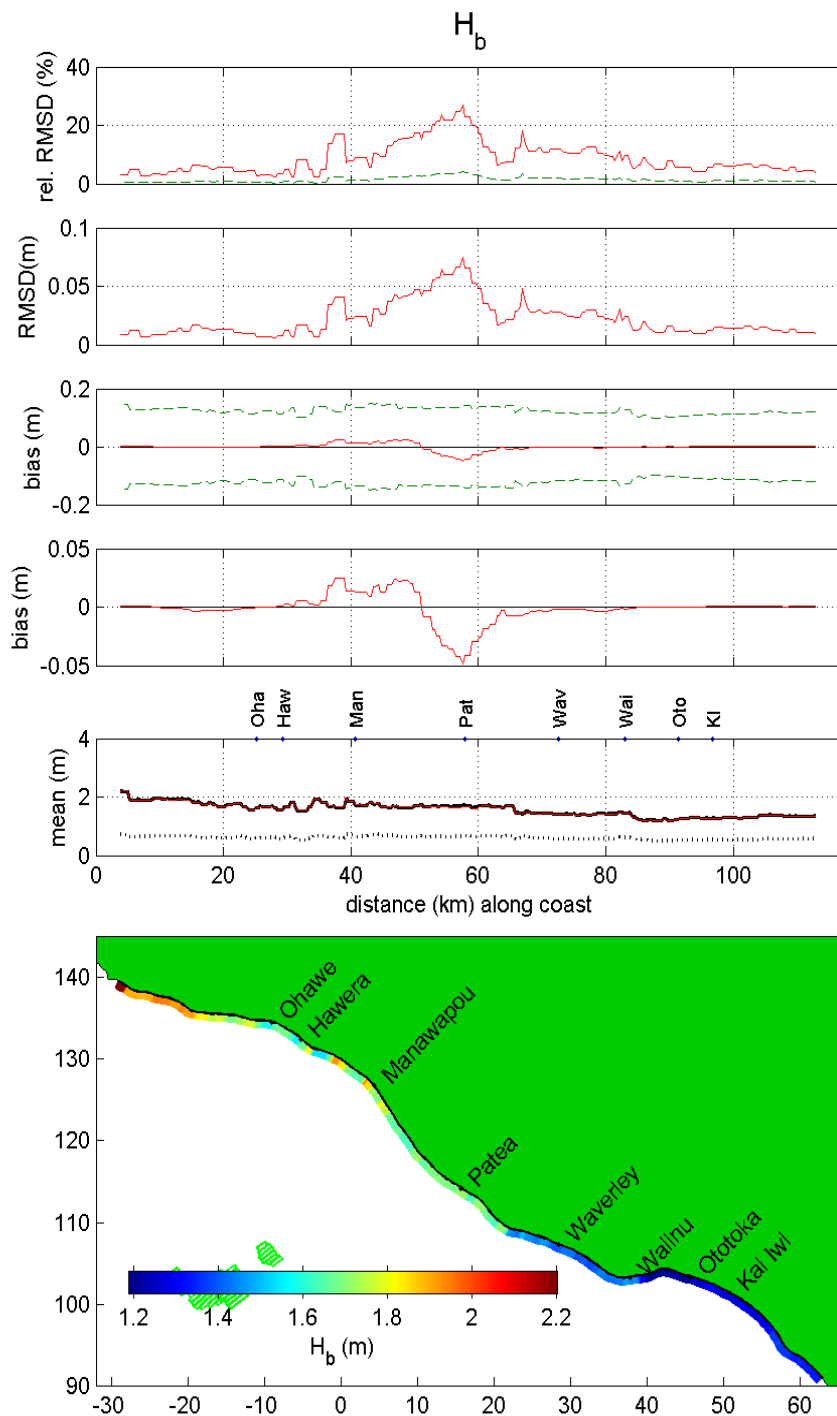


Figure 4-17: Breaking wave height H_b at the coast. The mean value (over a 12 month period) from the baseline simulation is shown by the colour-scaled ribbon in the bottom panel, and as a solid black line in the panel above, compared with the mean value from the case 1 simulation (red), and the standard deviation (SDh) from the baseline simulation (dashed black line). In the panels above that, the mean difference (bias = case 1 - baseline) between the two simulations is shown, plotted on its own and also plotted along with green dashed lines showing plus and minus half the baseline standard deviation (SDm). The top two panels show the root-mean-square difference (RMSD) between the two simulations, in absolute value (metres) and as a fraction of the baseline standard deviation (SDm) (red line) and mean magnitude (dashed green line).

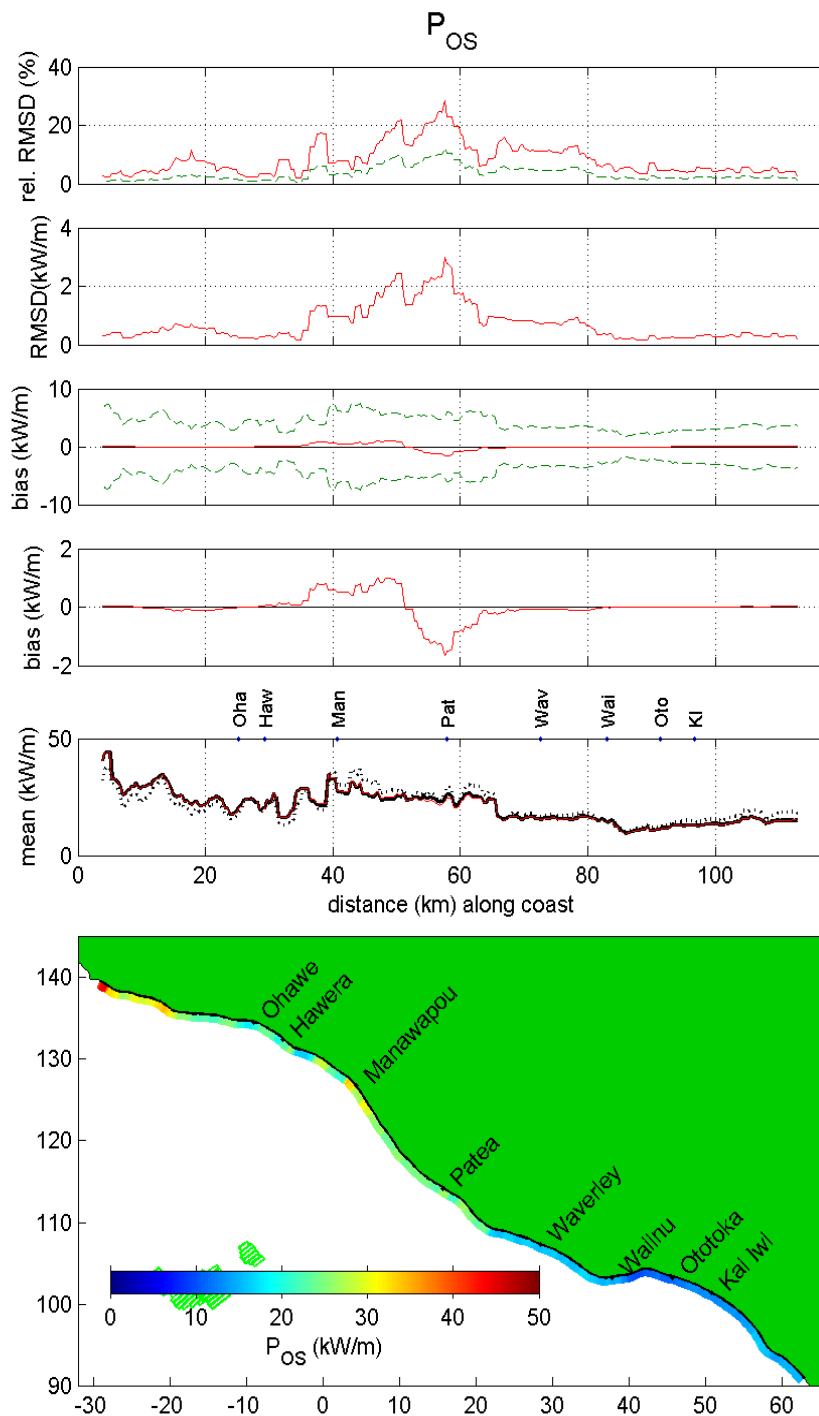


Figure 4-18: Net onshore flux factor P_{os} at the coast. The mean value (over a 12 month period) from the baseline simulation is shown by the colour-scaled ribbon in the bottom panel, and as a solid black line in the panel above, compared with the mean value from the case 1 simulation (red), and the standard deviation (SDh) from the baseline simulation (dashed black line). In the two panels above that, the mean difference (bias = case 1 - baseline) between the two simulations is shown, plotted on its own and also plotted along with green dashed lines showing plus and minus half the baseline standard deviation (SDm). The top two panels show the root-mean-square difference (RMSD) between the two simulations, in absolute value (kW/m) and as a fraction of the baseline standard deviation (SDm) (red line) and mean magnitude (dashed green line).

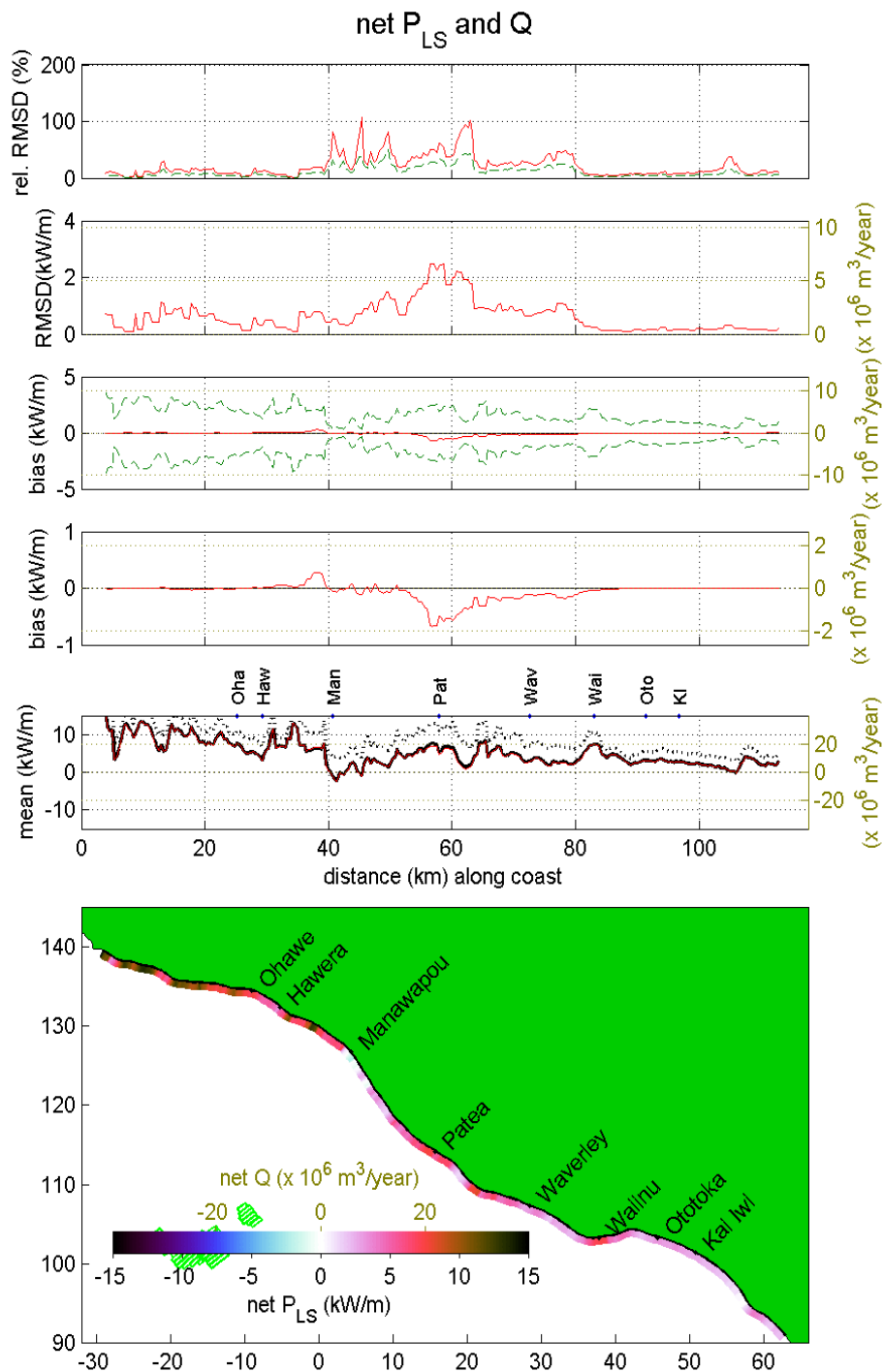


Figure 4-19: Net longshore flux factor P_{LS} (black scales) and sediment flux Q (gold scales) at the coast. The mean value (over a 12 month period) from the baseline simulation is shown by the colour-scaled ribbon in the bottom panel, and as a solid black line in the panel above, compared with the mean value from the case 1 simulation (red), and the standard deviation (SDh) from the baseline simulation (dashed black line). In the two panels above that, the mean difference (bias = case 1 - baseline) between the two simulations is shown, plotted on its own and also plotted along with green dashed lines showing plus and minus half the baseline standard deviation (SDh). The top two panels show the root-mean-square difference (RMSD) between the two simulations, in absolute value and as a fraction of the baseline standard deviation (SDm) (red line) and mean magnitude (dashed green line) of total P_{LS} .

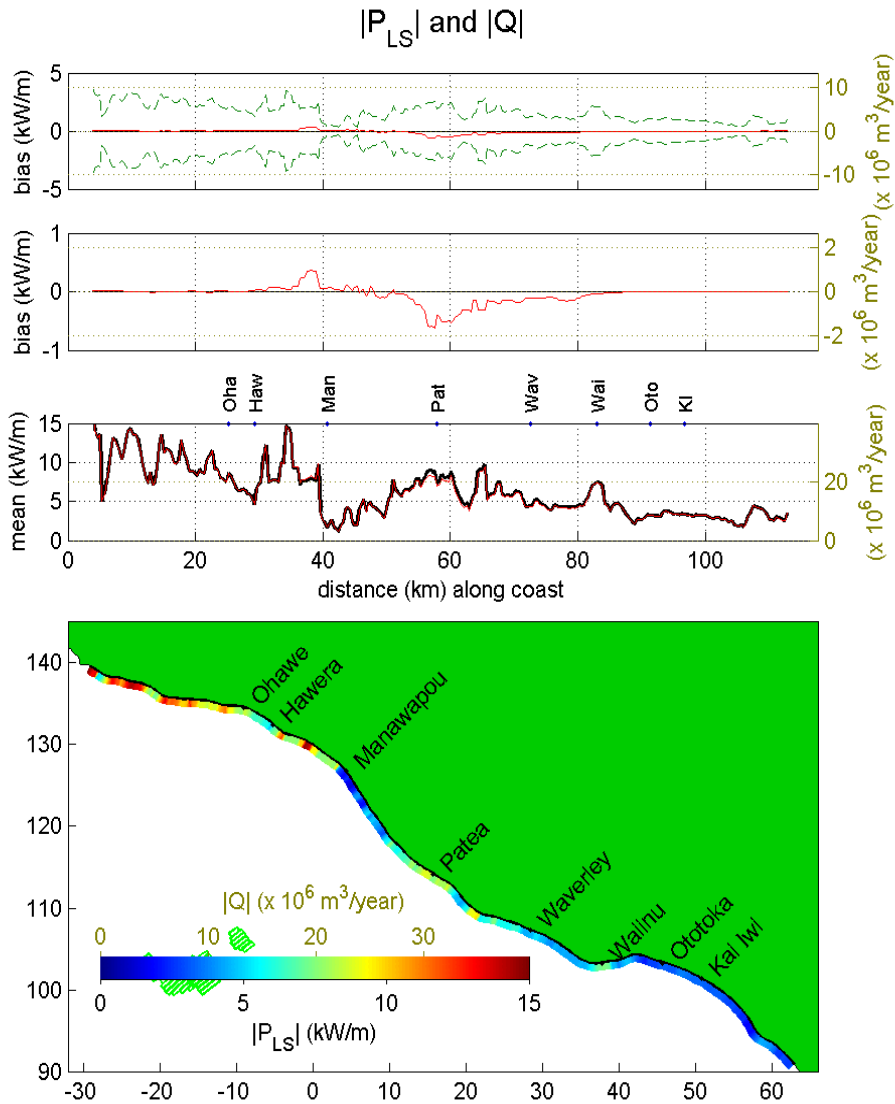


Figure 4-20: Magnitude of the longshore flux factor P_{Ls} (black scales) and sediment flux Q (gold scales). The mean value (over a 12 month period) from the baseline simulation is shown by the colour-scaled ribbon in the bottom panel, and as a solid black line in the panel above, compared with the mean value from the case 5 simulation (red), and the standard deviation (SDh) from the baseline simulation (dashed black line). In the two panels above that, the mean difference (bias = case 1 - baseline) between the two simulations is shown, plotted on its own and also plotted along with green dashed lines showing plus and minus half the baseline standard deviation (SDm) of total P_{Ls} (or Q).

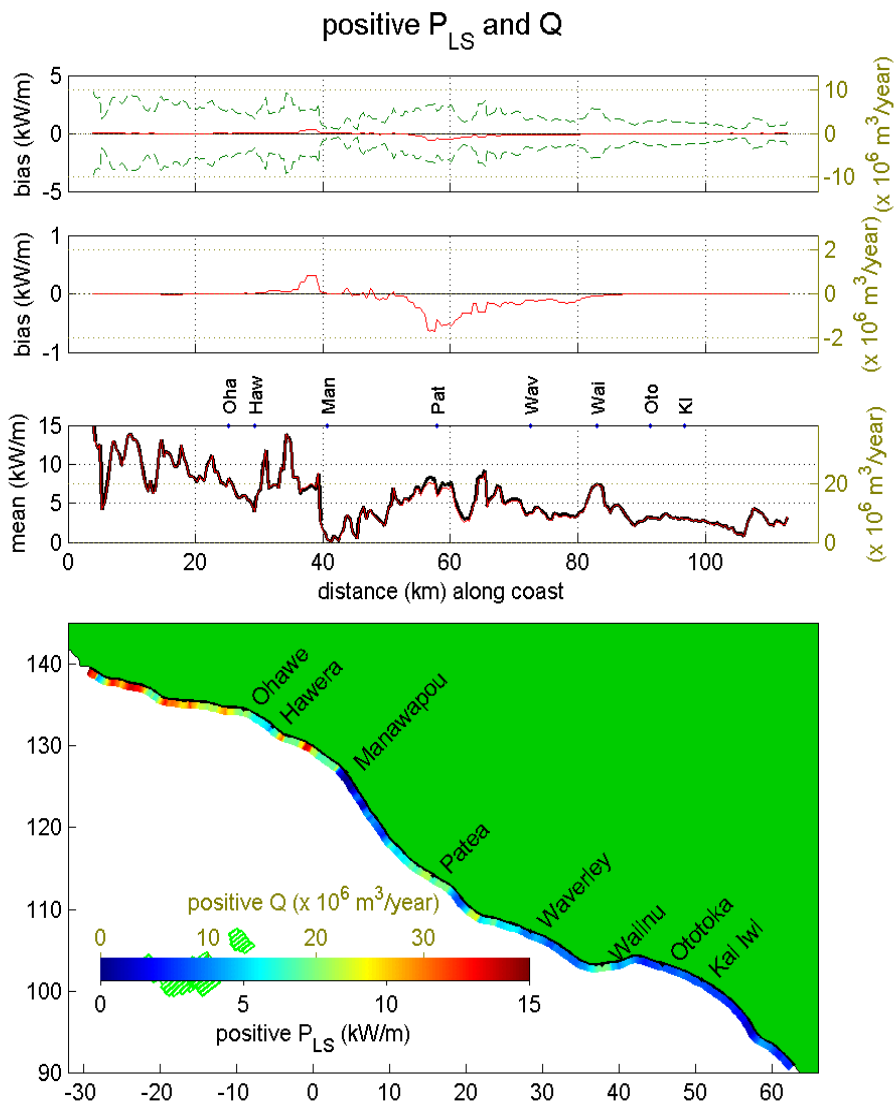


Figure 4-21: Magnitude of the longshore flux factor P_{LS} (black scales) and sediment flux Q (gold scales), averaged over times when they have positive values. The mean value (over a 12 month period) from the baseline simulation is shown by the colour-scaled ribbon in the bottom panel, and as a solid black line in the panel above, compared with the mean value from the case 1 simulation (red), and the standard deviation (SDh) from the baseline simulation (dashed black line). In the two panels above that, the mean difference (bias = case 1 - baseline) between the two simulations is shown, plotted on its own and also (top plot) plotted along with green dashed lines showing plus and minus half the baseline standard deviation (SDm) of total P_{LS} (or Q).

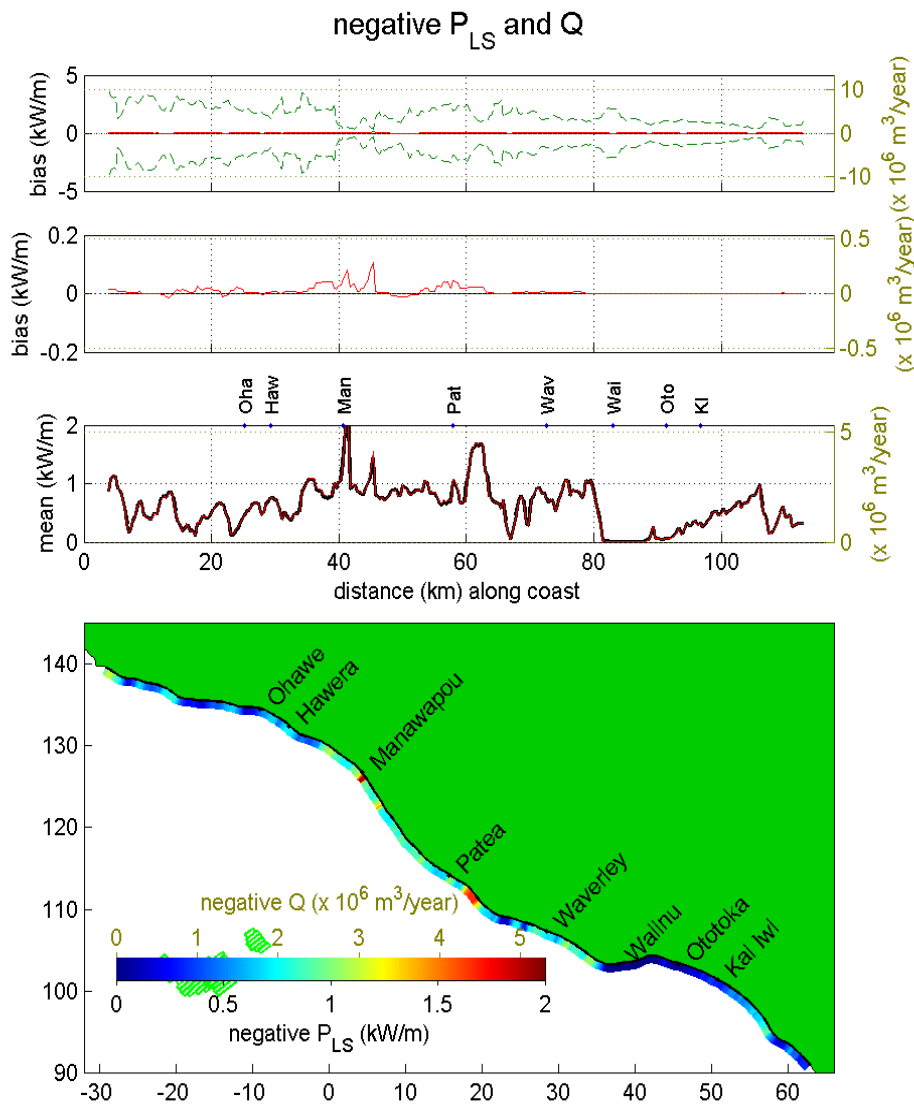


Figure 4-22: Magnitude of the longshore flux factor P_{LS} (black scales) and sediment flux Q (gold scales), averaged over times when they have negative values. The mean value (over a 12 month period) from the baseline simulation is shown by the colour-scaled ribbon in the bottom panel, and as a solid black line in the panel above, compared with the mean value from the case 1 simulation (red), and the standard deviation (SDh) from the baseline simulation (dashed black line). In the two panels above that, the mean difference (bias = case 1 - baseline) between the two simulations is shown, plotted on its own and also plotted along with green dashed lines showing plus and minus half the baseline standard deviation (SDm) of total P_{LS} (or Q).

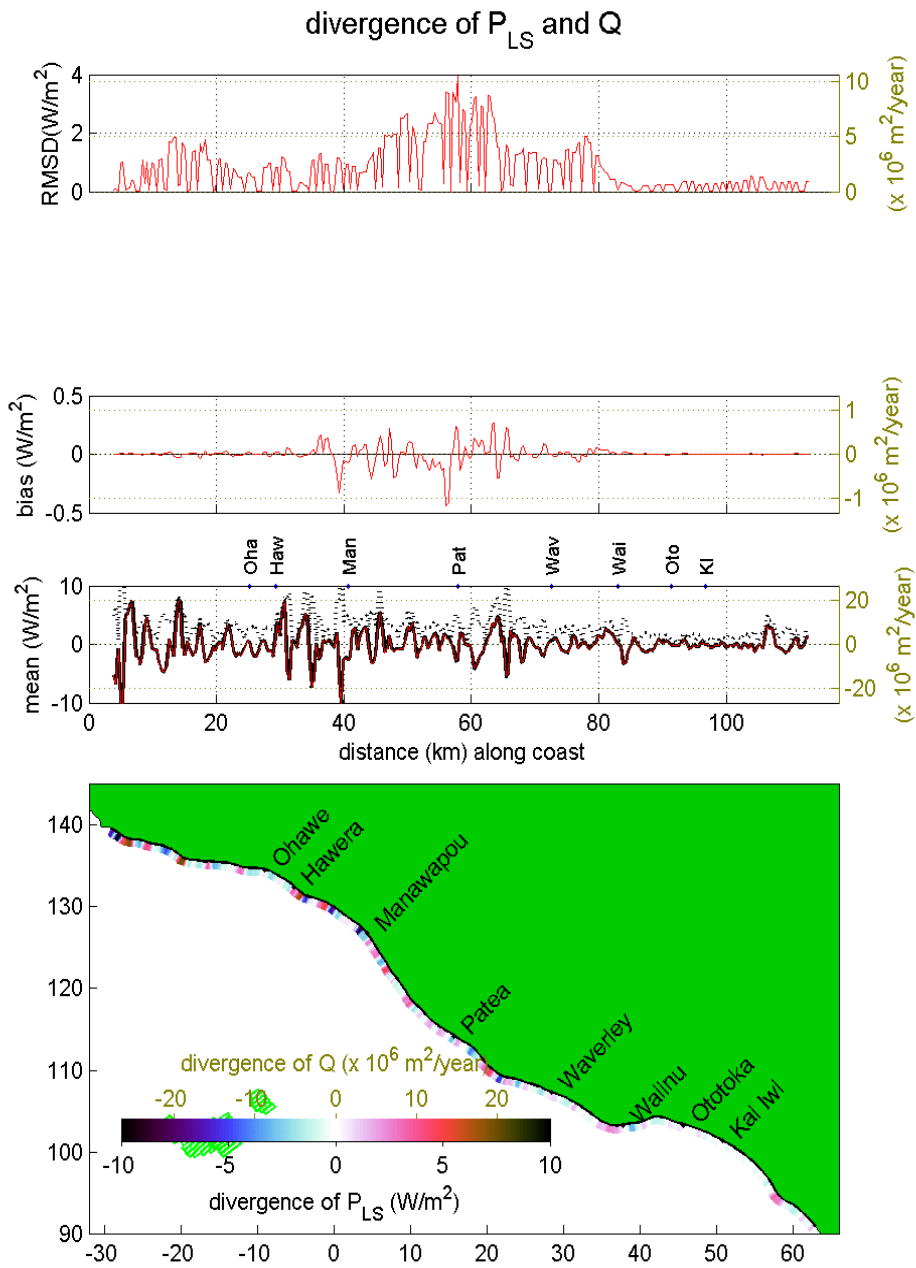


Figure 4-23: Divergence of the longshore flux factor P_{LS} (black scales) and sediment flux Q (gold scales). The mean value (over a 12 month period) from the baseline simulation is shown by the colour-scaled ribbon in the bottom panel, and as a solid black line in the panel above, compared with the mean value from the case 1 simulation (red), and the standard deviation (SDH) from the baseline simulation (dashed black line). In the panels above that, the mean difference (bias = case 1 - baseline) and the root-mean-square difference (RMSD) between the two simulations is shown.

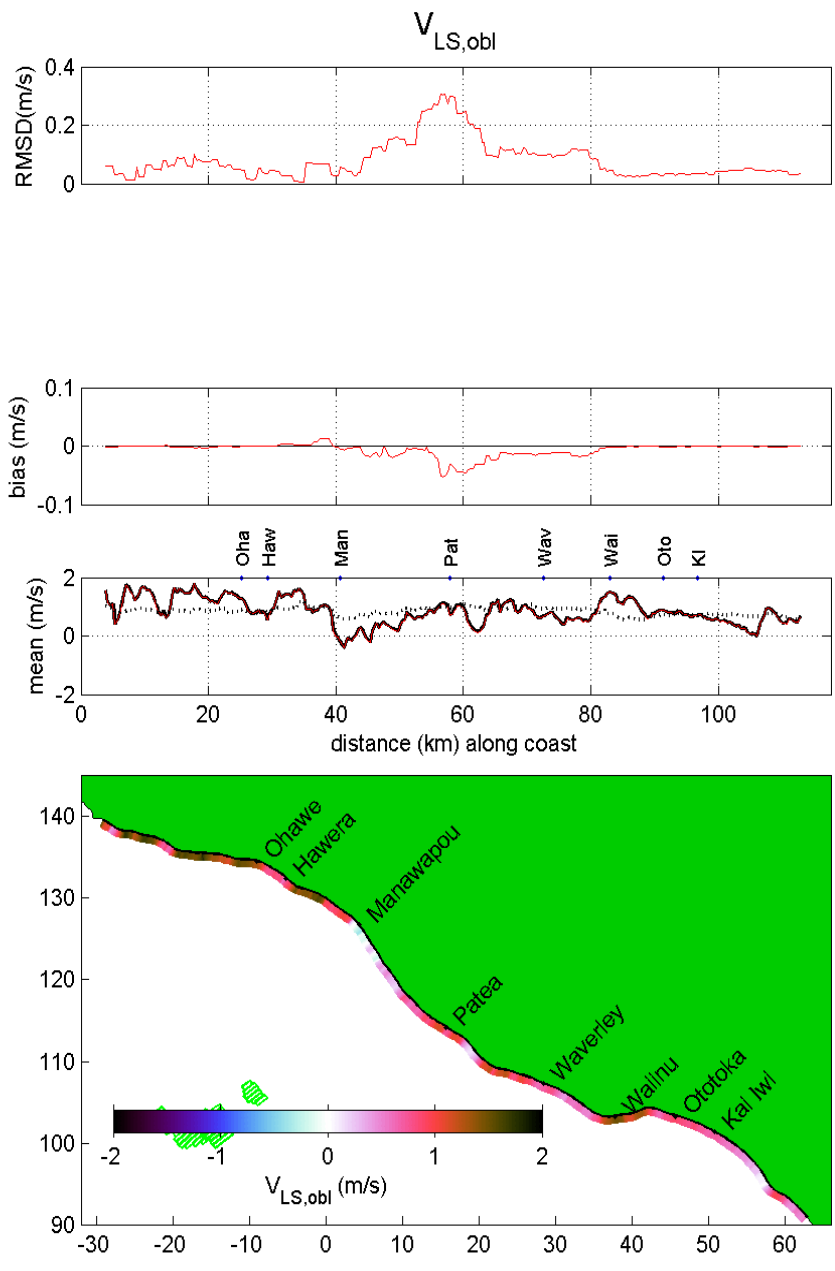


Figure 4-24: Component of longshore mean current associated with oblique wave incidence $V_{LS,obl}$. The mean value (over a 12 month period) from the baseline simulation is shown by the colour-scaled ribbon in the bottom panel, and as a solid black line in the panel above, compared with the mean value from the case 1 simulation (red), and the standard deviation (SDh) from the baseline simulation (dashed black line). In the panels above that, the mean difference (bias = case 1 - baseline) and the root-mean-square difference (RMSD) between the two simulations is shown, in absolute value (m/s).

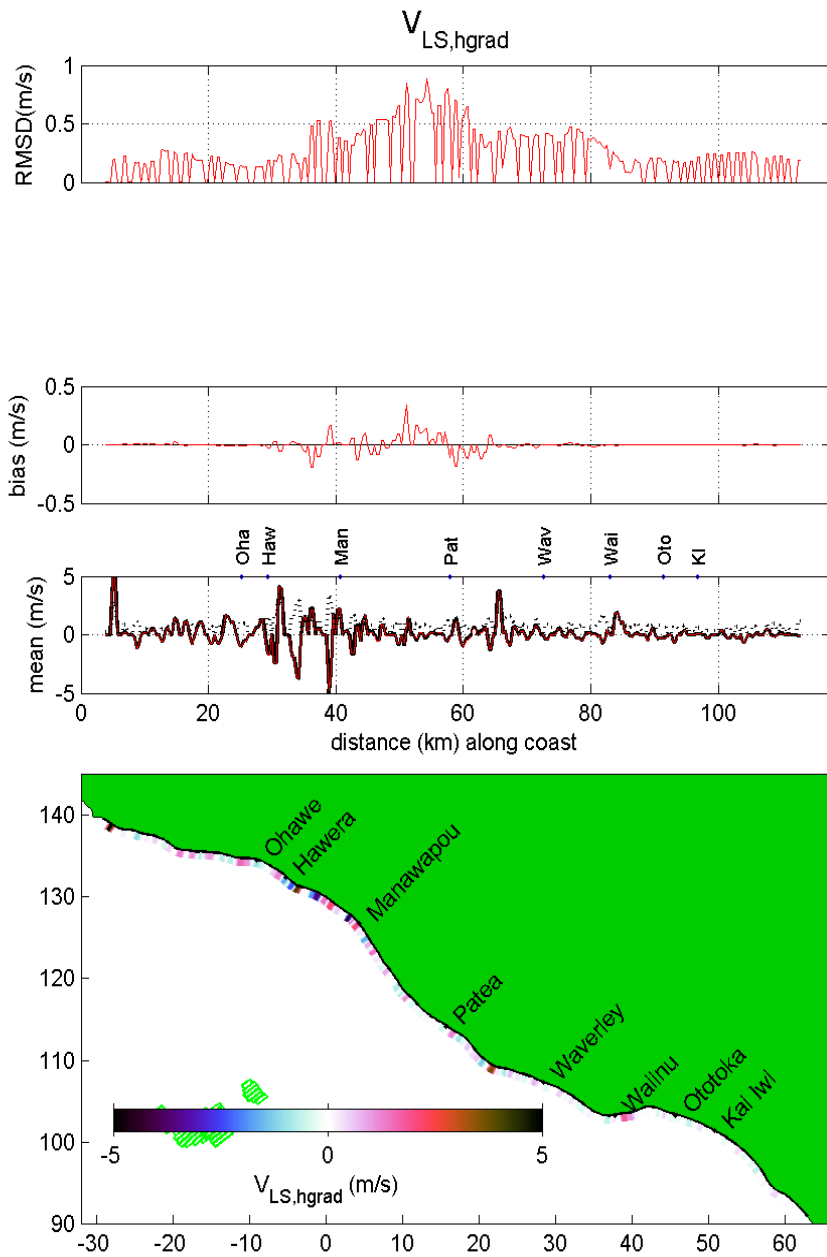


Figure 4-25: Component of longshore mean current associated with wave height gradient $V_{LS,hgrad}$. The mean value (over a 12 month period) from the baseline simulation is shown by the colour-scaled ribbon in the bottom panel, and as a solid black line in the panel above, compared with the mean value from the case 1 simulation (red), and the standard deviation (SDh) from the baseline simulation (dashed black line). In the panels above that, the mean difference (bias = case 1 - baseline) and the root-mean-square difference (RMSD) between the two simulations is shown, in absolute value (m/s).

4.2 Sensitivity to moored vessels – Phase 4

This set of tests used the same environmental scenarios as were used in testing sensitivity to bathymetry modification. Hence the baseline runs had the same physical inputs as the corresponding baseline runs for the bathymetry tests. The outputs were therefore the same as for Figure 4-3 and Figure 4-6, so we do not reproduce them here.

First we look at simulations assuming full reflection. Figure 4-26 shows the modification of the significant wave height field for each of the environmental scenarios, in the case of the FPSO lying in an E-W orientation at Position 1 (a relatively nearshore location within the mining areas). In the first two environmental scenarios, waves are incident from the WNW so, with full reflection and no transmission assumed, there is strong reflection of waves towards the north east. There is a reduction of wave height in the quadrant southeast of the vessel, due to blocking. Other scenarios, with different incident directions, produce quite different patterns of wave blocking and reflection.

Looking at the effects along the 10 m isobath (Figure 4-27) we see that the largest changes in wave height, all less than 1 cm, occur in the part of the coast between Manawapou and Patea. These can be either increases or decreases depending on incident wave direction. Mean wave directions are changed by less than 0.3° .

With the FPSO lying N-S at Position 2 (Figure 4-28), we see reflected waves generally towards the west, and reduced wave heights east of the vessel. At the 10 m isobath (Figure 4-29) we expect decreases of wave height of less than 2 cm in a wide section of the coast and, again, changes in mean wave direction of less than 0.3° .

Averaging over all environmental scenarios (Figure 4-30), we see that there are vessel orientations that produce wave height changes of up to 2 cm on the central part of the coast near Patea, and (other) orientations that produce wave height changes of up to 1.0 cm on the western part of the coast. Relative to the baseline mean values (Figure 4-31), these correspond to changes of less than 1.0% and 0.5%, respectively.

When the simulations were repeated with zero reflection, the regions of increased wave height from reflections are removed (e.g., comparing Figure 4-32 with Figure 4-26), leaving areas of reduced height which predominantly affect the eastern section of coastline, where the largest decrease in wave height for any of the vessel orientations (Figure 4-33) is less than 2.0 cm, while mean direction changes are less than 0.25° . Relative to the baseline values, wave height changes are less than 1.0% (Figure 4-34).

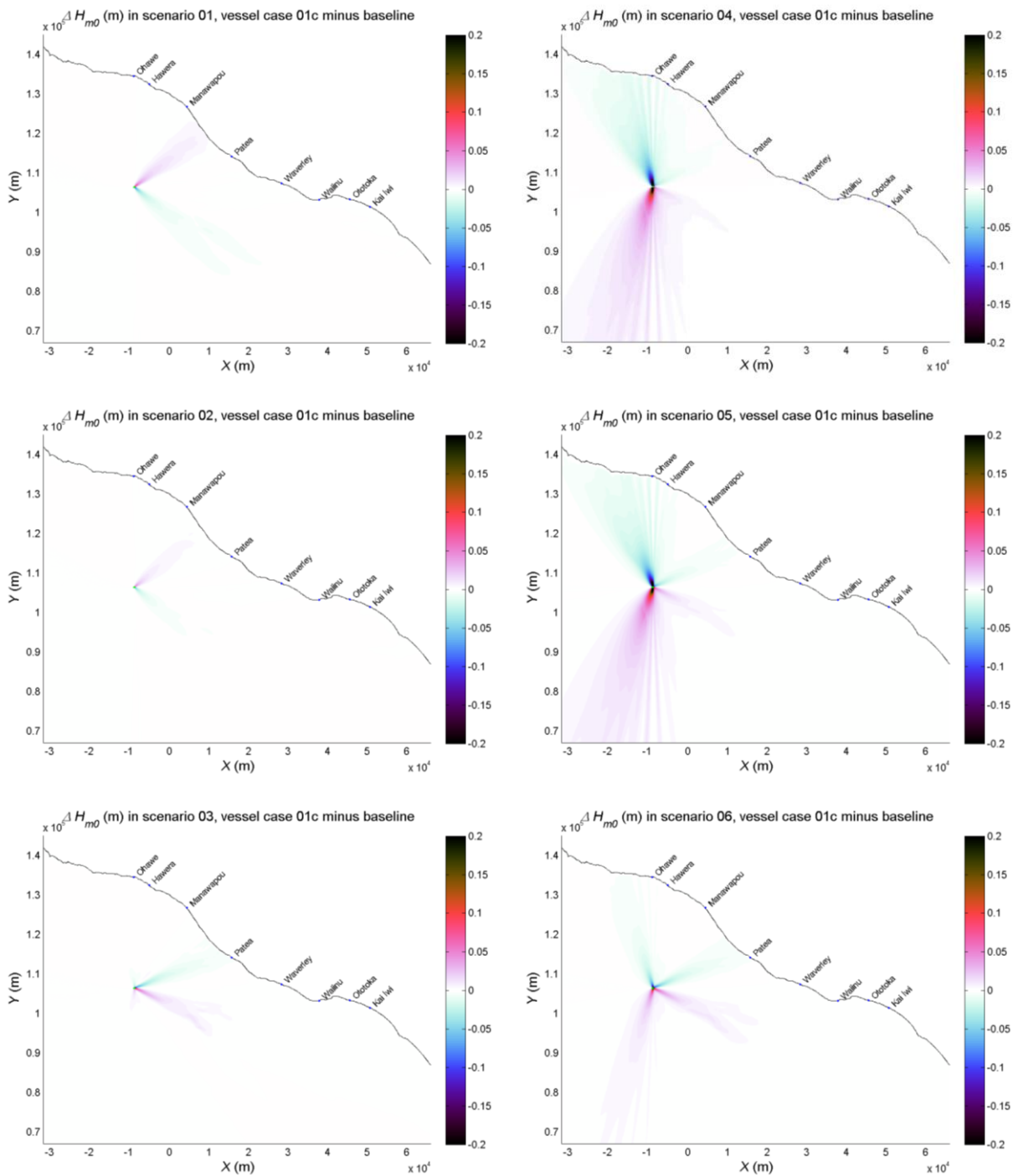


Figure 4-26: Difference between significant wave height over the model domain in simulations with and without a FPSO moored at Position 1 in orientation 1 (E-W), for each of the six environmental scenarios, assuming full reflection. The location of the FPSO used in the simulations is marked in green.

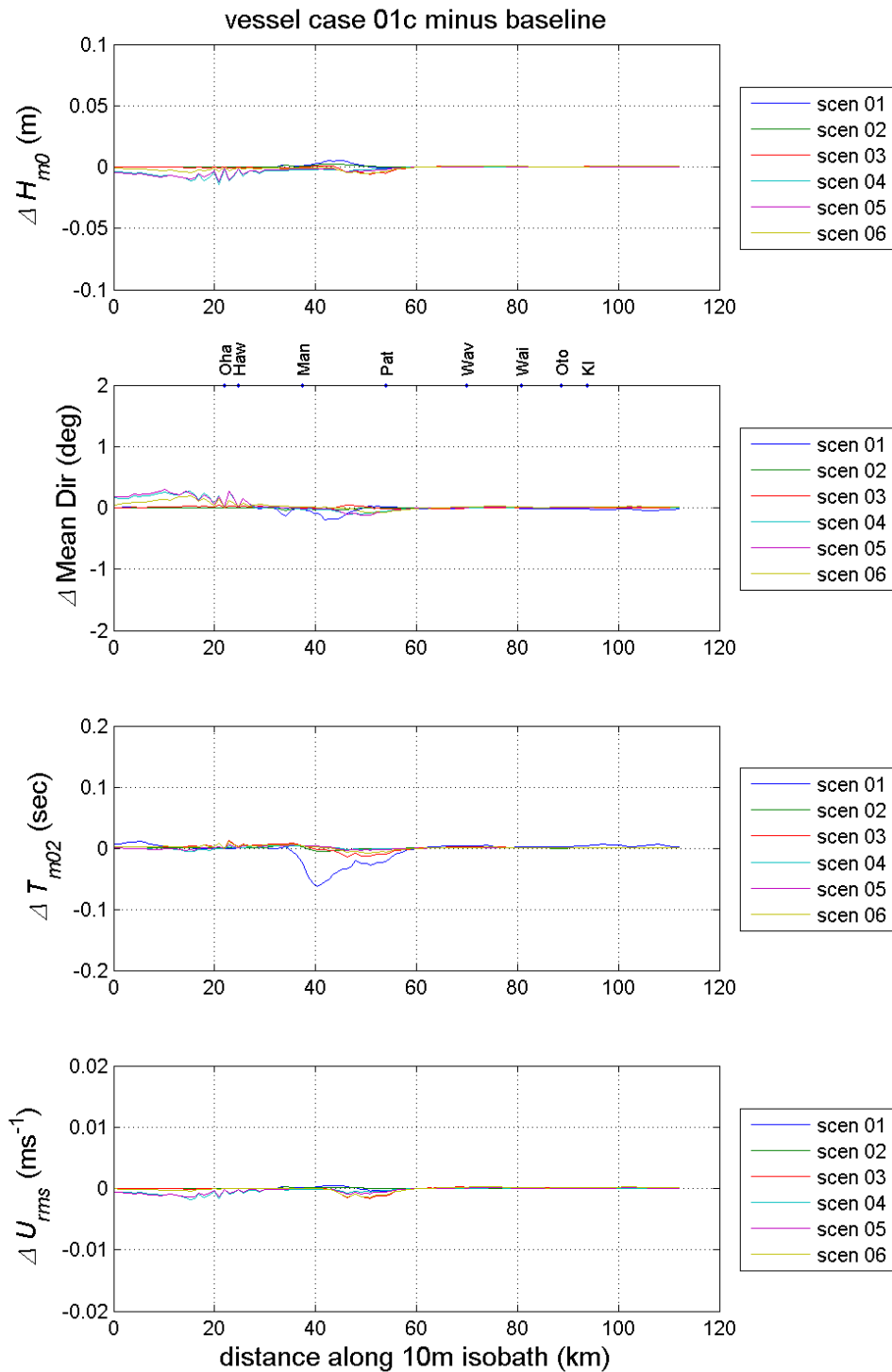


Figure 4-27: Difference between wave parameters at the 10 m isobath in simulations with and without a FPSO moored at position 1 in orientation 1 (E-W), for each of the six environmental scenarios, assuming full reflection. From top to bottom: significant wave height, mean wave direction, mean wave period, and root-mean-square bed orbital velocity.

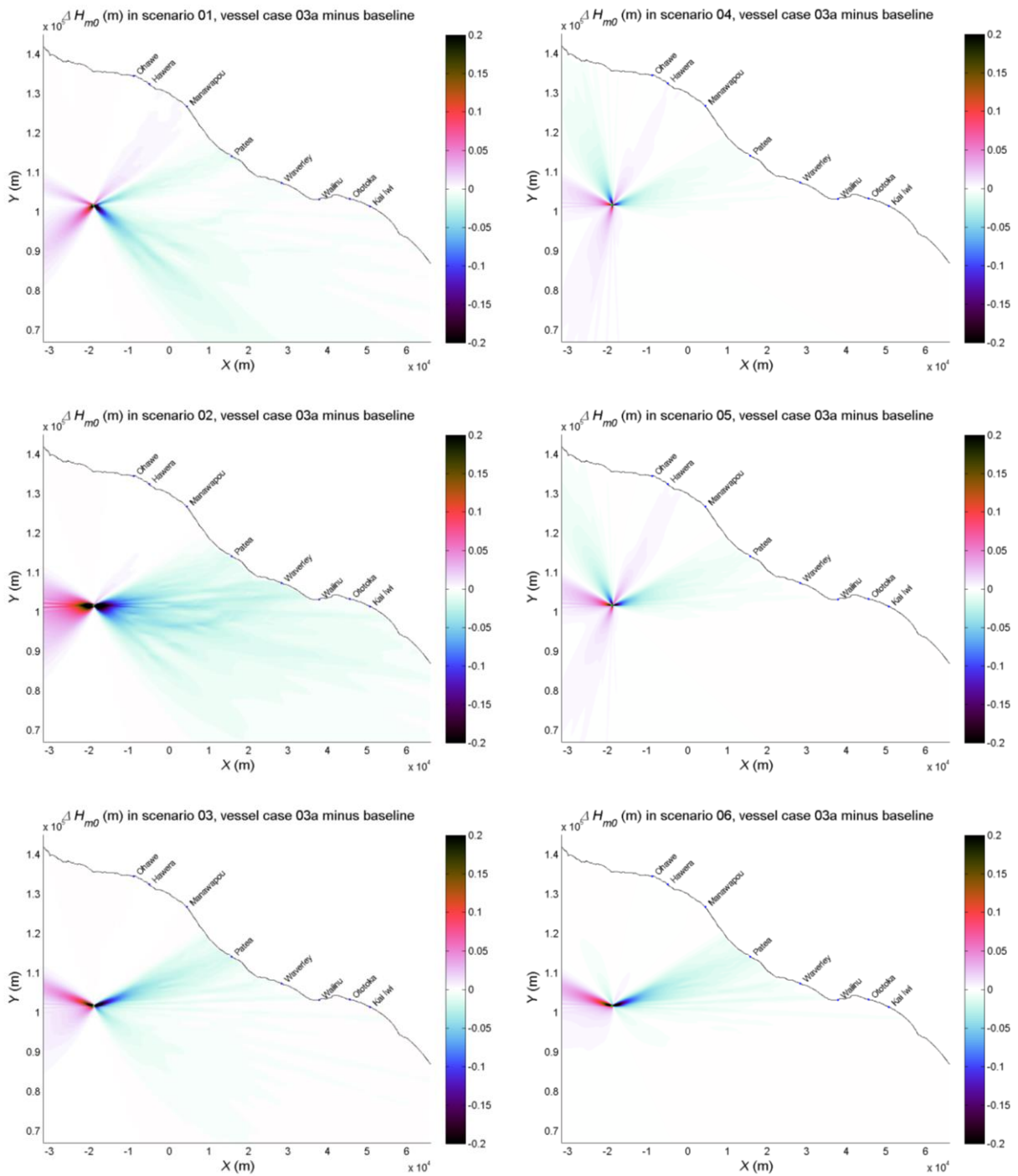


Figure 4-28: Difference between significant wave height over the model domain in simulations with and without a FPSO moored at position 2 in orientation 3 (N-S), for each of the six environmental scenarios, assuming full reflection. The locations of the FPSO used in the simulations is marked in green.

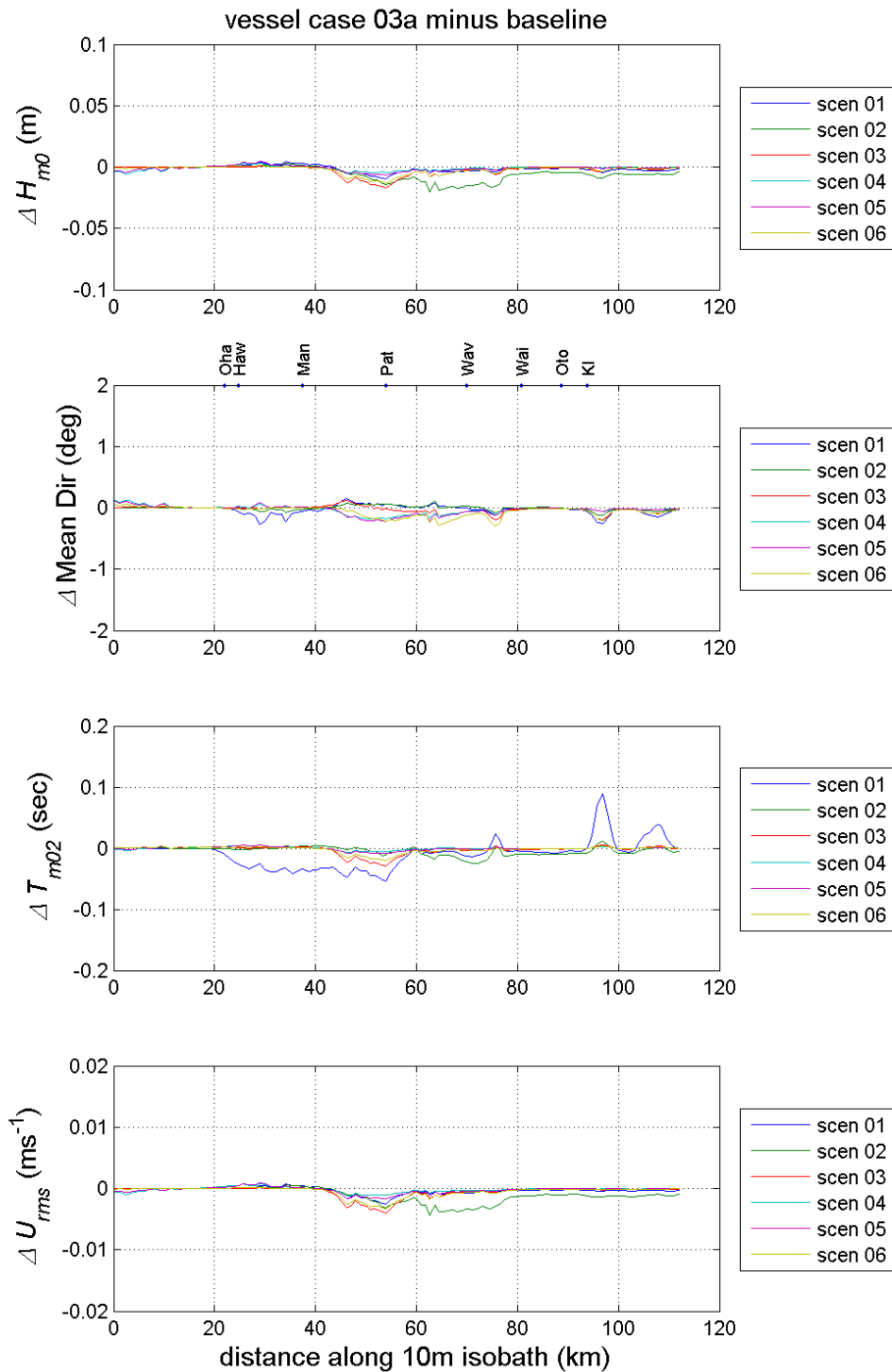


Figure 4-29: Difference between wave parameters at the 10 m isobath in simulations with and without a FPSO moored at Position 2 in orientation 3 (N-S), for each of the six environmental scenarios, assuming full reflection. From top to bottom: significant wave height, mean wave direction, mean wave period, and root-mean-square bed orbital velocity.

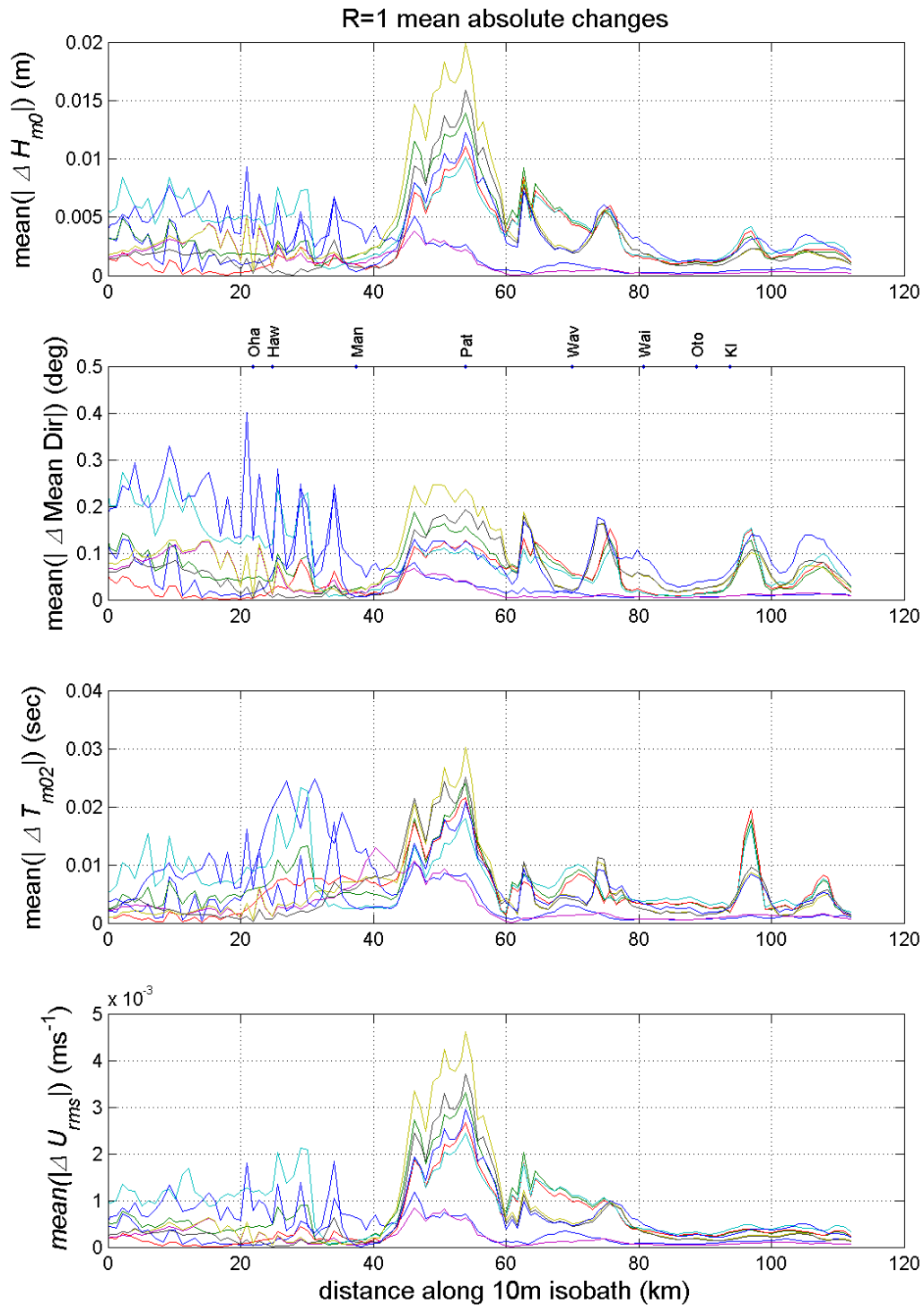


Figure 4-30: Mean values, over the 6 environmental scenarios, of the magnitude of the difference between wave parameters at the 10 m isobath in simulations with and without a moored FPSO assuming full reflection. From top to bottom: significant wave height, mean wave direction, mean wave period, and root-mean-square bed orbital velocity. Results for all vessel positions and orientations are overlaid.

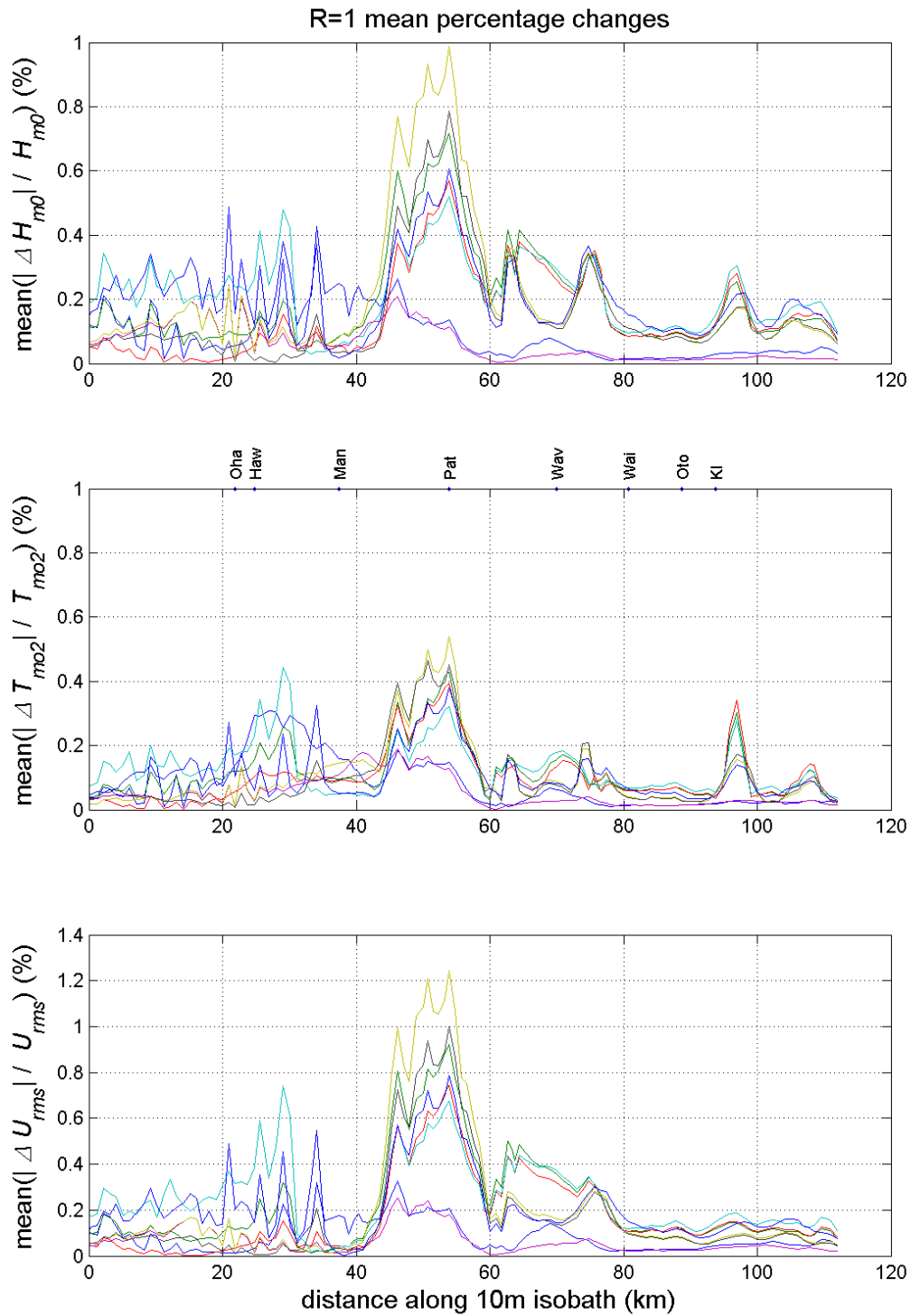


Figure 4-31: Mean values, over the 6 environmental scenarios, of the magnitude of the relative difference between wave parameters at the 10 m isobath in simulations with and without a moored FPSO assuming full reflection. From top to bottom: significant wave height, mean wave direction, mean wave period, and root-mean-square bed orbital velocity. Results for all vessel positions and orientations are overlaid.

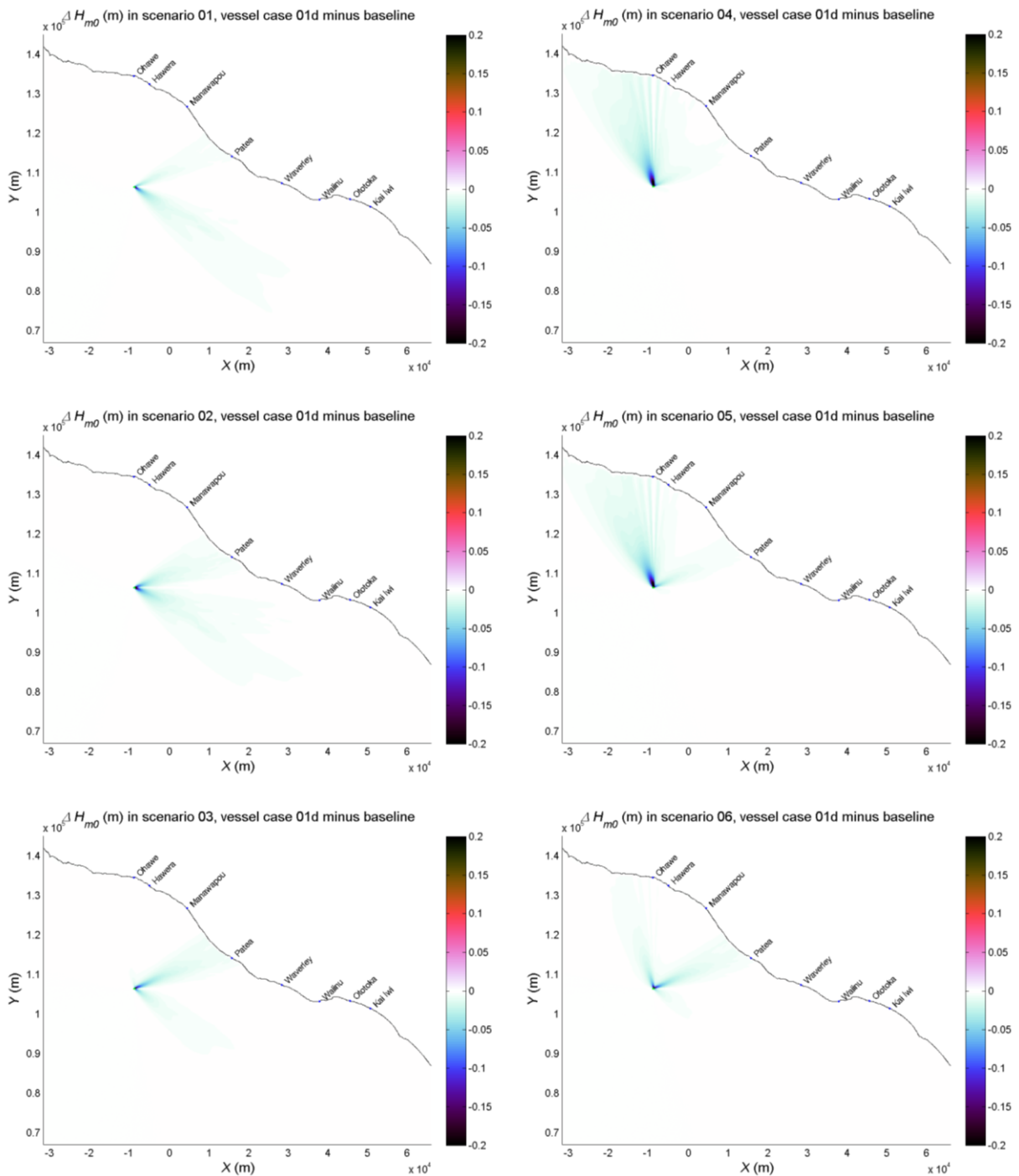


Figure 4-32: Difference between significant wave height over the model domain in simulations with and without a FPSO moored at Position 1 in orientation 1 (E-W), for each of the six environmental scenarios, assuming no reflection. The locations of the FPSO used in the simulations is marked in green.

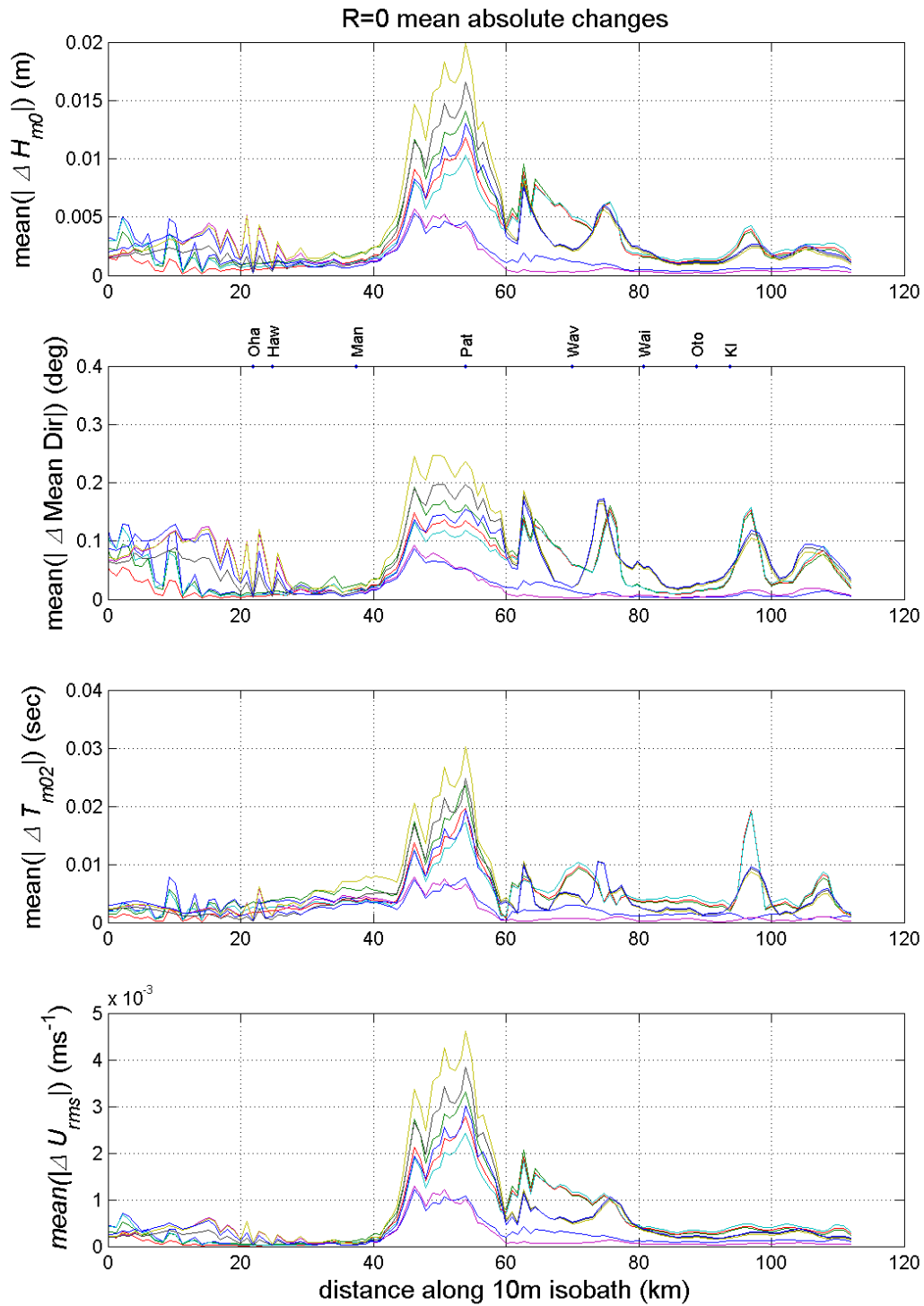


Figure 4-33: Mean values, over the 6 environmental scenarios, of the magnitude of the difference between wave parameters at the 10 m isobath in simulations with and without a moored FPSO assuming no reflection. From top to bottom: significant wave height, mean wave direction, mean wave period, and root-mean-square bed orbital velocity. Results for all vessel positions and orientations are overlaid.

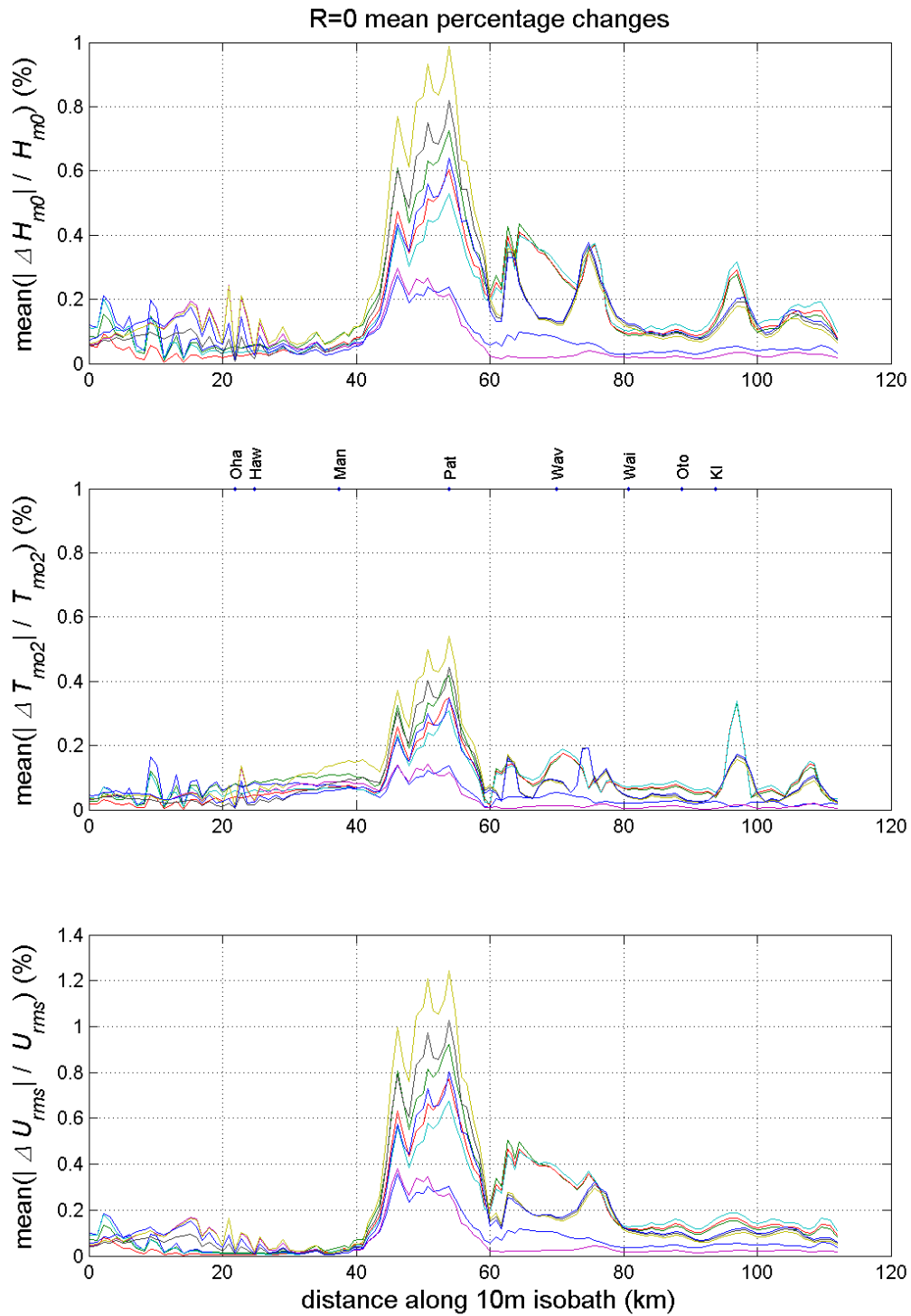


Figure 4-34: Mean values, over the 6 environmental scenarios, of the magnitude of the relative difference between wave parameters at the 10 m isobath in simulations with and without a moored FPSO assuming no reflection. From top to bottom: significant wave height, mean wave direction, mean wave period, and root-mean-square bed orbital velocity. Results for all vessel positions and orientations are overlaid.

5 References

- Booij, N., Ris, R.C., Holthuijsen, L.H. (1999) A third-generation wave model for coastal regions 1. Model description and validation. *Journal of Geophysical Research*, 104(C4): 7649–7666.
- CERC (1984) Shore protection manual. 4th Ed. Coastal Engineering Research Center, US Army Corps of Engineers, Vicksburg, Miss.
- Gorman, R.M. (2012) South Taranaki Bight Iron Sand Mining Nearshore Wave Modelling: Phase 2 and Phase 3 Studies. *NIWA Client Report* HAM2012-141, prepared for Trans Tasman Resources.
- Hadfield, M. (2012) Sediment plume modelling for South Taranaki Bight ironsand mining - Phase 3 Interim Report. *NIWA Client Report* No. WLG2012-51.
- Hadfield, M. (2013) Sediment plume modelling for South Taranaki Bight ironsand mining - Phase 3 Final Report (in preparation).
- Hicks, D.M. (1993) Modelling long-term change of the Pegasus Bay shoreline. *NIWA Christchurch Miscellaneous Report* No. 99.
- Isobe, M., Kondo, K., Horikawa, K. (1984) Extension of MLM for estimating directional wave spectrum. *Paper No. A-6, Proc. Symp. on Description and Modeling of Directional Seas*.
- Johnson, D. (2001) DIWASP, a directional wave spectra toolbox for MATLAB: User Manual. *Centre for Water Research, University of Western Australia, Research Report* WP-1601-DJ (V1.1).
- MacDiarmid, A., Anderson, O., Beaumont, J., Gorman, R., Hancock, N., Julian, K., Schwarz, J., Stevens, S., Sturman, J., Thompson, D., Torres, L. (2010) South Taranaki Bight iron sand mining baseline environmental study. *NIWA Client Report Number* WLG2010-46: 391.
- MacDonald, I., Budd, R., Bremner, D., Edhouse, S. (2013) South Taranaki Bight Iron Sand Mining: Oceanographic measurements data report. *NIWA Client Report* HAM2012-147, prepared for Trans Tasman Resources.
- Pallentin, A., Gorman, R.M. (2012) TTR bathymetry data, South Taranaki Bight WASSP ascii data processing. *NIWA Client Report* No. WLG2012-14.
- Ris, R.C., Holthuijsen, L.H., Booij, N. (1999) A third-generation wave model for coastal regions 2. Verification. *Journal of Geophysical Research*, 104(C4): 7667–7681.
- SWAN Group (2011) *SWAN user manual - SWAN Cycle III Version 40.85*. Delft University of Technology.
- Technip Mines (2012a) Executive Summary, Prefeasibility Study of Tangaroa Project. *Report Reference* 0061 005 Rev C: 55.

Technip Mines (2012b) Prefeasibility Study of Tangaroa Project. *Report Reference* 0061 004 Rev C: 304.

Tolman, H.L. (2002) Alleviating the Garden Sprinkler Effect in wind wave models. *Ocean Modelling*, 4(3-4): 269–289.

Appendix A Spectral wave statistics

The wave statistics output from a spectral model such as SWAN for comparison with measurements are derived from the directional wave spectrum $S(f, \theta)$, which represents the amount of energy associated with waves of frequency f travelling in direction θ .

Firstly, the full directional spectrum can be integrated over direction to obtain a 1-dimensional frequency spectrum

$$S(f) = \int_0^{2\pi} d\theta F(f, \theta) \quad (1)$$

While the full directional spectrum is difficult to obtain directly from measurements, the frequency spectrum can be simply derived as the power spectrum of a suitable record of sea surface elevation. From this, the peak frequency f_p , at which the maximum value $S(f_p)$ is located, and the corresponding peak period $T_p = 1/f_p$ are identified. Also, spectral moments

$$M_n = \int_0^{\infty} df f^n S(f) \quad (2)$$

are computed, allowing further statistics to be defined, in particular the significant wave height which is proportional to the variance in the sea level record:

$$H_{m0} = 4\sqrt{M_0} \quad (3)$$

and is approximately equivalent to an alternative definition as the mean value of the 1/3 highest waves observed. Other useful statistics include the (second moment) mean period

$$T_{m02} = \sqrt{M_0 / M_2} \quad (4)$$

and the spectral width

$$SW = 1 - \frac{M_2^2}{M_0 M_4} \quad (5)$$

We can also derived directional moments from the directional spectrum:

$$C_0 = \int_0^{\infty} df \int_0^{2\pi} d\theta F(f, \theta) \cos \theta, \quad (6)$$

$$S_0 = \int_0^{\infty} df \int_0^{2\pi} d\theta F(f, \theta) \sin \theta, \quad (7)$$

from which we can obtain the mean direction

$$\theta_{mean} = \arctan\left(\frac{S_0}{C_0}\right) \quad (8)$$

and the directional spread

$$\theta_{spread} = \sqrt{2 - \frac{2}{M_0} \sqrt{S_0^2 + C_0^2}}. \quad (9)$$

While the model predicts a wave spectrum at the sea surface, often measurements are made some distance under water, for example by measure a pressure signal associated with vertical excursions of water particles at the level of the instrument in the water column. These motions are attenuated relative to the equivalent motions on the surface (which the model predicts). A variance spectrum $S_{inst}(f)$ of vertical excursions recorded at a distance z above the sea bed in water of depth h is related to the equivalent spectrum at the surface by

$$S_{inst}(f) = S(f) \left[\frac{\cosh(k(f)h)}{\cosh(k(f)z)} \right]^2 \quad (10)$$

where $k(f)$ is the wavenumber associated with waves of frequency f , and can be found from the linear dispersion relation

$$(2\pi f)^2 = gk \tanh(kh) \quad (11)$$

In which $g = 9.81 \text{ ms}^{-2}$ is the acceleration due to gravity.

Given a suitable instrument record, it is possible to use the above attenuation factor to estimate the surface spectrum, but the attenuation factor becomes very large at higher frequencies, so that any high frequency noise in the record will be heavily amplified by this procedure. This can partly be avoided by restricting calculations to frequencies below a carefully chosen cut off frequency.

Alternatively, one can work in the other direction and convert the model-derived surface spectrum to an equivalent spectrum at instrument level, for direct comparisons with the measurements. Frequency cut offs may still need to be applied to the converted model spectra, but only to match a limited frequency range measurable by the particular instrument.

Appendix B Nearshore wave and sediment transport statistics

For a single-component sinusoidal wave of height H travelling with group velocity C_g , the energy flux (i.e., the energy crossing unit length of wave front per unit time) is a vector quantity directed normal to the wave crest, with magnitude

$$F = \frac{1}{8} \rho g C_g H^2 \quad (1)$$

where $\rho \approx 1025 \text{ kg.m}^{-3}$ is the density of seawater and $g = 9.81 \text{ m.s}^{-2}$ is the gravitational acceleration. For shallow water of depth h , the group velocity has magnitude

$$C_g \approx \sqrt{gh} \quad (2)$$

and the wave height on breaking is proportional to the depth, i.e.,

$$H_b \approx \gamma h_b, \quad (3)$$

with a constant of proportionality $\gamma \approx 0.5$. Hence the (conserved) magnitude of the energy transport at both the 10 m isobath and at the breakpoint is

$$F_b = F \approx \frac{\rho g^{1.5}}{8\gamma^{0.5}} H_b^{2.5}. \quad (4)$$

The SWAN modelling procedure provides an estimate of wave parameters on the 10 m isobath, but does not have sufficient resolution to directly compute wave transformation to the breaker zone. However, an estimate of wave height and direction at the breakpoint can be made by assuming that the seabed has simple topography shoreward of the 10 m isobath, with shore-parallel depth contours. Then conservation of energy flux F can be used to find H_b and h_b through Equations (3) and (4), while conservation of the longshore component of wave number gives

$$\frac{\sin \alpha_b}{\sin \alpha} = \frac{k}{k_b} \approx \sqrt{\frac{h_b}{h}} \quad (5)$$

where α and α_b are the angles between the wave propagation direction and the shore-normal direction at the 10 m isobath and at the breakpoint, respectively, and $h = 10 \text{ m}$ and h_b are the corresponding depths. Equivalently, the wave crests are at an angle α_b to the beach.

The energy transport at the breakpoint has longshore and onshore components $F \sin \alpha_b$ and $F \cos \alpha_b$ respectively. The flux of *longshore directed* wave energy across a *shore-parallel* line is then given by the longshore flux factor

$$P_{ls} = F \cos \alpha_b \sin \alpha_b = \frac{1}{2} F \sin 2\alpha_b \approx \frac{\rho g^{1.5}}{16\gamma^{0.5}} H_b^{2.5} \sin 2\alpha_b \quad (6)$$

while the flux of *onshore-directed* wave energy across a *shore-parallel* line is

$$P_{os} = F \cos^2 \alpha_b \approx \frac{\rho g^{1.5}}{8\gamma^{0.5}} H_b^{2.5} \cos^2 \alpha_b. \quad (7)$$

The longshore sediment flux can be approximated by an empirical relationship

$$Q = fKP_{ls} \quad (8)$$

where $f = 3308 \text{ m}^2.\text{s}^3.\text{kg}^{-1} = 1.05 \times 10^{-4} \text{ m}^2.\text{s}^2.\text{kg}^{-1}$ is a unit-conversion constant, while K is a dimensionless efficiency factor dependent on sediment properties. A value of $K = 0.8$ has been found to be appropriate for sandy beaches on the New Zealand east coast (Hicks 1993), although much lower values may be required where coarser material is present. For the present study we have adopted a single value of $K = 0.8$, and not attempted to incorporate information on the varying beach sediment properties along the coast by specifying spatially-variable K values. Rather, we focus on potential relative changes in the wave-driven forcing of beach processes.

For the present study in the South Taranaki Bight, transport along the coast from the north-west towards the south-east was deemed to be positive.

The longshore flux factor (Eqn. 6) for each shore station can be computed as a time series, and then averaged, e.g.,

$$P_{net} = \frac{1}{N} \sum_{n=1}^N P_{ls}(t_n) \quad (9)$$

Also of interest are the averages of solely positive (north-westward) and negative (south-eastward) components, i.e.

$$P_+ = \frac{1}{N} \sum_{Q>0} P_{ls}(t_n) \quad (10)$$

and

$$P_- = \left| \frac{1}{N} \sum_{Q<0} P_{ls}(t_n) \right| \quad (11)$$

From these we can derive a net/gross drift ratio

$$N/G = \frac{Q_{net}}{Q_+ + Q_-} \quad (12)$$

The drift/swash ratio is defined as the ratio of the mean magnitude of the longshore flux factor to the mean onshore energy transport:

$$D/S = \frac{\sum_{n=1}^N |P_{ls}(t_n)|}{\sum_{n=1}^N P_{os}(t_n)} \quad (13)$$

Also of interest is the divergence (in the longshore direction) $\partial P_{ls} / \partial y$ of the longshore flux factor. These represent an imbalance between transport into one end of a section of coast and transport out of the other end. Positive and negative values of these divergences respectively indicate zones of erosion or deposition.

Appendix C Wave model verification - Phase 4 full results

Time series of available wave statistics through the simulation from the model and from measurements for each instrument are compared in the plots below. Error metrics were obtained for significant wave height and second-moment mean period (available for all instruments), and these are presented in Table C-1 and Table C-2, respectively. These were obtained by interpolating model statistics to the times for which the corresponding measured values were available and taking the means of the model and measured values, the bias (modelled mean minus measured mean), the root-mean-square error (RMSE), and the Scatter Index (RMSE divided by the measured mean).

At the Baring Head buoy site, off the coast south-east of Wellington, the Greater Cook Strait model reproduced measured significant wave height satisfactorily for most of the record (Figure C-1), apart from under-predicting the highest event. The second-moment mean period was less well reproduced. We note that no measured spectra were available to ensure that consistent frequency ranges were used in deriving this statistic. Peak period does not have the same sensitivity to the high frequency tail, and for much of the record this was well reproduced, but in mixed sea state this quantity can be sensitive to fluctuations between the periods associated with different components of similar energy.

We next look at the more offshore of the instruments deployed in the South Taranaki Bight, i.e., the Waverider at Site 8 (Figure C-2) and the ADCPs at Sites 7 (Figure C-3) and 6 (Figure C-4). In each case the significant wave height is over predicted to some degree. The Site 8 Waverider shows the largest positive bias (Figure C-2(c)), at 0.252 m, or 15% of the recorded mean. An exception is during southerly conditions, e.g. for days 277-279, when the model heights are below the data. Mean period is generally under predicted while peak period shows no significant bias and spectral width is generally well reproduced.

The predicted mean wave direction at these three sites generally follows the measurements satisfactorily, except for missing some of the short-term shifts. Directional spread is, however, significantly under-predicted.

We note that in test simulations in which nonlinear interactions were included in the 100 m resolution model, higher values of directional spread were obtained, but the mean direction showed excessive diurnal oscillations, as well as producing excessive energy at high frequencies. These excessive oscillations in mean wave direction were not observed to the same degree in the Phase 3 verification simulations (Gorman 2012), which used parametric boundary conditions on the Greater Cook Strait grid and a coarser directional resolution, nor in the present set of simulations at 1 km resolution. In all simulations in which four-wave nonlinear interactions were computed, this was done using the Discrete Interaction Approximation, which can be problematic at higher directional resolutions, and can also tend to increase directional spread, excessively in some cases. It was concluded that this algorithm introduced erroneous nonlinear transfers between distinct components of mixed sea states, in the presence of tidal currents, and that the benefits of removing the nonlinear interaction terms from the nearshore model, in terms of better agreement for wave height and mean direction outweighed the poorer representation of directional spread.

Closer to shore at Site 5 (Figure C-5), there is a satisfactory agreement with significant wave height, with negligible bias. Further shoreward again, at the Dobie sites (Figure C-6 to Figure

C-9), there is also generally reasonable agreement with measured significant wave height during lower-energy conditions, but some of the higher events are either under predicted or, occasionally at Site 3, over predicted. Second-moment mean period also tends to have a low bias.

We should bear in mind the different frequency cutoffs used for Dobie (0.25 Hz) and other sites (0.6 Hz) when comparing error statistics, particularly for mean period, across sites, and focus on comparing Scatter Index, a relative measure, rather than absolute RMSE or Bias statistics.

A more detailed comparison may be made by comparing measured and modelled spectra. In Figure C-10 through Figure C-17 we show variation of the 1-dimensional frequency spectrum, as a function of time and wave frequency, in the form of colour-scaled plots of both measured and modelled spectra. Note that we have not modified the spectral discretisation of the measured or modelled spectra, or the time increments, simply plotting the two “as is”.

These plots are useful in identifying any clear discrepancies in particular parts of the spectrum, and we do note a tendency for some low frequency features to be more prominent in the modelled spectra than in the measured records.

To obtain a more quantitative comparison, we integrate the variance M_0 (Eqn 2) over selected frequency ranges, in this case corresponding to periods between 4, 7, 9, 11 and 25 seconds. This enables us to compare time series of measured and modelled variance in those selected ranges (Figure C-18 through Figure C-25).

At Site 8, we observe that most of the excess energy is contained in the 4-7 second range, while the other ranges show better agreement. The excess short period energy becomes less evident further inshore.

Finally, Figure C-26 to C-29 show measured and simulated energy ratios, integrating surface spectra over the same frequency bands as above, between each of the Dobie sites and the Site 8 Waverider (the most offshore measurement site). This will tend to normalise out errors due to inaccurate scaling of incident wave energy, and provide a useful indicator of how well the model transforms wave energy shoreward to the coast.

Each of these ratios vary in time through over an order of magnitude, and the low frequency variation is in general captured reasonably. The principle point of difference between measured and modelled values is seen in the 11-25 second band, where the model is unable to reproduce measured energy ratios significantly exceeding unity at Sites 1 and 3. The fact that this amplification does not occur at all the Dobie sites, or at all times (for example, it does not occur during the southerly conditions on days 277-279), suggests that wave amplification by bathymetric features not accurately represented in the model may be a cause. Site 1 is outside the area where updated bathymetry data have been collected for this project (Pallentin, 2012), and Site 3 near the boundary of this region.

Table C-1: Error statistics for the comparison of modelled and measured significant wave height at the instrument locations. Results are from the Xantia 100 m simulation, except at Baring Head, where the Greater Cook Strait 1 km model is used.

ID	Instrument	Model mean (m)	Data mean (m)	Bias (m)	RMSE (m)	Scatter Index
Site 1	Dobie	1.416	1.397	0.019	0.261	0.187
Site 2	Dobie	1.670	1.532	0.138	0.339	0.221
Site 3	Dobie	1.544	1.372	0.172	0.379	0.276
Site 4	Dobie	1.220	1.138	0.082	0.323	0.284
Site 5	ADCP	1.393	1.423	-0.030	0.401	0.282
Site 6	ADCP	1.835	1.757	0.078	0.401	0.228
Site 7	ADCP	1.978	1.850	0.128	0.458	0.248
Site 8	Waverider	1.889	1.637	0.252	0.460	0.281
Baring Head	Waverider	1.434	1.372	0.062	0.367	0.268

Table C-2: Error statistics for the comparison of modelled and measured second moment mean period at the instrument locations. Results are from the Xantia 100 m simulation, except at Baring Head, where the Greater Cook Strait 1 km model is used.

ID	Instrument	model mean (s)	data mean (s)	bias (s)	RMSE (s)	Scatter Index
Site 1	Dobie	7.610	8.568	-0.958	1.625	0.190
Site 2	Dobie	7.155	7.745	-0.590	1.112	0.144
Site 3	Dobie	7.640	8.130	-0.490	1.503	0.185
Site 4	Dobie	6.878	7.443	-0.565	1.341	0.180
Site 5	ADCP	4.586	4.477	0.109	1.086	0.243
Site 6	ADCP	4.971	5.228	-0.256	1.079	0.206
Site 7	ADCP	5.017	4.987	0.029	1.107	0.222
Site 8	Waverider	4.770	5.428	-0.658	1.189	0.219
Baring Head	Waverider	4.066	6.232	-2.166	2.553	0.410

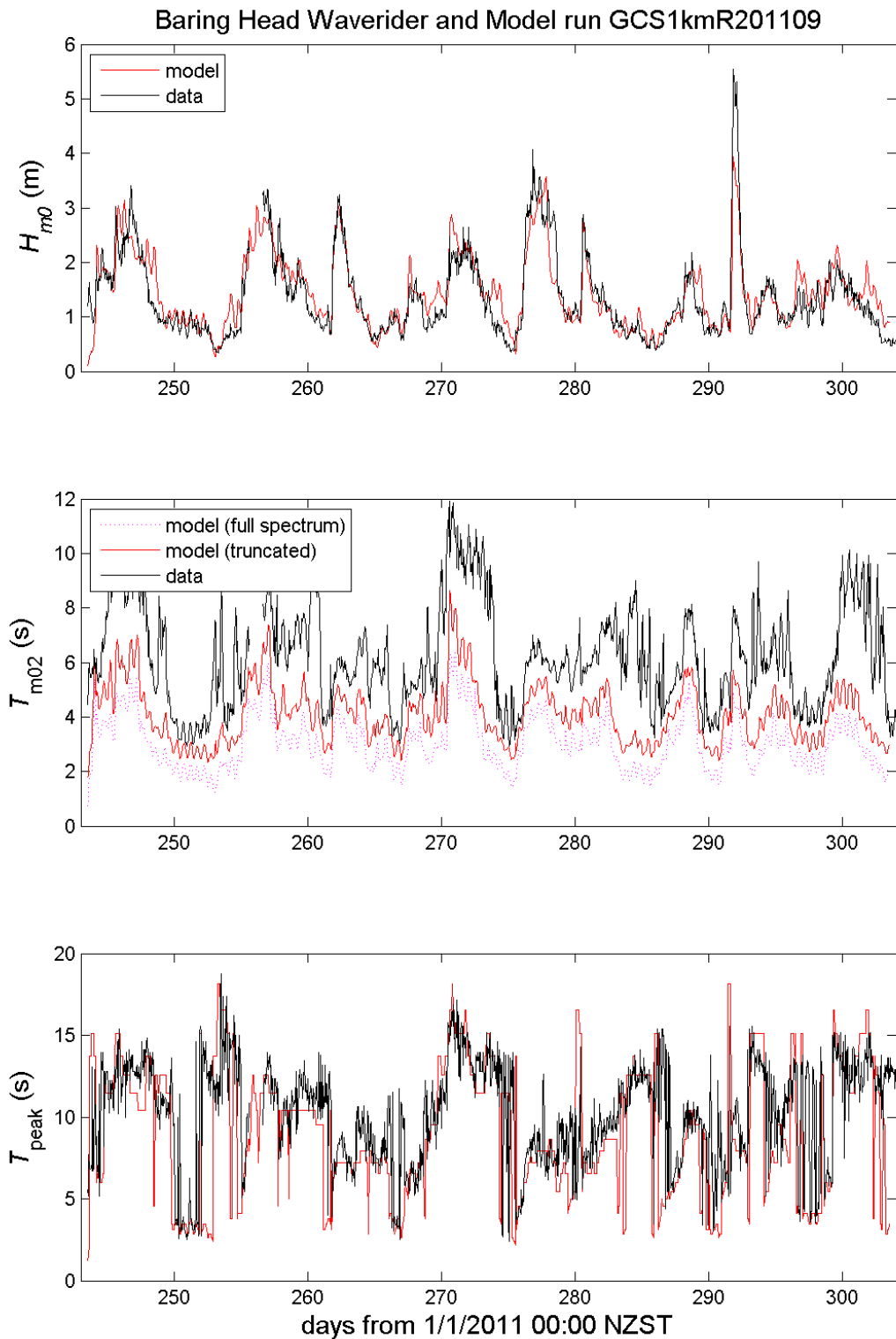


Figure C-1: Comparison of wave statistics measured at the Baring Head Waverider buoy, with outputs from the Greater Cook Strait wave model. From the top panel: significant wave height, second-moment mean wave period, and peak wave period. For mean period, the dashed magenta line shows statistics derived from model spectra over the full frequency range, while the solid lines show statistics derived from frequencies below a 0.6 Hz cutoff, from model (red) and measurements (black).

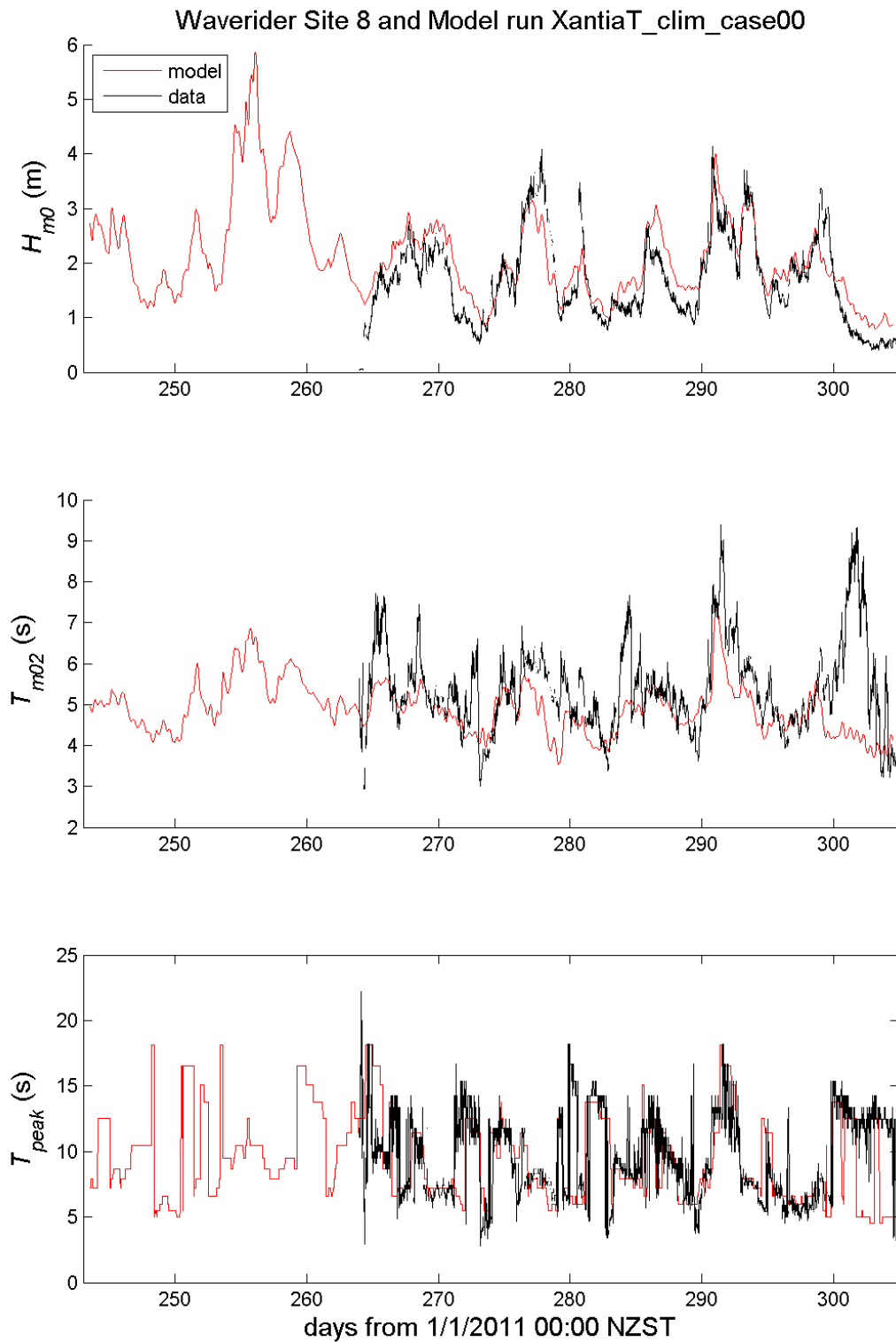


Figure C-2 (a): Comparison of wave statistics measured at the Site 8 Waverider buoy, with outputs from the Xantia 100m wave model. From the top panel: significant wave height, second-moment mean wave period, and peak wave period. The lines show statistics derived from frequencies below a 0.6 Hz cutoff, from the model (red) and measurements (black).

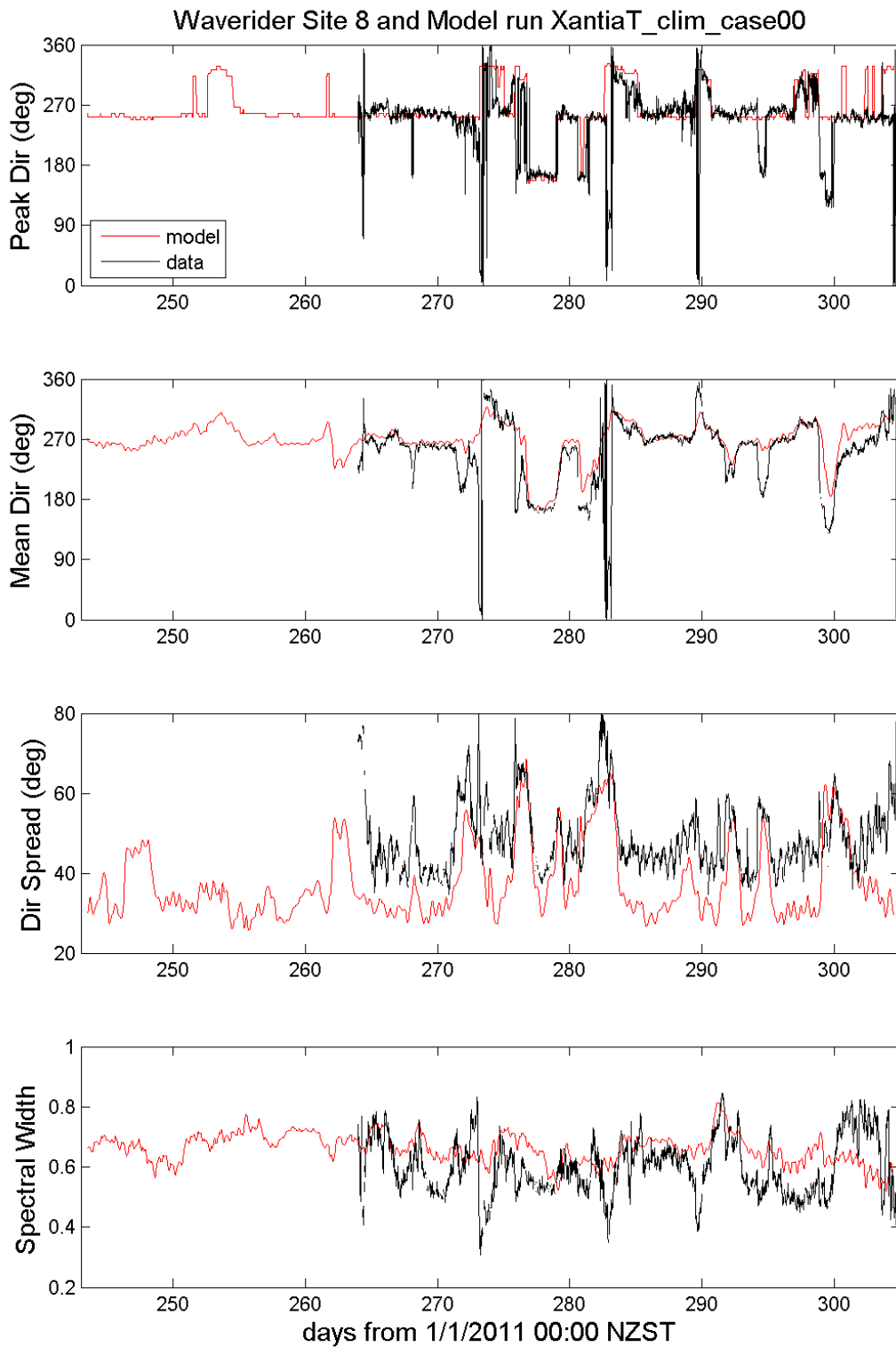


Figure C-2 (b): Comparison of wave statistics measured at the Site 8 Waverider buoy, with outputs from the Xantia 100m wave model. From the top panel: peak wave direction, mean wave direction, directional spread and spectral width.

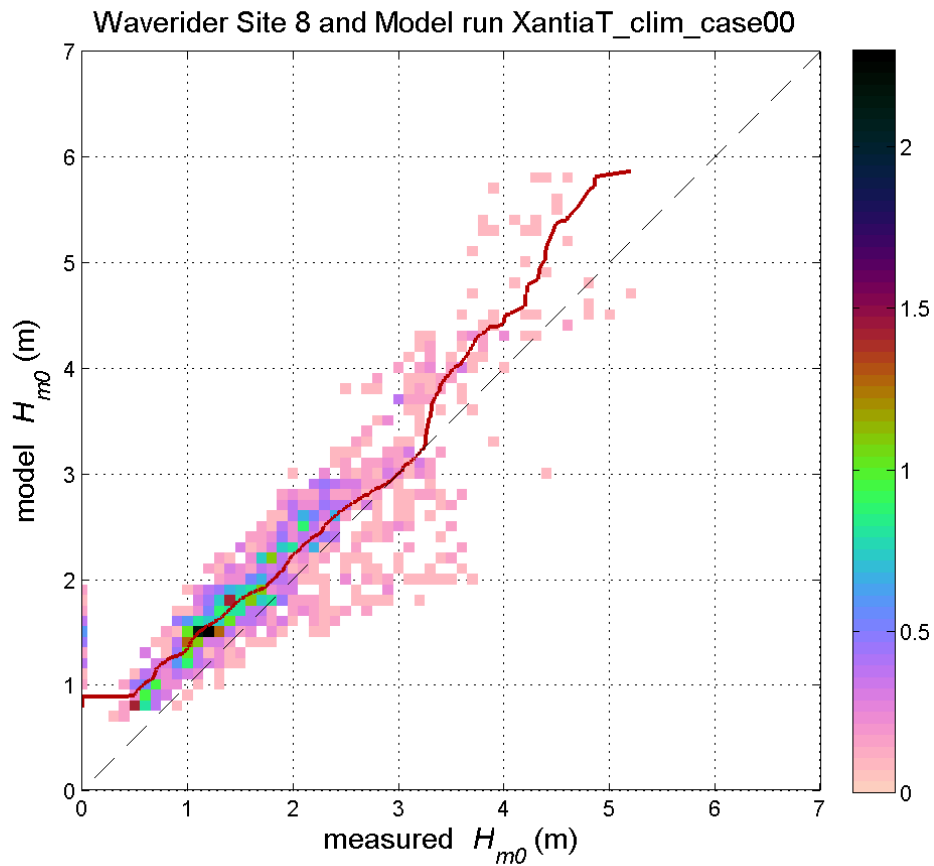


Figure C-2 (c): Comparison of significant wave height measured at the Site 8 Waverider buoy, with outputs from the Xantia 100m wave model. The colour scale shows probability of joint occurrence of measured and modelled values of significant wave height at surface level, while the solid red line gives a quantile-quantile plot.

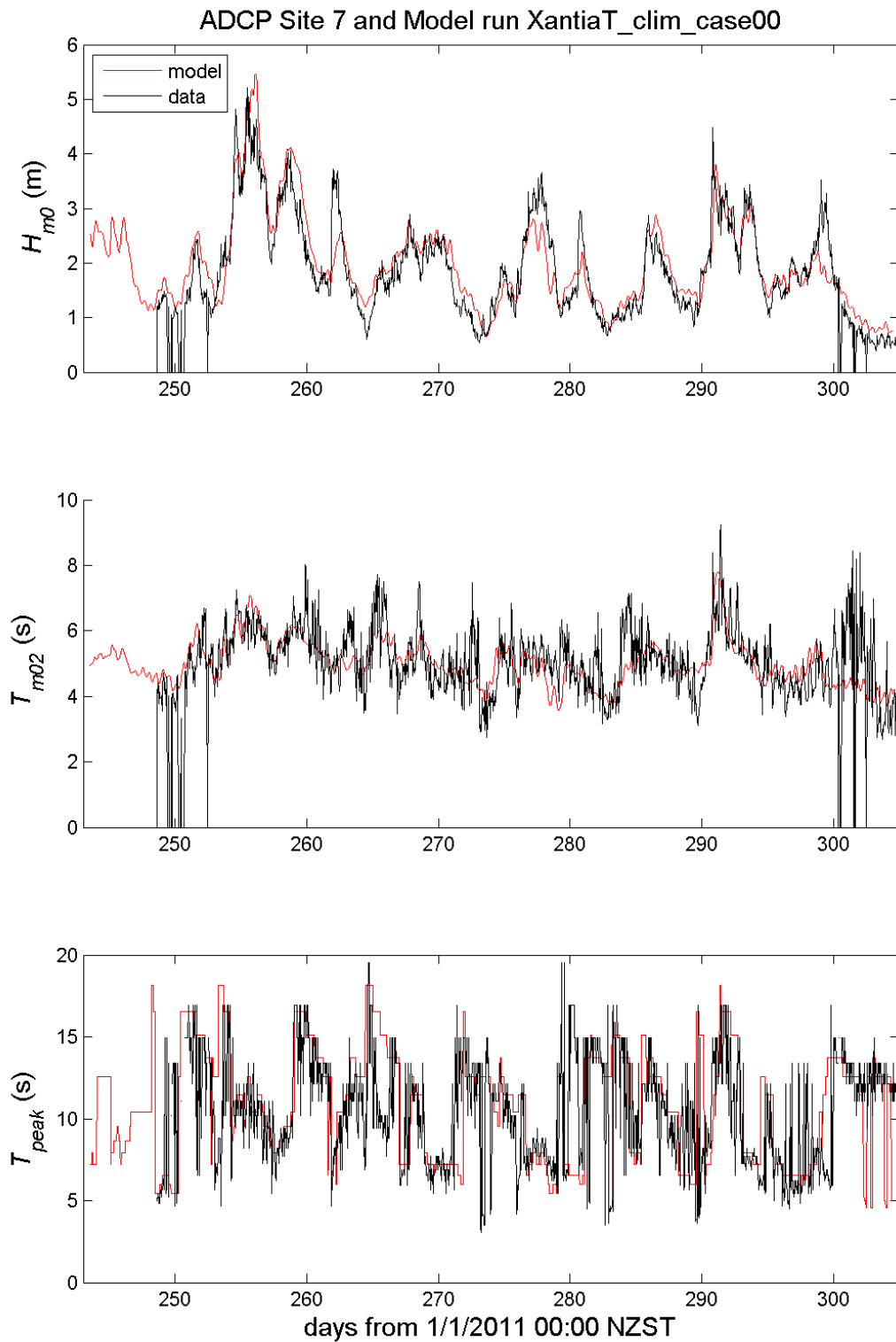


Figure C-3 (a): Comparison of wave statistics measured at the Site 7 ADCP with outputs from the Xantia 100m wave model. From the top panel: significant wave height, second-moment mean wave period, and peak wave period. The lines show statistics derived from frequencies below a 0.6 Hz cutoff, from the model (red) and measurements (black).

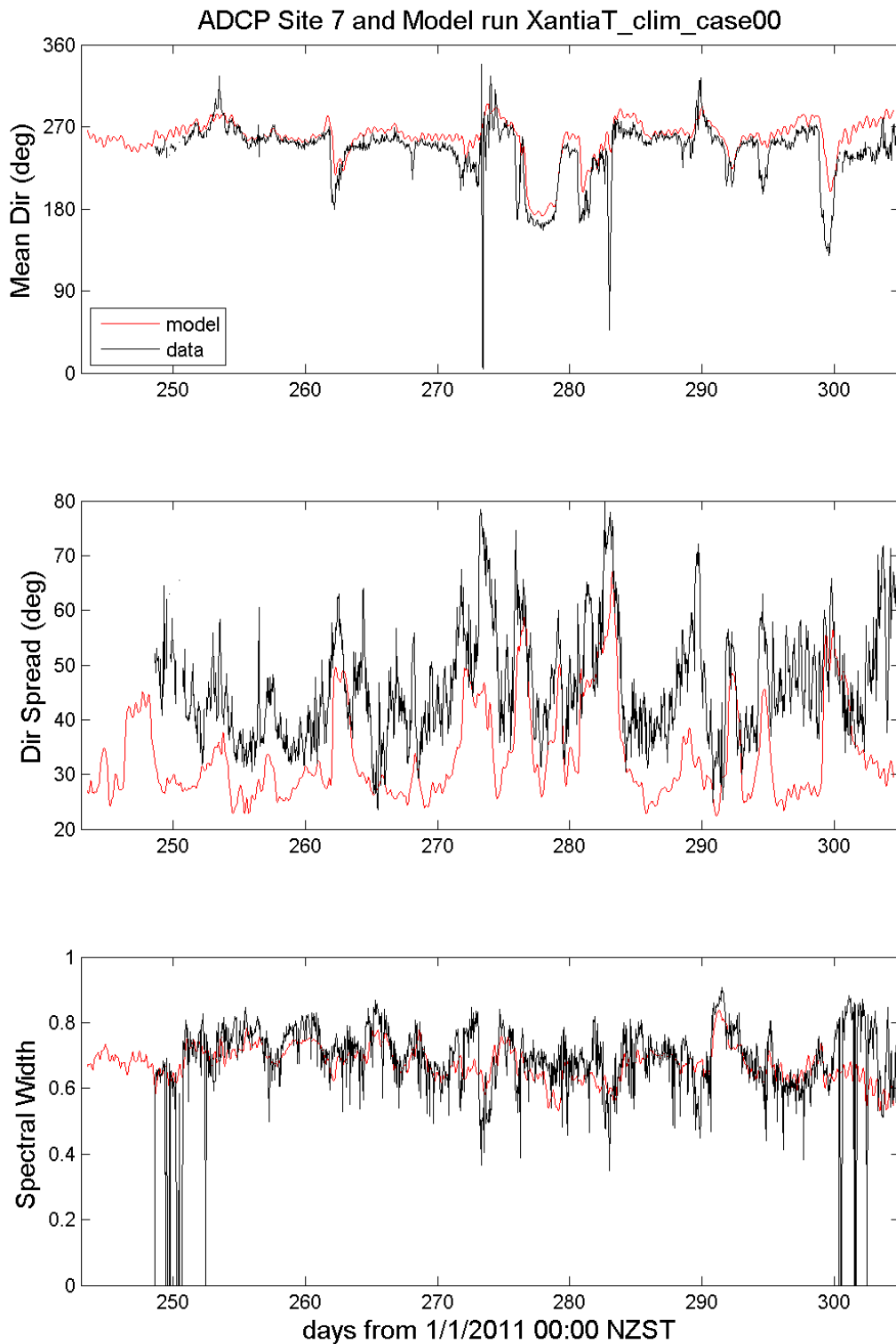


Figure C-3 (b): Comparison of wave statistics measured at the Site 7 ADCP with outputs from the Xantia 100m wave model. From the top panel: mean wave direction, directional spread and spectral width.

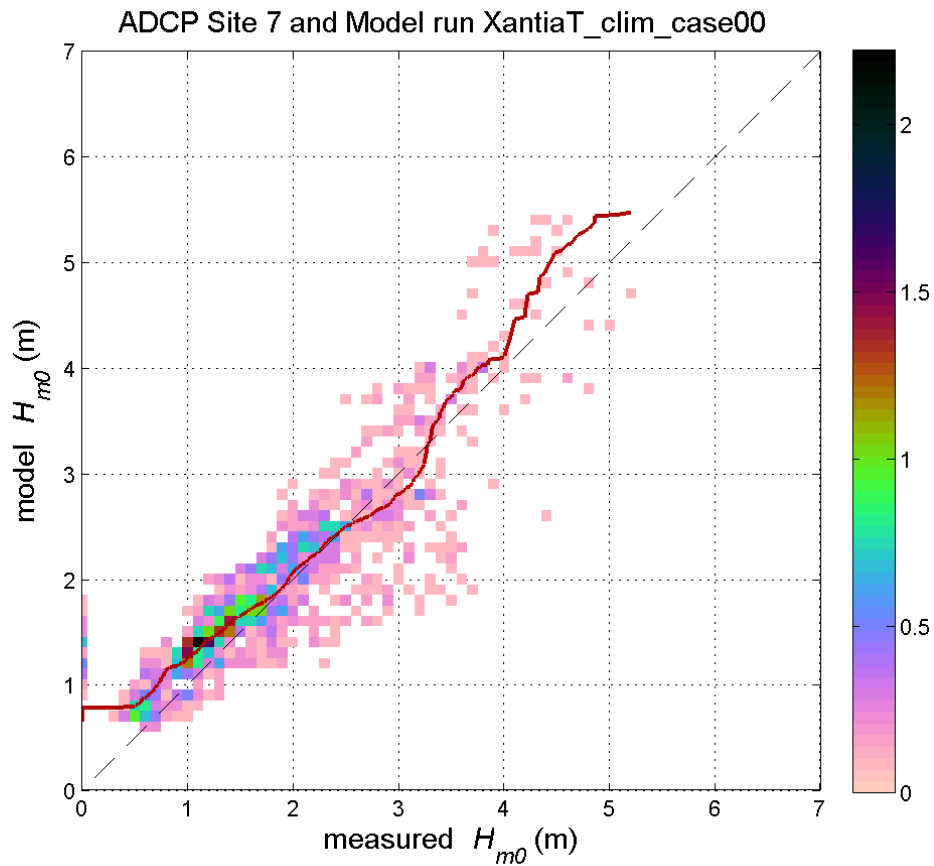


Figure C-3 (c): Comparison of significant wave height measured at the Site 7 ADCP with outputs from the Xantia 100m wave model. The colour scale shows probability of joint occurrence of measured and modelled values of significant wave height at surface level, while the solid red line gives a quantile-quantile plot.

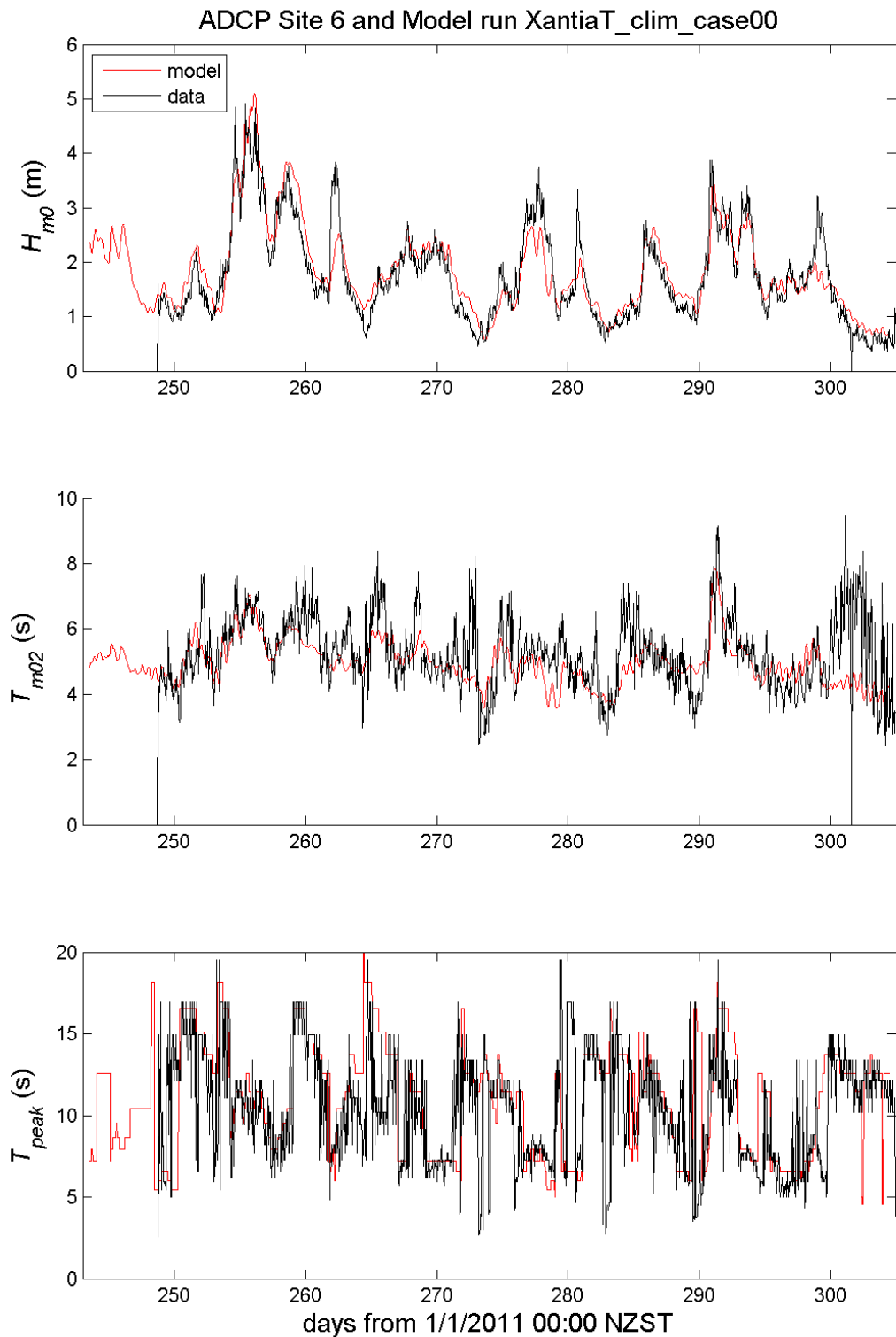


Figure C-4 (a): Comparison of wave statistics measured at the Site 6 ADCP, with outputs from the Xantia 100m wave model. From the top panel: significant wave height, second-moment mean wave period, and peak wave period. The lines show statistics derived from frequencies below a 0.6 Hz cutoff, from the model (red) and measurements (black).

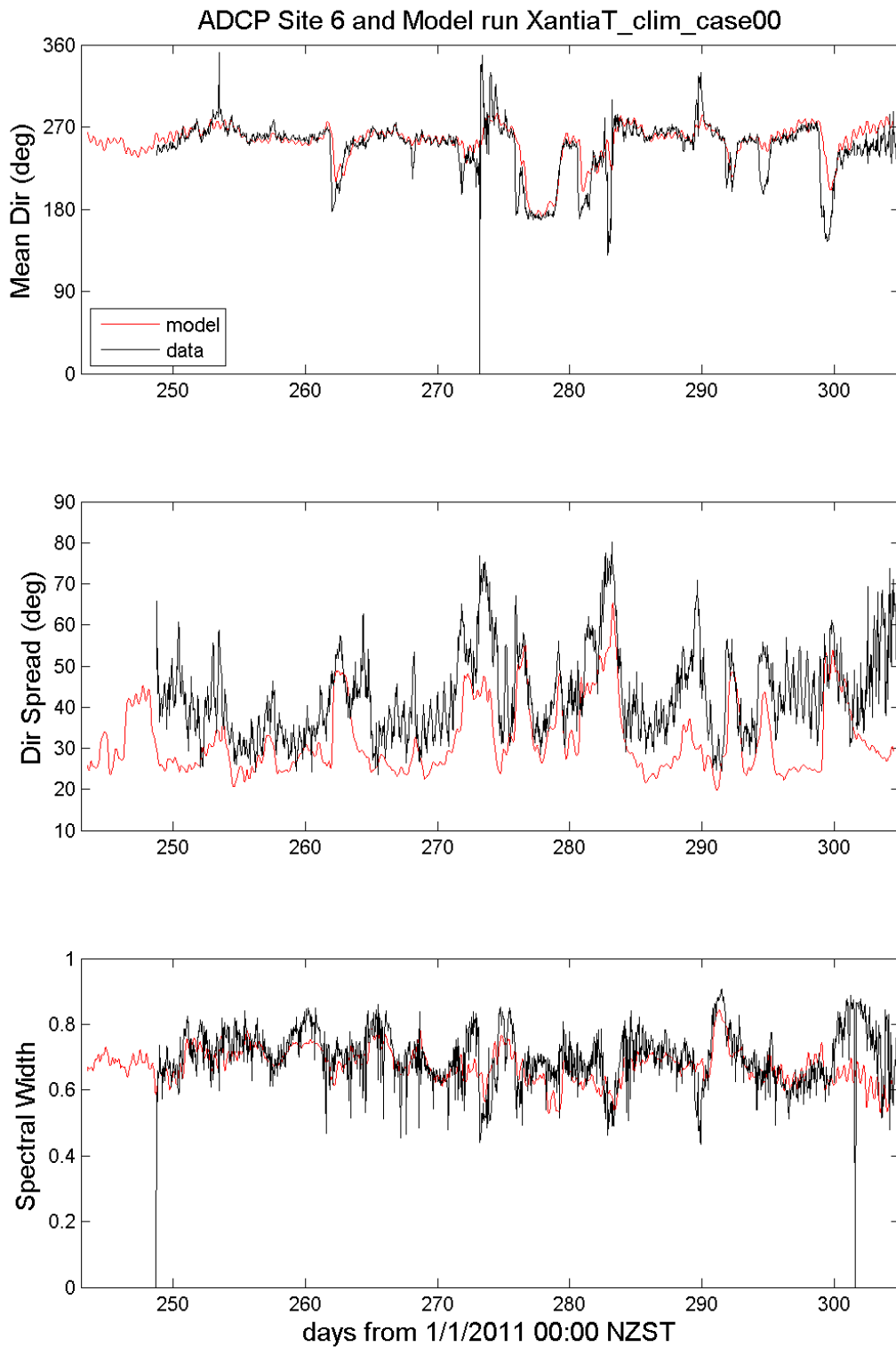


Figure C-4 (b): Comparison of wave statistics measured at the Site 6 ADCP, with outputs from the Xantia 100m wave model. From the top panel: mean wave direction, directional spread and spectral width.

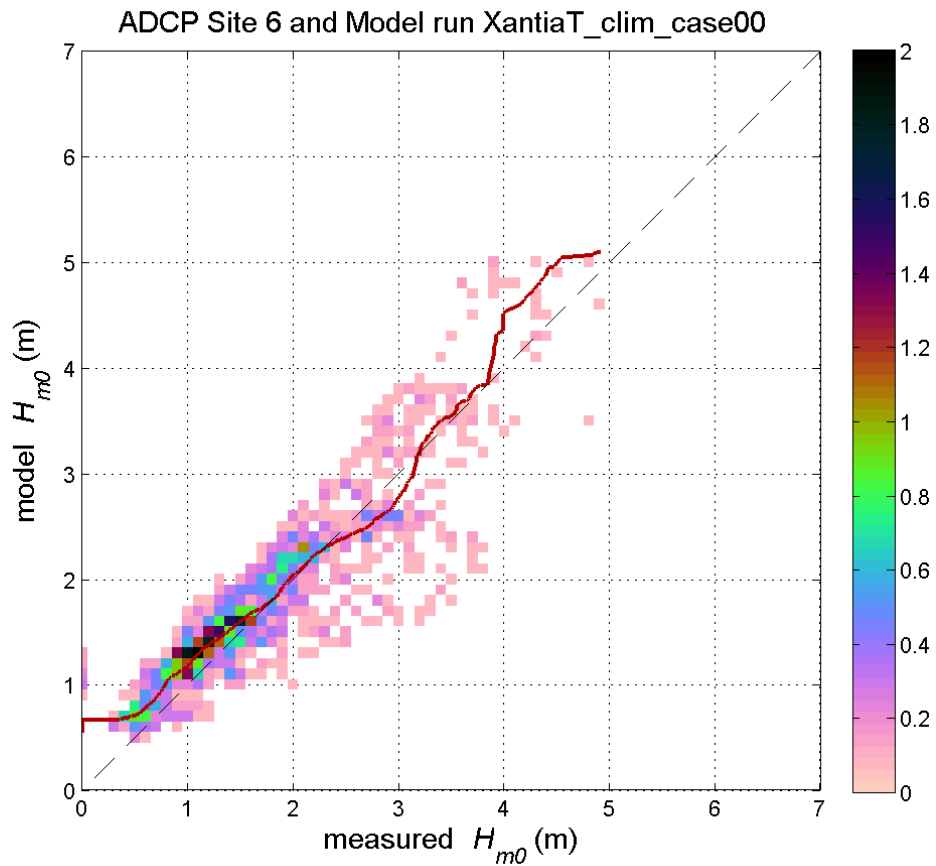


Figure C-4 (c): Comparison of significant wave height measured at the Site 6 ADCP with outputs from the Xantia 100m wave model. The colour scale shows probability of joint occurrence of measured and modelled values of significant wave height at surface level, while the solid red line gives a quantile-quantile plot.

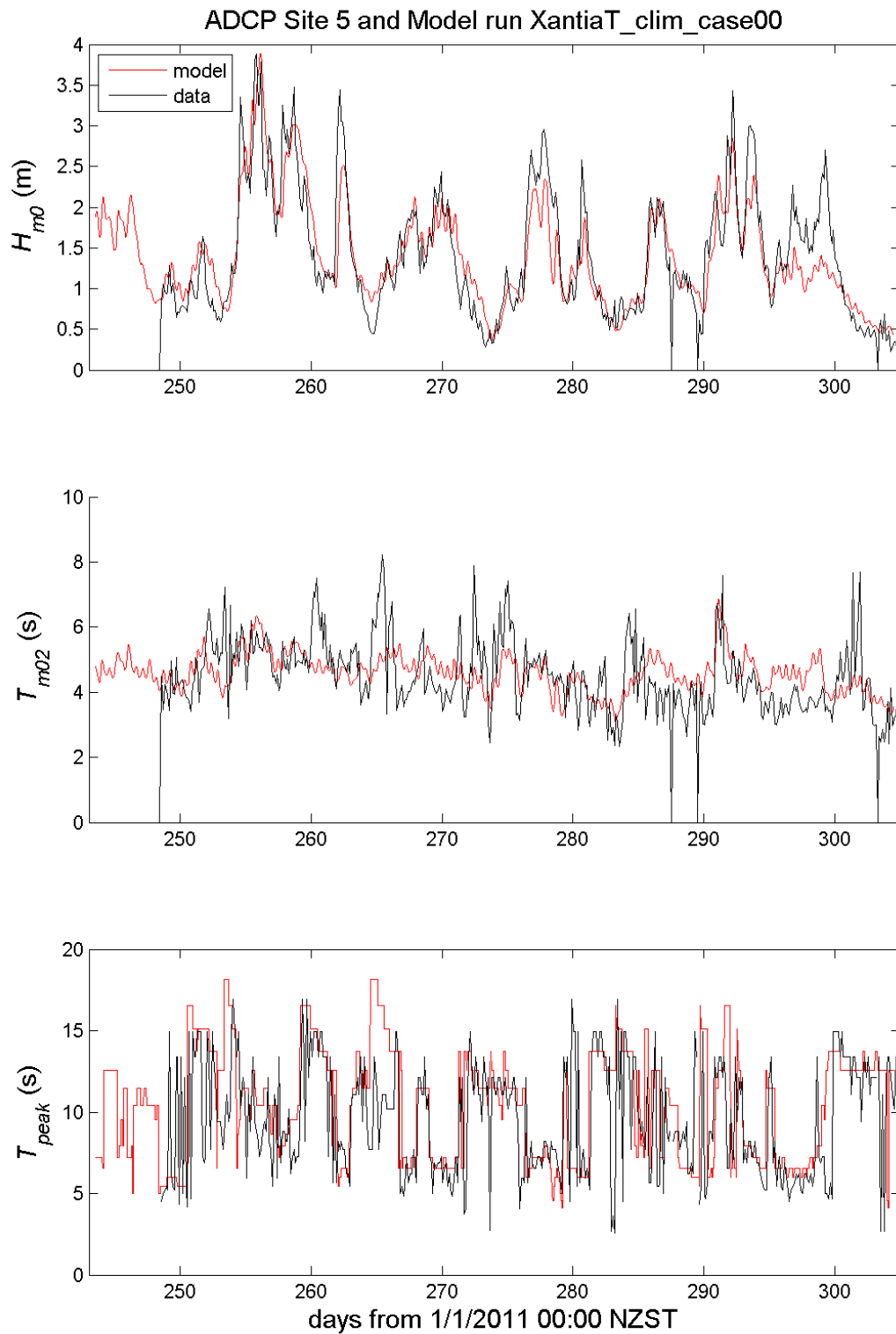


Figure C-5 (a): Comparison of wave statistics measured at the Site 5 ADCP, with outputs from the Xantia 100m wave model. From the top panel: significant wave height, second-moment mean wave period, and peak wave period. The lines show statistics derived from frequencies below a 0.6 Hz cutoff, from the model (red) and measurements (black).

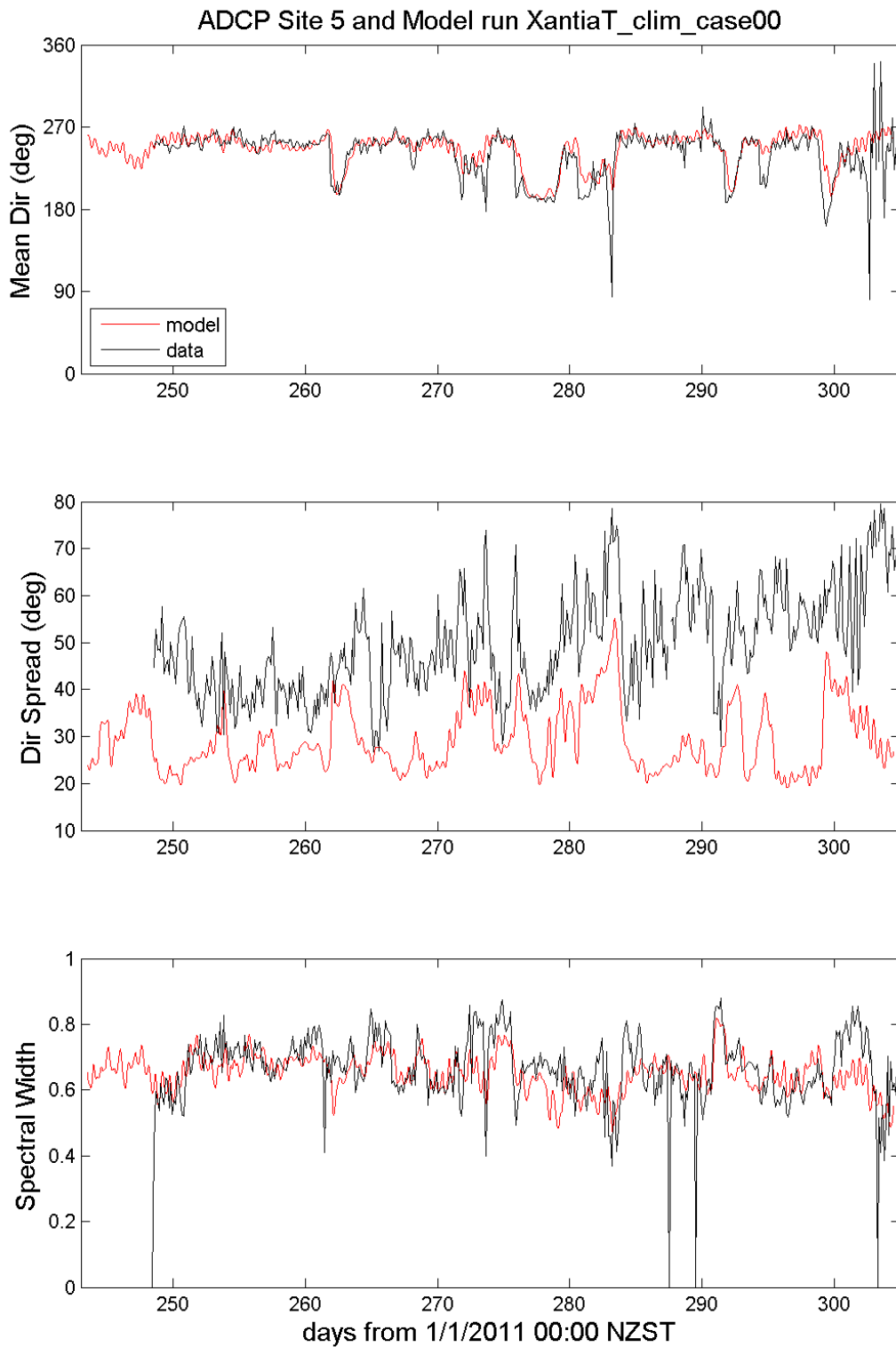


Figure C-5 (b): Comparison of wave statistics measured at the Site 5 ADCP, with outputs from the Xantia 100m wave model. From the top panel: mean wave direction, directional spread and spectral width.

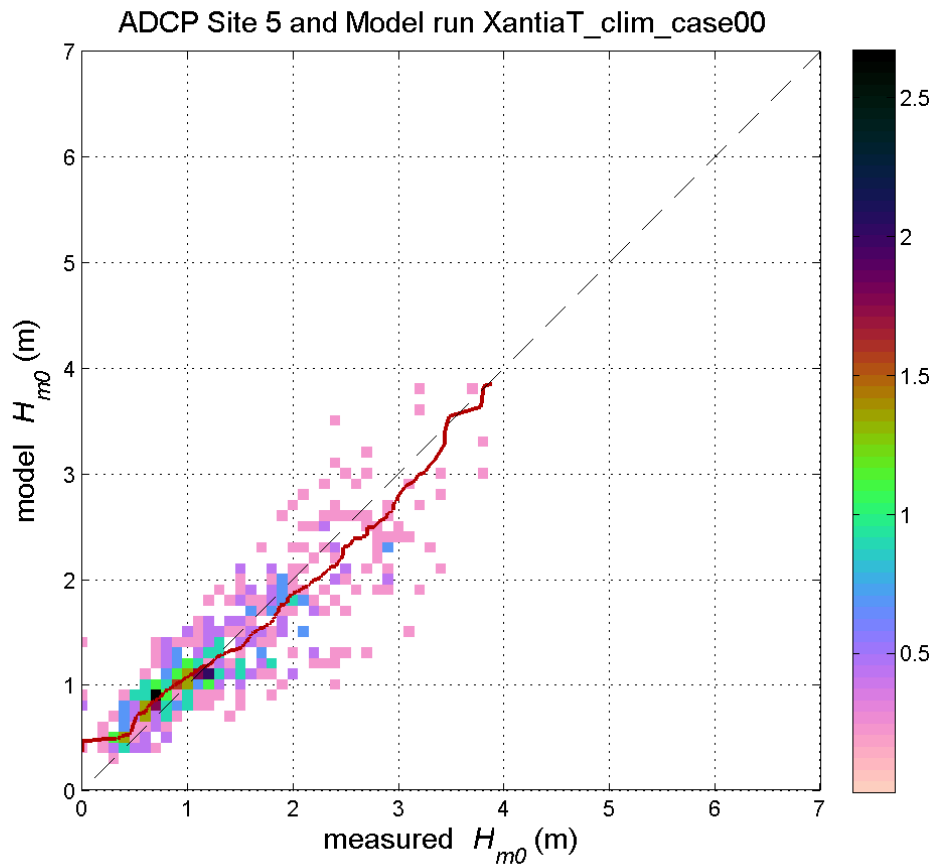


Figure C-5 (c): Comparison of significant wave height measured at the Site 5 ADCP with outputs from the Xantia 100m wave model. The colour scale shows probability of joint occurrence of measured and modelled values of significant wave height at surface level, while the solid red line gives a quantile-quantile plot.

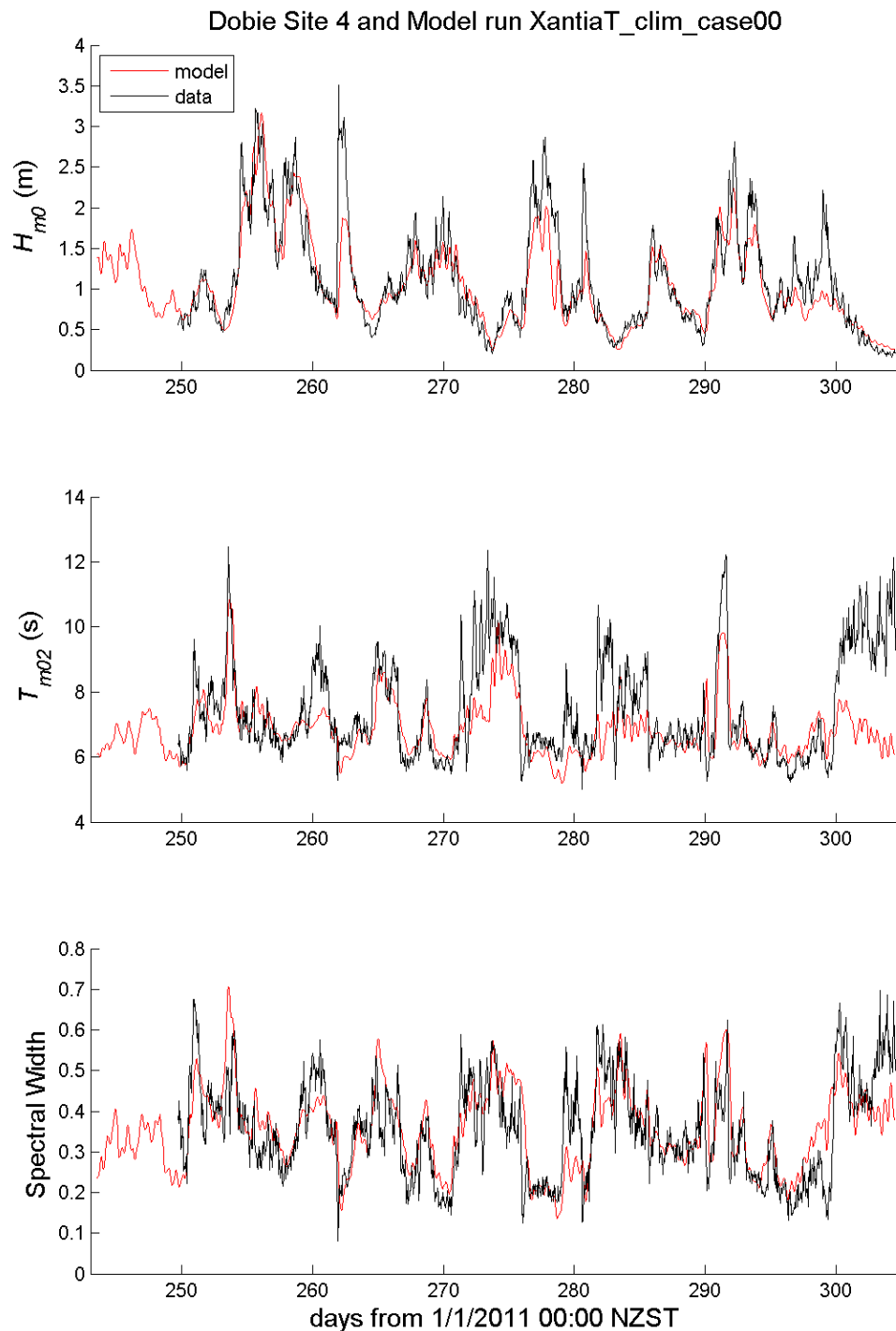


Figure C-6 (a): Comparison of wave statistics measured at the Site 4 Dobie, with outputs from the Xantia 100m wave model. From the top panel: significant wave height, second-moment mean wave period, and spectral width. The lines show statistics derived from surface level spectra, from the model (red) and measurements (black).

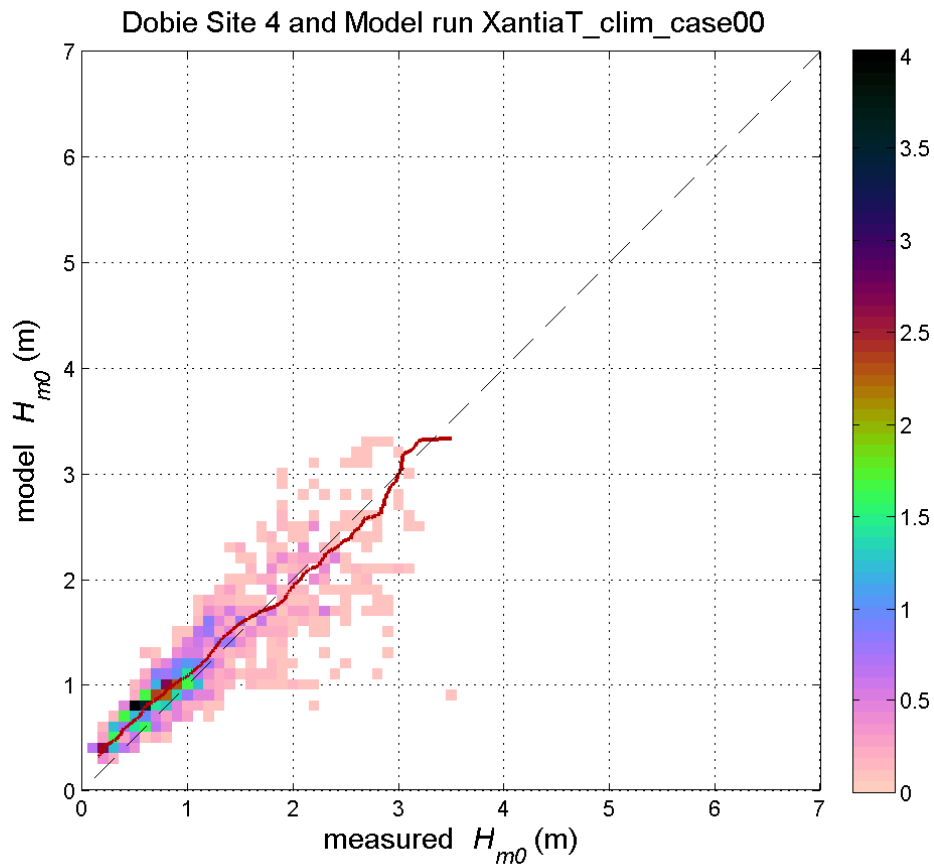


Figure C-6 (b): Comparison of significant wave height measured at the Site 4 Dobie with outputs from the Xantia 100m wave model. The colour scale shows probability of joint occurrence of measured and modelled values of significant wave height at surface level, while the solid red line gives a quantile-quantile plot.

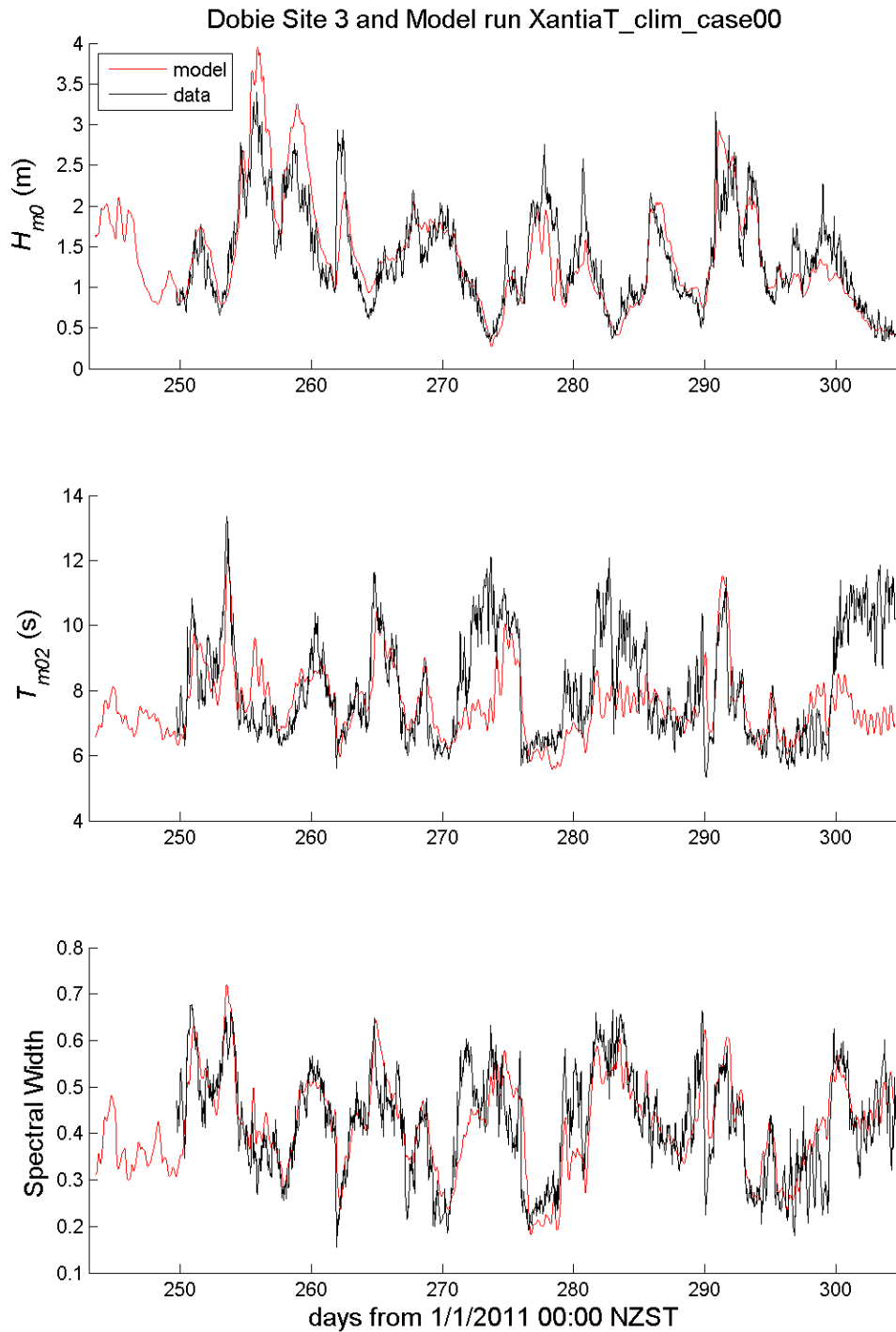


Figure C-7 (a): Comparison of wave statistics measured at the Site 3 Dobie, with outputs from the Xantia 100m wave model. From the top panel: significant wave height, second-moment mean wave period, and spectral width. The lines show statistics derived from surface level spectra, from the model (red) and measurements (black).

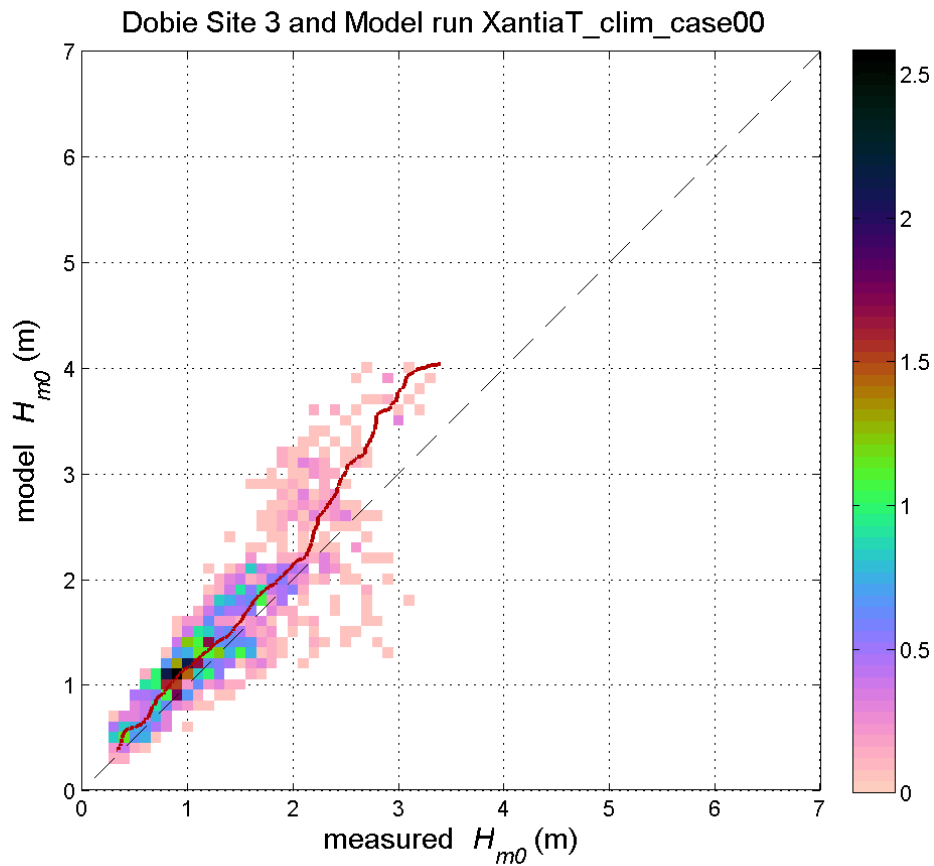


Figure C-7 (b): Comparison of significant wave height measured at the Site 3 Dobie with outputs from the Xantia 100m wave model. The colour scale shows probability of joint occurrence of measured and modelled values of significant wave height at surface level, while the solid red line gives a quantile-quantile plot.

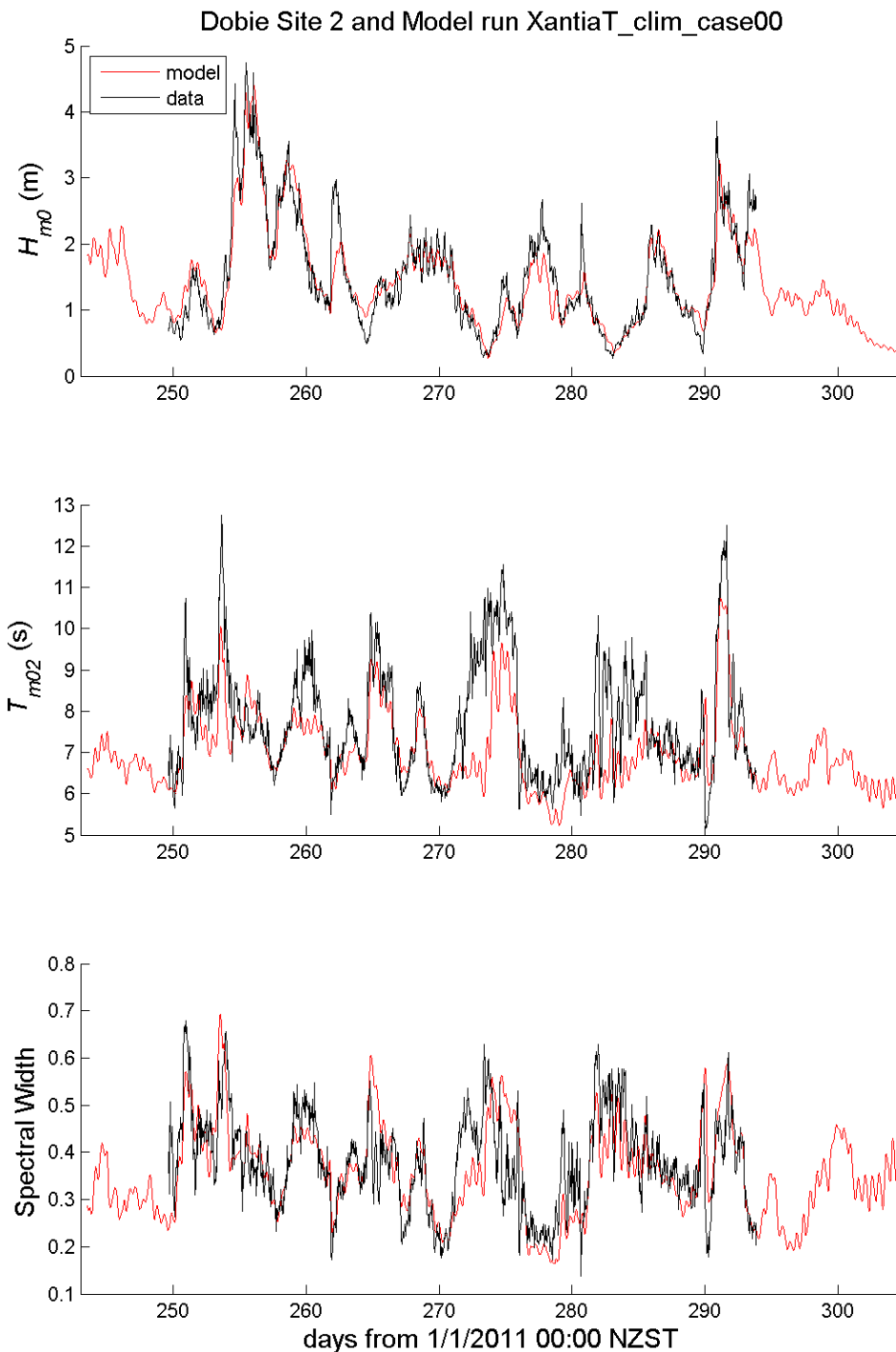


Figure C-8 (a): Comparison of wave statistics measured at the Site 2 Dobie, with outputs from the Xantia 100m wave model. From the top panel: significant wave height, second-moment mean wave period, and spectral width. The lines show statistics derived from surface level spectra, from the model (red) and measurements (black).

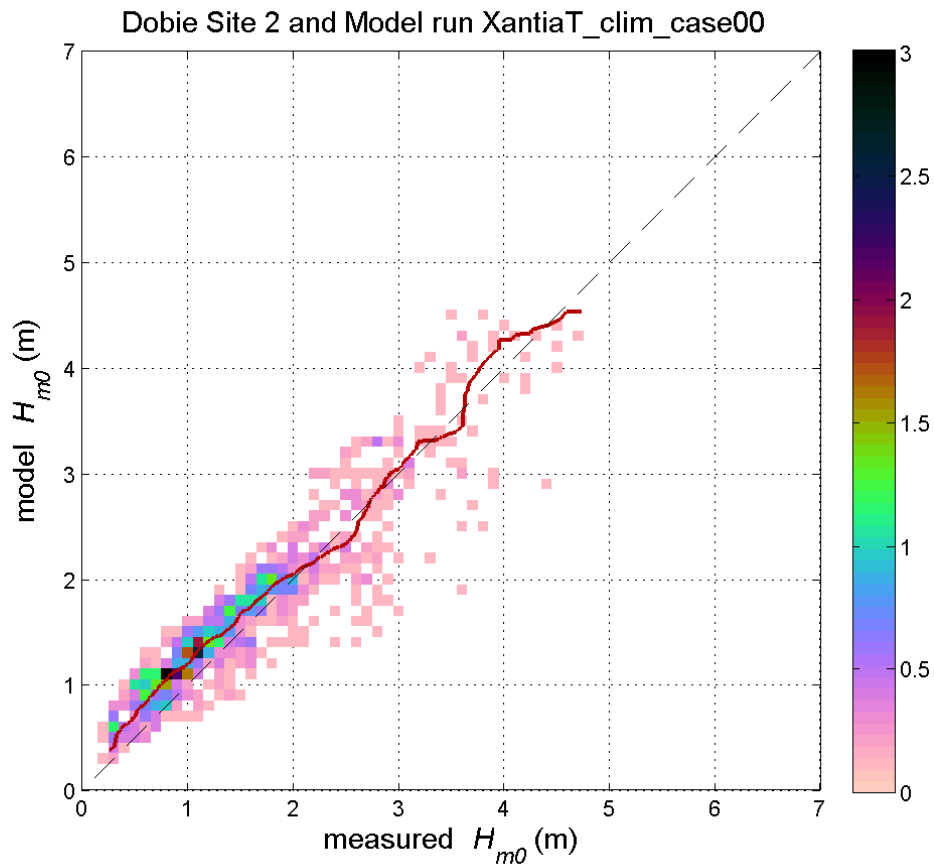


Figure C-8 (b): Comparison of significant wave height (at measured at the Site 2 Dobie with outputs from the Xantia 100m wave model. The colour scale shows probability of joint occurrence of measured and modelled values of significant wave height at surface level, while the solid red line gives a quantile-quantile plot.

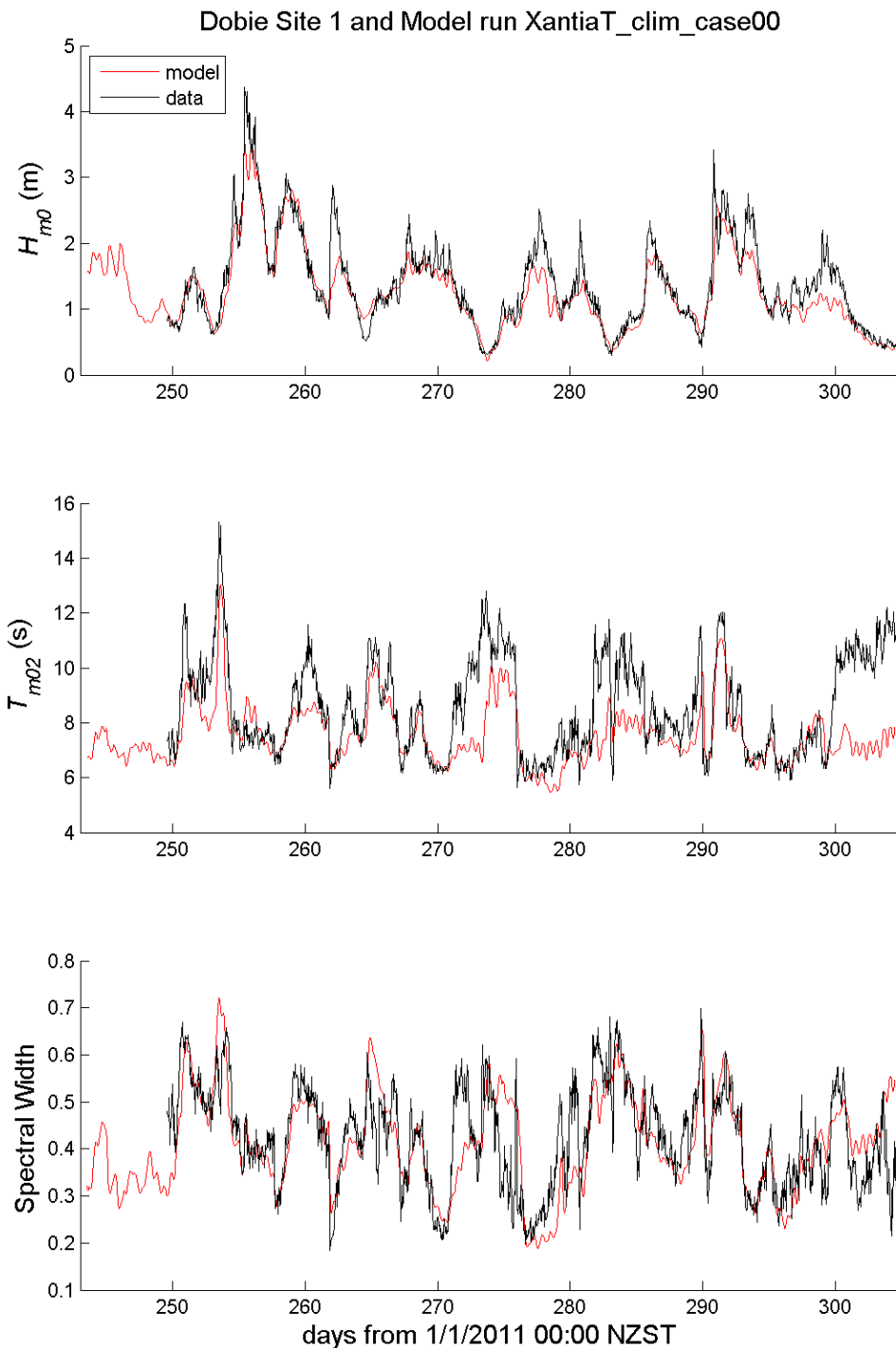


Figure C-9 (a): Comparison of wave statistics measured at the Site 1 Dobie, with outputs from the Xantia 100m wave model. From the top panel: significant wave height, second-moment mean wave period, and spectral width. The lines show statistics derived from surface level spectra, from the model (red) and measurements (black).

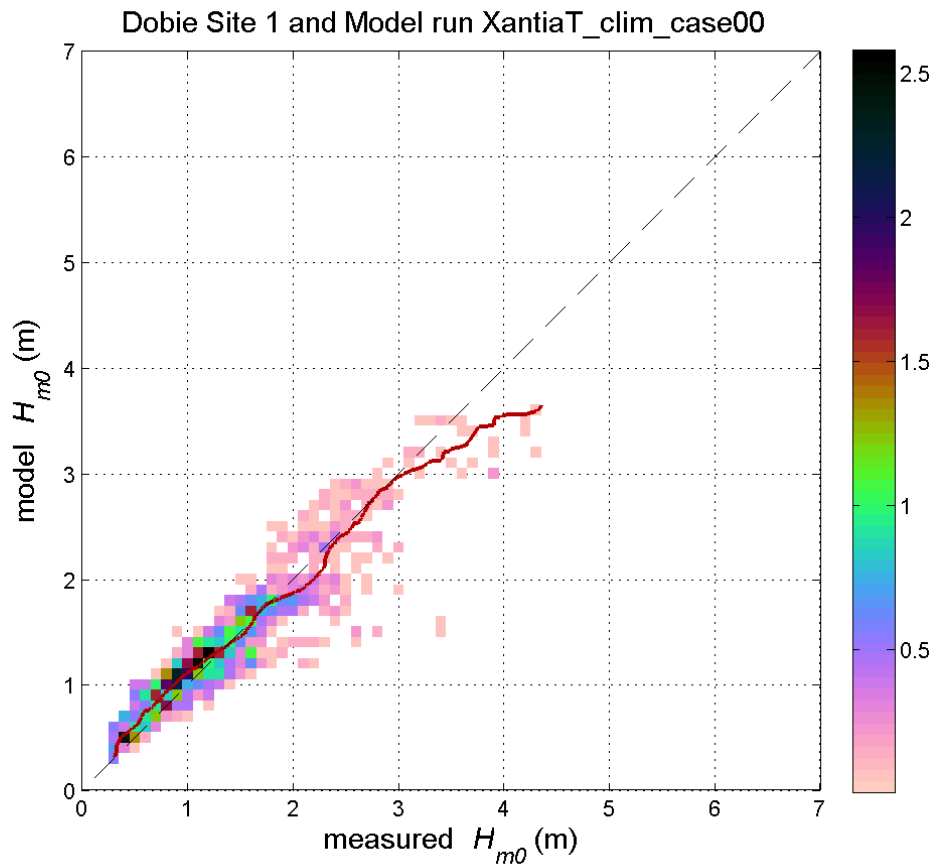


Figure C-9 (b): Comparison of significant wave height measured at the Site 1 Dobie with outputs from the Xantia 100m wave model. The colour scale shows probability of joint occurrence of measured and modelled values of significant wave height at instrument level, while the solid red line gives a quantile-quantile plot.

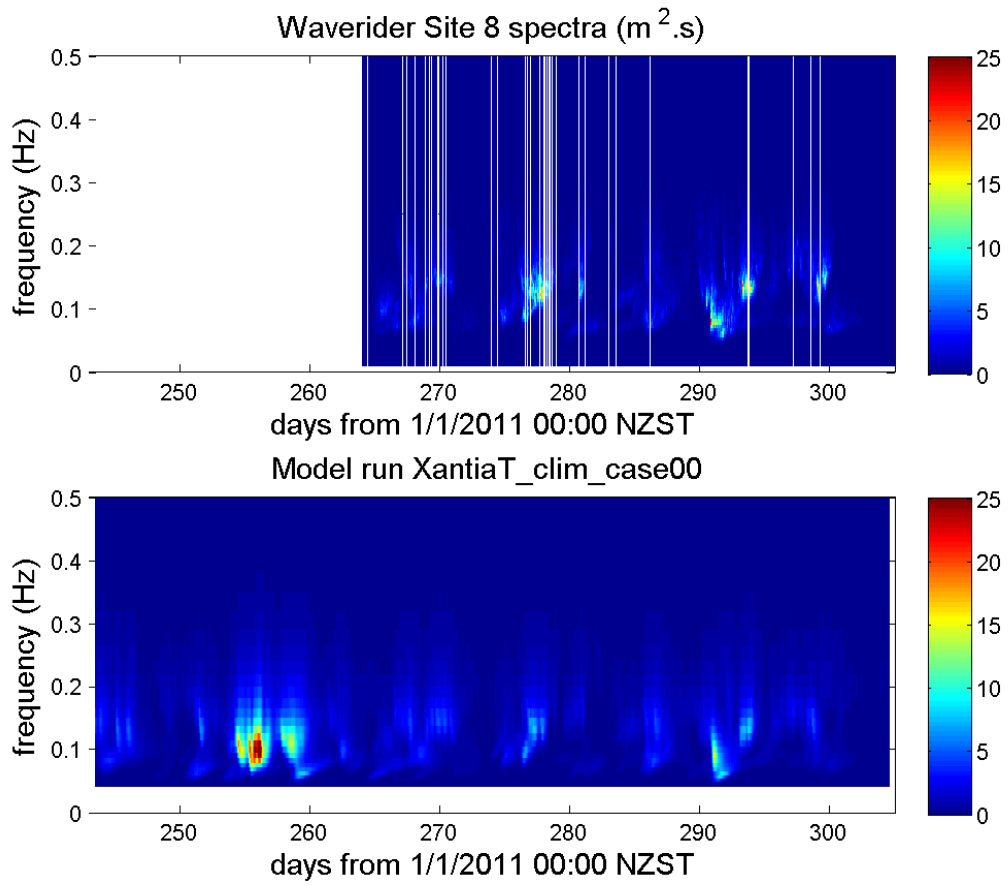


Figure C-10: Time sequence of frequency spectra at Site 8. From Waverider buoy data (top panel), and from the Xantia 100m wave model (bottom panel).

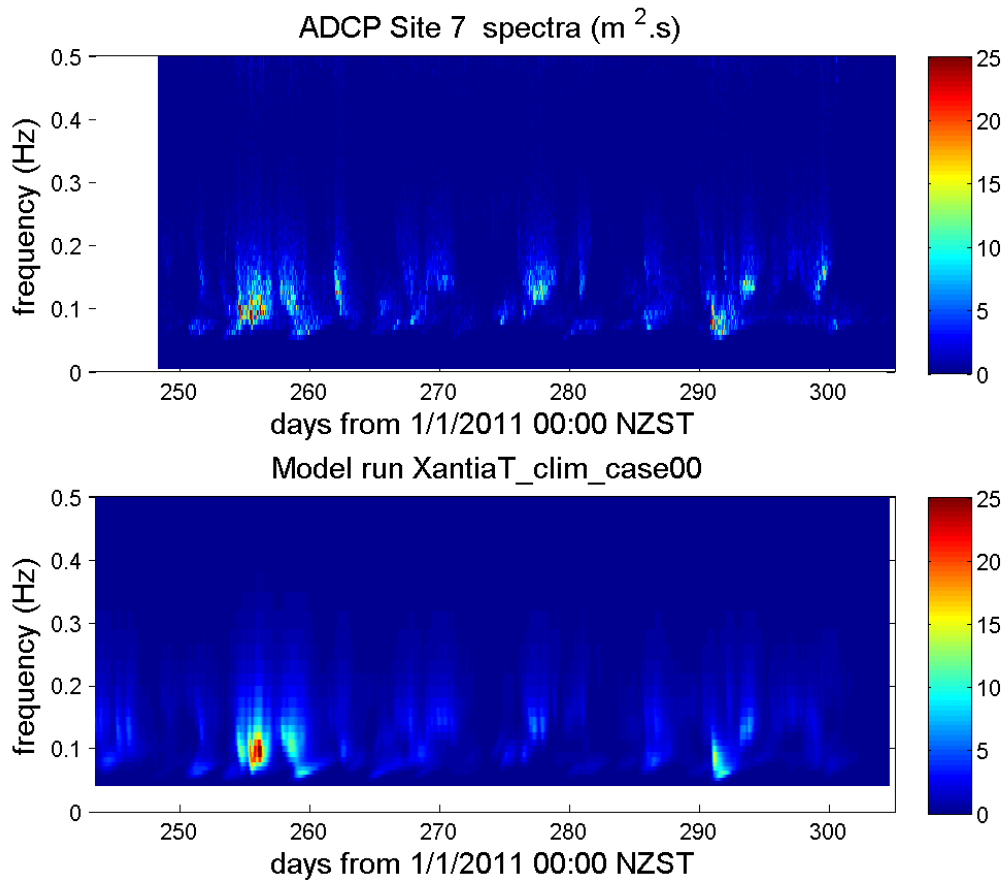


Figure C-11: Time sequence of frequency spectra at Site 7. From ADCP data (top panel), and from the Xantia 100m wave model (bottom panel).

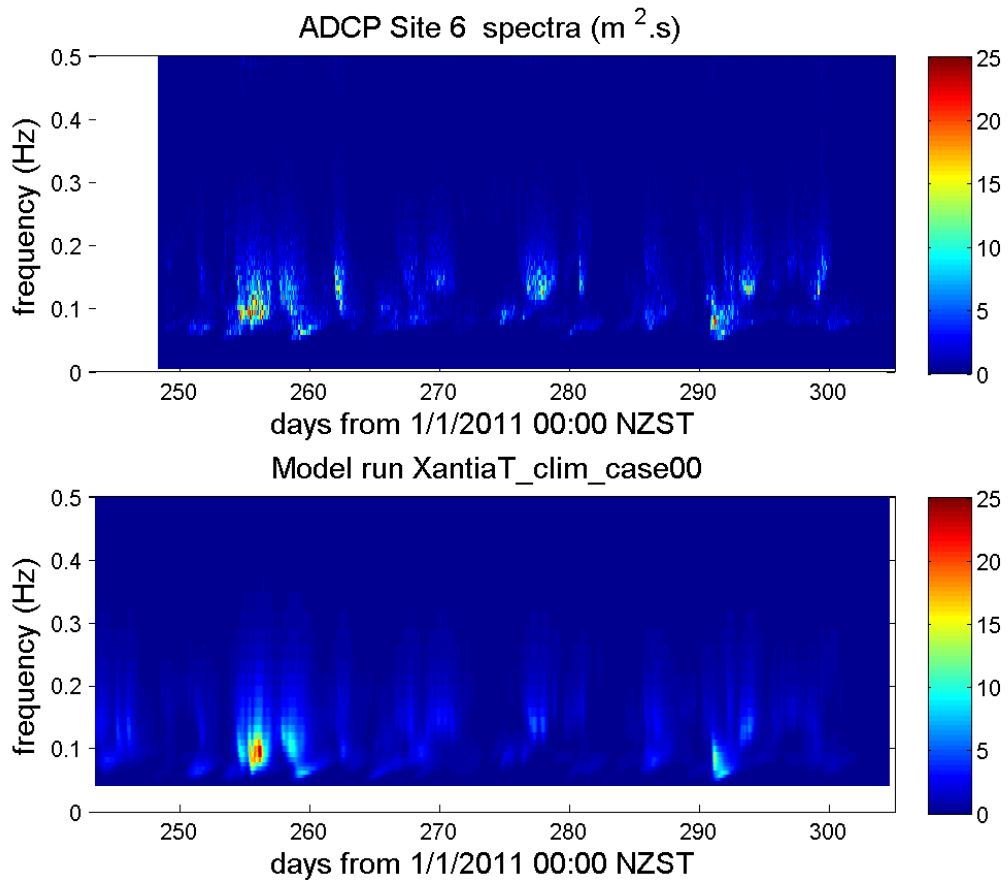


Figure C-12: Time sequence of frequency spectra at Site 6. From ADCP data (top panel) and from the Xantia 100m wave model (bottom panel).

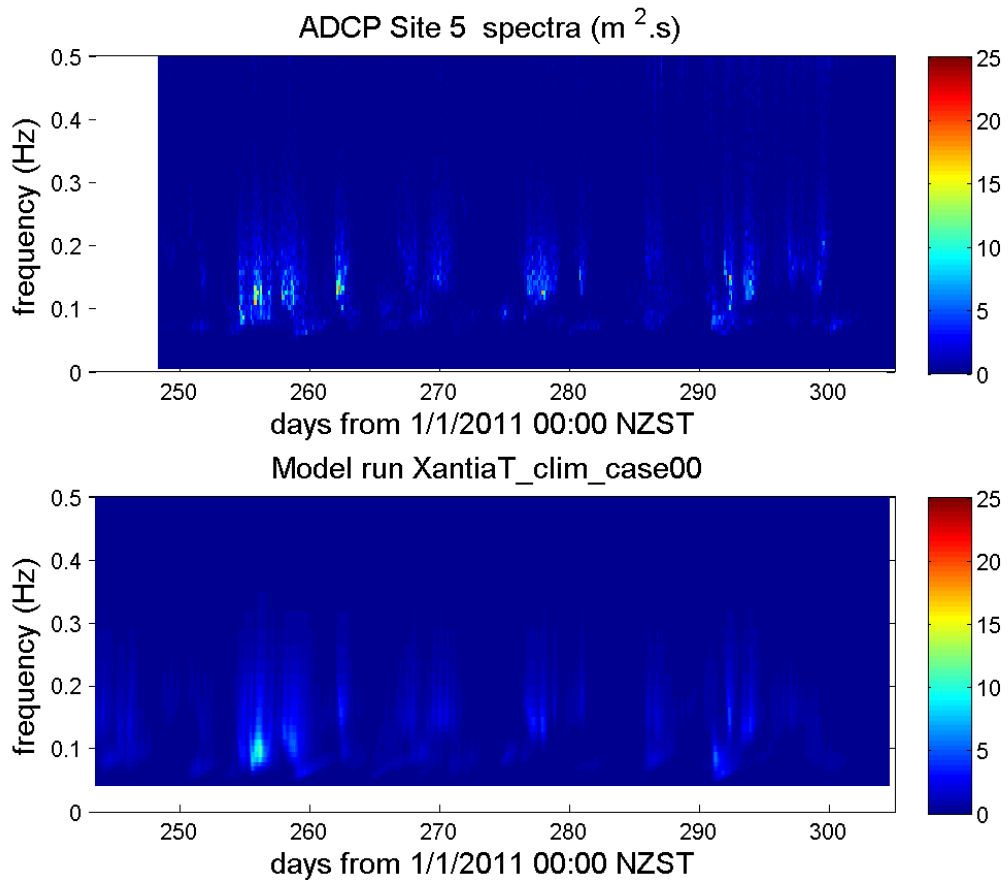


Figure C-13: Time sequence of frequency spectra at Site 5. From ADCP data (top panel), and from the Xantia 100m wave model (bottom panel).

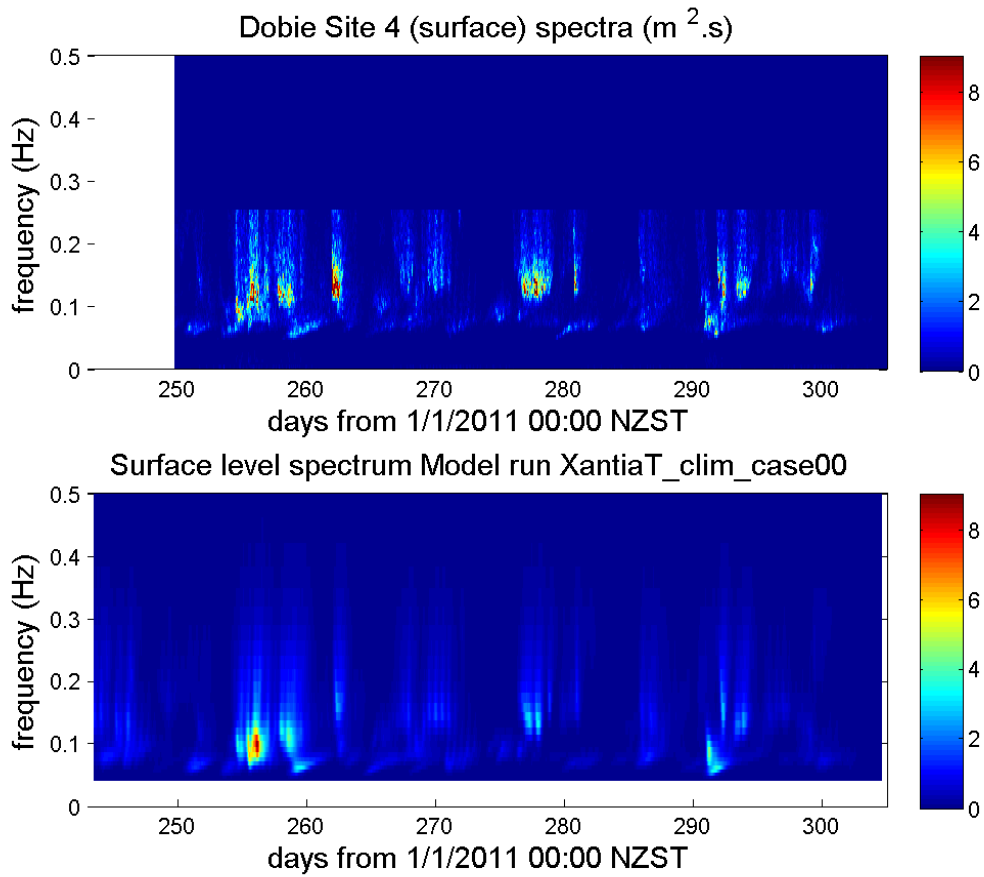


Figure C-14: Time sequence of frequency spectra at Site 4. From Dobie data at instrument level (top panel), and from the Xantia 100m wave model at instrument level (middle panel) and at the surface (bottom panel).

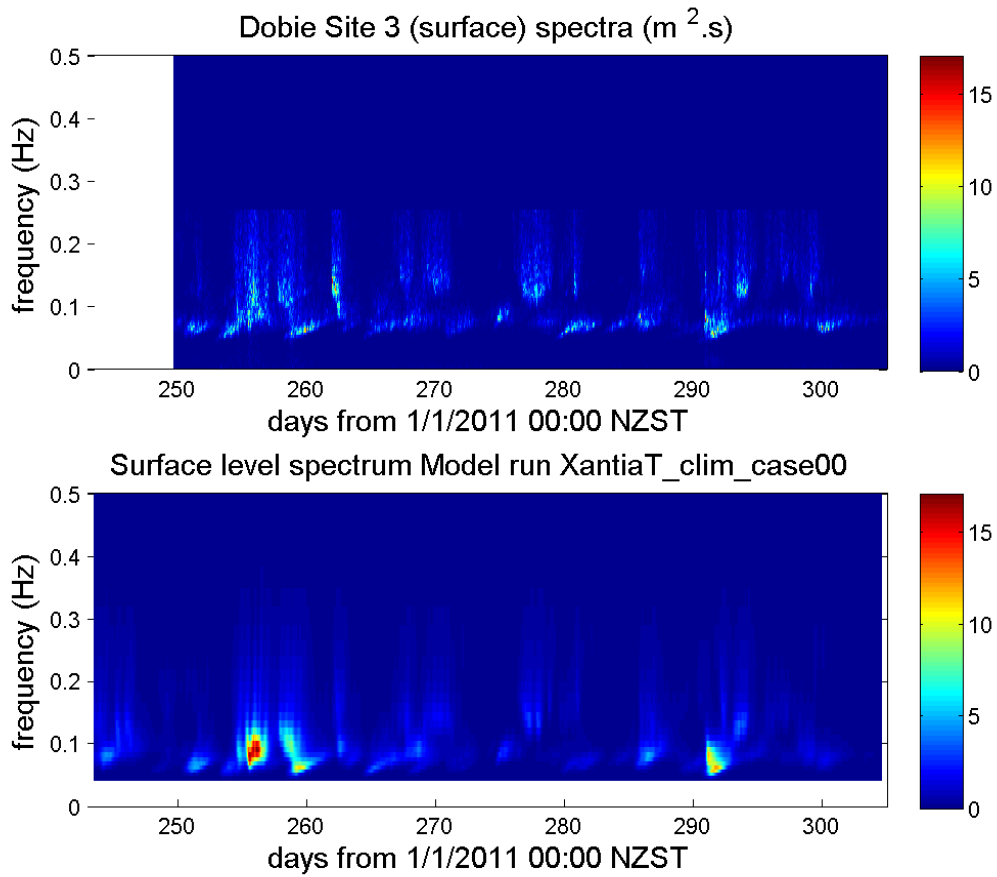


Figure C-15: Time sequence of frequency spectra at Site 3. From Dobie data at instrument level (top panel), and from the Xantia 100m wave model at instrument level (middle panel) and at the surface (bottom panel).

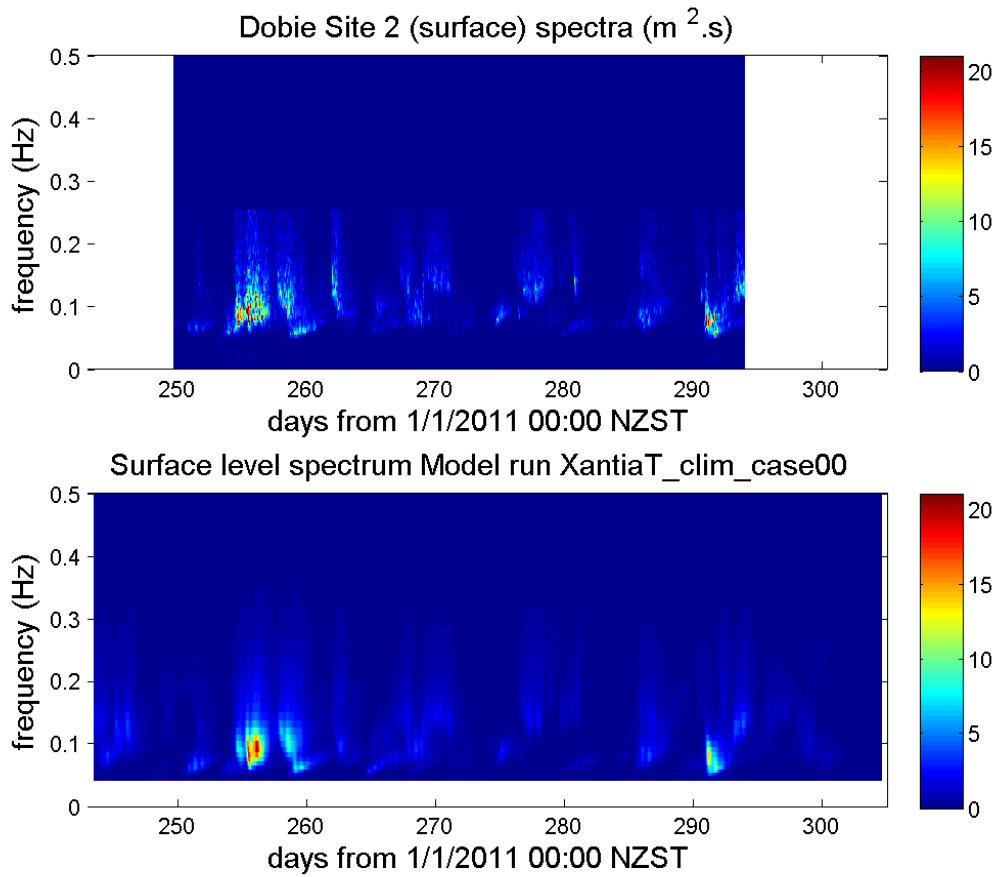


Figure C-16: Time sequence of frequency spectra at Site 2. From Dobie data at instrument level (top panel), and from the Xantia 100m wave model at instrument level (middle panel) and at the surface (bottom panel).

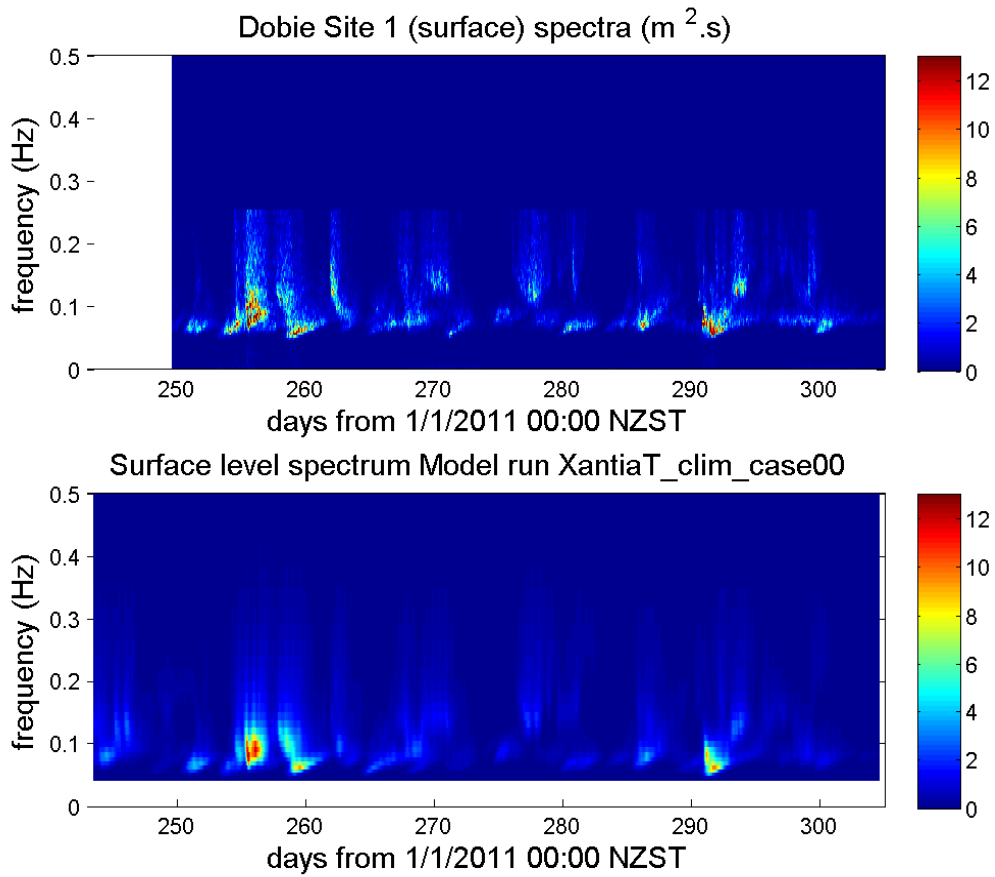


Figure C-17: Time sequence of frequency spectra at Site 1. From Dobie data at instrument level (top panel), and from the Xantia 100m wave model at instrument level (middle panel) and at the surface (bottom panel).

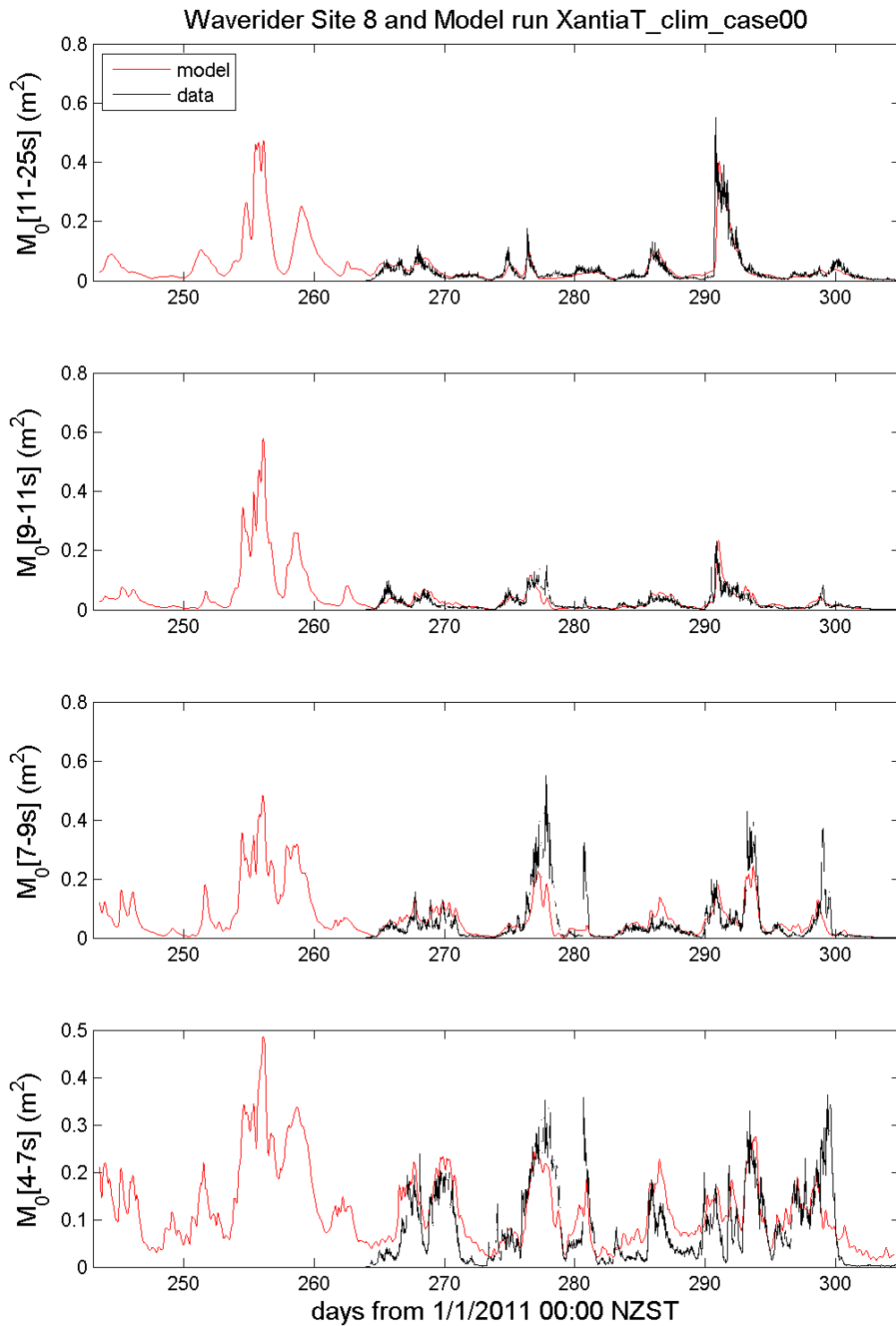


Figure C-18: Comparison of surface sea level variance within selected frequency bands at Site 8. Values derived from measured (black) and modelled (red) frequency spectra are plotted on a linear scale.

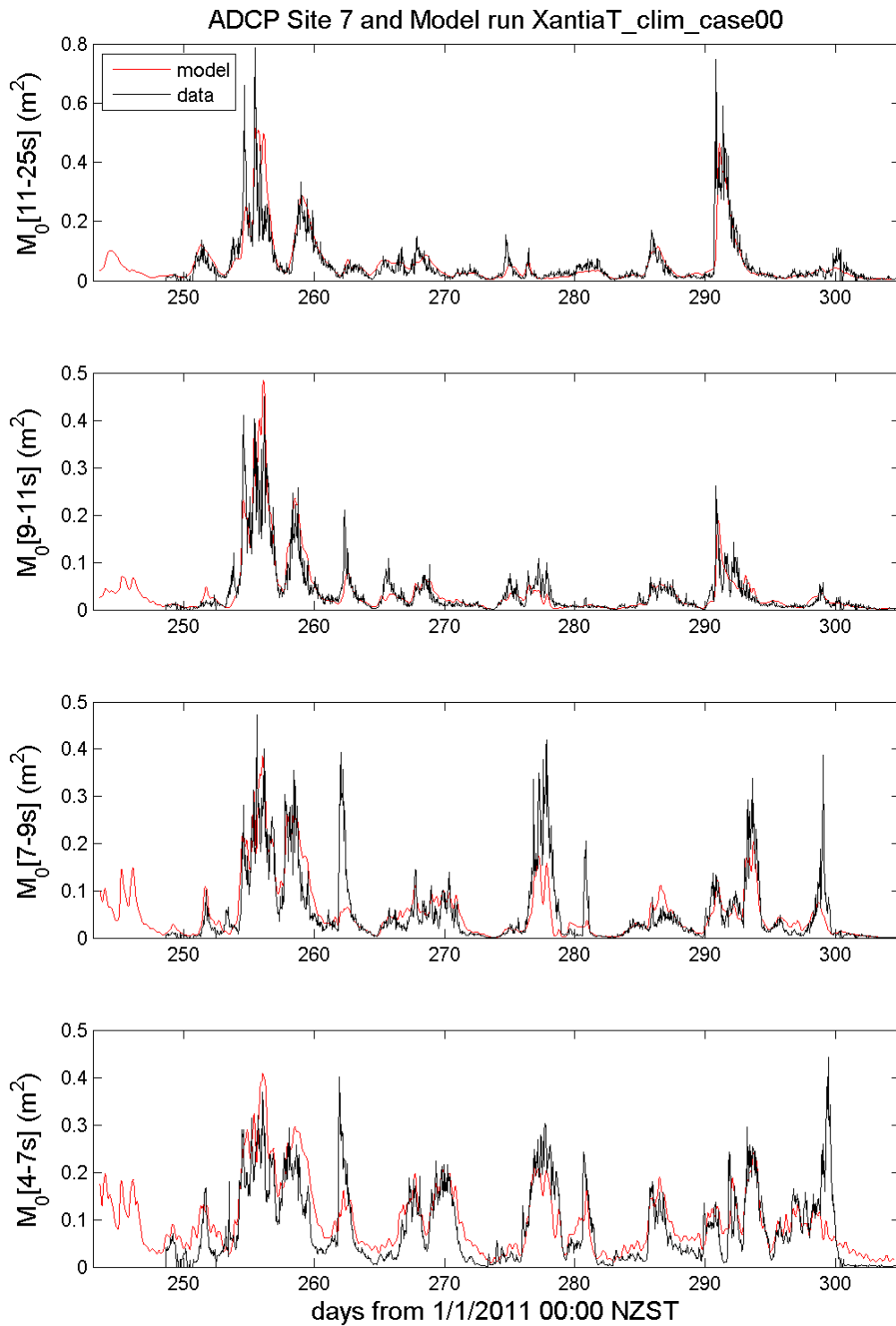


Figure C-19: Comparison of surface sea level variance within selected frequency bands at Site 7. Values derived from measured (black) and modelled (red) frequency spectra are plotted on a linear scale.

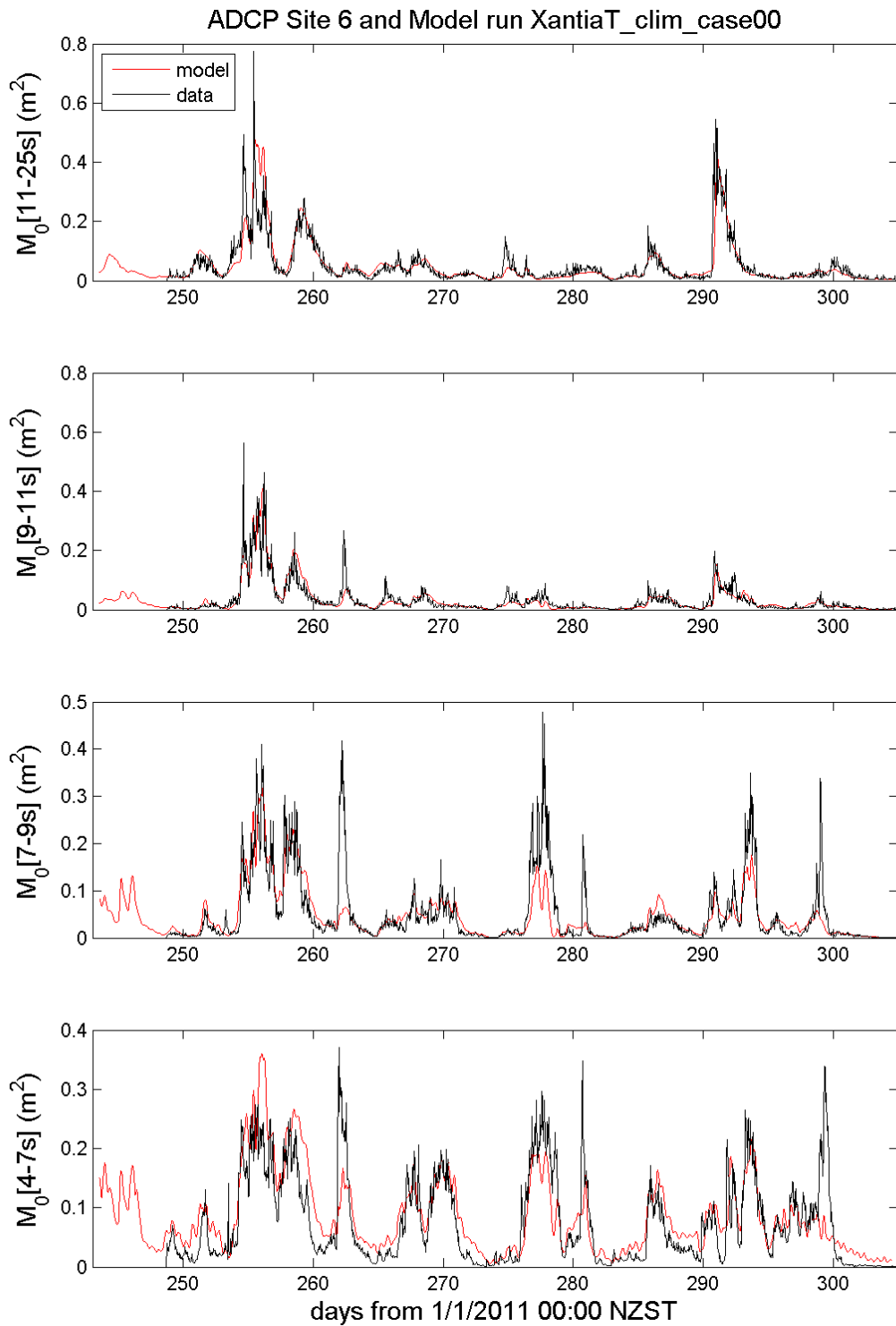


Figure C-20: Comparison of surface sea level variance within selected frequency bands at Site 6. Values derived from measured (black) and modelled (red) frequency spectra are plotted on a linear scale.

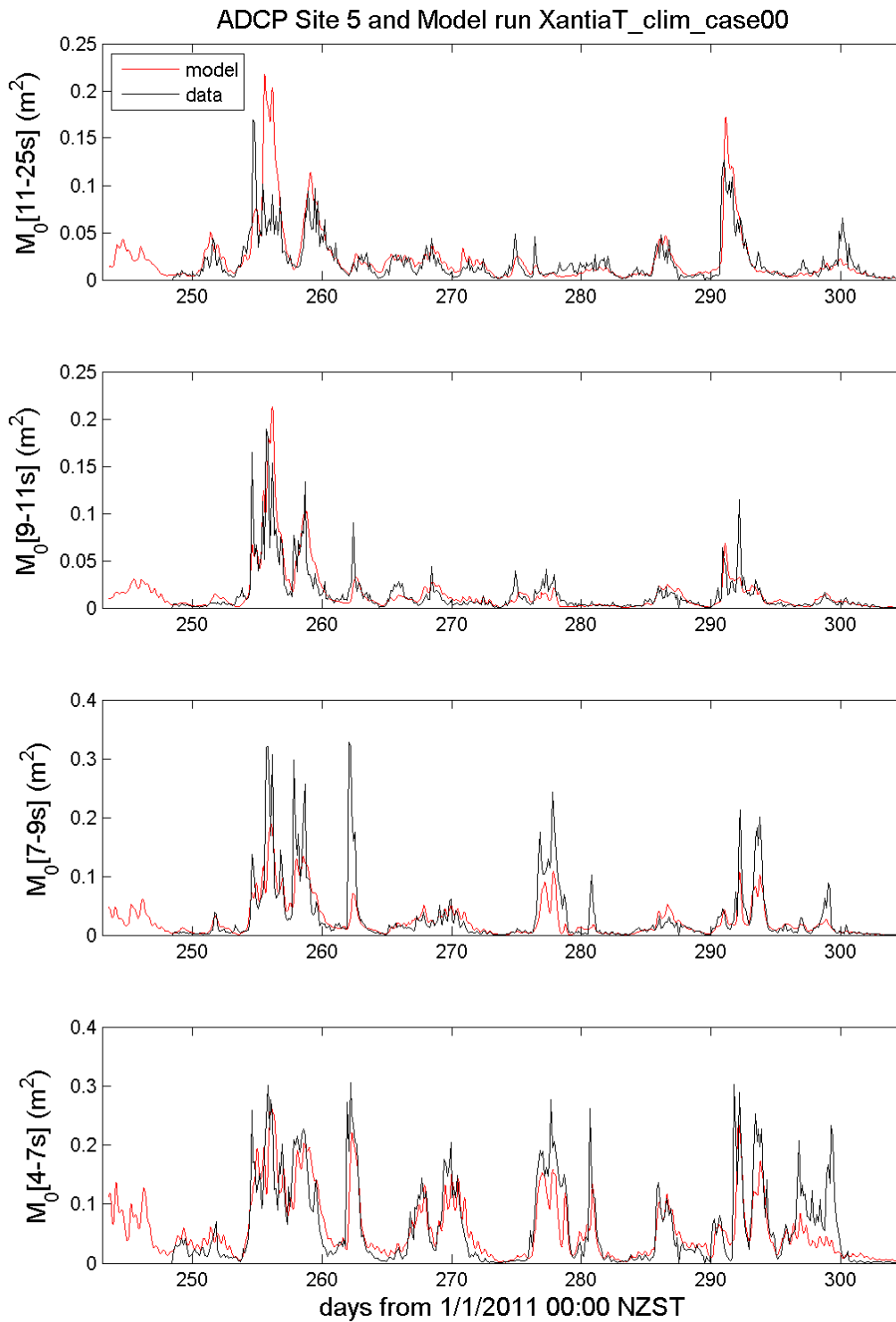


Figure C-21: Comparison of surface sea level variance within selected frequency bands at Site 5. Values derived from measured (black) and modelled (red) frequency spectra are plotted on a linear scale.

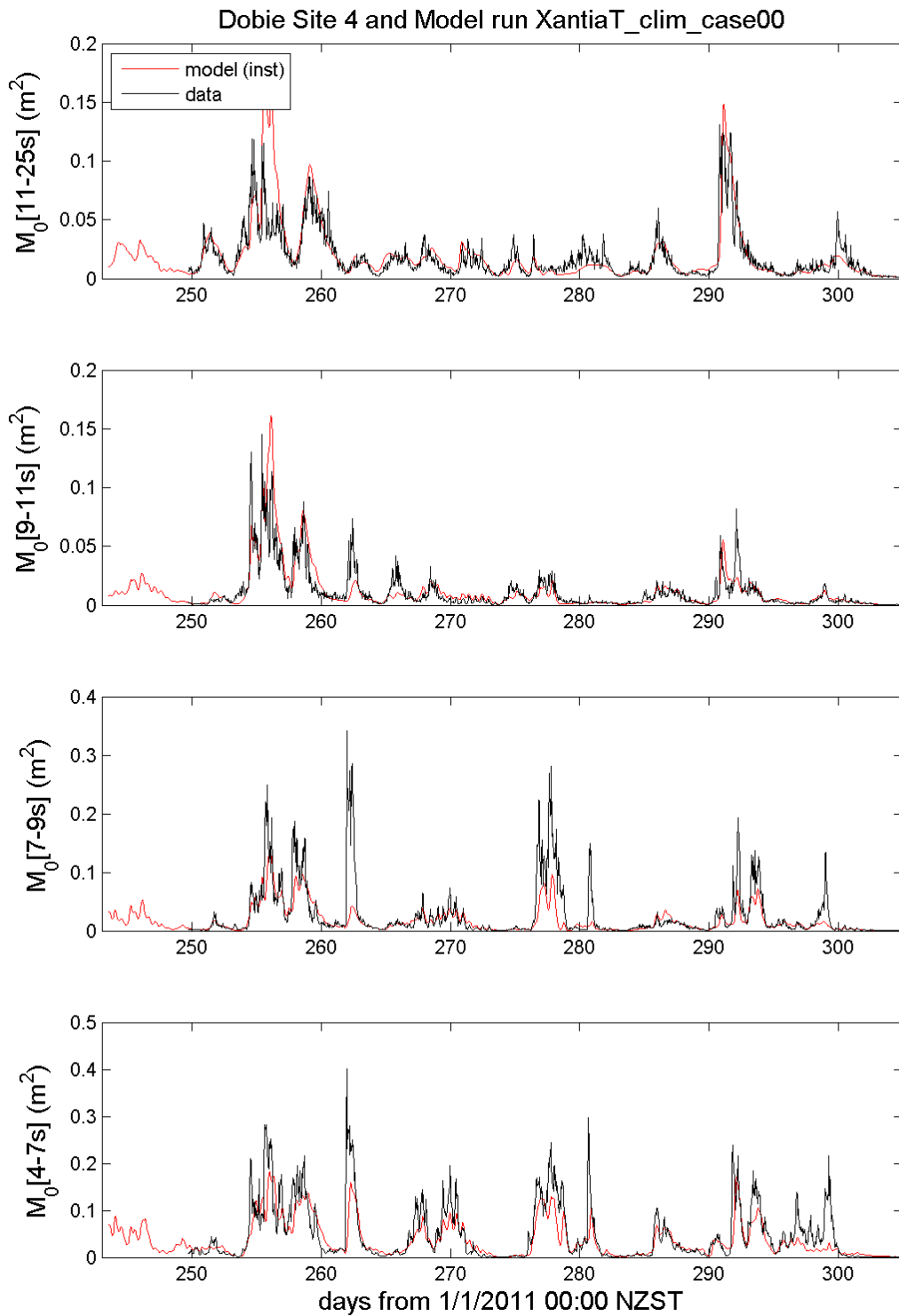


Figure C-22: Comparison of surface sea level variance within selected frequency bands at Site 4. Values derived from measured (black) and modelled (red) frequency spectra are plotted on a linear scale.

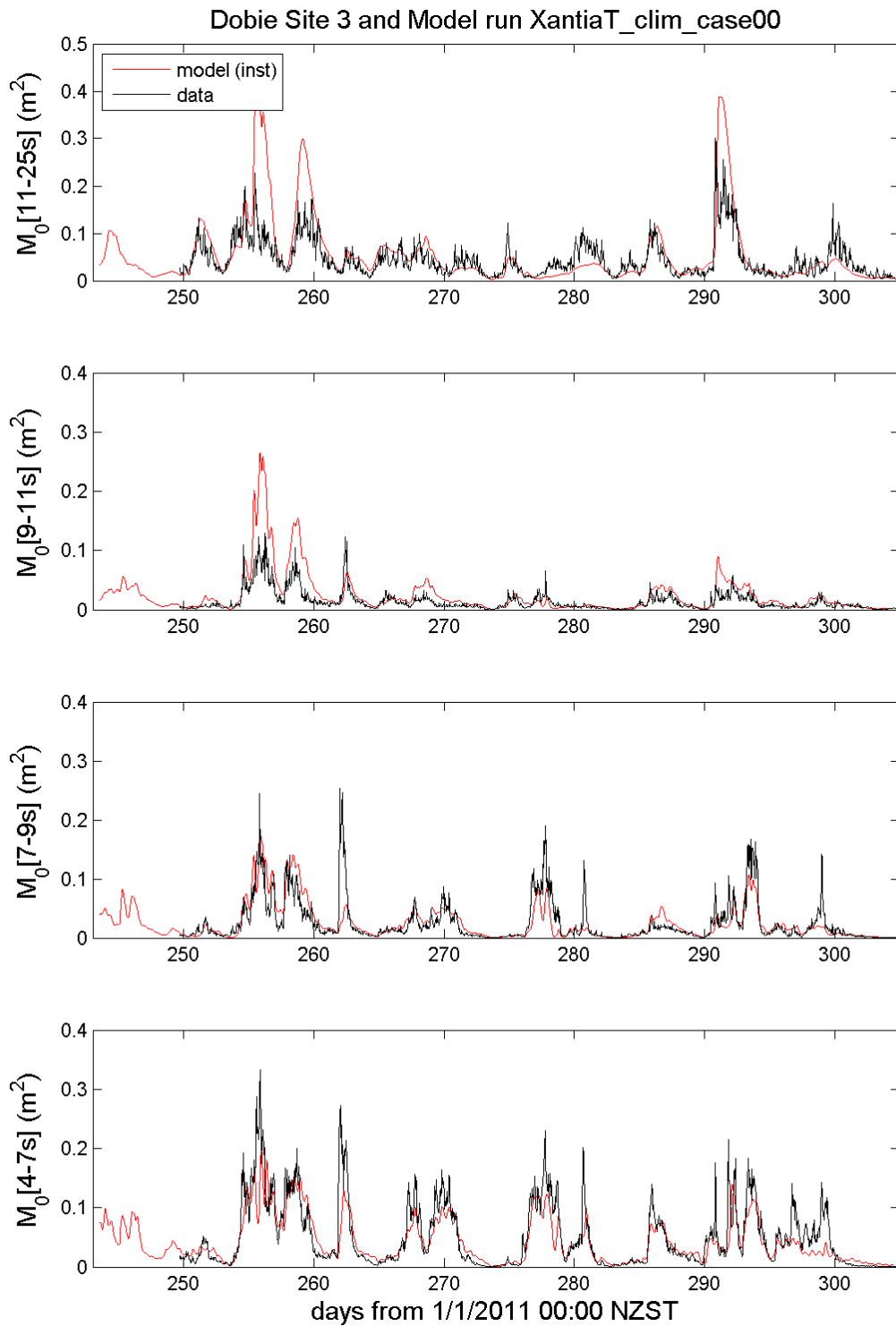


Figure C-23: Comparison of surface sea level variance within selected frequency bands at Site 3. Values derived from measured (black) and modelled (red) frequency spectra are plotted on a linear scale.

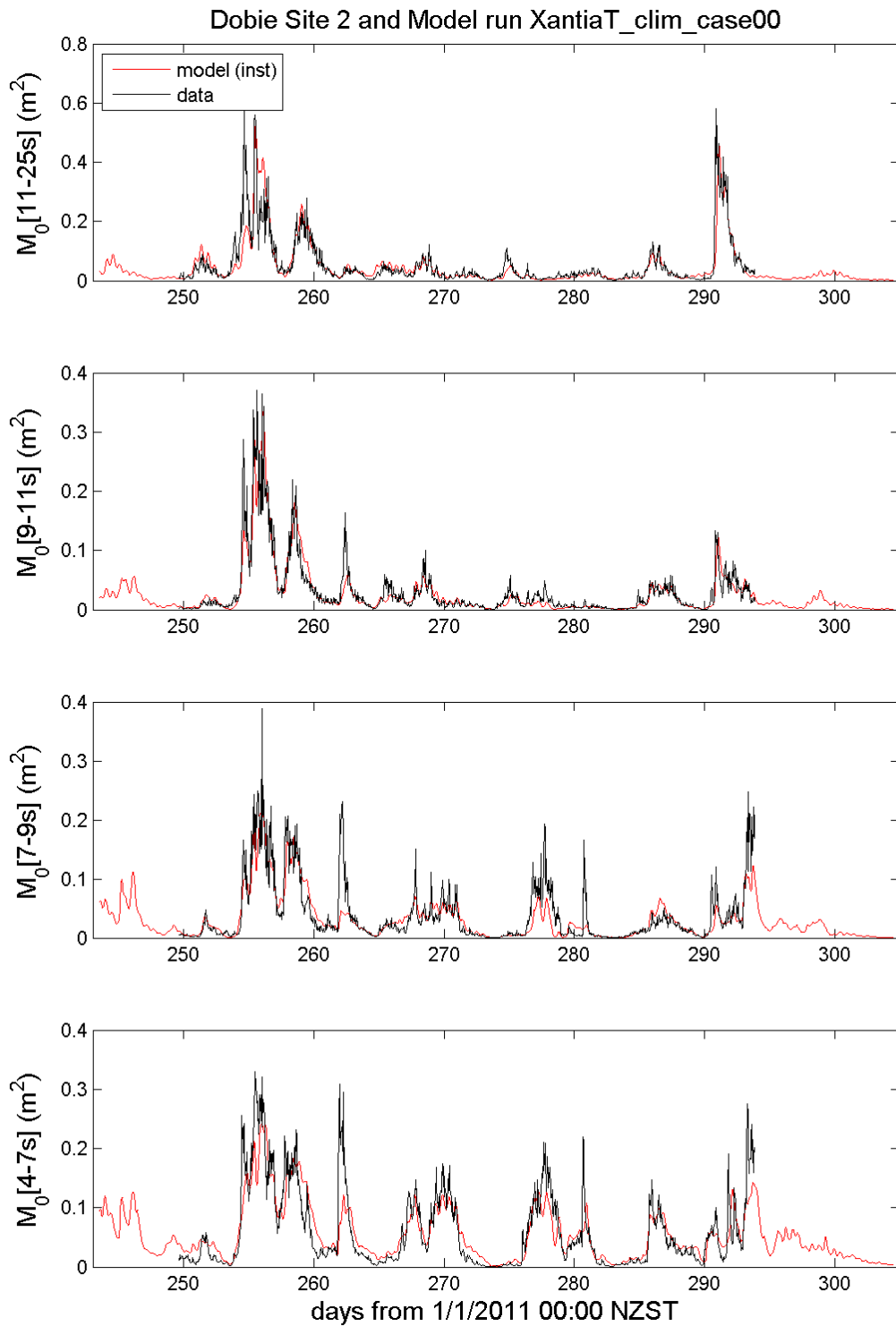


Figure C-24: Comparison of surface sea level variance within selected frequency bands at Site 2. Values derived from measured (black) and modelled (red) frequency spectra are plotted on a linear scale.

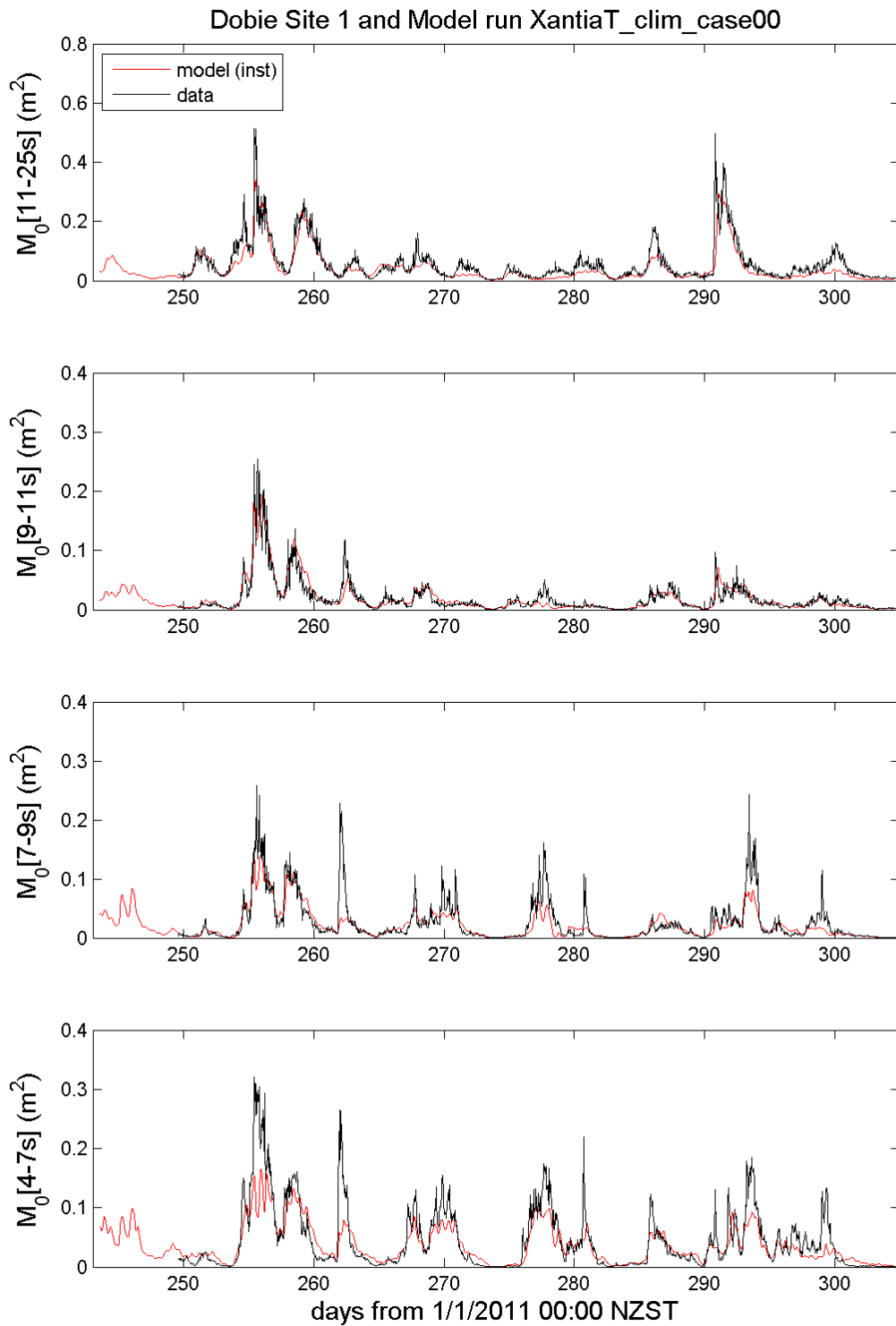


Figure C-25: Comparison of surface sea level variance within selected frequency bands at Site 1. Values derived from measured (black) and modelled (red) frequency spectra are plotted on a linear scale.

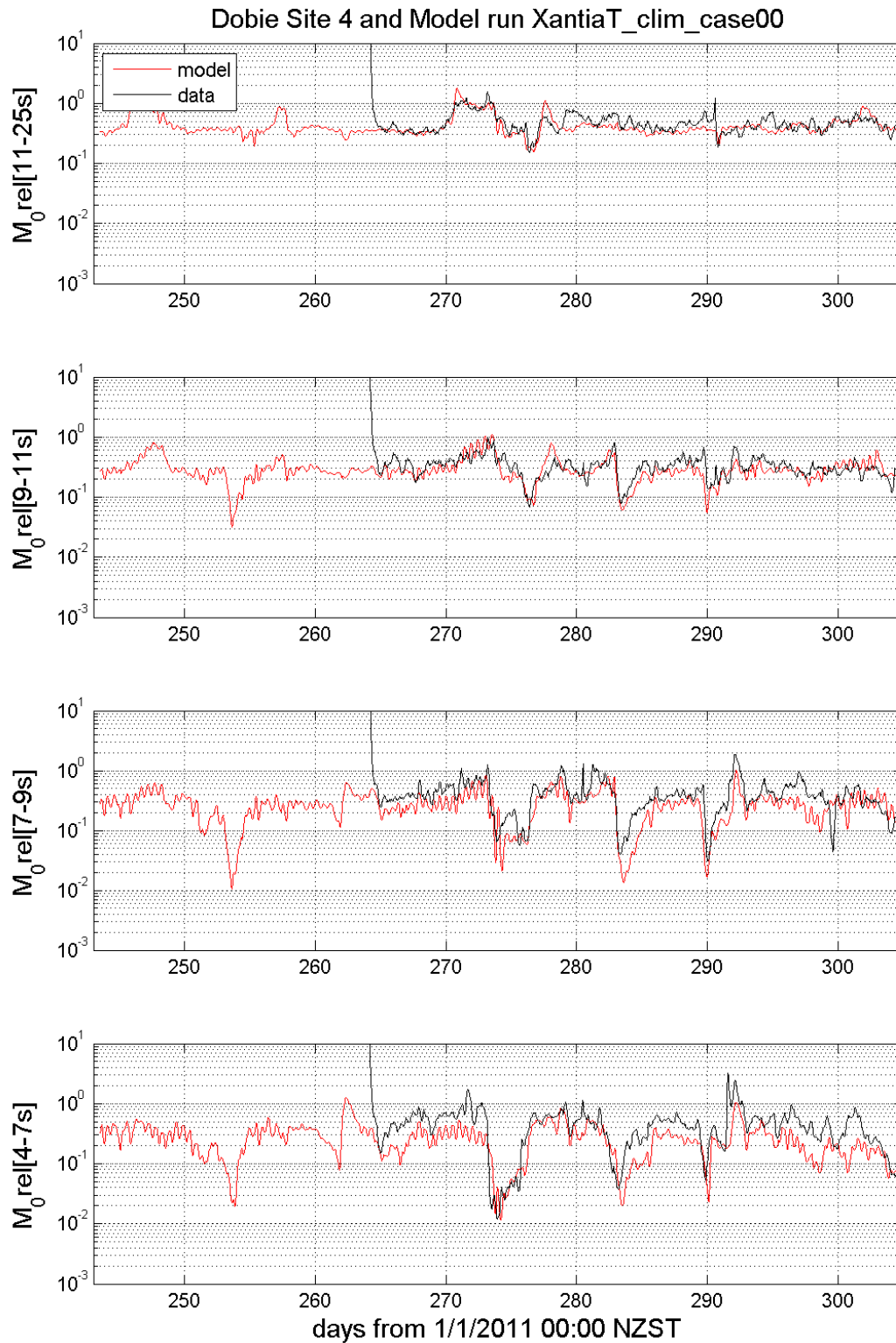


Figure C-26: Comparison of surface sea level variance within selected frequency bands at Site 4 normalised by the corresponding values at Site 8. Measured (black) and modelled (red) values are plotted on a log scale.

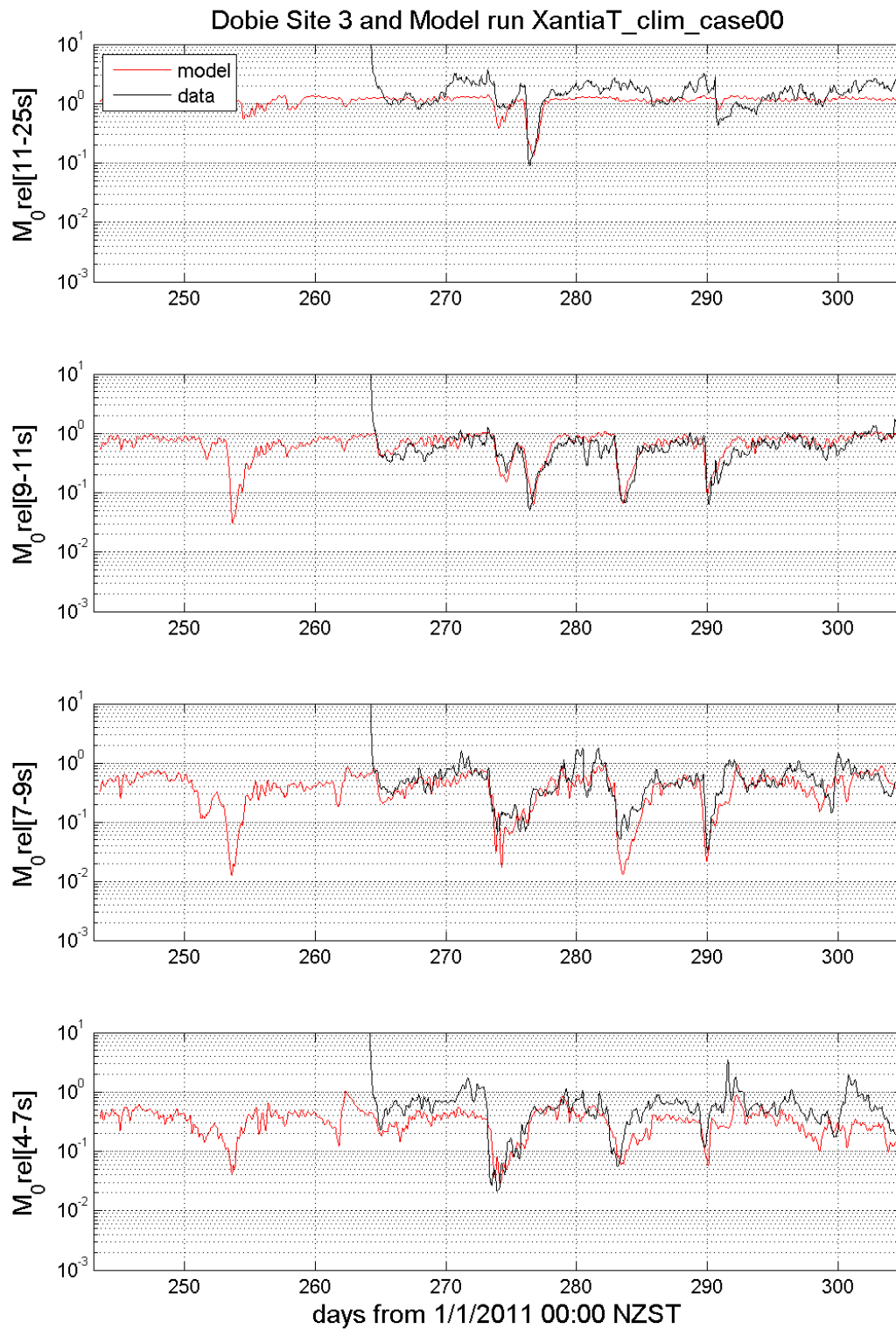


Figure C-27: Comparison of surface sea level variance within selected frequency bands at Site 3 normalised by the corresponding values at Site 8. Measured (black) and modelled (red) values are plotted on a log scale.

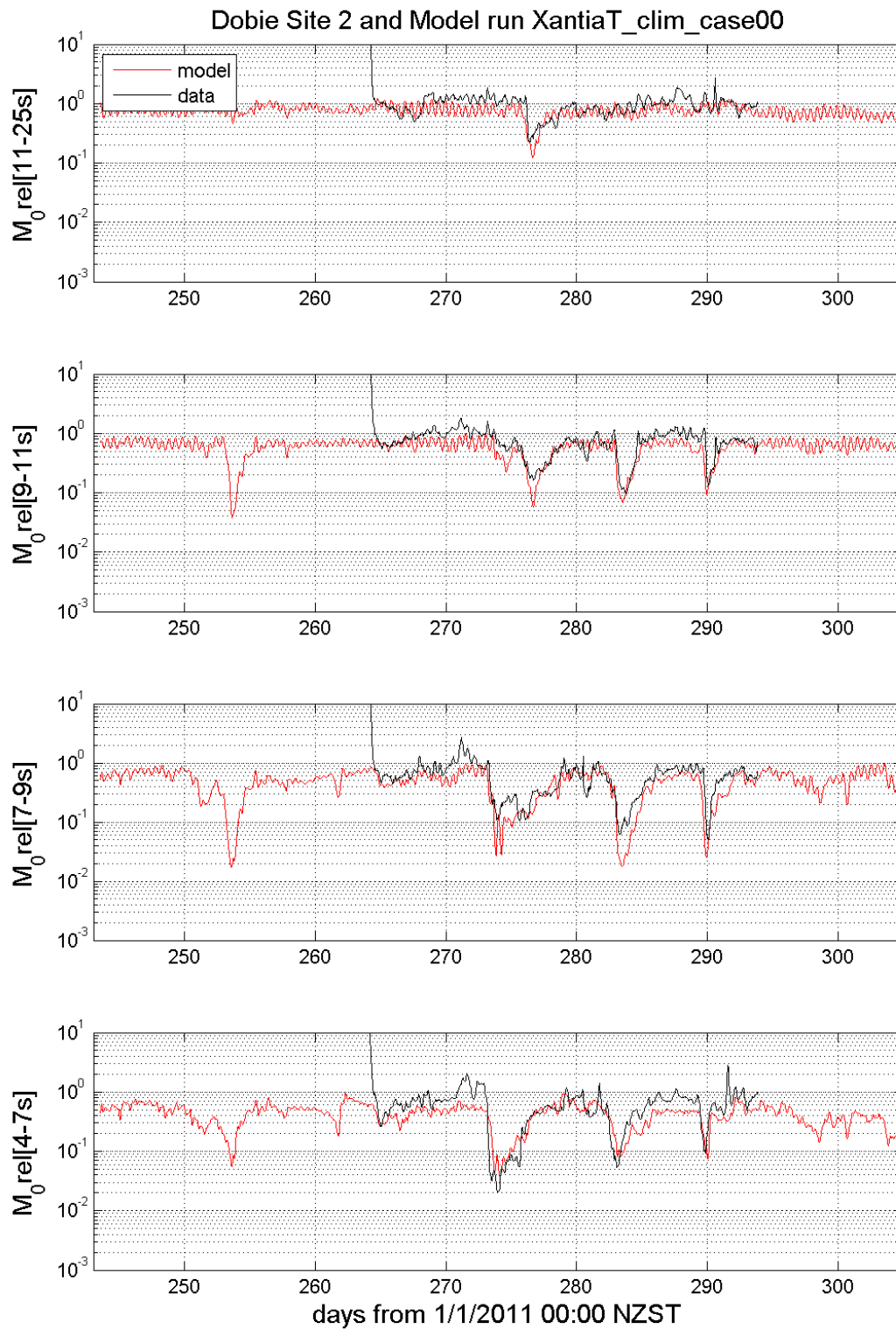


Figure C-28: Comparison of surface sea level variance within selected frequency bands at Site 2 normalised by the corresponding values at Site 8. Measured (black) and modelled (red) values are plotted on a log scale.

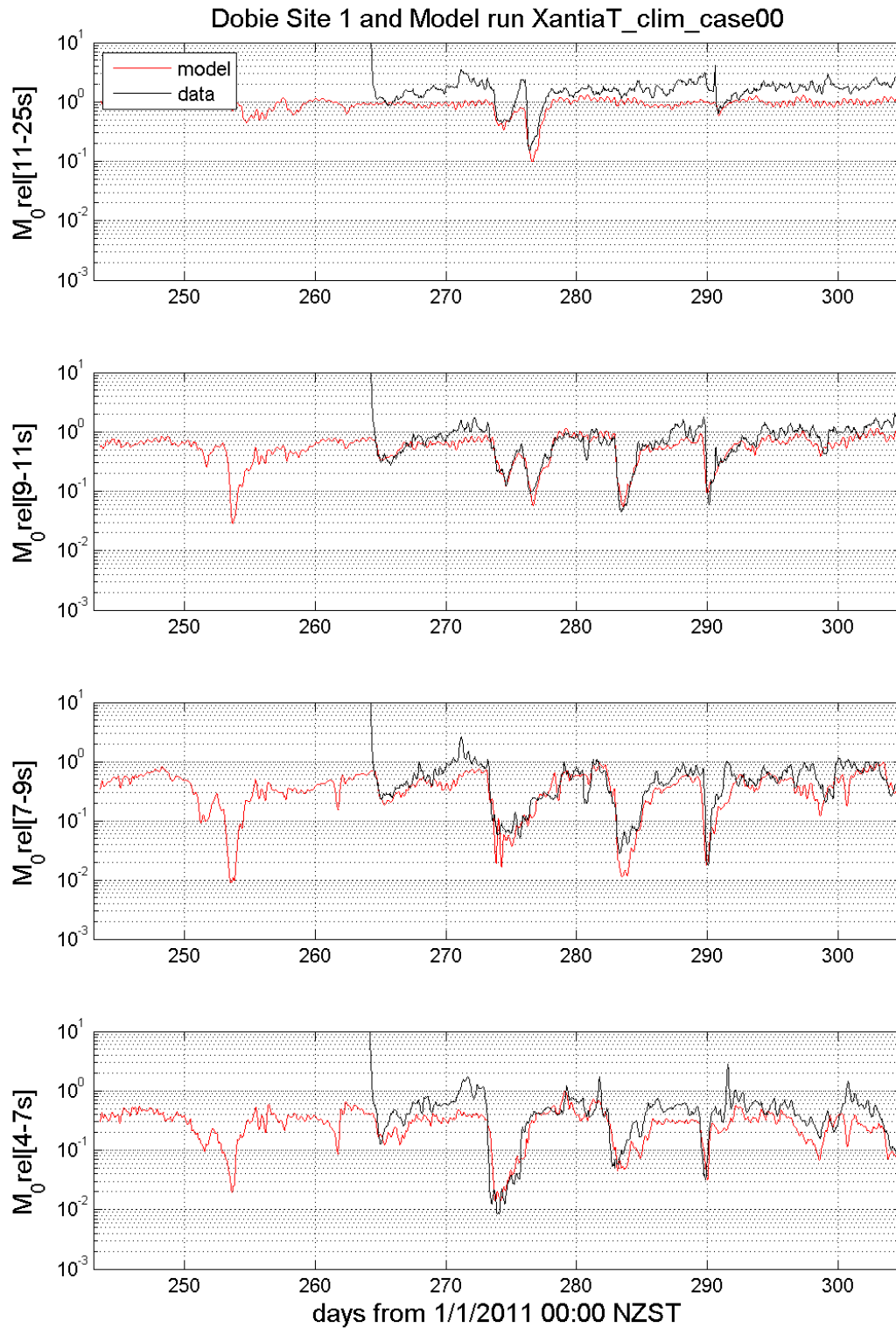


Figure C-29: Comparison of surface sea level variance within selected frequency bands at Site 1 normalised by the corresponding values at Site 8. Measured (black) and modelled (red) values are plotted on a log scale.

Appendix D Sensitivity to bathymetry modifications - Phase 4 full results

In this Section we present the complete results of each scenario-based simulation carried out in the Phase 4 sensitivity study. Firstly, Figure D-1 to Figure D-6 show the spatial distribution of significant wave height and mean wave direction in baseline simulations, with existing bathymetry, for each of the six environmental scenarios. Figure D-7 then shows the variation of significant wave height, mean wave direction, mean wave period and root-mean-square bed orbital velocity along the 10 m isobath for the same baseline simulations.

The remaining plots (Figure D-8 onwards) show the differences (modified – baseline) between each simulation with modified bathymetry and the corresponding baseline run. Even numbered plots show differences in significant wave height over the entire model domain, with red colours indicating increased wave height for the modified bathymetry, while blue colours indicate decreases. The odd numbered plots show corresponding differences in significant wave height, mean wave direction, mean wave period and root-mean-square bed orbital velocity along the 10 m isobath, with all environmental scenarios overlaid.

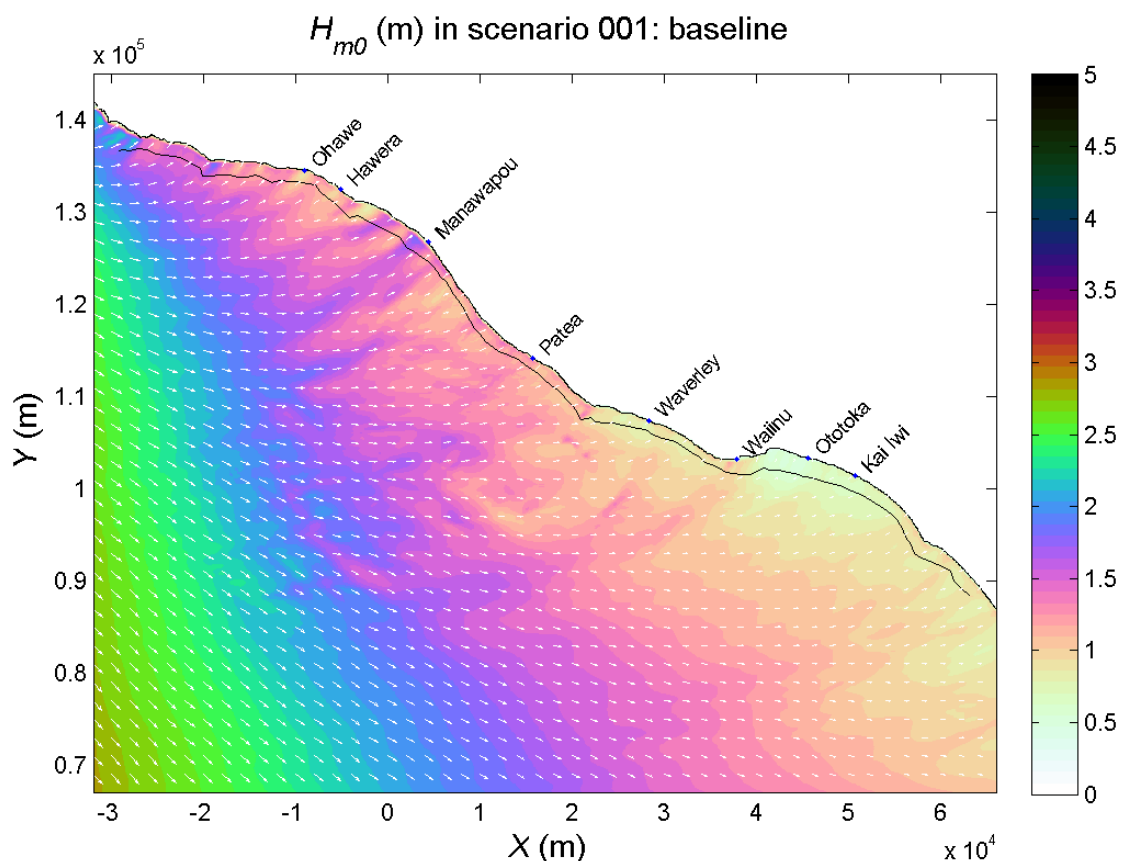


Figure D-1: Wave conditions in environmental scenario 1 of the Phase 4 simulations, with existing bathymetry. Significant wave height is shown by the colour scale, and mean wave direction by arrows.

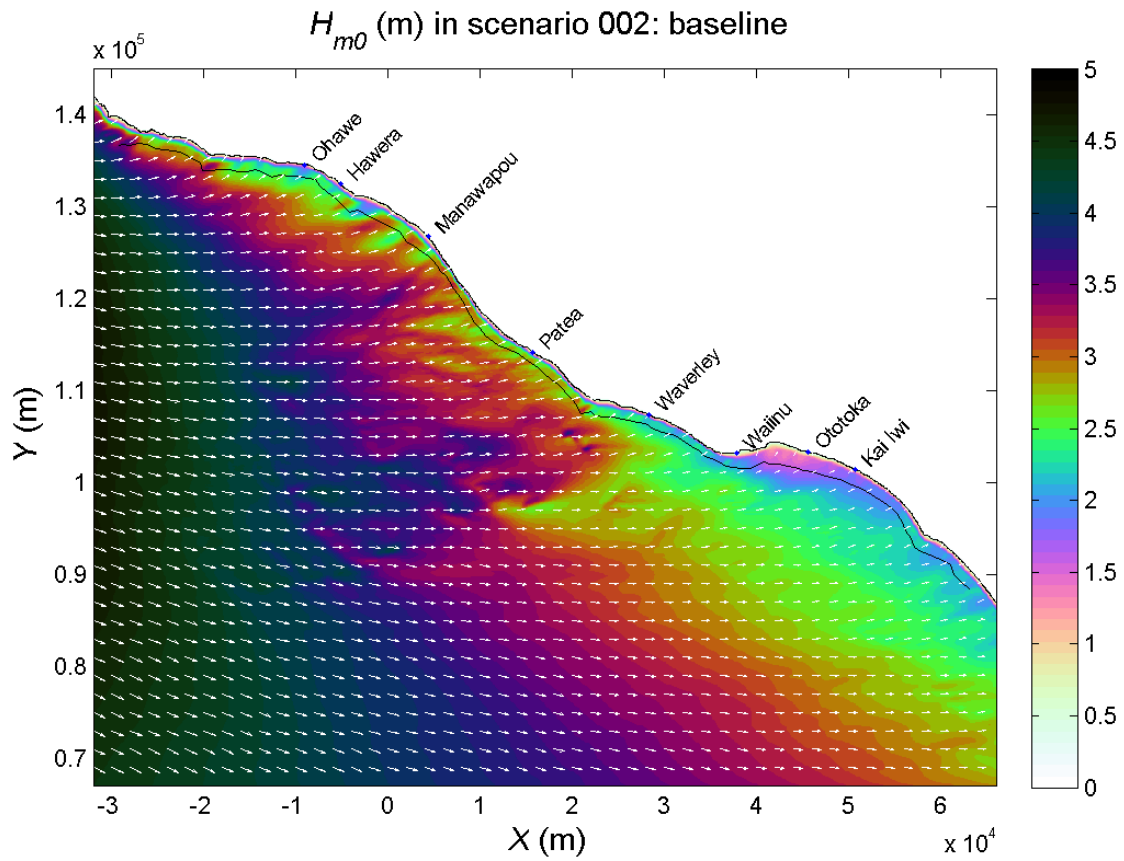


Figure D-2: Wave conditions in environmental scenario 2 of the Phase 4 simulations, with existing bathymetry. Significant wave height is shown by the colour scale, and mean wave direction by arrows.

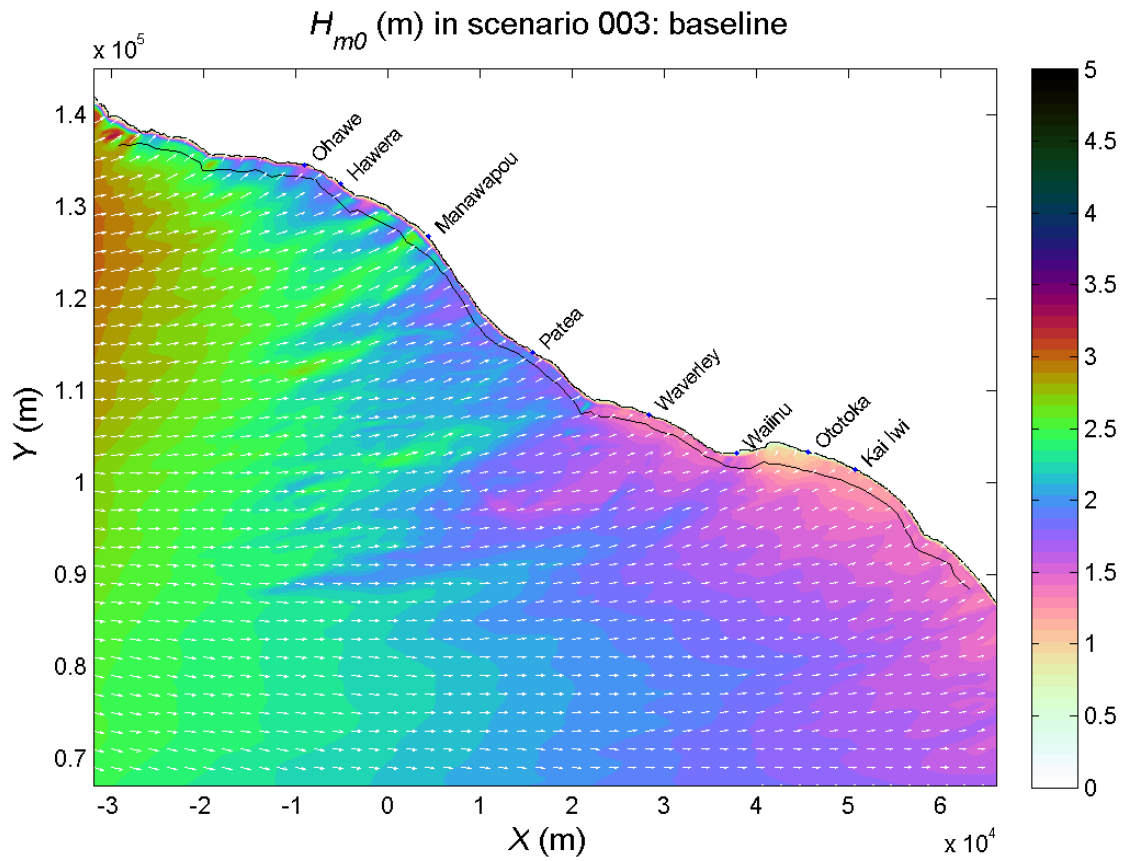


Figure D-3: Wave conditions in environmental scenario 3 of the Phase 4 simulations, with existing bathymetry. Significant wave height is shown by the colour scale, and mean wave direction by arrows.

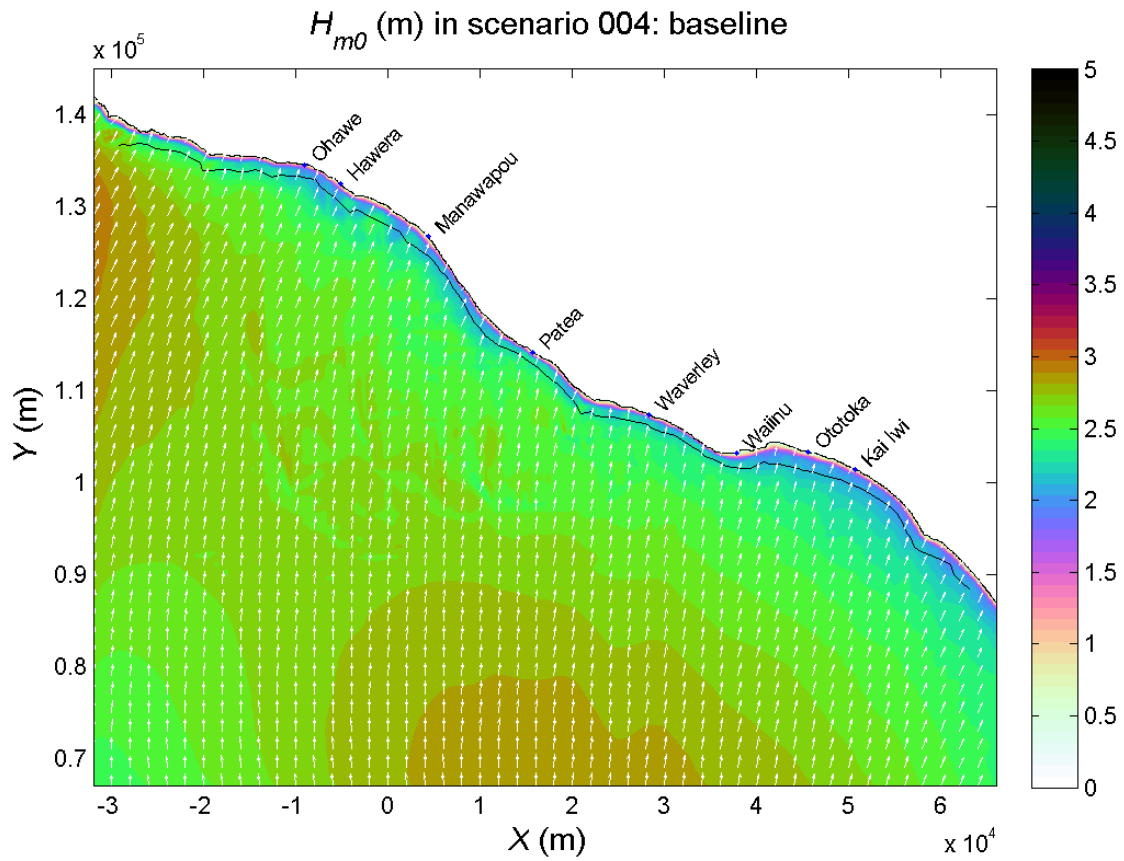


Figure D-4: Wave conditions in environmental scenario 4 of the Phase 4 simulations, with existing bathymetry. Significant wave height is shown by the colour scale, and mean wave direction by arrows.

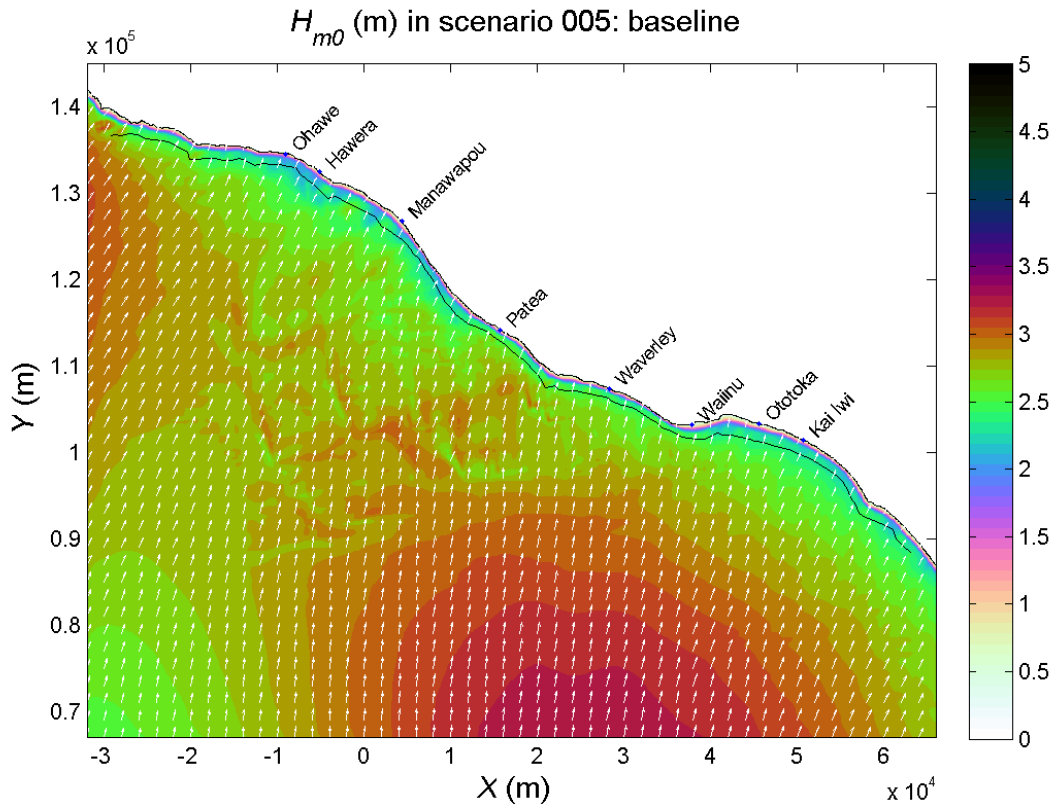


Figure D-5: Wave conditions in environmental scenario 5 of the Phase 4 simulations, with existing bathymetry. Significant wave height is shown by the colour scale, and mean wave direction by arrows.

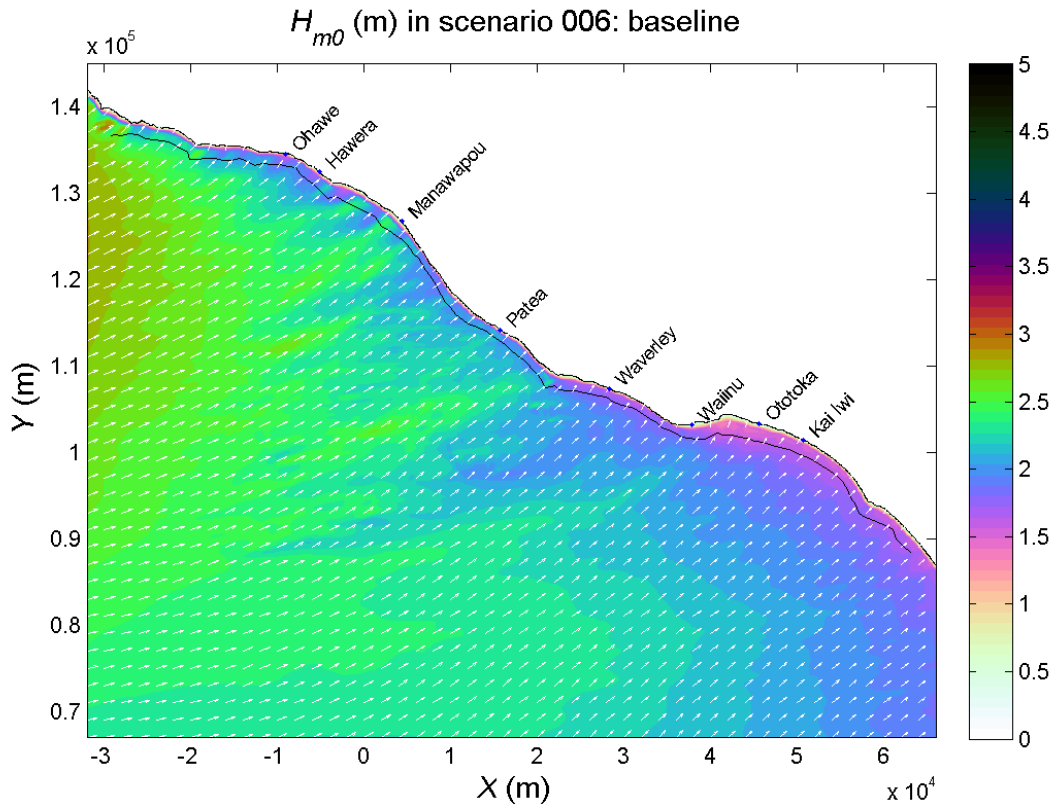


Figure D-6: Wave conditions in environmental scenario 6 of the Phase 4 simulations, with existing bathymetry. Significant wave height is shown by the colour scale, and mean wave direction by arrows.

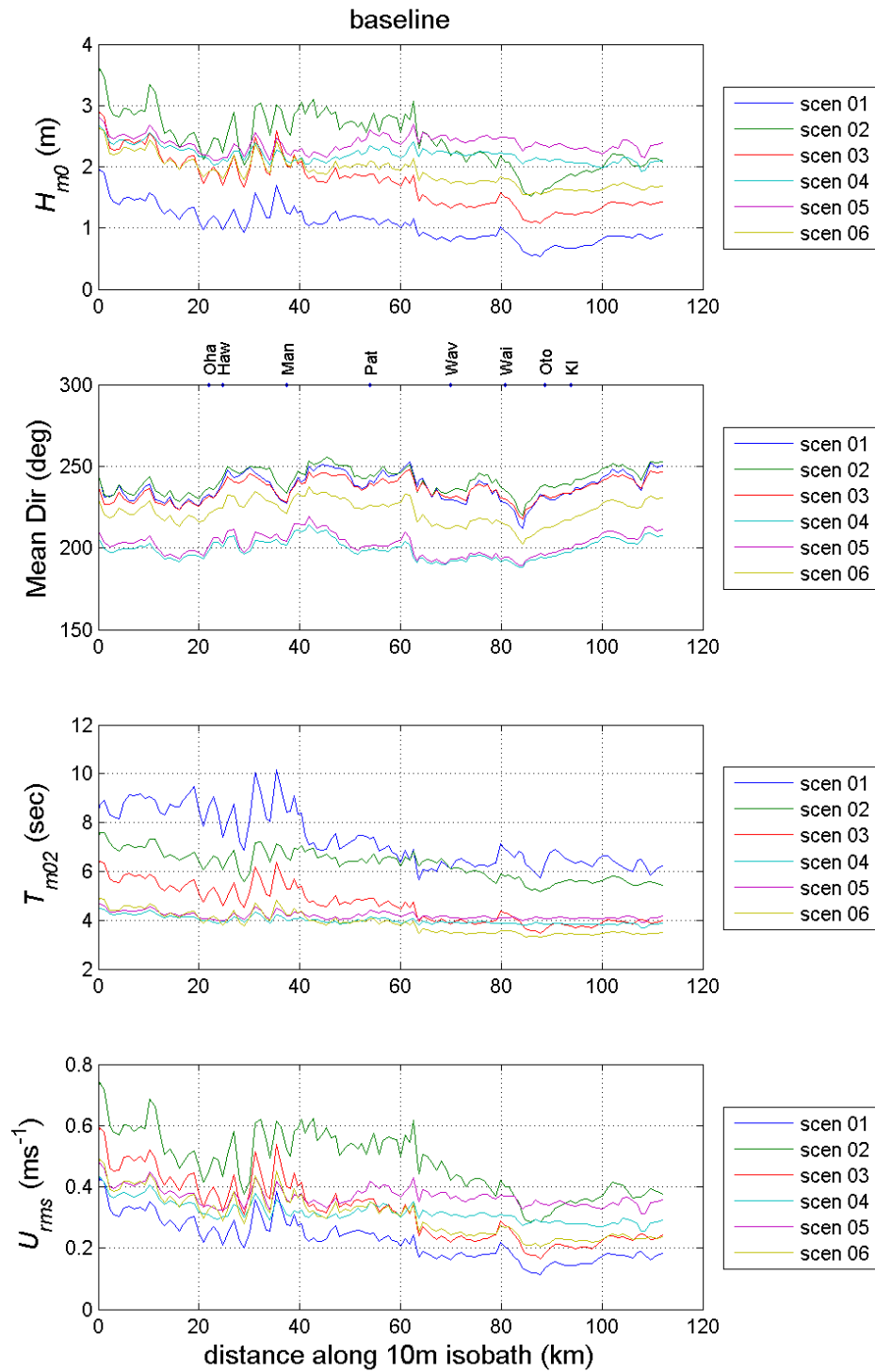


Figure D-7: Wave parameters at the 10 m isobath with existing bathymetry, in all 6 environmental scenarios. From top to bottom: significant wave height, mean wave direction, mean wave period, and root-mean-square bed orbital velocity.

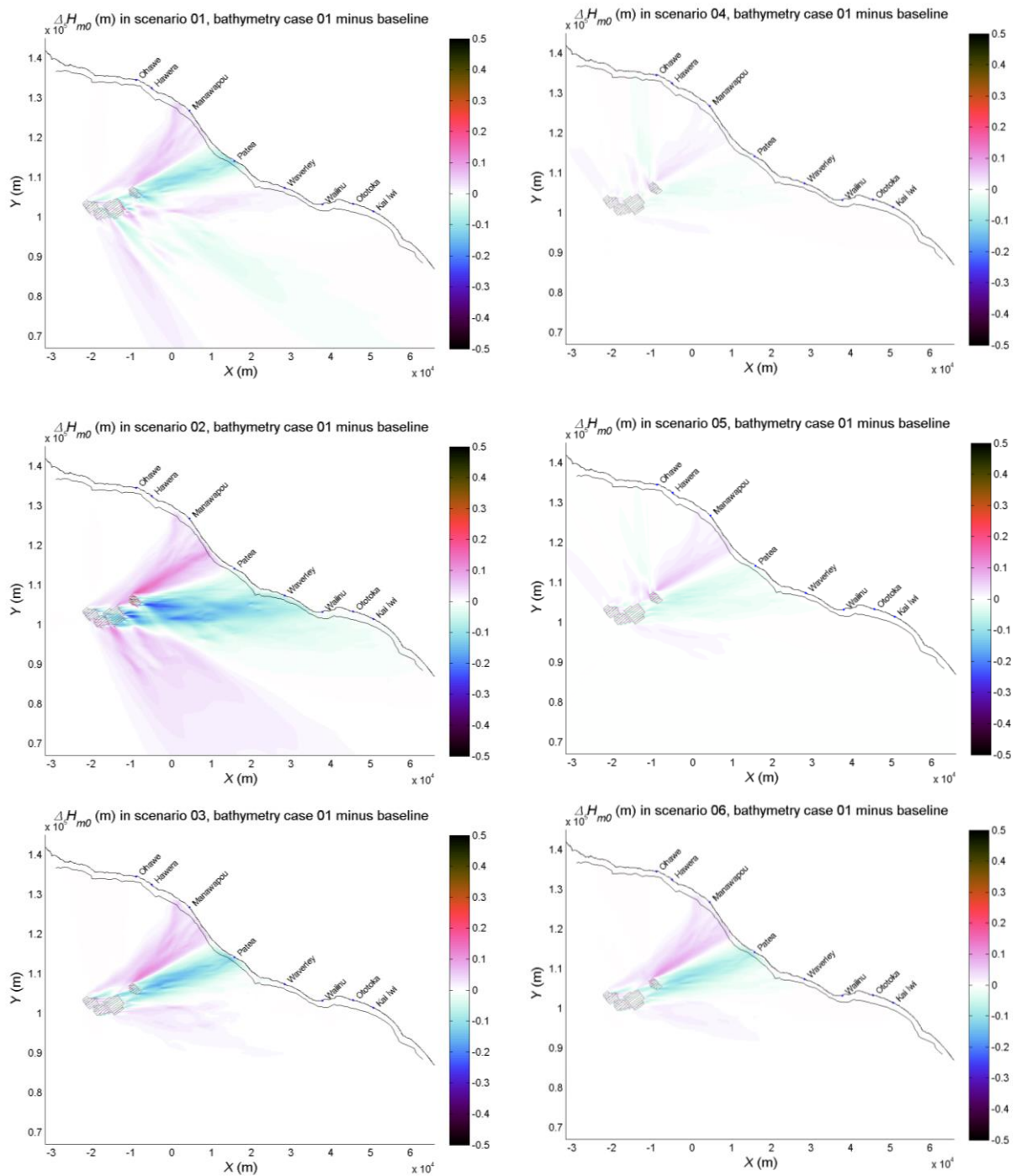


Figure D-8: Difference between significant wave height for case 1 and existing bathymetry, over the model domain, for each of the six environmental scenarios. The locations of the pit and mound used in the simulations are marked in red.

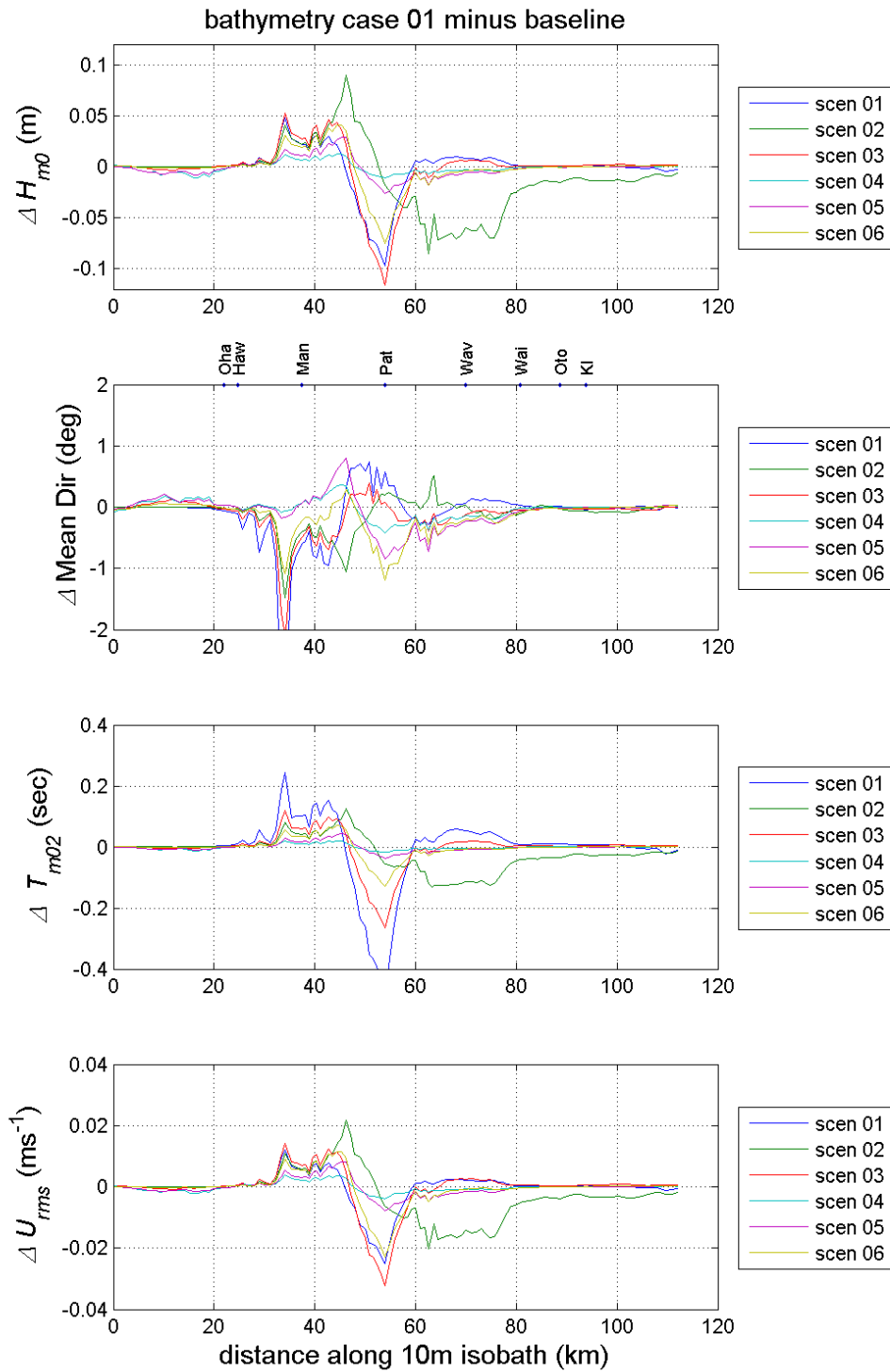


Figure D-9: Difference between wave parameters at the 10 m isobath for case 1 and existing bathymetry, in all 6 environmental scenarios. From top to bottom: significant wave height, mean wave direction, mean wave period, and root-mean-square bed orbital velocity.

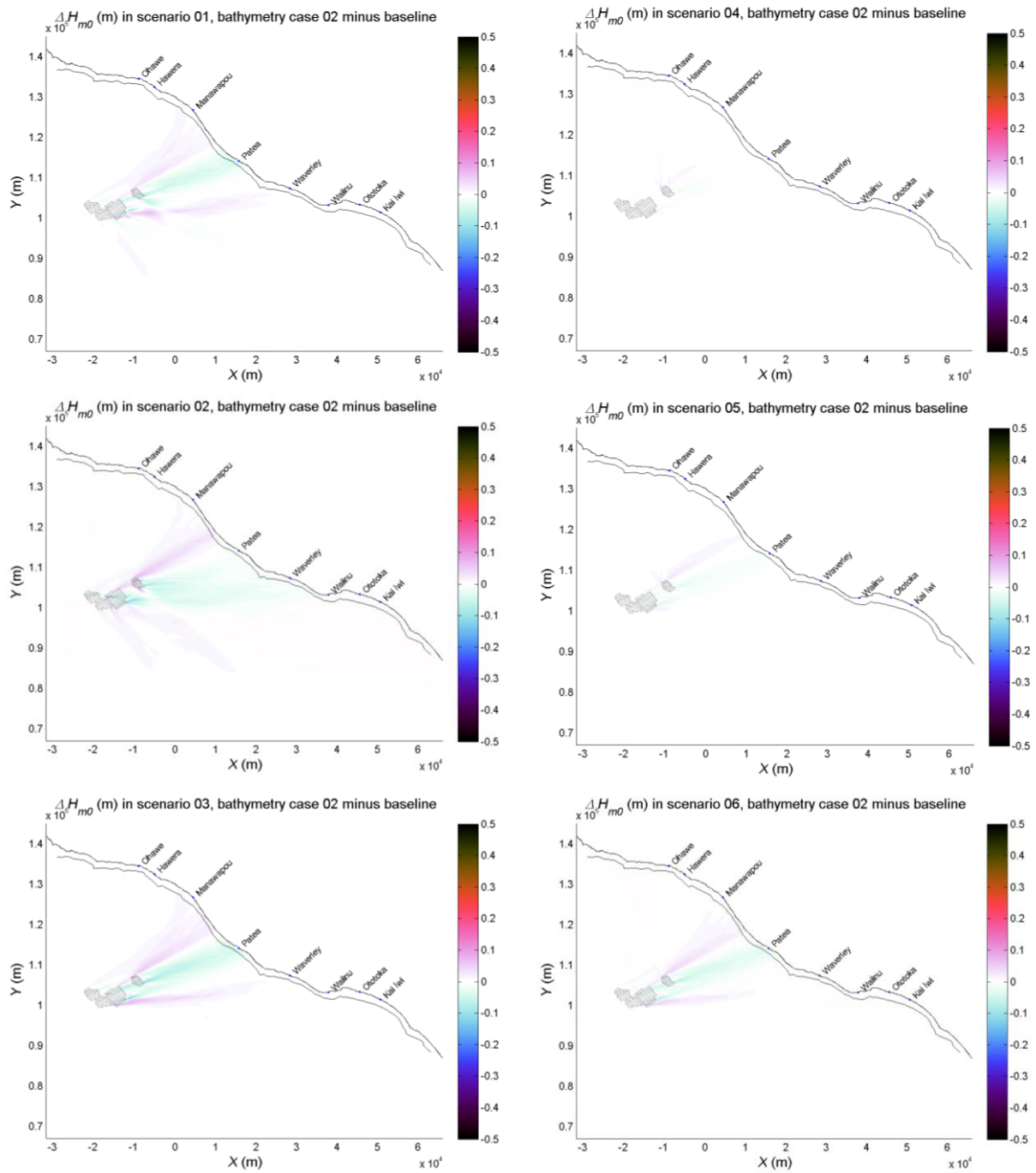


Figure D-10: Difference between significant wave height for case 2 and existing bathymetry, over the model domain, for each of the six environmental scenarios. The locations of the pit and mound used in the simulations are marked in red.

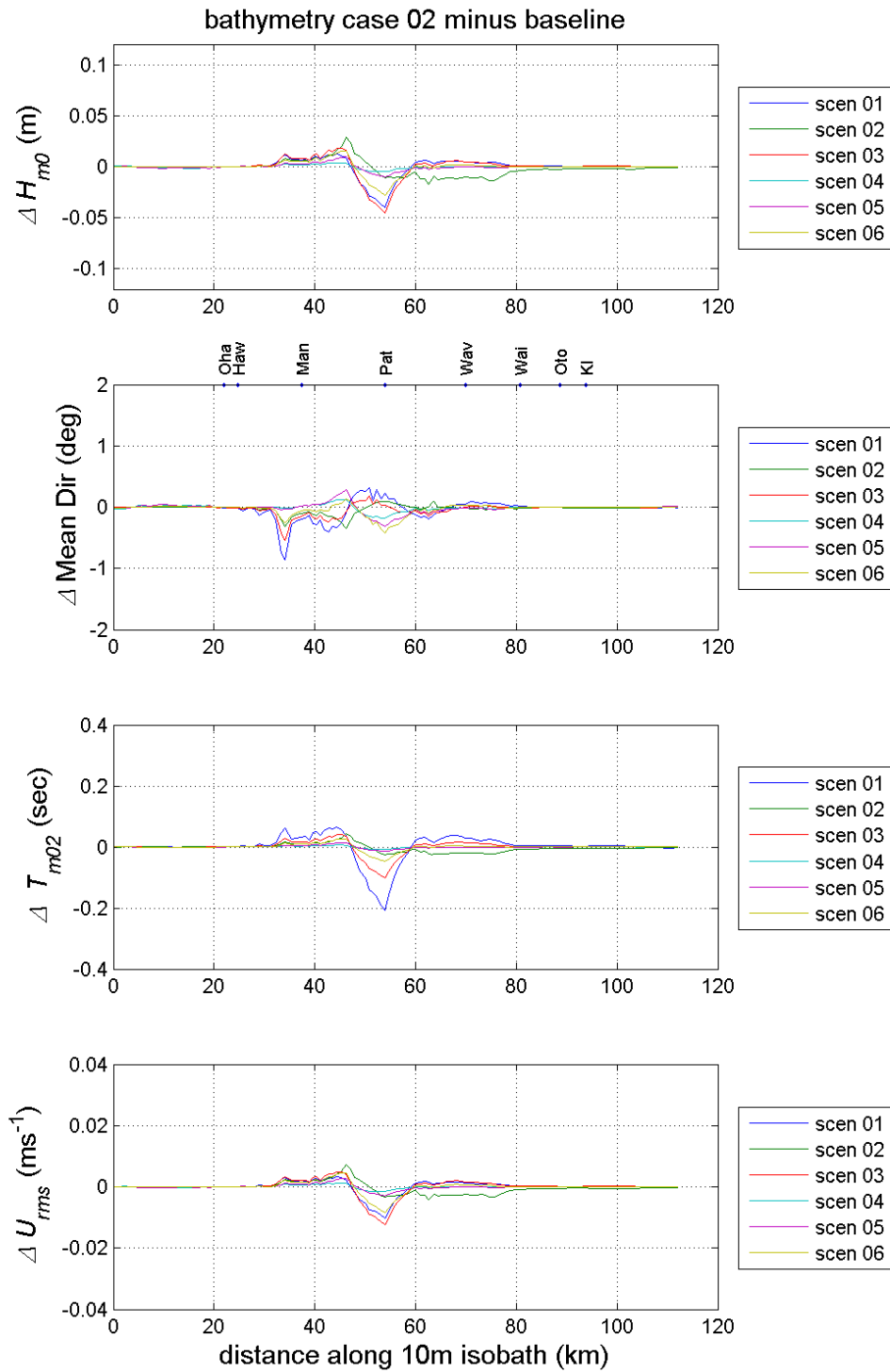


Figure D-11: Difference between wave parameters at the 10 m isobath for case 2 and existing bathymetry, in all 6 environmental scenarios. From top to bottom: significant wave height, mean wave direction, mean wave period, and root-mean-square bed orbital velocity.

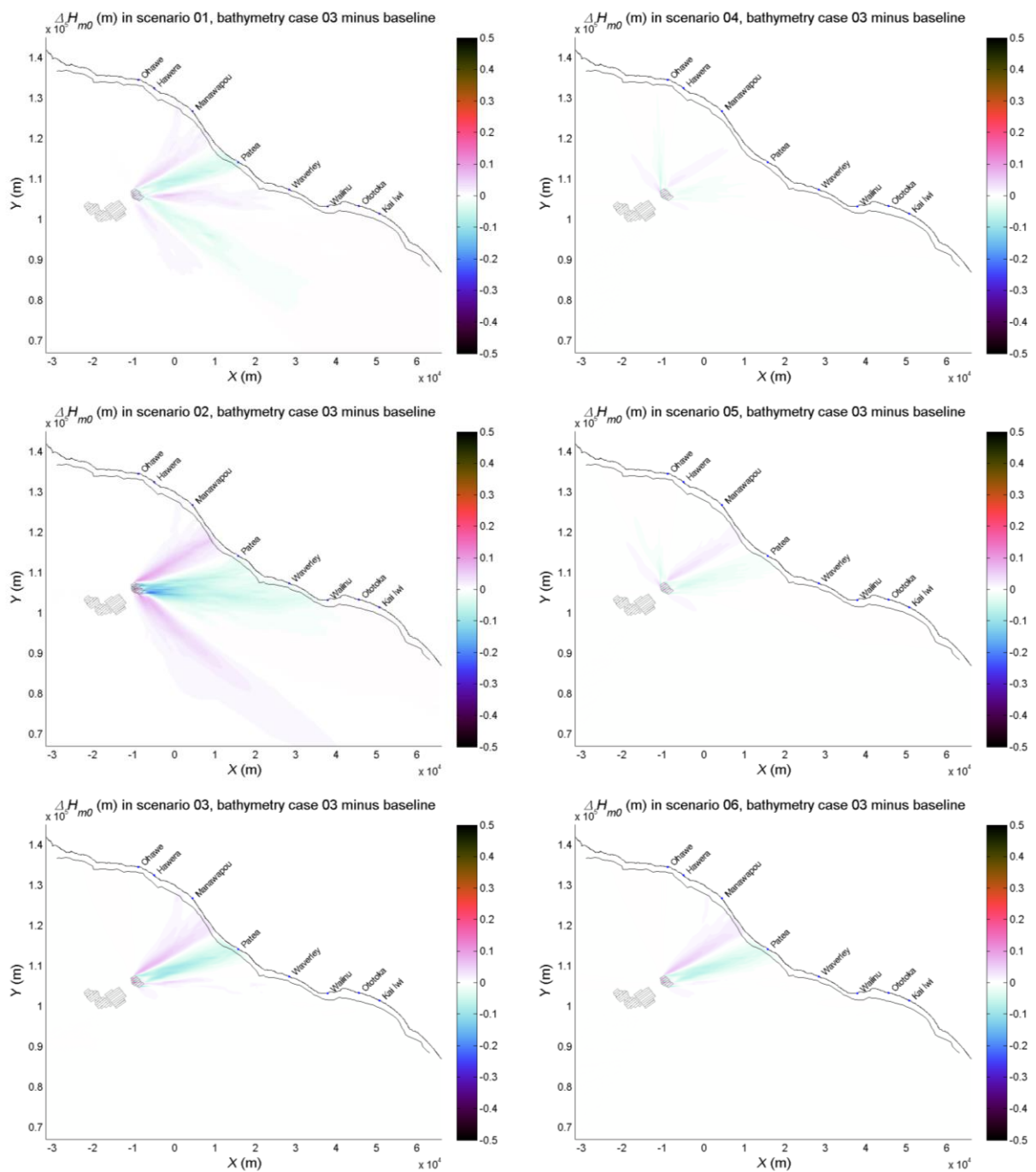


Figure D-12: Difference between significant wave height for case 3 and existing bathymetry, over the model domain, for each of the six environmental scenarios. The locations of the pit and mound used in the simulations are marked in red.

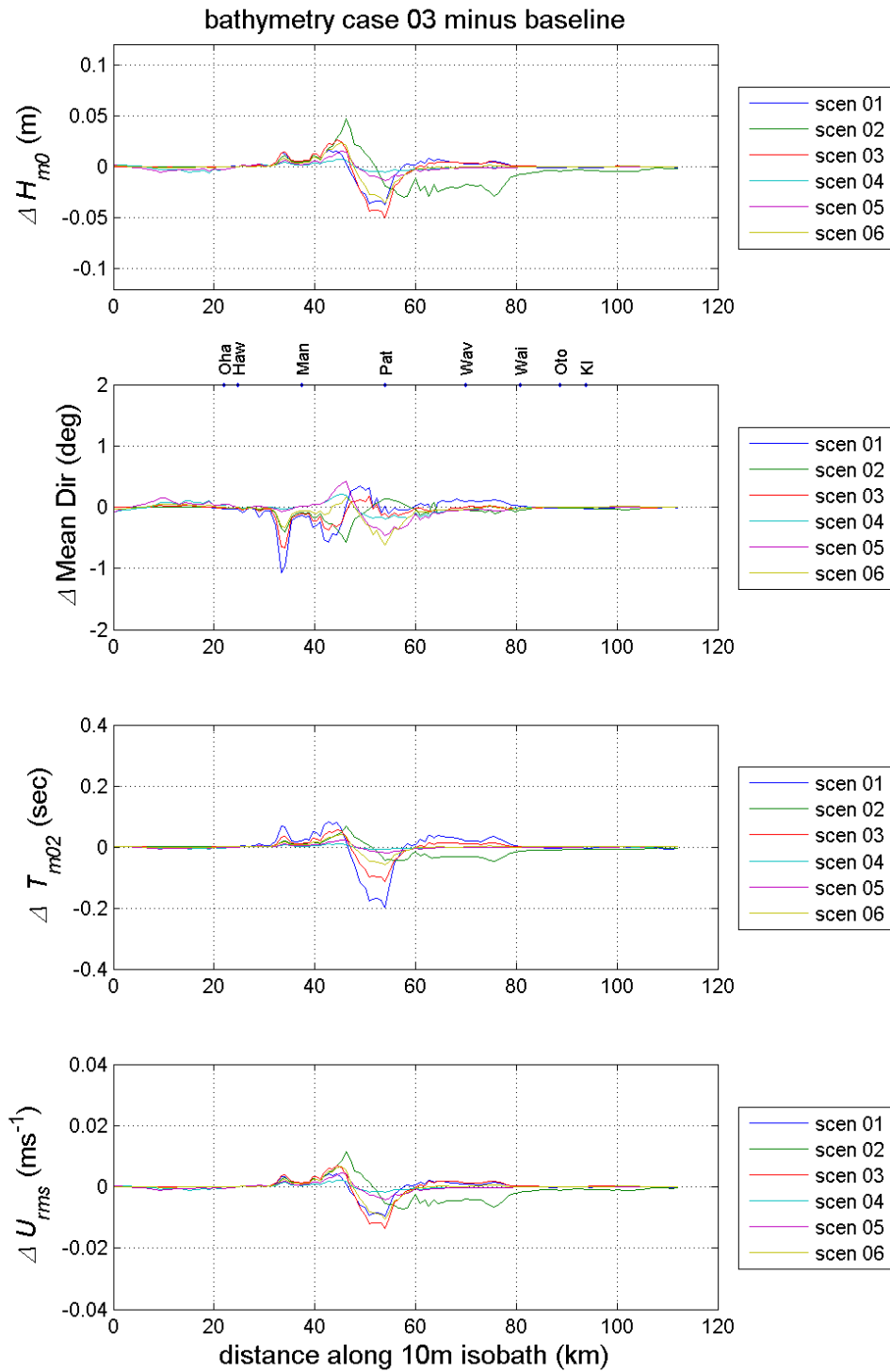


Figure D-13: Difference between wave parameters at the 10 m isobath for case 3 and existing bathymetry, in all 6 environmental scenarios. From top to bottom: significant wave height, mean wave direction, mean wave period, and root-mean-square bed orbital velocity.

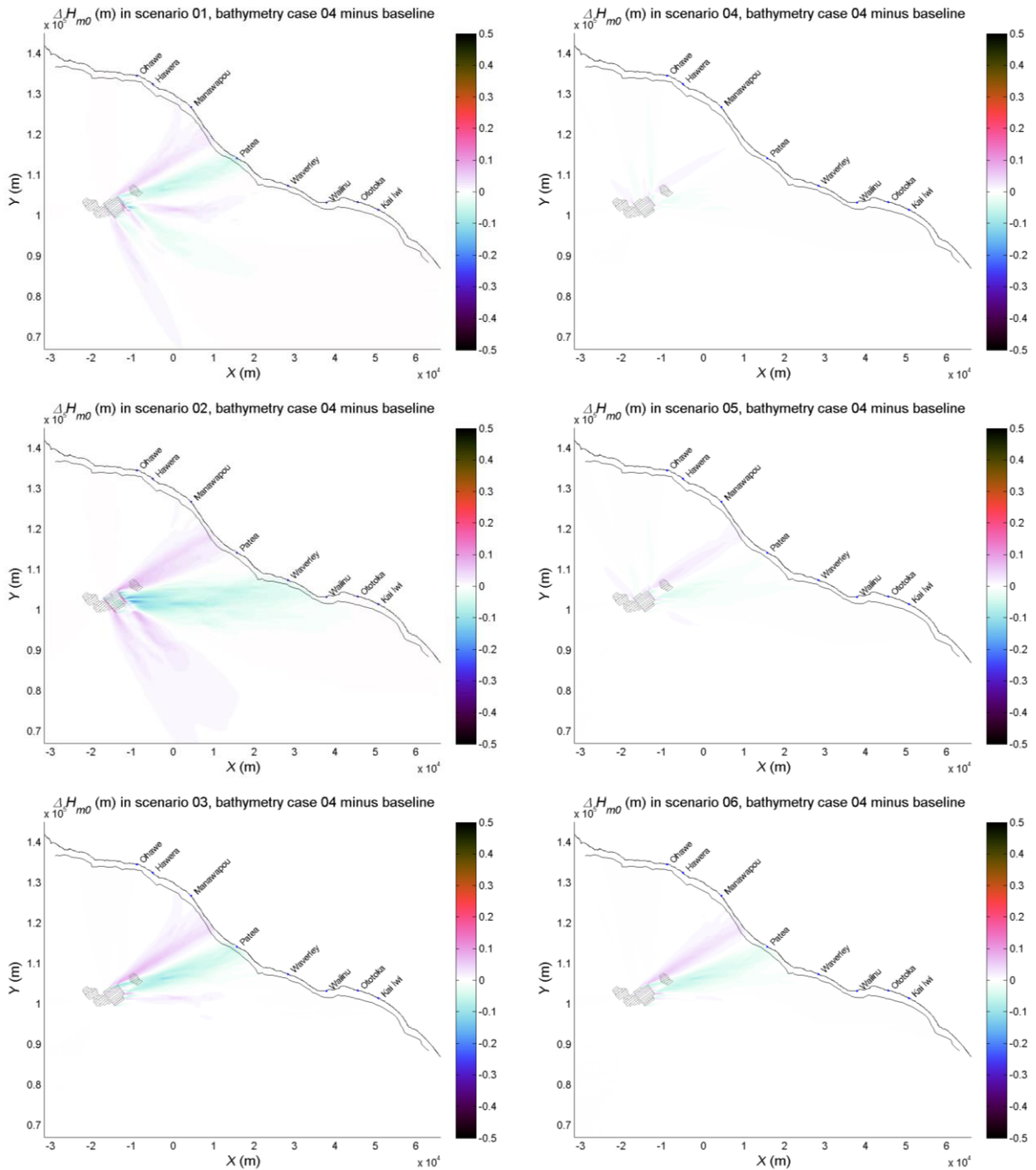


Figure D-14: Difference between significant wave height for case 4 and existing bathymetry, over the model domain, for each of the six environmental scenarios. The locations of the pit and mound used in the simulations are marked in red.

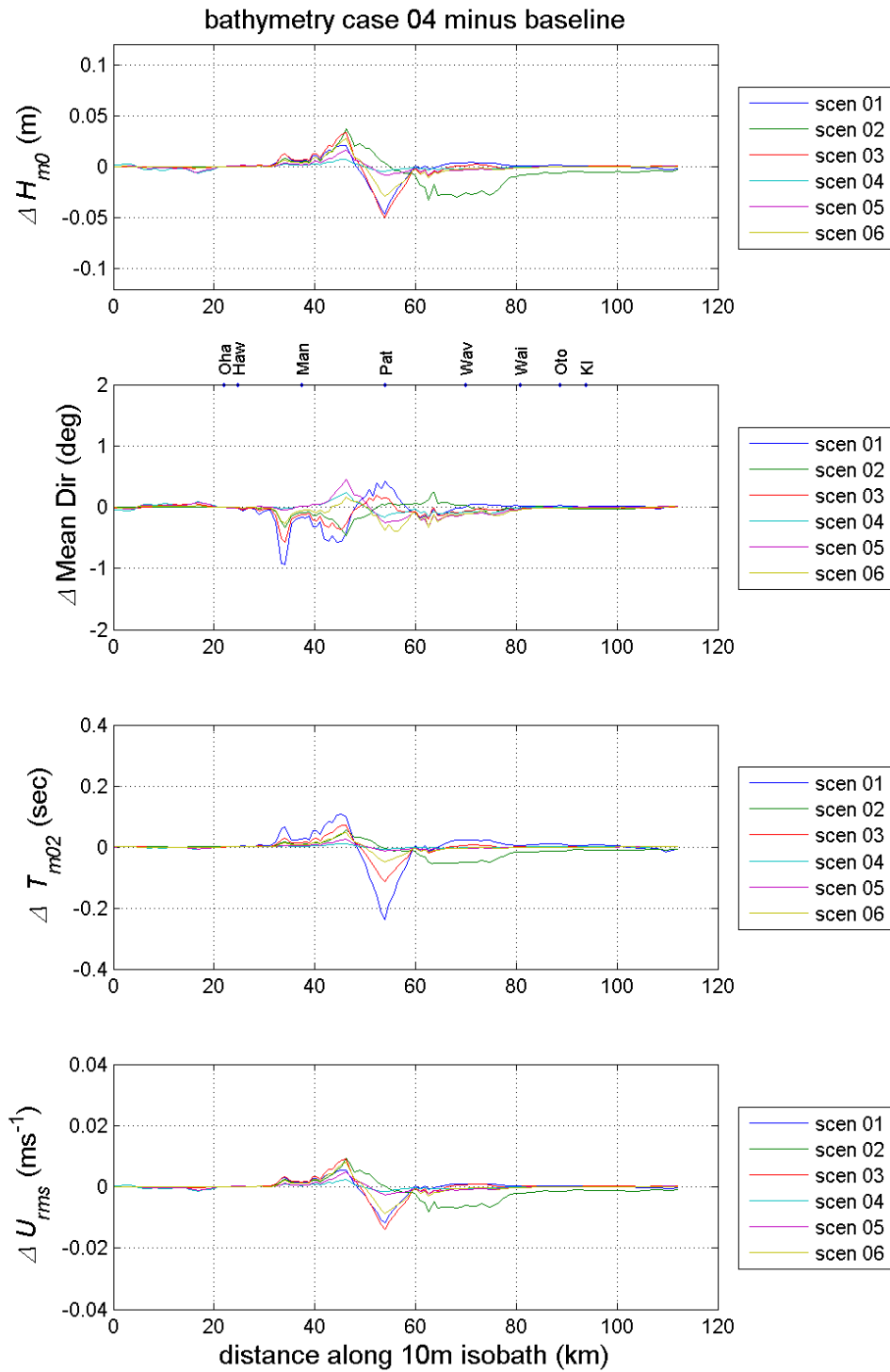


Figure D-15: Difference between wave parameters at the 10 m isobath for case 4 and existing bathymetry, in all 6 environmental scenarios. From top to bottom: significant wave height, mean wave direction, mean wave period, and root-mean-square bed orbital velocity.

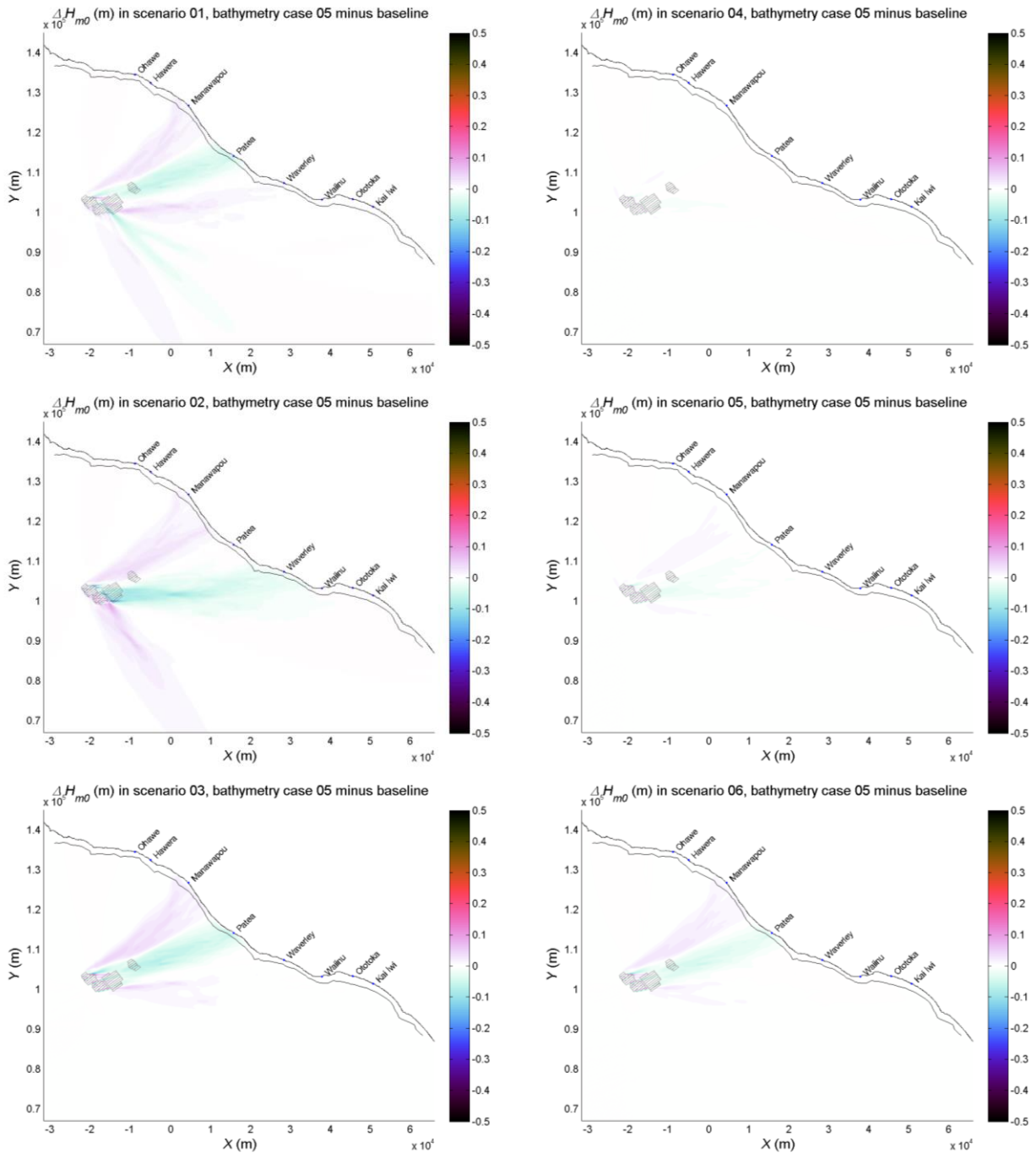


Figure D-16: Difference between significant wave height for case 5 and existing bathymetry, over the model domain, for each of the six environmental scenarios. The locations of the pit and mound used in the simulations are marked in red.

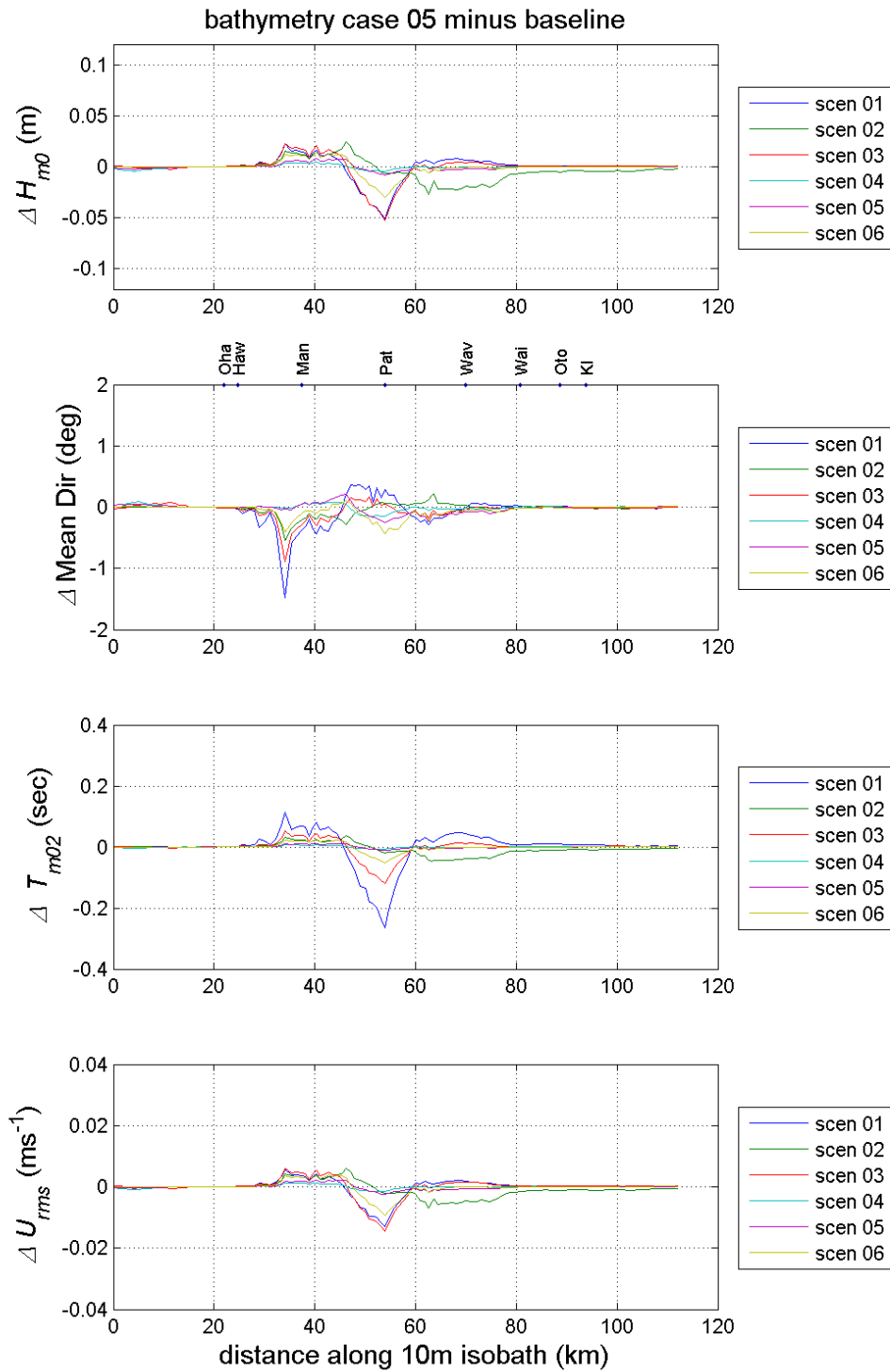


Figure D-17: Difference between wave parameters at the 10 m isobath for case 5 and existing bathymetry, in all 6 environmental scenarios. From top to bottom: significant wave height, mean wave direction, mean wave period, and root-mean-square bed orbital velocity.

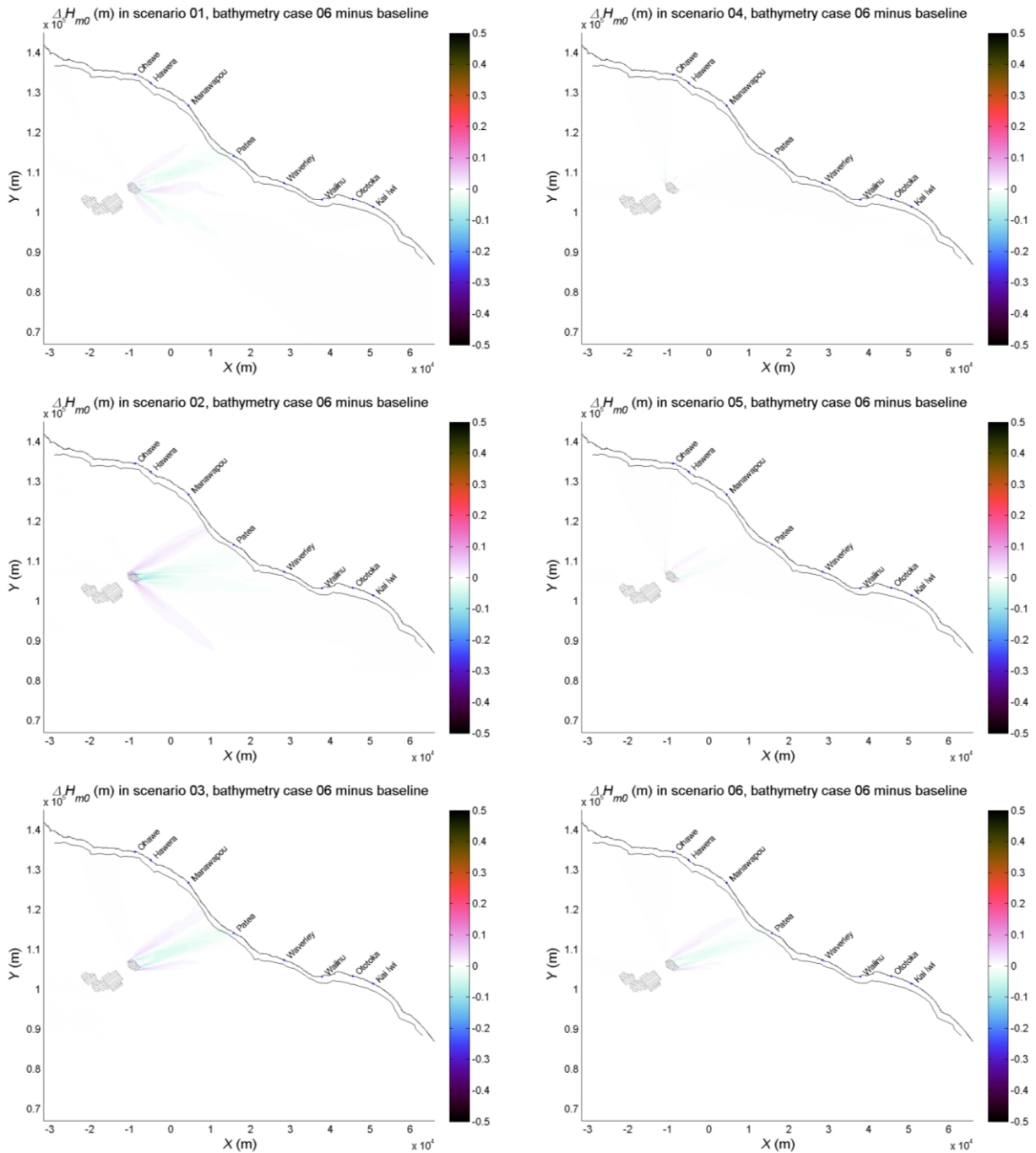


Figure D-18: Difference between significant wave height for case 6 and existing bathymetry, over the model domain, for each of the six environmental scenarios. The locations of the pit and mound used in the simulations are marked in red.

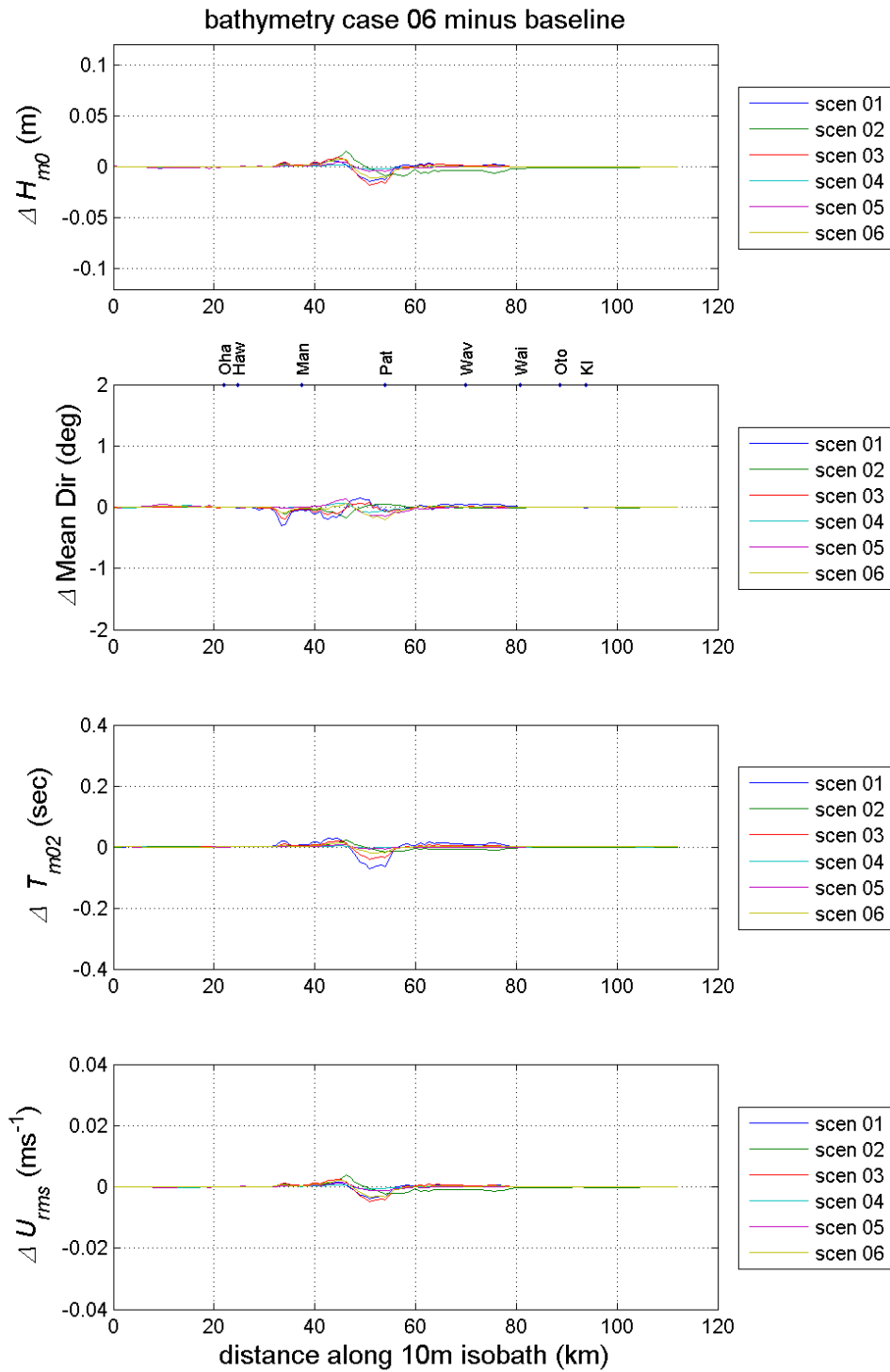


Figure D-19: Difference between wave parameters at the 10 m isobath for case 6 and existing bathymetry, in all 6 environmental scenarios. From top to bottom: significant wave height, mean wave direction, mean wave period, and root-mean-square bed orbital velocity.

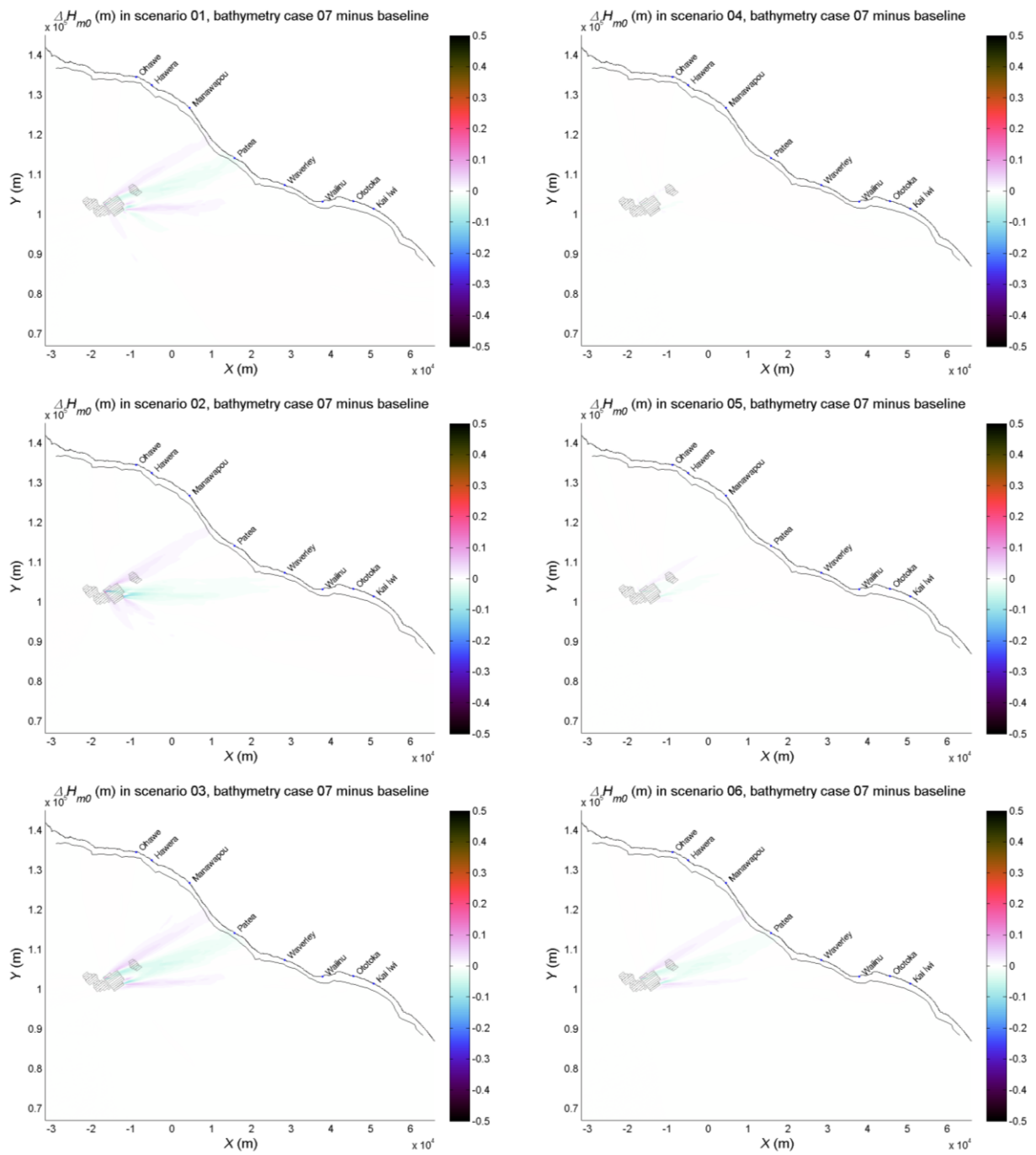


Figure D-20: Difference between significant wave height for case 7 and existing bathymetry, over the model domain, for each of the six environmental scenarios. The locations of the pit and mound used in the simulations are marked in red.

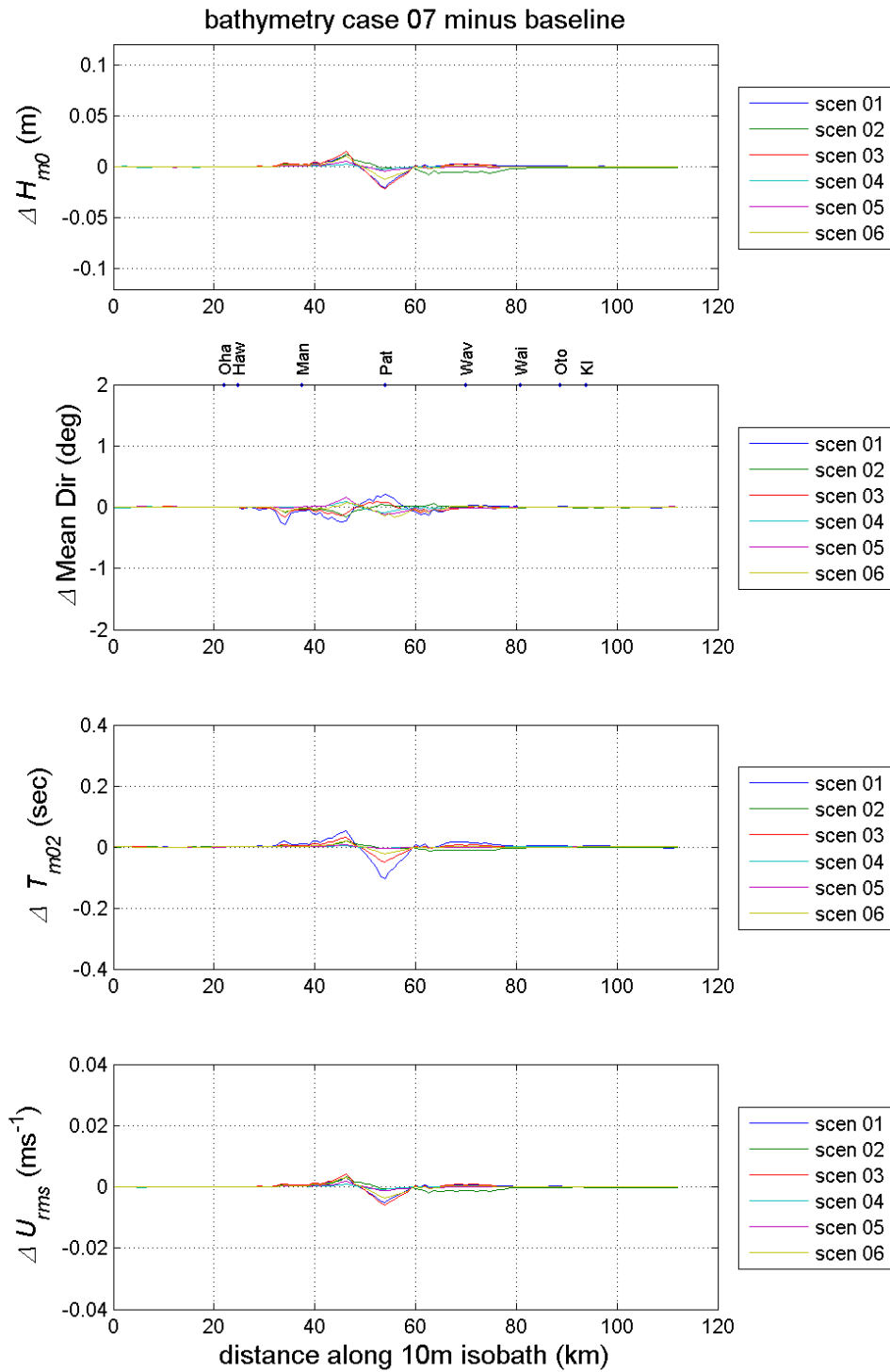


Figure D-21: Difference between wave parameters at the 10 m isobath for case 7 and existing bathymetry, in all 6 environmental scenarios. From top to bottom: significant wave height, mean wave direction, mean wave period, and root-mean-square bed orbital velocity.

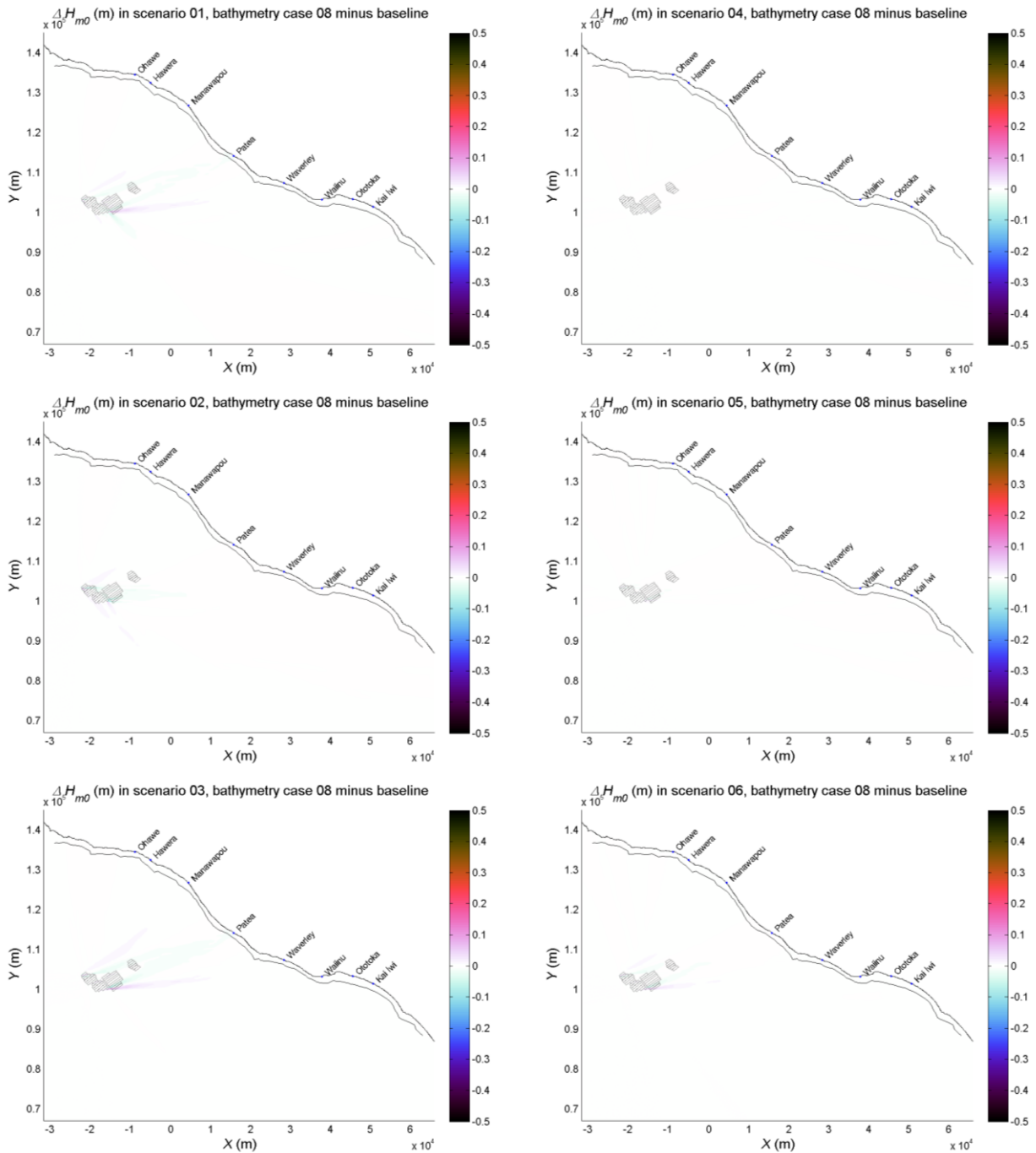


Figure D-22: Difference between significant wave height for case 8 and existing bathymetry, over the model domain, for each of the six environmental scenarios. The locations of the pit and mound used in the simulations are marked in red.

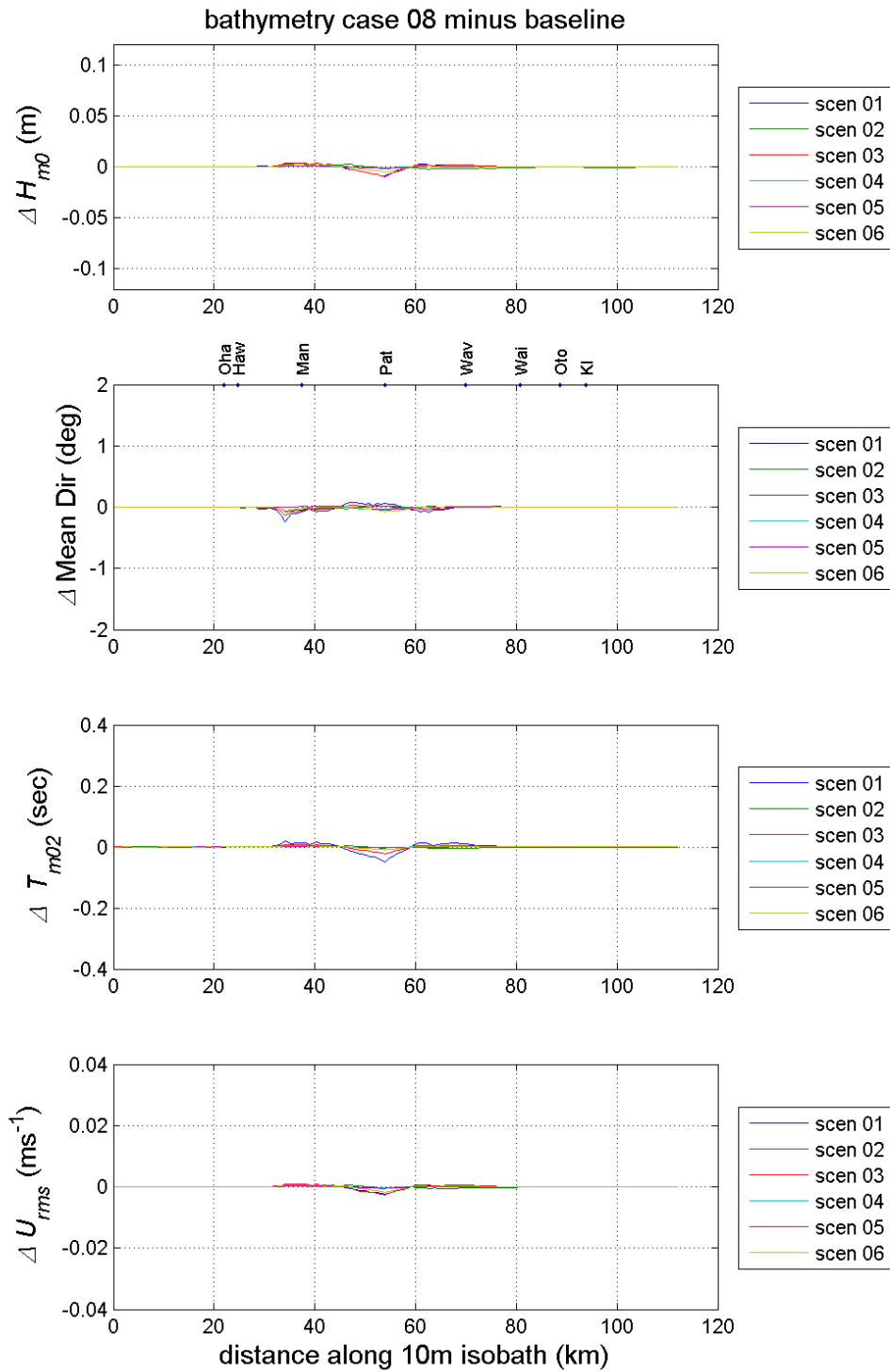


Figure D-23: Difference between wave parameters at the 10 m isobath for case 8 and existing bathymetry, in all 6 environmental scenarios. From top to bottom: significant wave height, mean wave direction, mean wave period, and root-mean-square bed orbital velocity.